Johannes Hummel

Displacement-based seismic design for multi-storey cross laminated timber buildings

Schriftenreihe Bauwerkserhaltung und Holzbau
Heft 8

Johannes Hummel

Displacement-based seismic design
for multi-storey cross laminated timber buildings

kassel
university

press

This work has been accepted by the Faculty of Civil and Environmental Engineering of the University of Kassel as a thesis for acquiring the academic degree of Doktor der Ingenieurwissenschaften (Dr.-Ing.).

1st Reviewer: Prof. Dr.-Ing. Werner Seim, University of Kassel
2nd Reviewer: Prof. Dr.-Ing. Ekkehard Fehling, University of Kassel
3rd Reviewer: Prof. Dr.-Ing. Massimo Fragiacomo, University of L'Aquila (Italy)

Defense day: 23rd September 2016

Editor

Prof. Dr.-Ing. Werner Seim
Universität Kassel
Fachbereich Bauingenieurwesen
Fachgebiet Bauwerkserhaltung und Holzbau
Kurt-Wolters-Straße 3
34125 Kassel
Tel. +49 (0) 561 804 2625
Fax +49 (0) 561 804 7647
wseim@uni-kassel.de
www.uni-kassel.de/fb14/tragwerk/

Preface of the editor

Multi-storey buildings with prefabricated cross-laminated timber elements are gaining increasing popularity due to advantages in terms of building physics, manufacturing efficiencies and structural performance. It can be expected that, not only countries with a long tradition of timber housing but also regions with growing population worldwide will define a significant market for this type of construction in the future.

In this context, seismic impact might become decisive. This trend must be supported by the provision of design procedures for the engineering community which are both reliable and feasible.

From the variety of calculation procedures, which have been proposed for earthquake design of building structures in the past, Johannes Hummel has focused on displacement-based design. He provides parameters and pre-definitions, explains all the necessary steps for application with CLT systems systematically and verifies the procedure by comprehensive studies. Additionally, it can be stated that some parts of his thesis, such as the transfer of provisions for inelastic spectra and the typology of elastic and inelastic spring elements, are of significance beyond the thesis itself.

In my opinion, both the derivations and the outcomes as presented are excellent according to international standards and I am convinced that this thesis provides an important contribution to the better understanding of modern timber structures under earthquake impact. Therefore, I hope for a wide dissemination in both research and engineering communities.

Kassel, January, 2017

Werner Seim

Preface of the author

This thesis was created during my time as a research assistant at the department of Building Rehabilitation and Timber Structures at the University of Kassel.

It is to the credit of my supervisor Professor Dr.-Ing. Werner Seim that this work could be realised, since he encouraged me as student and offered me the chance for a doctoral graduation. I express my sincere gratitude towards him for his patience and confidence in me and my skills. He helped me greatly to find a clear focus. I thank him for his ideas and suggestions which improved this work significantly.

I am proud that I could have Professor Dr.-Ing. Ekkehardt Fehling and Professor Dr. Massimo Fragiacomo to review my thesis, because they are well-known in the scientific community, especially in the field of earthquake engineering. I thank both for the critical evaluation of my thesis and their contribution in the defence commission. Furthermore, I would like to thank Professor Dr.-Ing. Christoph Butenweg and Professor Dr.-Ing. Oliver Reul for being part of the defence commission.

Sincere thanks go to my colleagues and former colleagues Dipl.-Ing. Michael Schick, Dr.-Ing. Lars Eisenhut, Dr.-Ing. Tobias Vogt, Dipl.-Ing. Horst Ulrich, Timo Claus M.Sc., Sonja Kühlborn M.Sc. and Kai Sommerlade M.Sc. for fruitful discussions and helpful suggestions with respect to my research topics. Moreover, they all have been "responsible" for a pleasant and constructive working atmosphere.

I want to thank Guido Osterbart, Dr.-Ing. Thomas Hahn, Dr.-Ing. Wolfgang Römer, Ralf Füllgraf, Willi Pohl, Katharina Knobel and Simone Otto for their assistance in preparing, performing and postprocessing experimental investigations.

Additionally, I would like to thank Bianca Böhner, who managed a couple of organisational tasks and formalities related to my dissertation and my defence.

Finally, a special thanks to my lovely wife, Maria, because she excused me from almost all daily work at home in the final stage of my thesis, which enabled me to concentrate solely on my thesis during that crucial phase. I appreciate her efforts, especially considering that she was pregnant with our son David during that time.

Kassel, January, 2017

Johannes Hummel

Contents

Contents

Notation

Acronyms

2S	Two-storeys
3D	Three-dimensional
4S	Four-storeys
8S	Eight-storeys
AB	Angle bracket
AP	Analysis procedure
BT	Box type
CLT	Cross laminated timber
CoR	Centre of rotation
CSM	Capacity spectrum method
CWO	Continuous wall with openings
DBD	Displacement-based design
DCM	Displacement coefficient method
DDBD	Direct displacement-based design
EC8	Eurocode 8: [EN 1998-1]
exp.	experimental
FBD	Force-based design
HD	Hold down
ISM	Inelastic spectra method
LFM	Lateral force method
LVL	Laminated veneer lumber
N2M	N2 method
NTHA	Nonlinear time history analysis
num.	numerical
PBD	Performance-based design
$P - \Delta$	Second order theory

PGA	Peak ground acceleration
PGV	Peak ground velocity
PP	Performance point
RC	Reinforced concrete
SAWS	Seismic Analysis of Woodframe Structures
SC	Self-tapping screw
MDOF	Multi degree of freedom
SDOF	Single degree of freedom
SWE	Single wall element
SWT	Shear wall type
THA	Time history analysis
YPSM	Yield point spectra method

Greek Upper-case Letters

Δ	Inter-storey drift, increment
Δ_t	Building drift
Γ	Participation factor
Ω	Overdesign factor

Lower-case Letters

a_g	Ground acceleration according to [EN 1998-1]
b_{ef}	Influence length
b_{il}	Width of interlayer
c	Damping coefficient
c_1, c_2, c_R, c_T	Constants to define R_μ-μ-T relationship according to [Vidi94]
c_i	Empirical coefficients of the R_μ-μ-T relationship
d	Lateral displacement on the top of the building, diameter, thickness of CLT elements
d^*	Lateral displacement on the top an equivalent SDOF system
d_{ef}	Effective thickness
d_m^*	Displacement of an equivalent SDOF system at plastic mechanism
d_y^*	Yield displacement of an equivalent SDOF system
f	Eigenfrequency
$f_{u,mean}$	Mean tensile strength

g	Gravity constant
h	Height
h_0	Shear span
k	Stiffness of an SDOF system
k^*	Stiffness of an equivalent SDOF system
k_{ini}, k_{init}	Initial stiffness
l_{cont}	Contact length
l_{ef}	Effective length
l_{SC}	Length of screw
m	Mass of an SDOF system
m^*	Mass of an equivalent SDOF system
$m_{i/j}$	Lumped mass in level i/j
n	Number
p	Uniform vertical load
q	Behaviour factor
$s_{i/j}$	Deflection in level i/j
t	Time
t_{il}	Thickness of interlayer
u	Displacement, deflection
u_0	Initial deflection
$\ddot{u}$	Acceleration
$\ddot{u}_g$	Acceleration of the ground motion record
u_i	Lateral displacement in level i
u_u	Ultimate displacement
$\dot{u}$	Velocity
u_y	Yield displacement
$\boldsymbol{\ddot{u}}$	Vector of acceleration
$\boldsymbol{u}$	Vector of displacement
$\boldsymbol{\dot{u}}$	Vector of velocity
x	x-direction, local
y	y-direction, local
z	z-direction, local

$z_{i/j}$	Altitude in level i/j

Greek Lower-case Letters

α_{el}	Modal mass coefficient for elastic behaviour
α_{inel}	Modal mass coefficient for inelastic behaviour
α_k	Proportionality factor for stiffness proportional damping
α	Modal mass coefficient, coefficient considering force interaction
α_m	Proportionality factor for mass proportional damping
δ	Applied displacement
ϵ	Error index
η	Damping correction factor, degree of utilisation
η_E	Convergence tolerance
γ_{Rd}	Overstrength factor
κ	Correction factor to account for different hysteretic behaviour
λ	Correction factor to account for effective modal mass
μ	Ductility, friction coefficient
μ_k	Friction coefficient for kinematic friction
ν	Poisson's ratio
$\phi_{i/j}$	Deflection of the mode shape in level i/j
ψ_E	Combination coefficient to determine quasi-permanent share [EN 1998-1]
ρ	Wood density
φ	Angle of rotation
ω	Circular frequency
ξ	Damping ratio
ξ_0	Nominal damping ratio
ξ_{eff}	Effective damping ratio
ξ_{eq}	Equivalent damping ratio
ξ_{hyst}	Hysteretic damping ratio

Upper-case Letters

A_{ed}	Seismic action
$\boldsymbol{C}$	Damping matrix
E	Young's modulus

$E_{0,mean}$	Mean Young's modulus of timber in grain direction
E_{bl}	Energy defined as area below the bilinear load-displacement curve
E_d	Dissipated energy
$E_{d,AE}$	Action effect due to seismic action
$E_{d,el}$	Dissipated energy for elastic behaviour
$E_{d,G}$	Action effect due to non-seismic action, quasi-permanent combination
$E_{d,nl}$	Dissipated energy for non-linear behaviour
E_{ef}	Effective Young's modulus
E_{il}	Young's modulus of interlayer
E_m^*	Area under the non-linear capacity spectrum
E_{nl}	Energy defined as area below the nonlinear load-displacement curve
E_S	Strain energy
F	Force
F_b	Base shear
$F_{b,el}$	Base shear for linear-elastic behaviour
$F_{b,nl}$	Base shear for non-linear behaviour
$F_b(t)$	Time-dependent base shear
F_D	Damping force
F^*	Resisting force of an equivalent SDOF system
F_{el}	Elastic strength demand
F_μ	Friction force
F_{inel}	Inelastic strength demand
$F_j(t)$	Time-dependent component force of component j
F_{max}	Maximum force, load-bearing capacity from testing
F_R	Load-bearing resistance
F_S	Resisting force
$\boldsymbol{F}_S$	Vector of inertia forces
G	Gravity load
G_k	Dead load
H	Height
$\boldsymbol{I}$	Vector of unity deflection
$\boldsymbol{K}$	Stiffness matrix

K	Stiffness
K_{ax}	Axial stiffness
L	Length
$\boldsymbol{M}$	Mass matrix
M	Overturning moment
N	Axial force
P	Vertical load, resultant
P_i	Point of the plastic mechanism
$P(t)$	Time-dependent external force
Q	Quantity
Q_k	Live load
Q_{mod}	Quantity modified
R	Resultant load
R_μ	Ductility-dependent reduction factor
R_{eff}	Curvature of the sliding surface
S	Soil factor according to [EN 1998-1]
S_a	Spectral acceleration
S_{ae}	Spectral acceleration of the elastic response spectrum
$S_{a,pi}$	Spectral acceleration at plastic mechanism
$S_{a,y}$	Spectral acceleration at yielding for an equivalent elastic-plastic SDOF system
S_d	Spectral displacement
$S_{d,y}$	Spectral displacement at yielding for an equivalent elastic-plastic SDOF system
S_v	Spectral velocity
T	Period
T_0	Characteristic period to define R_μ-μ-T relationship according to [Vidi94], transition period
T_1	Fundamental period, characteristic period according to [Newm82]
T_C	Control period of the elastic response spectrum according to [EN 1998-1]
T^*	Period of an equivalent SDOF system
T_{el}	Structural period for elastic behaviour
T_{inel}	Structural period for inelastic behaviour
T_{ini}	Initial period
V	Shear force
X	X-direction, global
Y	Y-direction, global
Z	Tensile force
Z	Z-direction, global

1 Introduction

1.1 Motivation and Purpose

Timber and timber-based products have become increasingly attractive as construction material for multi-storey buildings in recent years. The reason for the booming interest in timber structures is mainly the need for sustainable buildings and their outstanding performance in terms of building physics and load-bearing behaviour including earthquake impact. Timber constructions offer high standards regarding demands on building physics and energy consumption. It is possible to erect buildings much faster in comparison to other structural materials due to a high level of prefabrication and a comparatively lightweight construction. There are a large number of companies with great expertise in the prefabrication of structural timber elements. This advances the quality of timber buildings considerably.

Two main construction types have been established for multi-storey timber buildings in Europe. The first one is the traditional light-frame construction which is an assembly of a basic timber frame in combination with sheathing, usually oriented strand boards or gypsum fibre boards. The two parts, frame and sheathing, are connected with nails or staples. The second construction type is the massive wood construction with cross laminated timber (CLT or Xlam). Cross laminated timber is a timber product composed of several crosswise stacked board layers and was developed in Germany and Austria 25 years ago [Augu10]. The high interest in timber for multi-storey buildings is also an achievement of CLT. The latter is suitable for mid- and high-rise buildings due to its high load bearing capacity.

Regarding the seismic performance of timber structures, numerous experimental and analytical investigations have been carried out. Examples are impressive shaking table tests such as on a six-storey wood frame building [Pei10] and a seven-storey CLT-building [Cecc13]. One cannot really derive mathematical relationships directly from such complex tests, but they confirm the "good natural" structural behaviour of timber buildings under earthquake impact. However, timber structures are not a priori earthquake-proof. An appropriate seismic design of elements and details is necessary to ensure sufficient structural behaviour during an earthquake. According to the European standard [EN 1998-1] three main methods – force-based design (FBD), performance-based design (PBD) and the time history analysis – can be employed for seismic design. FBD is still the most common method for engineers in practice. This method uses elastic response spectra scaled by a behaviour factor q to calculate equivalent lateral seismic forces. On the other hand the non-linear time history analysis (NTHA), as the most comprehensive calculation method, is used to study the dynamic behaviour of a structural system close to reality. The NTHA needs ground motion records of real earthquakes or artificial accelerograms, a definition of non-linear hysteretic behaviour of the structural elements and efficient analysis software to determine the dynamic response of the structure in terms of inertia forces and deformations characteristics.

Alternatively, PBD can be used for the seismic design of multi-storey timber structures. The advantage of PBD is that buildings can be designed based on predefined characteristics and independent of behaviour factors q. Different displacement-based design (DBD) procedures as part of PBD have been developed in the last five decades [Free98; Fajf99; Prie00] and adapted for timber structures, see e.g. [Fili02; Pang07; Merg15]. However, a systematic study on the limitations and the application of DBD with reference to multi-storey CLT buildings has not yet been conducted.

This is where the present work becomes relevant. The purpose of this thesis is the application and the validation of DBD for multi-storey CLT buildings. This objective will be achieved on the basis of an analytical study of reference structures and a systematic comparison of design methods. The analytical study will obtain a basic understanding of the performance of the CLT construction under seismic action for different structural configurations. The comparison of different analysis methods will reveal the capabilities and limitations of DBD as a design method for multi-storey CLT buildings. It appears to be reasonable to focus on the CLT construction because of the potential of this material for engineered structures on the one hand and because of the ongoing discussion about basic definitions of structural characteristics on the other hand. The debate is mainly about an appropriate behaviour factor q. Several studies on the seismic behaviour of CLT structures were performed (see chapter 3) which aimed at the determination of a behaviour factor for the CLT construction. However, the research community does not yet completely agree upon the definition of behaviour factor q for CLT. This implies that the seismic performance of CLT structures is not yet fully understood.

This thesis intends to provide improved DBD procedures for low- and mid-rise CLT buildings which might be an alternative to the behaviour-factor-based seismic design. These procedures should be suitable for different configurations of CLT structures. This thesis should also have an exemplary nature for engineers in practice regarding the development of appropriate structural models for non-linear analyses and DBD of multi-storey CLT buildings. Input parameters and relationships, which are required for the application of DBD to CLT structures, will be provided. A further aim is the evaluation of existing DBD procedures in terms of their suitability for use with multi-storey CLT buildings.

1.2 Methodology

The structural behaviour of the CLT construction under seismic action will be evaluated by experimental and numerical investigations. The non-linear behaviour of substructures will be investigated by means of cyclic tests under realistic boundary conditions (see Fig. 1.1). Based on the test results, a hysteretic model which will be used in numerical simulations can be adjusted.
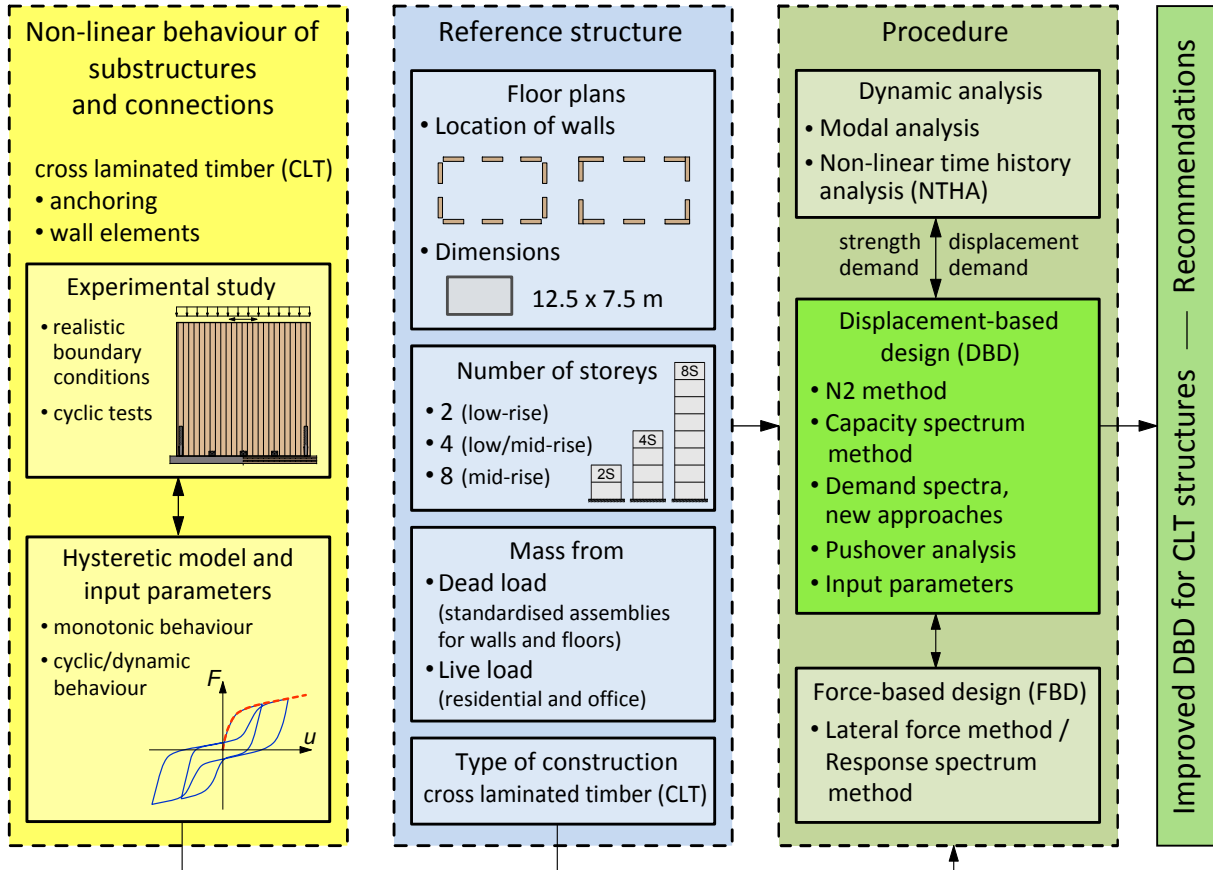
Figure 1.1: Methodology

Analysis models of CLT reference structures will be developed considering different configurations of the lateral load-resisting system and a multiple number of storeys (see section 5.3). Masses which are typical for residential and office buildings in respect of dead load and live load will be included. Three-dimensional (3D) structural models will be developed which are incorporated for DBD (see chapter 6) and NTHAs (see section 5.4). The reference structures will be designed preliminarily by means of force-based design. Equivalent structural models and earthquake action will be considered for all analysis procedures to allow a comparison of analysis results.

This work focuses on two common DBD methods – N2 method [Fajf99] and capacity spectrum method [Free98]. The inelastic behaviour of the structure is represented by a capacity curve from non-linear pushover analysis, respectively, a capacity spectrum. The seismic action is defined by inelastic or damped spectra. The inelastic response for a specific seismic event is found if the demand spectrum and the capacity spectrum intersect at the so-called performance point.

New approaches for the definition of the demand spectrum will be proposed based on the evaluation of test results (see chapter 4) and preliminary dynamic analyses (see section 6.1). Input parameters for non-linear analyses will be provided in section 5.1. The DBD procedures developed will be validated against results from NTHAs based on the strength and displacement demand.

In chapter 2, the fundamentals of structures under earthquake impact will be elaborated and the analysis methods will be introduced. Experimental and analytical investigations studying the seismic performance of multi-storey timber structures, especially CLT, which were carried out in the past will be presented in chapter 3. A review of modelling approaches of multi-storey CLT structures and the application of DBD to CLT structures will also be given in that chapter.

2 Structures under Earthquake Impact

Earthquakes are ground motions which are caused mainly by a relative movement of tectonic plates, e.g. the plate boundary of the African plate and Eurasian plate as depicted in Figure 2.1a. When one plate slides along another one, stresses occur in the Earth's crust which becomes degraded abruptly. Through this degradation of stresses, a substantial amount of energy – in the form of seismic waves – will be released.

Since these seismic waves occur deep in the Earth's crust – in the range of 5 to 40 km below sea level [Bach02] – and change their characteristics while propagating, the local seismic risk for buildings can differ significantly from place to place. It can be traced back basically to an interaction of three main factors [Müll84]

    (1) the seismicity of the region (building location),

    (2) ground conditions (local ground and deep geology) and

    (3) the vibration behaviour of the structure (resonance, non-linear processes)

which will be discussed briefly in the following sections.

2.1 Seismicity and ground conditions

The seismicity of a specific region can be expressed in various ways. A classification which is focused on structural design purposes where the seismicity is represented by the horizontal ground acceleration. Therefore, seismic hazard maps with peak values of the horizontal ground acceleration are provided, for example, by GIARDINI ET AL. [Giar03] or can be found in the national annexes of Eurocode 8 (e.g. [DIN EN 1998-1]).

The peak ground acceleration (PGA) indicates the highest acceleration of the local ground. The PGAs in seismic hazard maps are usually representative of stiff soil like rock. With reference to the horizontal PGA, regions can be classified from very low to very high seismic hazard as displayed in Table 2.1.

Earthquake hazard potential	Peak ground acceleration (PGA) in m/s^2	in g
Very low hazard	0 - 0.4	0 - 0.04
Low hazard	0.4 - 1.4	0.04 - 0.14
Medium hazard	1.4 - 2.4	0.14 - 0.24
High hazard	2.4 - 4.0	0.24 - 0.40
Very high hazard	> 4.0	> 0.40

Table 2.1: Seismic classification based on peak ground acceleration (PGA) [Schm06]

The seismic hazard in Europe reach from regions with a very high seismic hazard located in Southeast Europe (Italy, Greece and the Balkans) to regions without any seismic risk, as shown in Figure 2.1a.

Since earthquakes are extraordinary natural events whose occurrence is unpredictable, these maps are created on the basis of records from previous seismic activities and advanced statistics. The horizontal accelerations in Figure 2.1 correspond to a return period of 475 years with 10 % probability of exceedance in 50 years. The return period is a statistical parameter representing the distance of time between two decisive events. The probability of exceedance describes the possibility that a certain percentage of events can lie over the expected values (here PGA) within a reference period (here 50 years). That means that higher PGAs may occur within a period of 50 years in 10 % of cases.

(a) Europe   **(b)** Germany
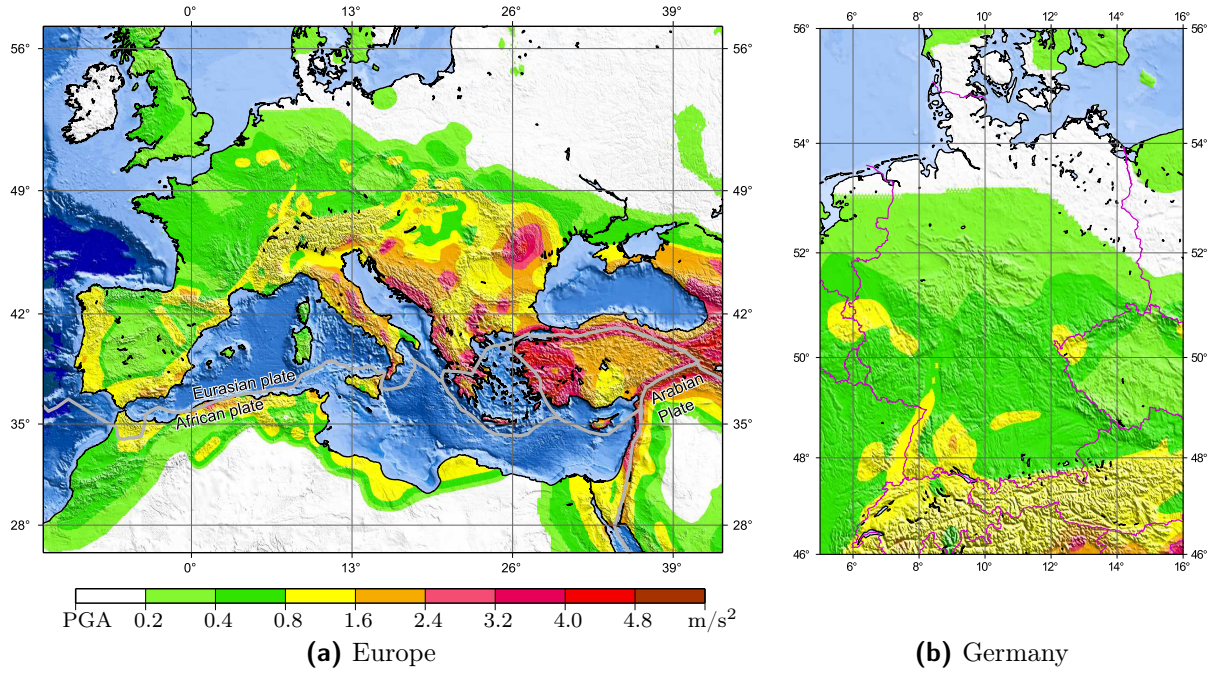
Figure 2.1: Seismic hazard maps for horizontal PGA [Giar03]

The horizontal accelerations as defined in Figure 2.1 are also termed *reference peak ground acceleration*, as they relate exclusively to the probability of exceedance, mentioned previously, and to stiff soil.

However, in many cases the ground conditions differ from stiff soil. Other ground conditions such as sand, gravel or clay lead to an amplification of the ground acceleration [Newm82] and yield a shift of the most critical range of ground shaking for any structure. This amplification effect is considered with soil factors. Whereas the European standard [EN 1998-1] considers only ground types which are not subdivided, the German standard [DIN EN 1998-1/NA] distinguishes between local ground conditions (depth up to 20 m) and deep geology (deeper than 20 m).

For a detailed discussion please refer to [Müll84; Bach02; Smit88; Clou93].

2.2 Structural Vibration Behaviour

While the previous section discussed impact and risk which result from natural activity and hence cannot be controlled, this section looks at the structural behaviour under dynamic loading.

Vibrations within the structure are the structural response caused by dynamic excitations such as earthquakes which are time dependent in contrast to static actions. The structure

response can, however, be controlled in a predictable way and the structural vibration behaviour describes the performance of buildings under dynamic excitation. There are a number of parameters which characterise the vibration behaviour of a structural system:

(1) eigenfrequency – stiffness and mass,

(2) viscous damping and

(3) energy dissipation.

The first fundamental parameter is the eigenfrequency f respectively the period T. The eigenfrequency represents the relation between structural stiffness k and mass m as equation (2.1) indicates.

$$f = \frac{1}{T} = \frac{1}{2 \cdot \pi} \cdot \omega \tag{2.1}$$

with the circular frequency

$$\omega = \sqrt{\frac{k}{m}} \tag{2.2}$$

This equation is the solution of the equation of motion for a single degree of freedom (SDOF) system, see Figure 2.3a, see Eq. (2.3), for linear dynamics and free vibration.

$$m \cdot \ddot{u} + c \cdot \dot{u} + F_S(u) = P(t) \tag{2.3}$$

with m mass
         c damping coefficient
         F_S resisting force, $F_S = k \cdot u(t)$ for linear-elastic systems
         $P(t)$ external force, $P(t) = 0$ for free vibration
         $\ddot{u}$ absolute acceleration, $\ddot{u}(t) = \mathrm{d}^2 u / \mathrm{d}t^2$
         $\dot{u}$ relative velocity, $\dot{u}(t) = \mathrm{d}u / \mathrm{d}t$
         u relative displacement

The equation of motion includes the relation between the resisting inner force and the lateral displacement ($F_S - u$–relationship) which can be elastic or inelastic.

The most critical case for the vibration response is when the frequency of the excitation meets the natural frequency of the structure (resonance domain). Then the structural vibration will be amplified.

The relevant accelerations appear in a frequency range of approximately 0.5 to 10 Hz for earthquakes (see Fig. 2.2). The natural frequency of normal buildings with up to four to five storeys range from nearly 1 to 10 Hz. The natural frequency decreases for higher buildings but is mainly in the frequency range which also applies to earthquakes. However, there is a higher sensitivity for normal buildings than for high-rise buildings. This is illustrated in Figure 2.2, which shows the spectral density of the dynamic action effects wind and earthquake in relation to the frequency range of the main types of structures. The spectral density is the result of signal processing of a time series. The time series is analysed in terms of its frequency content and the corresponding amplitude.
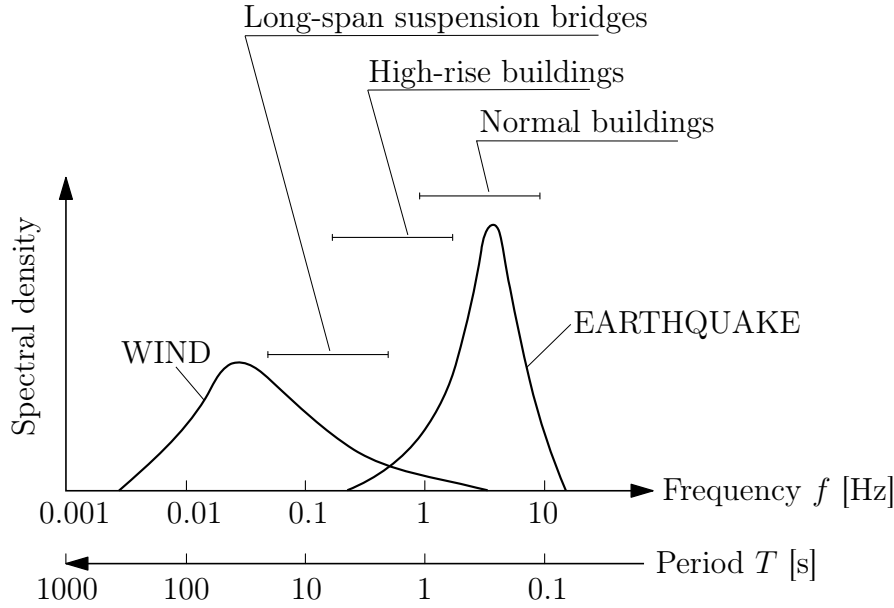
Figure 2.2: Spectral density of the action effects wind and earthquake in relation to the range of the natural frequency of main types of structures, after [Augu84]
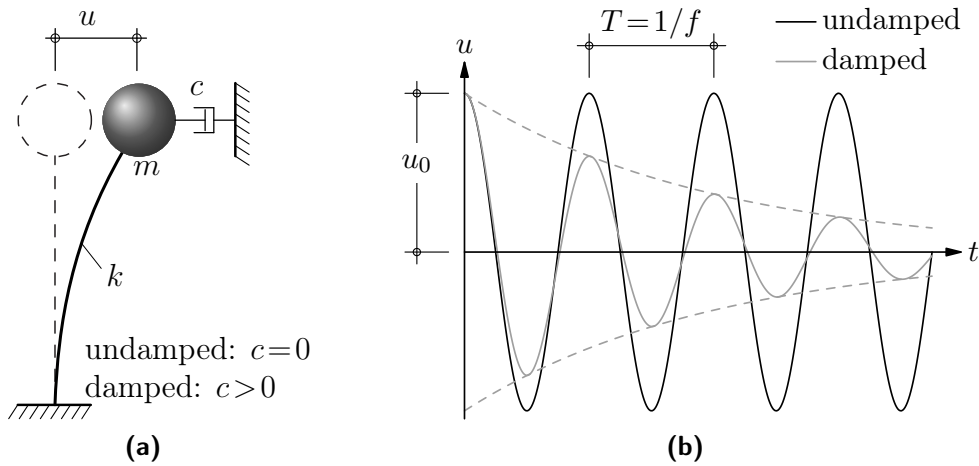
Figure 2.3: (a) SDOF-system (free vibration) and (b) harmonic vibration of an undamped and damped SDOF-system

The natural frequency of multi-storey buildings can be determined by different approaches similar to Eq. (2.1) or by full modal analysis, see for example [Kein67; Bach02; Brun11; Seim14]. Therefore, the distribution of mass and stiffness are required as input parameters. While mass distribution is comparatively easy to describe – given by gravity loads considering permanent service loads – the determination of stiffness is not that simple [Seim14]. This applies especially to timber structures and indicates that the natural frequency stands and falls with the attempt of stiffness of the structure. Derivation of stiffness characteristics for CLT elements will be discussed in detail in chapters 4 and 5.

The amplitude of a free shaking system decreases gradually with time (see Fig. 2.3b). This effect is caused by damping processes due to energy dissipation while vibrating. Where damping reduces the vibration amplitude, it does not affect the natural frequency, significantly (see Fig. 2.3b). Damping effects are of different natures: Damping, for example, can be obtained in a material's micro-structure or in contact areas due to friction.

Comparatively simple mathematical models were developed to capture the principal aspects of damping. One of these mathematical models – linear viscous damping – was already introduced in Eq. (2.3). Linear viscous damping defines a damping force F_D to be proportional to velocity $\dot{u}$.

$$F_D = c \cdot \dot{u} \tag{2.4}$$

The damping coefficient c can be calculated with

$$c = 2 \cdot \xi \cdot \omega \cdot m \tag{2.5}$$
$$= 2 \cdot \xi \cdot \sqrt{k \cdot m}. \tag{2.6}$$

The damping ratio ξ is typically determined by means of experimental tests. Estimates of the damping ratio for different materials are given in Table 2.2.

material	$\xi\,[\%]$
reinforced concrete (RC)	1 to 2
steel	0.4 to 1
timber	1 to 3
masonry	1 to 2

Table 2.2: Ratio of viscous damping ξ for linear elasticity [Kein67; Werk08]

The linear viscous damping model is used to capture energy dissipation effects for linear-elastic behaviour. Under extreme loads such as heavy earthquakes, energy dissipation is mainly caused by plastic deformations of structural elements. The structural behaviour is then completely non-linear. The amount of energy which can be dissipated by non-linear deformation depends on the plastic deformation capacity of single structural elements coacting in a three-dimensional (3D) structure. The plastic deformation capacity is also called ductility μ and is defined as the ratio between ultimate deformation u_u and yield deformation u_y. For the definition of ductility according to Eq. (2.7) the real load-displacement curve needs to be idealised towards an elastic-plastic curve (see Fig. 2.4)

$$\mu = \frac{u_u}{u_y} \tag{2.7}$$

In order to transfer the real load-displacement curve into an equivalent bilinear curve, yield displacement u_y and ultimate deformation u_u have to be identified. In particular, the definition of the yield point might become difficult, since load-displacement curves do not usually exhibit a specific point where yielding occurs. Different methods are available to determine the yield displacement, see e.g. PARK [Park89] and MUÑOZ ET AL. [Muño08]. The definition of yield displacement and ultimate deformation will be discussed more precisely in context of experimental investigations (see section 4) and displacement-based design (see section 6). Limitations of the ultimate deformation u_u are governed mainly by drift limits and post failure behaviour.
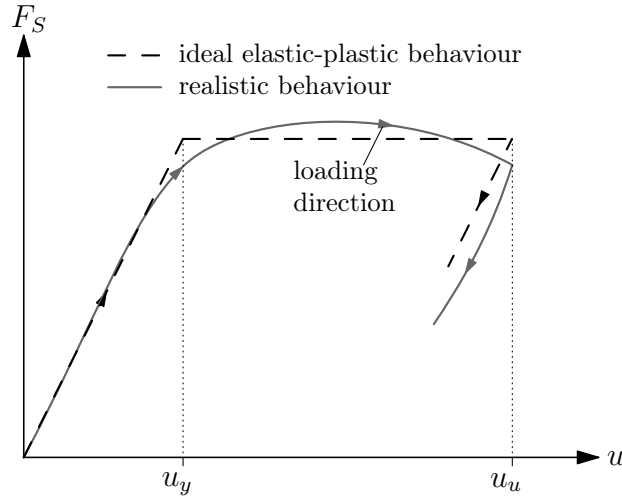
Figure 2.4: Idealisation of a load-displacement curve, definition of yield displacement u_y and ultimate deformation u_u

The two contributions which account for energy dissipation – damping and ductility – are illustrated schematically in Figure 2.5.
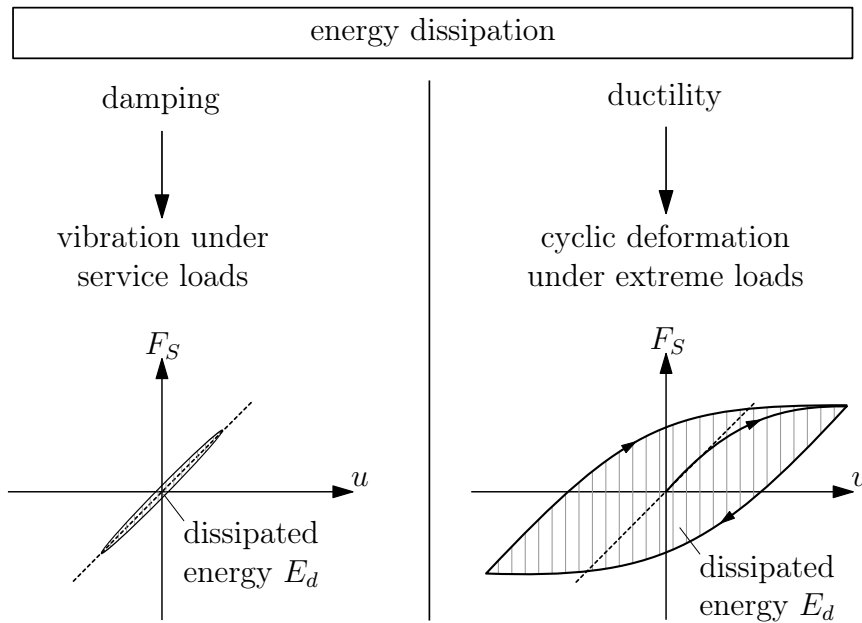
Figure 2.5: Contributions to energy dissipation – damping and ductility [Pete96]

The energy which can be dissipated by damping or plastic deformation is equal to the area which is enclosed by the load-displacement curve. Such load-displacement curves – called hysteresis – are formed under cyclic or dynamic loading (see section 4). It becomes clear from Figure 2.5 that the energy dissipation capacity is significantly higher for ductile behaviour than for linear elastic behaviour with viscous damping.

However, the energy dissipation capacity is dominated by the hysteretic behaviour of structural elements.
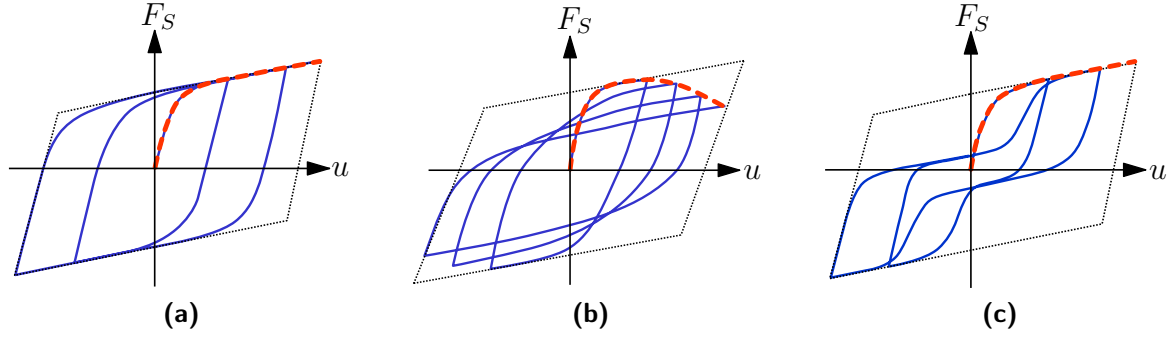
Figure 2.6: Types of hysteretic behaviour (schematic); (a) elastic-plastic, (b) elastic plastic with loss of strength and stiffness, and (c) pinched

The energy which is dissipated within one hysteresis loop depends on the material and structural detailing such as connections, as well as the type of loading (see Fig. 2.6). The ideal shape is a robust hysteresis with simple yielding, also termed elastic plastic hysteretic behaviour (see Fig. 2.6a). The elastic-plastic hysteretic behaviour is representative of steel structures. Figure 2.6b shows the hysteretic behaviour with loss of strength and stiffness. Reinforced concrete (RC) structures may exhibit such a behaviour. A further shape is the pinched hysteresis curve (see Fig. 2.6c), which is typical for timber structures (see sections 3 and 4).
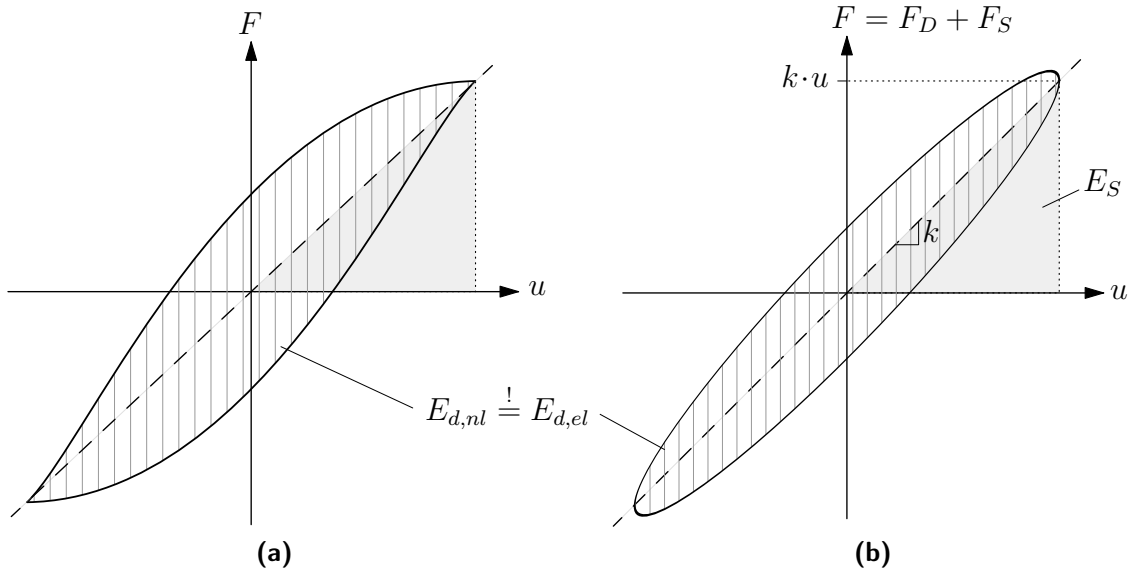
Figure 2.7: Hysteretic and linear damping

Energy dissipation caused by inelastic behaviour can be interpreted as a damping effect. In order to describe non-linear hysteretic behaviour with the same approach as for viscous damping, a common procedure is to linearise the non-linear damping behaviour. The linearisation is achieved by substituting the actual hysteresis loop (see Fig. 2.7a) with an ellipse of equal area (cf. Fig. 2.7b). That leads to the hysteretic damping approach according to Eq. (2.8). The elliptic curve (see Fig. 2.7b) ensues when linear behaviour and viscous damping are assumed. This approach was first presented by CHOPRA [Chop95].

$$\xi_{hyst} = \frac{E_d}{4 \cdot \pi \cdot E_S} \tag{2.8}$$

with E_d dissipated energy per cycle
         E_S strain energy, $E_S = \frac{1}{2} \cdot k \cdot u^2 = \frac{1}{2} \cdot F \cdot u$

2.3 Representation of seismic actions

Earthquakes have an effect in all three spatial dimensions. However, the effects acting in the horizontal directions are most critical for regular multi-storey buildings. For that reason horizontal ground accelerations are defined. The horizontal peak ground acceleration alone (see section 2.1) is not sufficient to describe the characteristic of earthquakes with respect to structural design. Specific information, such as maximum amplitude and frequency content of the local ground excitation, is necessary. Depending on the calculation method (see section 2.4), time series or response spectra are used to represent the ground motion.

2.3.1 Time History

The progress of displacement u_g, velocity $\dot{u}_g$ and acceleration $\ddot{u}_g$ of the ground over time can be measured with seismographs during an earthquake. Such a time series can be used directly for earthquake analysis. There are databases available, such as *PEER Strong Ground Motion Database* [Anch14] or *European Strong-Motion Data* [Ambr02], where time history data can be found. Such databases usually provide the ground motion records along three components of the translational acceleration (accelerogram) – two horizontal and one vertical (see Fig. 2.8). With accelerograms the intensity of the earthquake can be categorised by means of the absolute value of acceleration – PGA (see section 2.1) – as well as the duration of the earthquake. The PGA for stiff soil is equivalent to the ground acceleration a_g as used in [EN 1998-1].

Time histories of real earthquakes can be used for experimental and numerical investigations on structures and structural elements. However, no two time histories are the same even for the same earthquake if records from different monitoring places are compared. As the maximum acceleration and the frequency content also differ, it is advisable to use several time histories for design purposes.
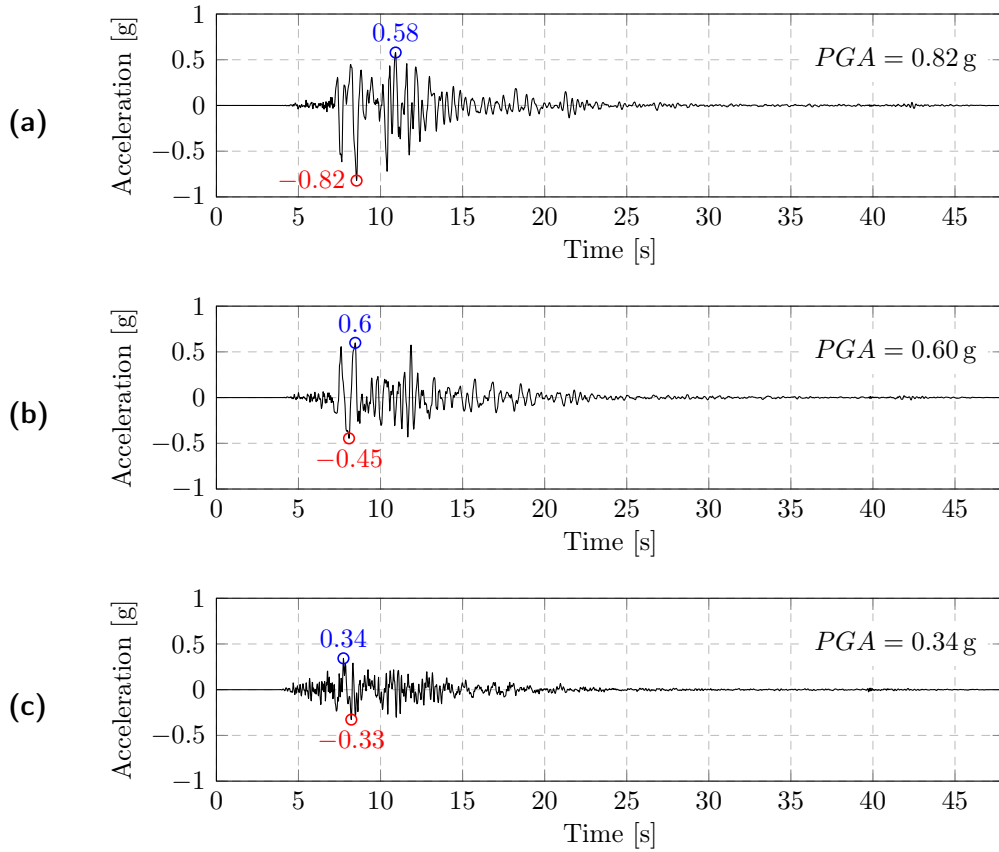
Figure 2.8: Time history of the Kobe earthquake in 1995; (a) horizontal north-south (NS) component, (b) horizontal east-west (EW) component, (c) vertical component

2.3.2 Response Spectra

A response spectrum is a compact description of the seismic action. Response spectra were introduced in combination with the response spectrum method (see section 2.4) for simplified earthquake analysis in which the principles of static structural design are used.

A response spectrum can be created by resolving the equation of motion for a plethora of SDOF systems – each with a different eigenfrequency – under earthquake excitation, see Eq. (2.3). Here, the external force is given by Eq. (2.9).

$$P(t) = -m \cdot \ddot{u}_g \tag{2.9}$$

However, such a pure spectrum (see Fig. 2.9) is still inconvenient for the seismic design of buildings. Smoothed response spectra could be derived on the basis of investigations of NEWMARK [Newm82]. Since a smoothed response spectrum covers a wider range of accelerograms and a general definition of the spectrum can be given which also considers different soil conditions, it is more suitable for engineering design.

In the meantime a few different types of response spectra have evolved (see below). The type of the response spectrum depends mainly on the calculation method (see section 2.4). However, the basis of different spectra is the elastic response spectrum. It is a generalised representation of the response of linear elastic SDOF-systems. Elastic response spectra are defined by code regulations (e.g. [EN 1998-1]). The following three spectral values are distinguished corresponding to the three types of motion:
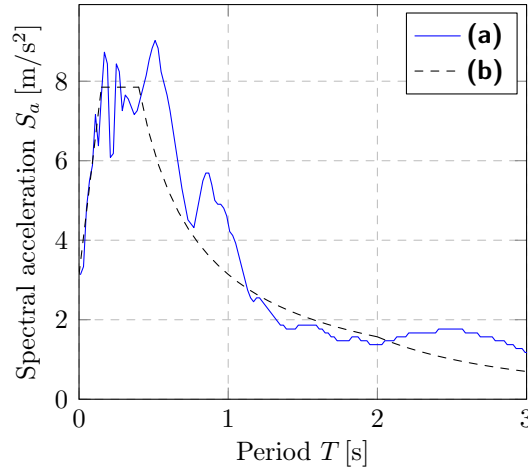
Figure 2.9: (a) elastic response spectrum of the El Centro earthquake 1940 (NS component, $PGA = 3.14\,\mathrm{m/s^2}$) with 5% damping and (b) smoothed response spectrum (for rock, $a_g = 3.14\,\mathrm{m/s^2}$, $\xi = 5\%$) according to [EN 1998-1]

- spectral acceleration S_a,
- spectral velocity S_v and
- spectral displacement S_d.

The most common form of the elastic response spectrum is the S_a-T–diagram (spectral acceleration over period, see Fig. 2.9) with 5 % damping. However, the elastic response spectrum can be adapted for other damping ratios (see Tab. 2.2). Equation (2.10) is applied to convert spectral acceleration into spectral velocity and spectral displacement.

$$S_a = \omega \cdot S_v = \omega^2 \cdot S_d \tag{2.10}$$

The different elastic response spectra are depicted in Figure 2.10. All three spectral values can also be summarised in one diagram (see Fig. 2.10c). For design purposes only spectral acceleration and spectral displacement are required.

The following response spectra are used with reference to structural seismic design:

Design Spectra
The design spectrum is basically a scaled elastic response spectrum. The elastic response spectrum is scaled by a reduction factor – called behaviour factor q. The behaviour factor q generally considers energy dissipation due to plastic deformations (see section 2.2) which lead to a reduction of the inertia loads within the structure. The q-factor is an estimate of the real structural behaviour of a 3D structure in the post-elastic range. The application is limited to construction types for which q-factors are defined.

Inelastic Spectra
An inelastic spectrum is obtained by considering an inelastic SDOF system with realistic hysteretic behaviour. Various researchers have worked on this topic (e.g. MIRANDA & BERTERO [Mira94]). The outcomes of these investigations are different approaches towards a reduction factor R_μ depending on ductility and eigenfrequency to derive inelastic spectra from the elastic response spectrum. Different non-linear structural behaviour was considered to determine consistent formula for the R_μ-factor. However, a general definition of the inelastic spectrum can not be found for the wide variety of different structural elements and systems.

Damped Spectra

A damped spectrum is an elastic response spectrum which is scaled by the value of equivalent viscous damping – a combination of hysteretic damping and viscous damping. Equivalent viscous damping ξ_{eq} accounts for energy dissipation caused by inelastic deformations (see section 2.2). By means of equivalent viscous damping the energy dissipation capacity for arbitrary hysteretic behaviour is considered.
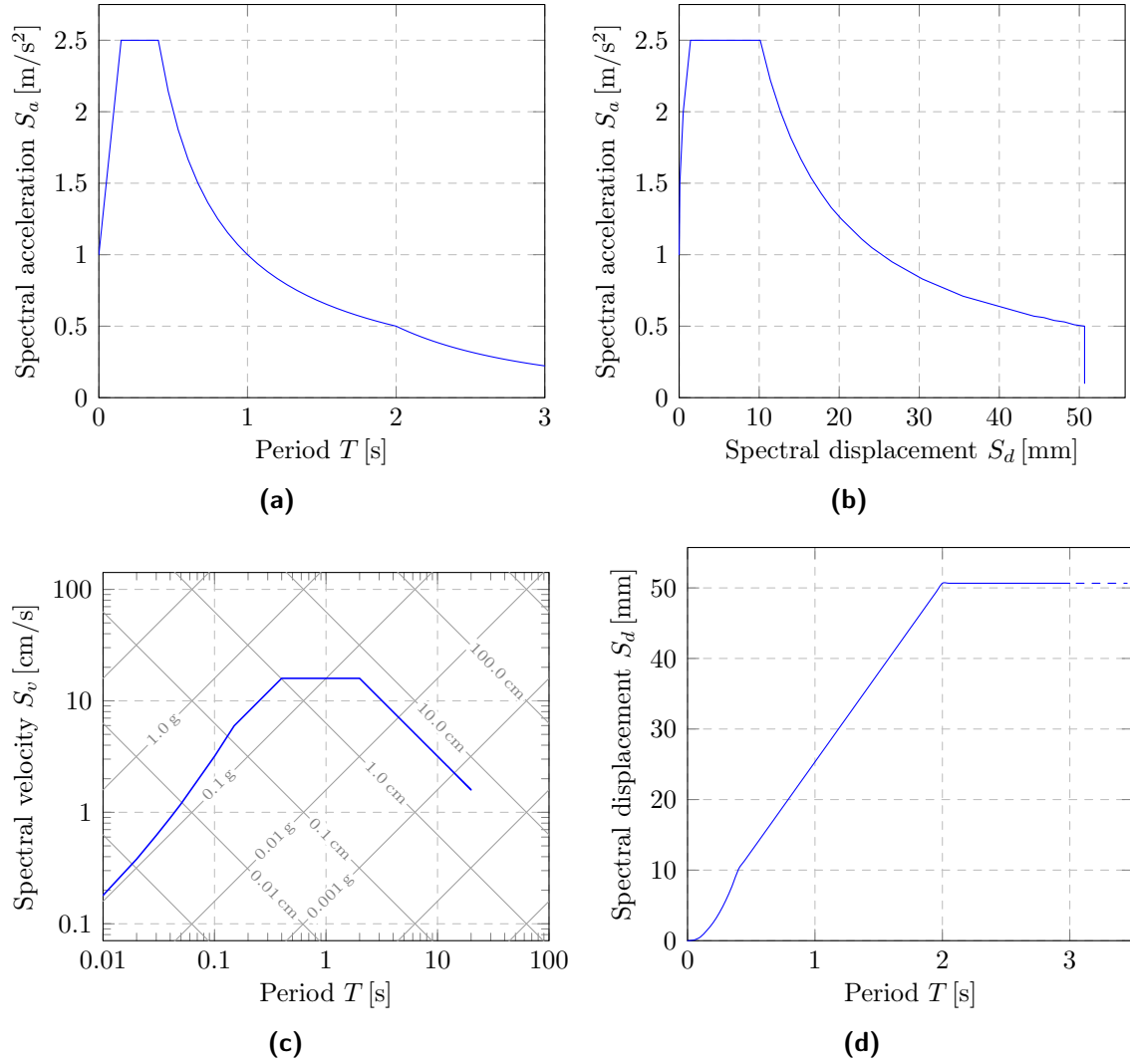
Figure 2.10: Different representations of the elastic response spectrum (soil type rock, $a_g = 1.0\,\mathrm{m/s^2}$, $\xi = 5\%$) according to [EN 1998-1]; (a) spectral acceleration over period, (b) spectral acceleration over spectral displacement, (c) spectral velocity over period (logarithmic), and (d) spectral displacement over period

Further details to the different types of spectra will be given in context with the calculation methods in section 2.4.

2.3.3 Artificial Time Series

Using time series which correspond to elastic response spectra for dynamic analyses and tests on shaking tables are indispensable to make results comparable. In most cases, ground motion records of real earthquakes do not really match the elastic response spectrum (e.g. Fig. 2.9). For that reason artificial time series are used for full dynamic analysis and for testing. Such artificial time series can be generated on the basis of the elastic response spectrum (see Fig. 2.11).
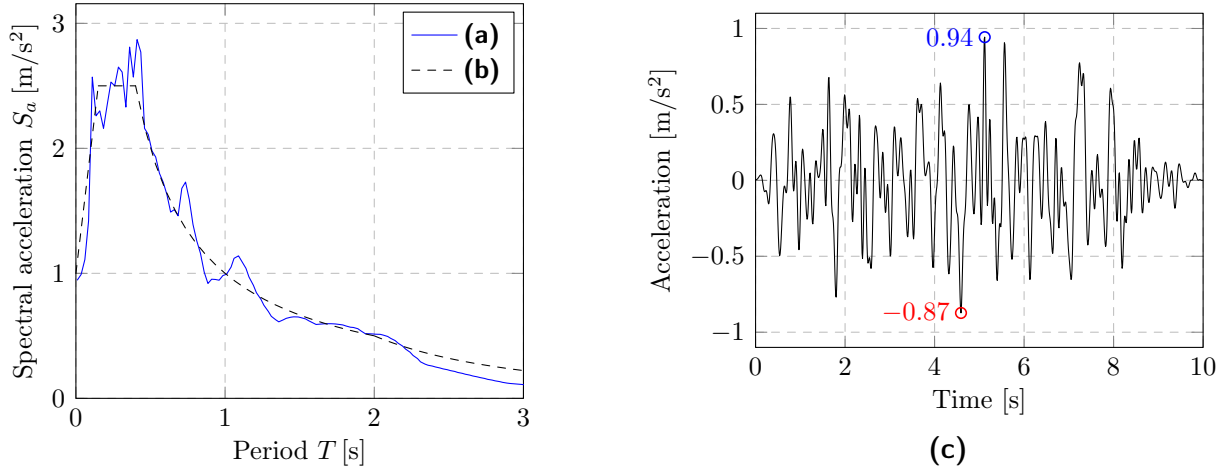
Figure 2.11: (a) Elastic response spectrum of the artificial time history in Figure 2.11c, (b) elastic response spectrum (see Fig. 2.10a) and (c) artificial time history compatible to elastic response spectrum

The generation of an artificial ground motion record ("synthetic earthquake") from elastic response spectra is described, for example, by MESKOURIS ET. AL. [Mesk11] and MÜLLER AND KEINTZEL [Müll84]. In general, synthetic earthquakes are based on random processes.

2.4 Calculation methods and numerical modelling

2.4.1 Overview

Different calculation methods can be used for the design of buildings and other structures under earthquake impact (see Tab. 2.3):
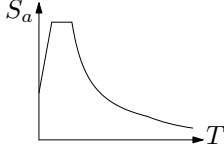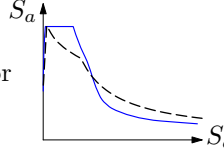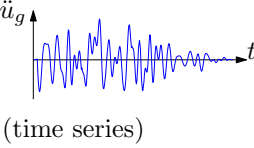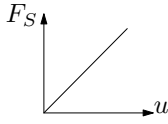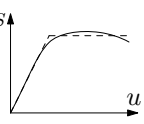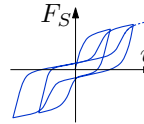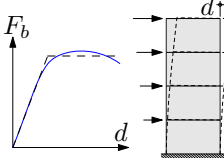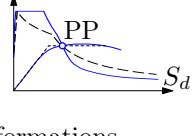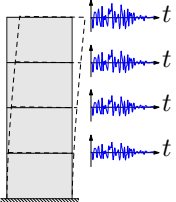
- force-based design (FBD),
- performance-based design (PBD) and
- dynamic response analysis.

Force-based design is the first choice engineering method. A linear elastic analysis is used to determine the component stresses as a result of equivalent lateral force representing the seismic action (*lateral force method*).

The PBD refers to a methodology in which structural design criteria are expressed in terms of performance objectives, see [Ghob01; ATC-40]. Drift limits are common performance criteria. This implies that a displacement-based design (DBD) is suitable for achieving predefined performance objectives (see section 6). Displacement-based design is usually related to non-linear static analyses.

The dynamic response analysis is a general method to solve dynamic problems. Herein, the non-linear time history analysis (NTHA) is a convenient calculation method to study the structural behaviour under earthquake impact very close to reality.

Table 2.3 gives a brief overview of the calculation methods, the corresponding parameters required for input and their outcomes of analysis. The three methods are presented in the table from left to right with increasing reference to reality and complexity. It must be noted that the DBD procedure illustrated in Table 2.3 is not representative of all DBD approaches, but it goes back to the beginning of displacement-based design (see section 2.4.3). Depending on the calculation methods – FBD and DBD – different response spectra are taken as demand spectra. The different types of response spectra and how they are defined are described in section 2.3.2.

	LATERAL FORCE METHOD (LFM)	DISPLACEMENT-BASED DESIGN (DBD)	NONLINEAR TIME HISTORY ANALYSIS (NTHA)
INPUT	design spectrum scaled by q	inelastic or damped spectrum	ground motion (time series)
	distribution of stiffness and mass		
	component behaviour, linear model	component behaviour, non-linear model	component behaviour, hysteretic model
			damping model
OUTPUT	spectral acceleration S_a → base shear F_b → equivalent lateral forces F_i → component forces	capacity curve (via pushover analysis) → performance point (PP) → inter-storey drifts → component deformations	time series of: acceleration, velocity and displacement in each level → time series of: component forces $F_j(t)$, base shear $F_b(t)$

Table 2.3: Calculation methods for earthquake analysis

Proper analysis models and suitable analysis programs are required to perform earthquake analysis with the methods displayed in Table 2.3. Numerical models in combination with finite element software (FE software) are commonly employed. High-performance computer programmes, such as ABAQUS [Dass] or OPENSEES [McKe], are indispensable for non-linear static analyses and, in particular, for non-linear dynamic analyses.

Associated with the given calculation methods different levels of discrimination of a structure are possible:

- single degree of freedom (SDOF) model,
- multiple degree of freedom (MDOF) model, or
- detailed 3D model.

SDOF models or SDOF systems have already been presented in section 2. An MDOF model is a cantilever beam with lumped masses. Masses of the structure are concentrated in the floor level. These are planar models which can only capture lateral deflection without torsional effects. Three-dimensional models are applied to consider effects which can hardly be incorporated by planar systems, such as

- realistic distribution of vertical loads from roof/floor slab to structural elements,
- interaction between horizontal and vertical loads, and
- 3D interaction of slab and wall elements.

Further influences are P-Δ effects and irregularities in plan and elevation which can be good reasons to use 3D models.

In any case, the analysis model must account for the component behaviour – linear or non-linear – and the distribution of mass and stiffness. Masses which result from gravity loads – dead load and the quasi-static share of live load – should be considered for seismic analyses.

$$m = \left(G_k \text{ "+" } \psi_E \cdot Q_k\right)/g \tag{2.11}$$

with G_k dead load

Q_k live load

ψ_E combination coefficient to determine quasi-permanent share of the live load according to [EN 1998-1]

g gravity constant, $g = 9.81 \, \text{m/s}^2$

Seismic design of buildings structures is usually narrowed to excitations in the horizontal directions. Nevertheless, there are some cases where the vertical component should also be considered:

- horizontal cantilever components,
- large spans,
- beams or slabs which support columns, and
- high vertical acceleration or special characteristics of the ground motion in vertical direction.

There is basic guidance given in standards and guidelines – such as [EN 1998-1; FEMA 273; FEMA 274; FEMA 440; FEMA P695; Deie10] – on how to model real structures with reference to requirements regarding the calculation method. The implementation of the analysis models into analysis programmes, as used for numerical simulations, is explained in detail in section 5. The calculation methods are further elaborated in the following subsections.

2.4.2 Lateral Force Method

The lateral force method is a simplification of the response spectrum method where only the first period T_1 of the structure is considered. The full response spectrum method incorporates all relevant vibration contributions, not only the first one. However, a linear elastic analysis forms the basis in both cases.

Within the lateral force method the base shear F_b is calculated as product of the mass of the structure m and spectral acceleration S_a. The base shear represents the sum of all inner forces which arise inside the structure due to earthquake impact.

$$F_b = S_a(T_1) \cdot m \cdot \lambda \qquad \text{with } m = \sum m_i \tag{2.12}$$
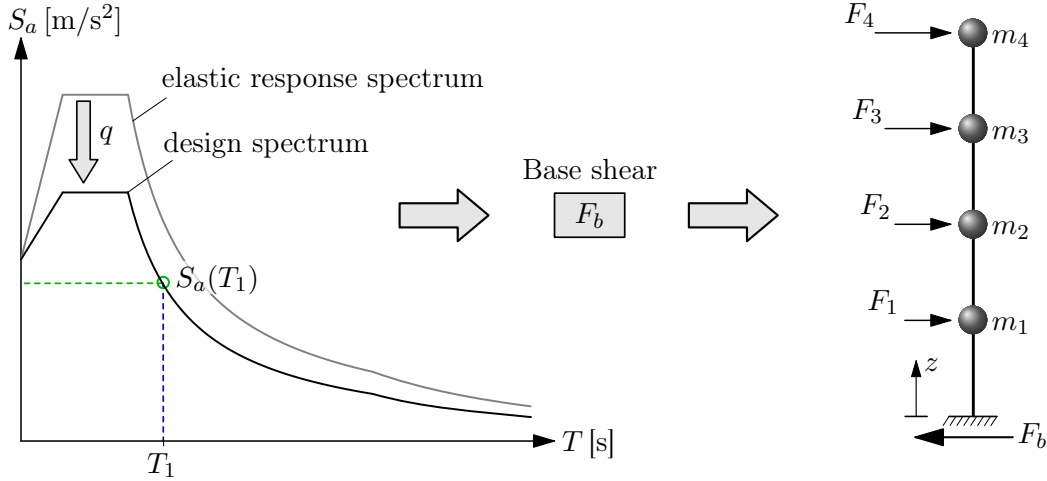
Figure 2.12: Basic procedure of the lateral forces method

The spectral acceleration is obtained from the design spectrum for the period of the structure. The factor λ accounts for the effective seismic mass of multi-storey buildings.

Equivalent lateral forces F_i are determined from the base shear for each floor level.

$$F_i = F_b \frac{z_i \cdot m_i}{\sum z_j \cdot m_j} \tag{2.13}$$

With these equivalent lateral loads a linear, static analysis is carried out to determine the component forces. These forces are used to design structural components. The structure is commonly represented as an equivalent MDOF system for the determination of base shear and equivalent lateral forces (see Fig. 2.12).

The procedure is relatively simple, however, there are at least two parameters which should be discussed initially. The first is the behaviour factor q and the second is the fundamental period T_1.

The behaviour factor q is used to transfer the elastic response spectrum into the design spectrum (see section 2.3.2). [EN 1998-1] provides specific values of the behaviour factor depending on the structural material and construction type. However, it should be kept in mind that q-values are rough estimations in order to capture various conditions on the level of a 3D structure and single elements. Furthermore, it must be noted that the behaviour factors which are given in [EN 1998-1] can only be reached if it is guaranteed that a brittle failure of any part of the structure does not occur. Therefore, capacity design principles should be followed [Paul90; Paul92; Foll11].

Moreover, the determination of the structural period is subject to a couple of uncertainties. There are several methods available to compute the fundamental period [Seim14]. From this variety a method should be selected which can capture the main effect of the structural system. One of these methods is the RAYLEIGH equation [Rayl77] which is convenient, for example, for timber structures. A cantilever beam with lumped masses (see Fig. 2.12) might be used to account for distribution of mass and stiffness of the structure. The cantilever beam is described by the parameters bending stiffness (EI) and shear stiffness (GA). The definition of stiffness is essential in this context. However, [EN 1998-1] does not provide specific information whether the elastic tangent stiffness or a reduced tangent stiffness should be applied.

2.4.3 Displacement-based Seismic Design

In contrast to FBD, DBD is independent of the eigenfrequency of the structure. Components forces result directly from the so-called pushover analysis. Thus, the seismic performance of the structure can be determined for the post-elastic range. The illustration in Table 2.3 refers to the capacity spectrum method (see below). However, this method was the basis for several DBD procedures.

DBD procedures – overview

Several DBD procedures have been developed for different purposes in the last decades (see Tab. 2.4). The first step to DBD was to substitute the structural system by an equivalent linear system which reproduces the energy dissipation capacity [Shib76; Soze83].

Method		Purpose	References
capacity spectrum method	CSM	evaluation of the seismic performance of existing or retrofitted structures and seismic design of new buildings, including concrete constructions	FREEMAN ET AL. [Free04; Free98; Free78; Free75]
displacement coefficient method	DCM	seismic assessment of existing buildings and design of new buildings, including moment-resisting frames and wall structures from steel or reinforced concrete	KRAWINKLER ET AL. [Gupt98; Sene97; Rahn93; Nass91]
direct displacement-based design	DDBD	seismic design for a specified performance level of moment-resisting frames and wall structures, dual wall/frame buildings, bridges, seismically isolated structures and wharves including reinforced and prestressed (precast) concrete, structural steel, masonry and timber	PRIESTLEY ET AL. [Prie07b; Prie07a; Sull06; Sull04; Prie00; Prie93]
inelastic spectra method	ISM	seismic design of buildings and evaluation of existing buildings, different materials can be considered	CHORPA AND GOEL [Chop01; Chop99a; Chop99b]
N2 method	N2M	seismic evaluation of both existing and newly designed buildings, including concrete and steel structures with moment-resisting frames characteristics	FAJFAR ET AL. [Fajf05; Fajf00; Fajf99; Fajf96; Fajf94; Vidi94; Fajf88]
yield point spectra method	YPSM	design for different performance levels, comparatively simple, including concrete structure	ASCHHEIM ET AL. [Asch03; Asch00; Asch99]

Table 2.4: Overview of displacement-based design (DBD) procedures

Based on that FREEMAN ET AL. [Free78; Free75] proposed the first coherent DBD method which was later called capacity spectrum method (CSM). Herein, the basic idea had been to create the capacity curve by means of a pushover analysis, using dynamic characteristics to convert the capacity curve into the S_a-S_d format and find an intersection point with the demand spectrum indicating the displacement demand as a graphical solution (see Tab. 2.3). FREEMAN ET AL. used damped spectra as demand spectra. KRAWINKLER ET AL. [Rahn93; Nass91] focused on a non-graphical method where the displacement demand is determined by a set of parameters which account for the inelastic dynamic behaviour of the structure. Both methods – the capacity spectrum method and the displacement coefficient method – are presented in the document [ATC-40]. A reverse procedure was proposed by PRIESTLEY ET AL. [Prie07b; Prie00] where displacement or inter-storey drifts are the initial stage of design. Therefore, PRIESTLEY makes use of displacement-period spectra (S_d-T format) instead of the S_a-S_d format. CHOPRA AND GOEL [Chop99a; Chop99b] suggested a procedure based on the capacity spectrum method including inelastic spectra as demand spectra instead of damped spectra. FAJFAR [Fajf05] developed a method which uses the methodology of CSM in combination with inelastic spectra. However, the method was synchronised for a R_μ-μ-T relationship which is typical for steel and concrete structures [Vidi94] and was termed N2 method. ASCHHEIM [Asch03] presented a procedure with a similar format and a graphical solution as used in CSM. This method – called yield point spectra method – requires the definition of a yield displacement to create inelastic spectra and to determine displacement demand and base shear.

Some of these methods have aimed at seismic design for new buildings and others focused on checking seismic performance of existing structures. Three methods – CSM, DDBD and the N2 method – have matured for seismic design of buildings [Prie00]. [EN 1998-1] refers to the N2 method in annex B. CSM and DDBD, however, have not yet found their way into the European Standard. The reason is that [EN 1998-1] did not adopt the linear substitute structure approach upon which CSM and DDBD are based [Merg15].

Capacity spectrum method and N2 method

The N2 method can be introduced in parallel to CSM for the following reasons:
- CSM is the basic DBD method and allows a graphical solution.
- The N2 method uses basically the same procedure, except the definition of the demand spectrum.
- The seismic action is defined in the same format (S_a-S_d format): inelastic spectra for the N2 method and damped spectra for CSM.

Figure 2.13 shows the main steps for DBD of multi-storey buildings with CSM and N2 method including performance levels as part of performance-based design. It should be noted that the scheme was adapted slightly in order to cover both methods.

Both methods make use of the premise that the MDOF system of a multi-storey building can be reduced to a SDOF system. This allows the utilisation of response spectra to represent the seismic action (see section 2.3.2). The global behaviour of the structure is determined by means of a non-linear static analysis - the pushover analysis. Therefore, the component behaviour of the structure and the elastic response spectrum are required as input for the analysis (see Table 2.3). Outcomes of both methods are target values of base shear and lateral displacement. The latter is used to determine inter-storey drifts and component deformations. Inter-storey drifts can than be employed to check performance objectives.
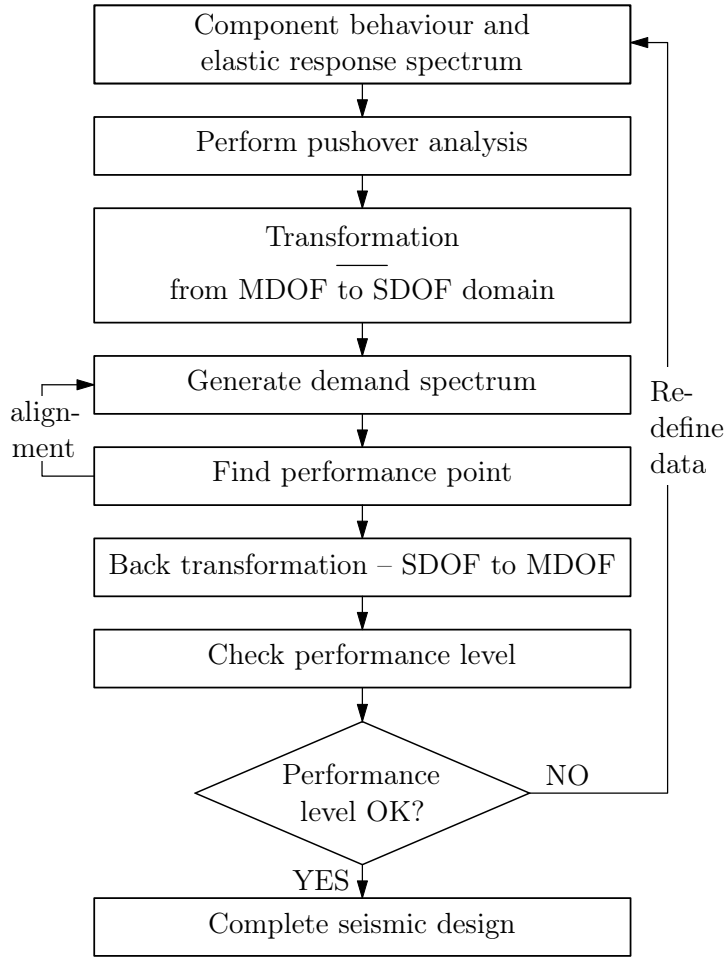
Figure 2.13: Main steps of DBD with CSM and N2 method

Input data

The elastic response spectrum and member characteristics As input data for the analysis have to be defined first. CSM and N2 method require the elastic response spectrum in the S_a-S_d format (see section 2.3.2). Predefined seismic performance levels are considered, such as inter-storey drift limits. Member characteristics are defined as load-displacement relationship (F_S-u relationship). Therefore, analytical approaches can be used, if available, or F_S-u relationships can be derived from substructure testing (see section 4). Furthermore, distribution of masses, respectively, gravity loads must be known.

Pushover analysis

The pushover analysis builds the basis of the two DBD methods considered and is applied to create the capacity curve. The capacity curve represents the inelastic building capacity as a relationship between base shear F_b and the control displacement d (see Fig. 2.14). The displacement of the roof at the centre of the mass – termed *top displacement* – is usually taken as the control displacement. The capacity curve is determined for constant gravity loads and monotonically increasing lateral loads with different load patterns. According to [EN 1998-1] at least two lateral load distributions – *uniform* pattern and *linear* pattern – should be applied.

$$F_i = \frac{s_i \cdot m_i}{\sum s_j \cdot m_j} F_b \qquad \begin{array}{ll} \text{uniform:} & s_{i/j} = 1 \\ \text{linear:} & s_{i/j} = z_{i/j} \end{array} \qquad (2.14)$$
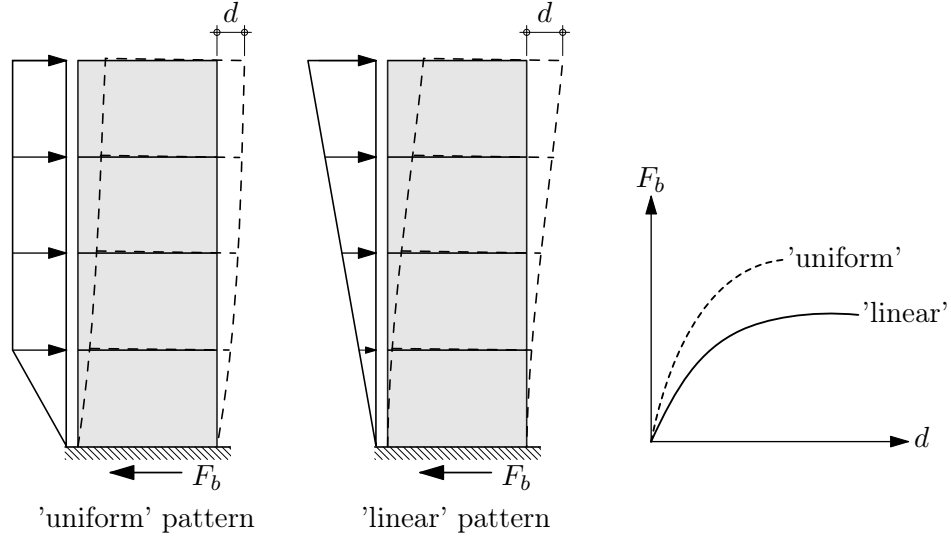
Figure 2.14: Pushover analysis – load patterns for uniform mass distribution and capacity curve

The *uniform* load pattern presumes that the acceleration in each level is constant. This means that the lateral forces are proportional to mass. The *linear* pattern is an approximation of the first elastic mode shape for bending. In that case, $s_{i/j}$ can be replaced by $z_{i/j}$ and Eq. (2.13) applies which means that the distribution of lateral forces is proportional to height and mass.

Application of different load patterns are intended to represent the distribution of inertia forces [Kraw98] and to account for different mode shapes, since DBD is directly connected with the modal transformation (see below).

[EN 1998-1], [ATC-40] and [FEMA 440] provide additional information regarding the application of the non-linear static pushover analysis.

The Newton Raphson method or modifications of it are applied to solve the non-linear static problem, see for example [Wrig08].

Modal transformation

The DBD procedures make use of the principles of the modal analysis to transform an MDOF system into an equivalent SDOF system. By means of the modal transformation the relation between distribution of masses and horizontal deformation amplitude of the structure is considered. Normalised deformation shapes (mode shape) are taken for the characterisation of the lateral deformation of the structure. The distribution of masses is approximated by a MDOF system with lumped masses. Figure 2.15 shows a MDOF system with exemplarily four masses and the first elastic mode. The basic procedure is to calculate modal parameters for the first mode shape. Advanced procedures also involve higher order mode effects (see e.g. [Aydi03]).

The basic procedure will be presented, once briefly. The equivalent mass m^* represents the mass of the equivalent SDOF system and results from weighting each mass m_i by the corresponding amplitude of the mode shape ϕ.

$$m^* = \sum_{i=1}^{n} m_i \cdot \phi_i \qquad (2.15)$$

Furthermore, the participation factor Γ is used to convert base shear and top displacement.

$$\Gamma = \frac{\sum\limits_{i=1}^{n} m_i \cdot \phi_i}{\sum\limits_{i=1}^{n} m_i \cdot \phi_i^2} = \frac{m^*}{\sum\limits_{i=1}^{n} m_i \cdot \phi_i^2} \tag{2.16}$$

This relationship for Γ is determined by right multiplication and left multiplication of the equation of motion of MDOF systems (see section 2.4.4) with the mode-shape vector $\boldsymbol{\phi}$.

In addition, the capacity spectrum method makes use of the modal mass coefficient α. Here the following relationship applies:

$$\Gamma \cdot m^* = \alpha \cdot m \qquad \rightarrow \alpha = \frac{\Gamma \cdot m^*}{m} = \frac{\left[\sum\limits_{i=1}^{n} m_i \cdot \phi_i\right]^2}{\sum\limits_{i=1}^{n} m_i \cdot \sum\limits_{i=1}^{n} m_i \cdot \phi_i^2} \tag{2.17}$$
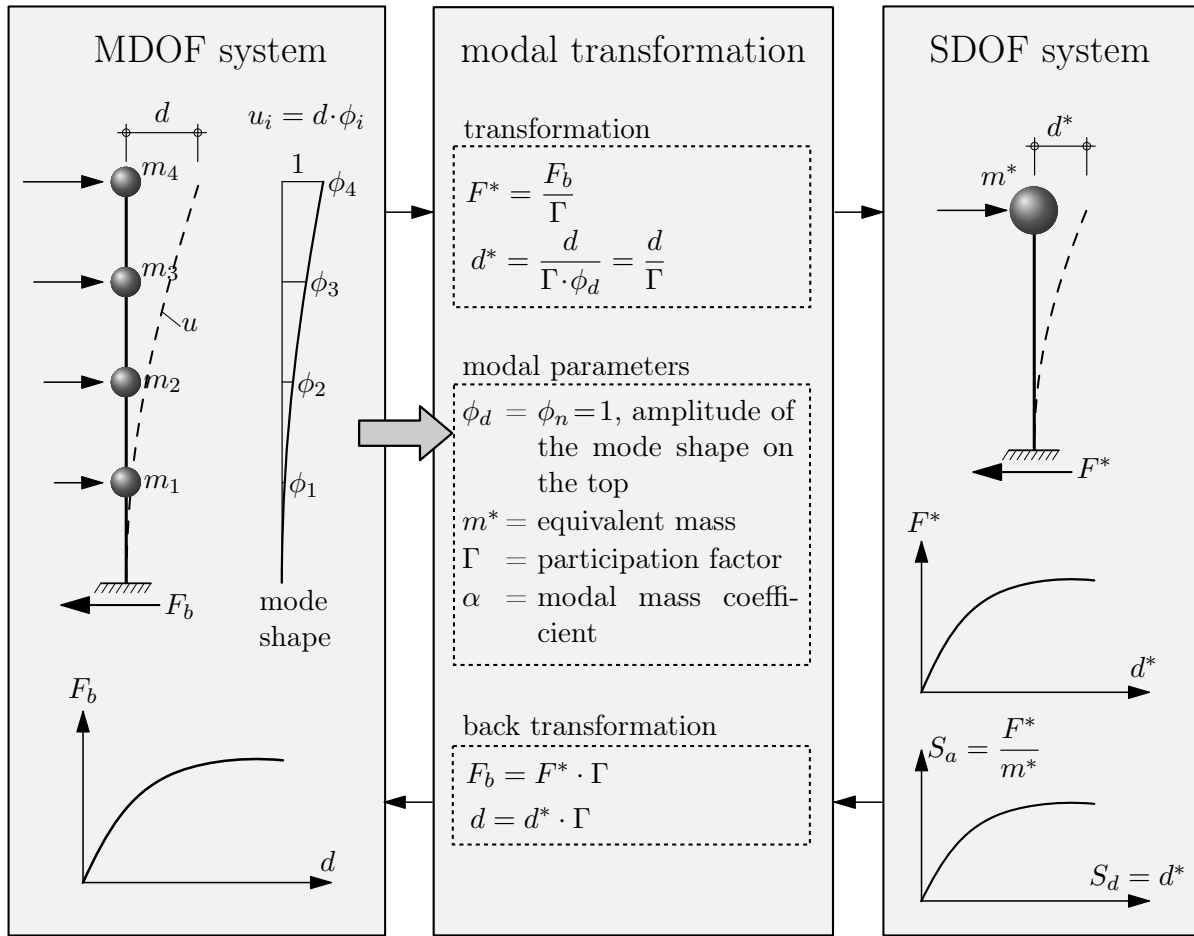
Figure 2.15: Transition between MDOF system and SDOF system

The modal parameters define the transition between the MDOF and the SDOF system respectively the capacity curve and the capacity spectrum. The spectral values for the

capacity spectrum are determined with Eqs. (2.18) and (2.19)

$$S_a = \frac{F^*}{m^*} = \frac{F_b}{\Gamma \cdot m^*} = \frac{F_b}{\alpha \cdot m} \tag{2.18}$$

$$S_d = \frac{d}{\Gamma \cdot \phi_d} = \frac{d}{\Gamma} \tag{2.19}$$

The procedure normalises the mode shape in such a way that the amplitude of the mode shape on the top ϕ_d is equal to 1. If arbitrary normalised mode shapes are included, the amplitude ϕ_d has to be considered in the determination of the deflection of the equivalent SDOF system d^* and the spectral displacement S_d, respectively.

The nomenclature chosen does not exactly refer to the one used in the [ATC-40] document, where only the first mode shape is considered for transformation. In fact, the presented formulae for transformation presented are consistent with the N2 method and they are more general, since they allow the inclusion of arbitrary mode shapes.

The same relationships are used later to reconvert SDOF quantities into MDOF quantities.

Demand spectrum and performance point

In contrast to the previous steps, which are more or less the same for both methods, CSM and N2 method use completely different definitions to create the demand spectrum. This becomes clear from Table 2.5. The capacity spectrum method makes use of equivalent viscous damping to convert the elastic response spectrum into the demand spectrum. The N2 method uses an inelastic spectrum, which is obtained from the elastic response spectrum by means of the bilinear R_μ-μ-T relationship depicted (see section 2.3.2).

Effective damping and ductility have to be determined on the basis of the capacity spectrum. Then, the capacity spectrum is checked for an intersection with the demand spectrum (see Fig. 2.16). This point is termed *performance point* and indicates the seismic performance of the equivalent SDOF system with respect to the maximum acceleration and the maximum relative displacement.
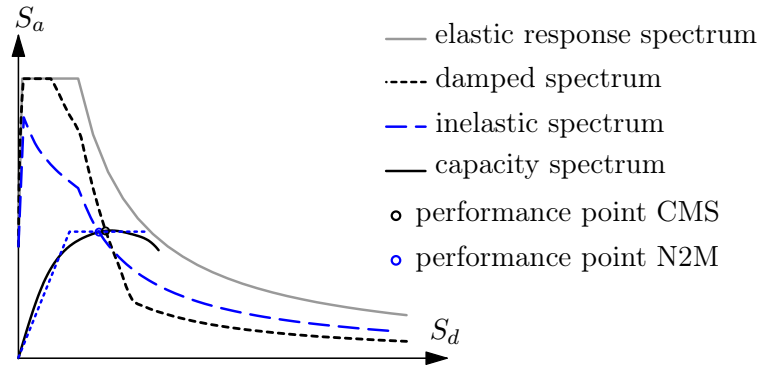
Figure 2.16: Performance point determination with CSM and N2 method

It might be more convenient to generate a transition curve as the demand spectrum for CSM [Kawa99] to eliminate an adverse iteration process. Therefore, damping approaches which are dependent or independent of lateral deflection can be applied [Fili02; Humm15]. Within the procedure presented in Table 2.5 which is the procedure proposed by FREEMAN ET AL. [Free78; Free75] effective damping is a function of the weighting factor κ. Values for κ are given in [ATC-40] depending on the hysteretic behaviour of the structure.

The N2 method allows a closed-form solution due to the bilinear R_μ-μ-T relationship (see Tab. 2.5).
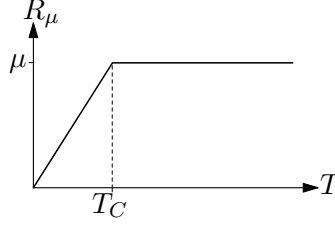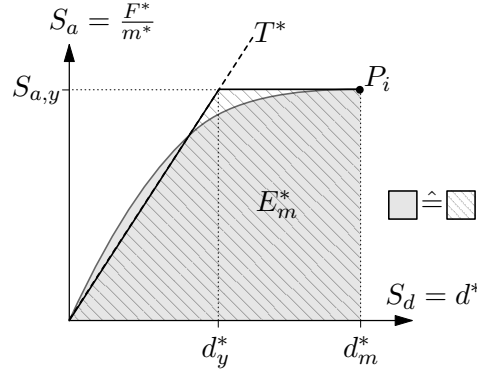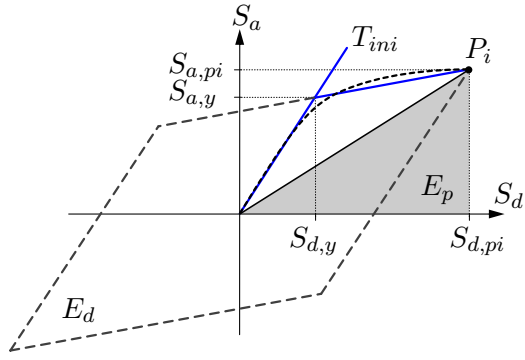
CSM	N2 method
Spectral values for damped spectra	Spectral values for inelastic spectra

<table>
<tr><td>

Spectral values for damped spectra

$$S_a = S_{ae}(\eta) \tag{2.20}$$

$$S_d = \frac{T^2}{4 \cdot \pi^2} S_{ae}(\eta) \tag{2.21}$$

using the damping correction factor

$$\eta = \sqrt{\frac{10}{5 + \xi}} \geq 0.55 \tag{2.22}$$

for damping values $\xi \neq 5\%$ (see section 2.3.2)

Equivalent viscous damping is obtained by

$$\xi_{eff} = \xi_0 + \kappa \cdot \xi_{eq} \tag{2.23}$$

and

$$\xi_{eq} = \frac{2}{\pi} \cdot \frac{S_{a,y} \cdot S_{d,pi} - S_{d,y} \cdot S_{a,pi}}{S_{a,pi} \cdot S_{d,pi}} \tag{2.24}$$

ξ_0 – nominal damping ratio
(5% or see Tab. 2.2)

κ – modification factor account for hysteresis behaviour

A definition of the initial stiffness is required to determine the initial period T_{ini}. Equal energy under the non-linear and the bilinear capacity spectrum is considered.

</td><td>

Spectral values for inelastic spectra

$$S_a = \frac{S_{ae}}{R_\mu} \tag{2.25}$$

$$S_d = \frac{\mu}{R_\mu} \cdot \frac{T^2}{4 \cdot \pi^2} S_{ae} \tag{2.26}$$

with the R_μ-μ-T relationship

determining the the period T^*

$$T^* = 2 \cdot \pi \sqrt{\frac{d_y^*}{S_{a,y}}} = 2 \cdot \pi \sqrt{\frac{m^* \cdot d_y^*}{F_y^*}} \tag{2.27}$$

with

$$d_y^* = 2 \cdot \left(d_m^* - \frac{E_m^*}{S_{a,pi}} \right) \tag{2.28}$$

and the reduction factor R_μ

$$R_\mu = \frac{S_{ae}(T = T^*)}{S_{a,y}} \tag{2.29}$$

ductility μ is given by

$$\mu = (R_\mu - 1)\frac{T_C}{T} + 1 \quad \text{with } T \leq T_C \tag{2.30}$$

$$\mu = R_\mu \quad\quad\quad\quad\quad \text{with } T > T_C \tag{2.31}$$

</td></tr>
</table>

Table 2.5: Determination of the demand spectrum according to CSM and N2 method

2.4.4 Time history analysis

In contrast to the static procedures (see section 2.4.2 and 2.4.3), the structural response for earthquake impact can be predicted in the time domain with the time history analysis. The inelastic component behaviour under cyclic ground motion is considered directly by means of implemented hysteresis models (see Tab. 2.3). Energy dissipation which is traced back to damping in the linear range or other non-modelled effects is considered as viscous damping. The dynamic response of the structure is usually computed for multiple input ground motions because of the inherent variability of different ground motion records (see section 2.3.1).

The equation of motion as given in Eq. (2.32) must be solved within NTHA for systems with MDOF under earthquake excitation $\ddot{u}_g$.

$$\boldsymbol{M}\ddot{\boldsymbol{u}} + \boldsymbol{C}\dot{\boldsymbol{u}} + \boldsymbol{F}_S(\boldsymbol{u}) = -\boldsymbol{M}\boldsymbol{I}\ddot{u}_g(t) \tag{2.32}$$

Mass matrix and gravity loads

It is usually adequate to concentrate structural masses at the floor level as lumped masses [Deie10]. That means that only horizontal directions of excitation are affected. Torsional effects are also considered. The corresponding matrix $\boldsymbol{M}$ is called lumped mass matrix. However, there are special cases where the mass effect in vertical direction should be considered (see section 2.4.1).

The gravity loads should also be included in THA as static loads. Gravity loads affect the force and deformation characteristics of structural elements and lateral deformation due to P-Δ effects. In the analysis, gravity loads are applied first and remain constant while the excitation of the earthquake ground motion occur.

Damping

In order to capture the effects of damping in the THA of MDOF systems the RAYLEIGH damping formulation is employed commonly where the damping matrix is a combination of stiffness and mass proportional damping.

$$\boldsymbol{C} = \alpha_m \boldsymbol{M} + \alpha_k \boldsymbol{K} \tag{2.33}$$

The proportionality factors α_m and α_k can be determined by means of the structural period T and the damping value ξ. For example, 5% viscous damping might be taken into account as included in the elastic response spectrum (see section 2.3.2). In the non-linear case the stiffness matrix $\boldsymbol{K}$ is not specified explicitly. The stiffness changes during the analysis. The initial stiffness matrix can be used to avoid variation of the damping matrix during analysis.

Vector of inertia forces

The vector of inertia forces represents the non-linear characteristics of all structural components in a model. The hysteretic behaviour of specific elements are captured by F_S-u relationships for recurrent loading (hysteretic model). The hysteretic model has to reflect the hysteresis shape which is characteristic for the construction type considered (see section 2.2).

This implies that the hysteretic model must realistically account for

- deformation capacity,
- failure modes,
- energy dissipation, and
- degradation and strength and stiffness

in order to obtain reliable results from NTHA.

Input ground motions

Ground motions as input for dynamic analysis should be selected in a sufficient variety. Accelerograms of real earthquakes (see section 2.3.1) or artificial time sereis (see section 2.3.3) can be applied as input ground motions. According to [EN 1998-1] THA should be carried out with at least seven ground motion records or three artificial time series to consider different ground motion characteristics.

Solution strategy

The most common solution strategy for dynamic problems is the NEWMARK method – also known as the linear acceleration method – which provides an incremental solution of the equation of motion Eq. (2.32). Thereby, the acceleration is assumed to be linear between time t_n and t_{n+1}. The NEWMARK method is used in combination with the NEWTON RAPHSON iteration in the time step (see e.g. [Chop95; Wrig08]) for non-linear dynamic problems.

2.5 Derivation of Seismic Performance Factors

Seismic performance factors are parameters which summarise non-linear effects of energy dissipation and 3D interaction of structures under earthquake impact, such as inelastic deformations and energy dissipation. In [EN 1998-1] the behaviour factor q is the most crucial value for seismic design with force-based design (see section 2.4.2). For some DBD methods ductility-period-dependent reduction factors R_μ are applied (see section 2.4.3) to create demand spectra. Approaches for the determination of behaviour factors and the basis of the reduction factor incorporated in the N2 method are presented in this section.

2.5.1 Behaviour factor q

The behaviour factor generally accounts for the capability of structures to exhibit ductile non-linear behaviour connected with energy dissipation. However, an explicit definition of this factor is not included in the standards. The q-values which are specified in codes and regulations and on which basis they were fixed sometimes appears to be a mystery for engineers. A common and widely accepted definition is that the behaviour factor is the ratio of the 'theoretical' elastic strength demand F_{el} and the inelastic strength demand F_{inel}

$$q = \frac{F_{el}}{F_{inel}} \tag{2.34}$$

'Theoretical' indicates herein that ideal elastic behaviour is assumed to define F_{el}. The inelastic strength demand is the strength required in the structure to withstand an earthquake within predefined ductility respectively displacement limits [Kapp99].

Several approaches have been proposed to determine behaviour factors, whereas most of them are based on the definition of Eq. (2.34). Some of these approaches are as follows:

- Base shear approach (see e.g. [Popo11]),
- PGA approach (see [Salv96; Cecc02; Cecc08; Cecc10; Ferr12]),
- displacement-based determination (see [Kraw98; Mist06]),
- ESECMaSE approach (see [Fehl08]) and
- FEMA approach (see [FEMA P695]).

Base shear approach

The core of this approach is to carry out time history analysis for elastic and inelastic structural behaviour. Firstly, the behaviour is considered as absolute elastic and then the dynamic analysis is performed with realistic inelastic hysteretic behaviour.
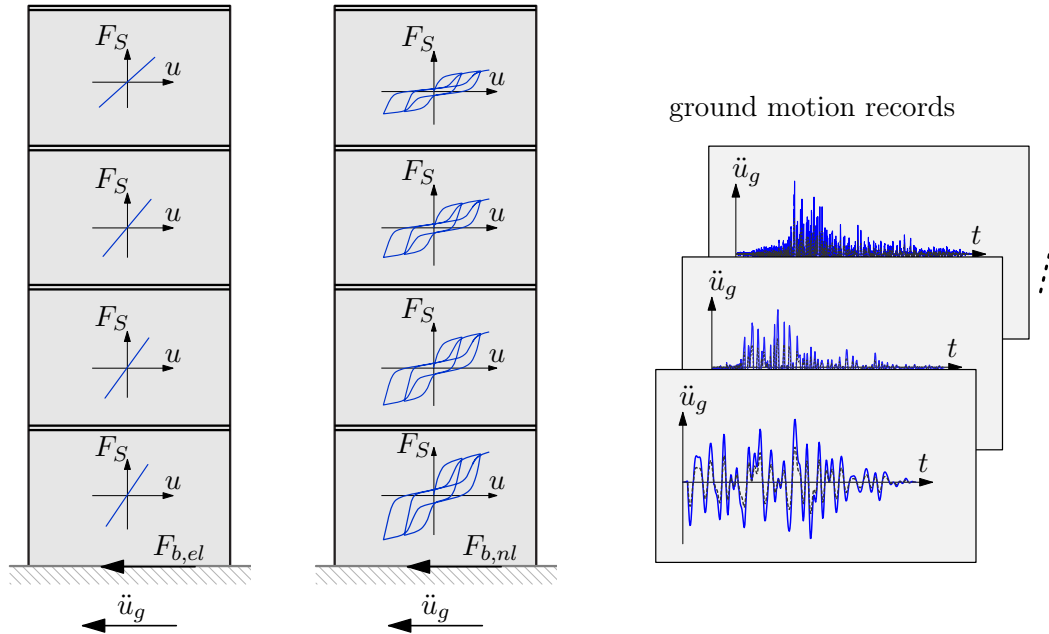
Figure 2.17: Systematic for determining behaviour factors with the base shear approach

The ratio of the base shear from linear THA $F_{b,el}$ and the base shear from NTHA $F_{b,nl}$ defines the behaviour factor for a certain ground motion.

$$q = \frac{F_{b,el}}{F_{b,nl}} \tag{2.35}$$

A set of ground motions records is used as input. Each ground motion yields a q-value. The average of q-values for a set of ground motions is taken as the behaviour factor.

PGA approach

The first step of this approach is to design the structure for a behaviour factor of $q = 1$ – assuming full elastic behaviour – and a specific peak ground acceleration PGA_{design} according to force-based design. Then, a non-linear analytical model of the structural system is developed considering realistic mechanical properties. The properties are obtained by means of cyclic tests on components of the lateral load resisting system such as wall elements. NTHAs with a series of ground motions are carried out, each with increasing
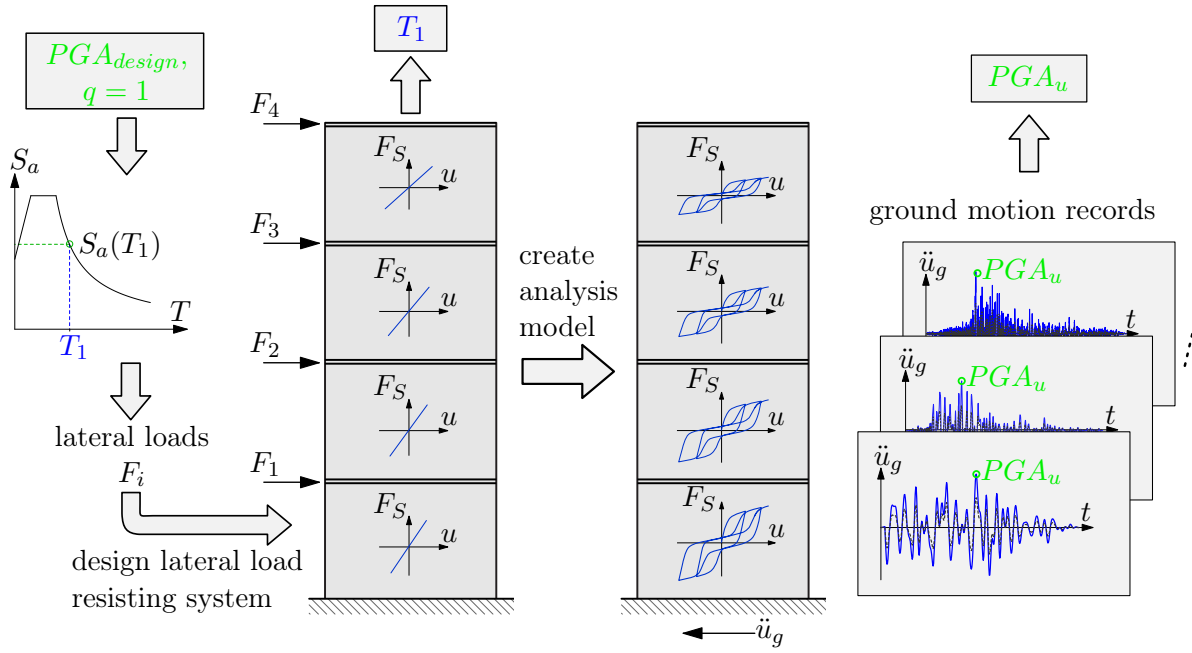
Figure 2.18: Systematic for determining behaviour factors with the PGA approach

PGA, until a predefined collapse criterion – such as failure of anchoring or a deformation limit – is reached.

This defines the near-collapse peak ground acceleration PGA_u. The behaviour factor is then calculated as ratio between design and near-collapse peak ground acceleration.

$$q = \frac{PGA_u}{PGA_{design}} \tag{2.36}$$

Displacement-based determination

This approach makes use of DBD respectively PBD to determine the behaviour factor. With

$$F_{el} = S_a(T_{el}) \cdot m \cdot \alpha_{el} \tag{2.37}$$

and

$$F_{inel} = S_a(T_{inel}) \cdot m \cdot \alpha_{inel} \tag{2.38}$$

Eq.(2.34) can be rewritten as

$$q = \frac{S_a(T_{el}) \cdot m \cdot \alpha_{el}}{S_a(T_{inel}) \cdot m \cdot \alpha_{inel}} \tag{2.39}$$

This equation is related to the capacity spectrum method as illustrated in Figure 2.19

ESECMaSE approach

In the ESECMaSE project [ESEC] results from linear THA analyses and from experimental investigation were used to evaluate behaviour factors. Firstly, pseudo-dynamic and/or shaking table tests are carried out on wall elements and structural systems. Subsequently, the elastic stiffness determined from the test results is taken to perform linear THA. The
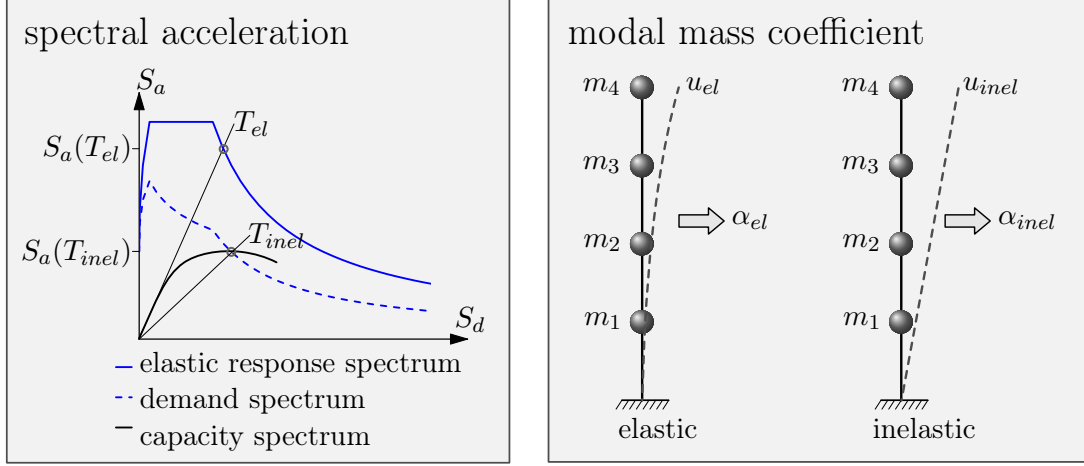
Figure 2.19: Systematic for DBD of behaviour factors

behaviour factor is calculated as the ratio between the base shear from the linear dynamic analysis $F_{b,el}$ and the base shear obtained from testing $F_{b,exp}$.

$$q = \frac{F_{b,el}}{F_{b,exp}} \tag{2.40}$$
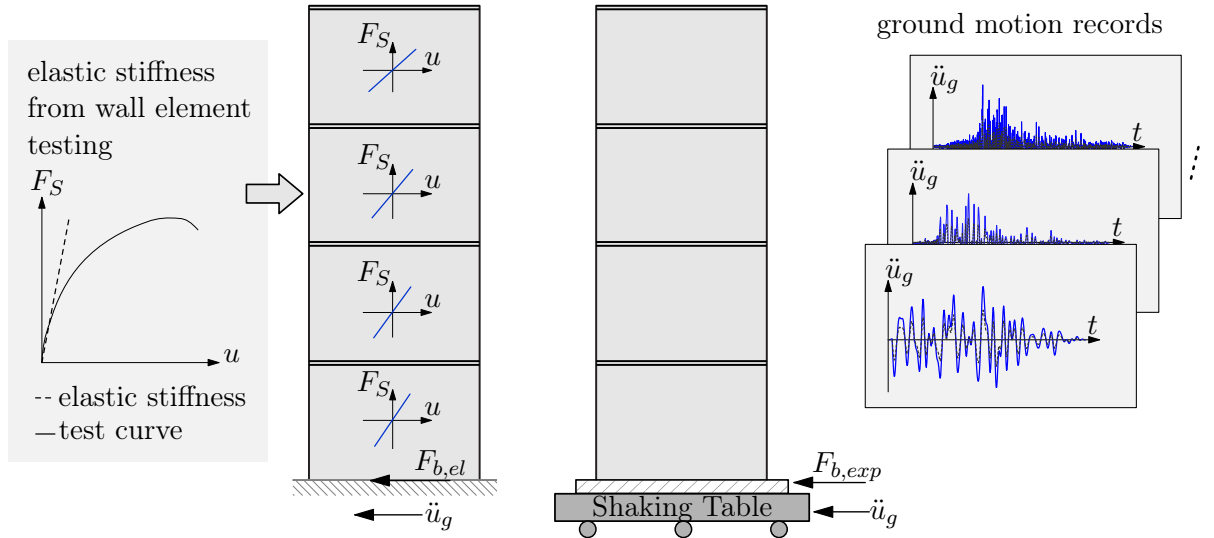
Figure 2.20: Systematic for determination of behaviour factors with the ESECMaSE approach

FEMA approach

The [FEMA P695] document contains a methodology whereby a trial value of the behaviour factor can be confirmed or rejected for a construction type and specific performance objectives. The trial value of the behaviour factor, which is used to design an archetype of a construction with FBD, is evaluated in terms of the acceptability of the collapse margin ratio. The collapse margin ratio CMR is the fundamental parameter characterising the structural collapse margin safety and can be determined by means of collapse fragility curves (see Fig. 2.21) using the spectral value of the maximum considered earthquake S_{MT}. The median collapse intensity $\hat{S}_{CT}$ can be read from the fragility curve. NTHAs

31

are performed with a non-linear model of the archetype construction and for a series of ground motion records to generate such fragility curves.

In the next step, the so-called adjusted collapse margin ratio $ACMR$ is calculated to consider the spectral shape of the ground motion record set. Therefore, spectral shape factors SSF are predefined in the [FEMA P695] document.
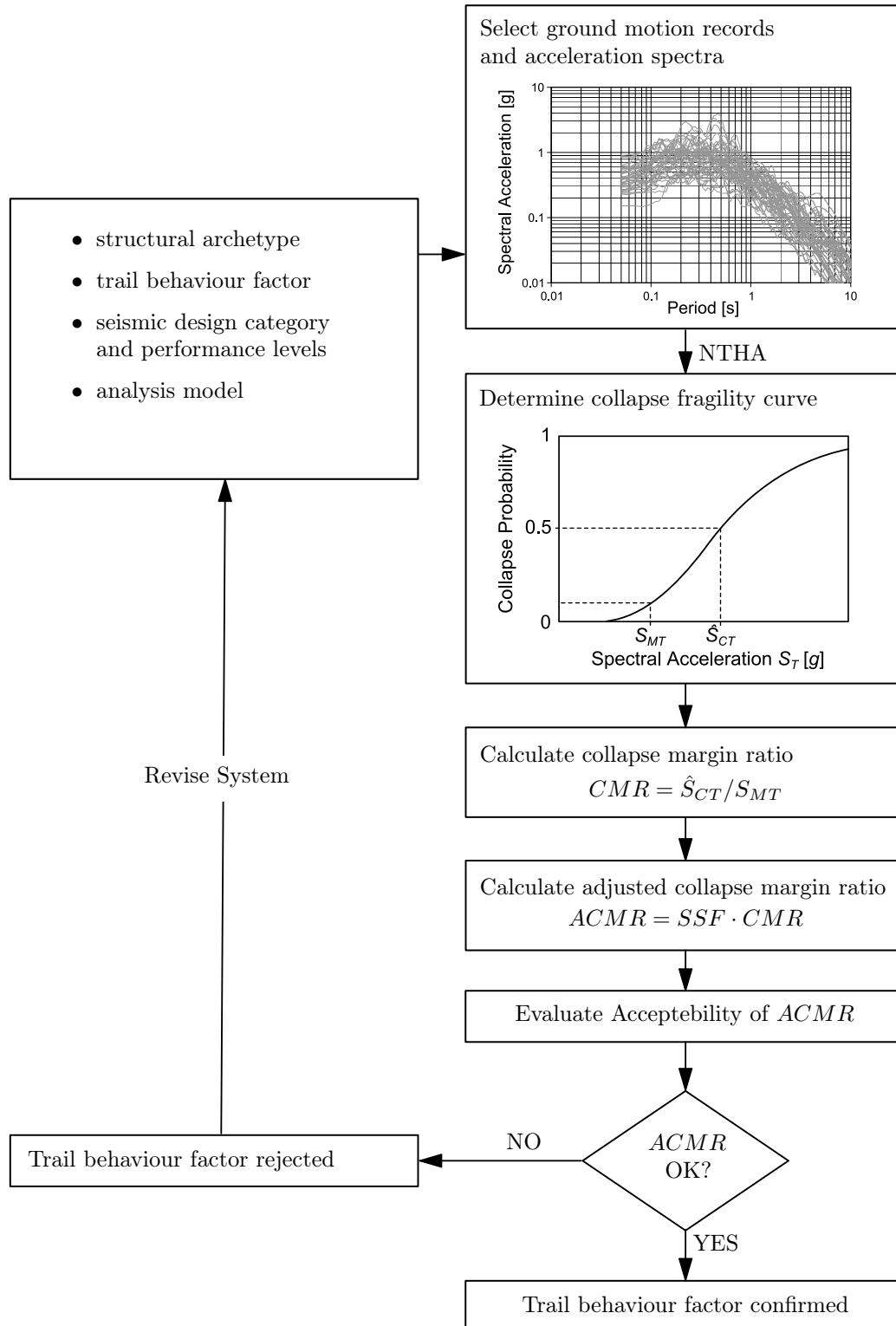
Figure 2.21: Methodology according to FEMA P695 adapted for behaviour factor evaluation

The last step is to compare the $ACMR$ with acceptable values of adjusted collapse margin ratio $ACMR_{acc}$.

$$ACMR \geq ACMR_{acc} \tag{2.41}$$

If Eq. (2.41) is fulfilled the behaviour factor chosen is suitable for the archetype. Otherwise, the system must be revised and the procedure (see Fig. 2.21) starts again. It should be noted that the methodology presented in Figure 2.21 was slightly adapted for behaviour factor evaluation. This procedure was demonstrated by SEIM ET AL. [Seim15].

2.5.2 Ductility-period-dependent reduction factor R_μ

A R_μ-μ-T relationship is required to transfer the elastic response spectrum into an inelastic spectrum which is used for some DBD methods – for example, the N2 method (see section 2.3.2). Several R_μ-μ-T relationships were developed for this purpose, for example, by MIRANDA AND BERTERO [Mira94].

The R_μ-μ-T relationship that has been recently applied within the N2 method (see Tab. 2.5) is a simplification of the relationship proposed by VIDIC ET AL. [Vidi94]. This R_μ-μ-T relationship was found by means of a parametric study on inelastic SDOF systems considering two hysteretic models (see Fig. 2.22).

(a)   **(b)**

Figure 2.22: Hysteresis models considered for the determination of the R_μ-μ-T relationship – (a) bilinear elastic-plastic model (EP-model), (b) stiffness degrading Q-model

A bilinear R_μ-μ-T relationship was derived from the study, see Eqs. (2.42) to (2.45) and Figure 2.23.

$$R_\mu = c_1 \cdot (\mu - 1)^{c_R} \cdot \frac{T}{T_0} + 1 \qquad \text{for } T \leq T_0 \qquad (2.42)$$

$$R_\mu = c_1 \cdot (\mu - 1)^{c_R} + 1 \qquad \text{for } T > T_0 \qquad (2.43)$$

with

$$T_0 = c_2 \cdot \mu^{c_T} \cdot T_1 \qquad (2.44)$$

and

$$T_1 = 2 \cdot \pi \cdot \frac{c_v \cdot PGV}{c_a \cdot PGA} \qquad (2.45)$$

PGA and PGV are the peak ground acceleration and peak ground velocity, respectively. The parameters c_a and c_v are the corresponding amplification factors. Values for the amplification factors are provided by NEWMARK AND HALL [Newm82].
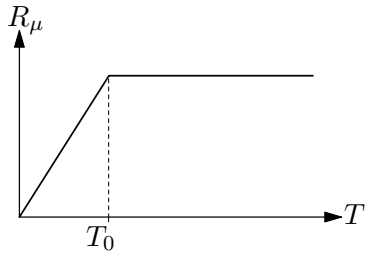
Figure 2.23: R_μ-μ-T relationship (for $c_R = 1.0$) according to [Vidi94]

	model				
hysteresis	damping	c_1	c_R	c_2	c_T
Q-model	mass prop.	1.0	1.0	0.65	0.30
Q-model	stiff. prop.	0.75	1.0	0.65	0.30
EP-model	mass prop.	1.35	0.95	0.75	0.20
EP-model	stiff. prop.	1.10	0.95	0.75	0.20

Table 2.6: Constants c_1, c_2, c_R and c_T according to [Vidi94]

Different constants c_i were found depending on the hysteretic behaviour and the damping model – proportional to mass or stiffness (see Tab. 2.6).

The R_μ-μ-T relationship was simplified, as shown in Table 2.5, to be used within the DBD procedure documented in [EN 1998-1], annex B.

MERGOS AND BEYER [Merg15] enhanced the N2 method with reference to light-timber structures. THAs were performed for a set of inelastic SDOF systems and ground motion records to evaluate the validity of the current R_μ-μ-T relationship of the N2 method for wood-frame structures. SDOF systems included an appropriate hysteretic behaviour and 5% viscous damping. The Wayne-Stewart hysteretic model [Stew87] was chosen with a post-yield stiffness of 10% of the elastic stiffness to represent the characteristics of light-frame wall elements. A total of 80 ground motion records were taken; 60 account for low and moderate seismicity regions and 20 for high seismicity regions. By means of this study MERGOS AND BEYER found that a new R_μ-μ-T relationship, see Eqs. (2.46) to (2.48) and Table 2.7, would match the characteristics of light-frame timber structures.

$$R_\mu = 1 + \left[(\mu - 1) \cdot \left(\frac{T}{T_C} \right)^{\beta_s} \right]^{1/\alpha} \qquad \text{for } T < T_C \qquad (2.46)$$

$$R_\mu = 1 + [\mu - 1]^{1/\alpha} \qquad \text{for } T \geq T_C \qquad (2.47)$$

with

$$\beta_s = 1 - (1 - \beta) \cdot \frac{T}{T_B} \tag{2.48}$$

Seismicity	α	β
Low to moderate	1.00	0.55
High	1.30	1.00
All	1.10	1.00

Table 2.7: Constants α and β according to [Merg15]

2.6 Summary of chapter 2

In this chapter the fundamentals of structures under earthquake impact were discussed with reference to calculation methods and parameters required for seismic design. Important parameters for seismic design are natural period, ductility and viscous damping. Different calculation methods were presented including input data, procedure and outcomes. In addition to FBD and THA, DBD was presented in more detail, since this thesis focuses on PBD. FBD and THA are considered for comparison. The capacity spectrum method and the N2 method are chosen to represent two different DBD approaches.

It can be seen that these static procedures make use of the principles of equivalent SDOF systems and modal analysis. It should be noted that these principles imply linear elastic behaviour which is the most critical issue of the static design methods – FDB and DBD. Seismic performance factors are utilised within static design procedures to account for inelastic behaviour. The determination of such parameters – behaviour factor q and reduction factor R_μ – are explained in section 2.5. The parameters may differ between the several approaches and depend on the hysteretic behaviour considered. For the N2 method a new R_μ-μ-T relationship was derived by MERGOS AND BEYER [Merg15] which account for hysteretic behaviour with pinching and stiffness and strength degradation representative of light-frame structures.

The issues mentioned in this chapter are mainly general aspects of seismic design and relates basically to varies structural types. Special features which are inherent for timber structures will be exposed in the next chapter.

3 CLT structures under seismic action – State-of-the-art

The previous chapter discussed the fundamentals of the seismic design of structures. This chapter deals with the performance of timber structures under earthquake impact. The performance of different structural systems was studied in the past by experimental and numerical investigations on entire structures and structural elements. A review of the most relevant investigations on cross laminated timber (CLT) structures is presented in the following sections. Some issues which relate to light-frame structures will also be discussed.

3.1 Experimental research on structures, substructures and connections

Experimental investigations on timber structures can be divided into two main groups – structures and substructures. Structures might be whole buildings or assemblies of full-scale structural elements. Substructures are structural elements of the lateral load-resisting system, such as walls or diaphragms. Monotonic and cyclic tests on structural components and connections have been carried out to evaluate the behaviour of timber structures under seismic action and have been documented by various authors.

While a permanent increasing deformation is applied in tests with monotonic loading, the load direction changes in cyclic tests at certain displacement amplitudes. Both the displacement applied u and the corresponding load F are recorded during the test. A series of different loading protocols are available [EN 12512; EN 26891; ISO 16670; ISO 21581; Kraw01]. The influence of different loading protocols on the load-displacement behaviour was discussed by several researchers, see e.g. [Vogt12].

Dynamic tests on structural elements and structures have been performed on uniaxial and triaxial shaking tables. With the shaking table horizontal and even, vertical displacements can be applied at the base in order to simulate the ground motion of an earthquake or an artificial time history. The structural response in terms of displacements, accelerations and forces can be measured at different positions on the structure.

3.1.1 University of Ljubljana tests

Research at the University of Ljubljana was focused on the racking behaviour of wall elements, especially CLT. A series of experimental investigations were performed in the scope of a comprehensive study on CLT wall elements:

- tests on a small number of anchoring units (angle brackets) under cyclic loading [Duji06c; Duji08],
- tests on CLT wall panels under monotonic and cyclic loading and various boundary conditions [Duji04; Hris05; Duji06b; Duji08; Stoj08], and

- shaking table tests on CLT wall panels under earthquake excitation [Duji06a; Duji06d; Hris12].

Cyclic tests on CLT wall panels

Different configurations of CLT wall elements were tested where dimensions, types of anchoring and vertical load were varied. CLT wall elements with dimensions of 2.44 by 2.44 m and 3.20 by 2.72 m were incorporated. Different types of angle brackets were used for anchoring. Uniform vertical load up to 15 kN/m and eccentric vertical load as a result of rotation of the CLT element were considered. In addition, 14 CLT wall elements with openings (window and door) were tested.

Figure 3.1 shows two configurations of the wall element test and the corresponding load-displacement curves for cyclic loading. An irregular distribution of angle brackets was chosen for the solid wall element to remain consistent with the configuration with openings.

① 3-layer CLT element (t=94 mm)

② angle bracket ABR105 fixed to CLT panel by 10 ring shank nails $\varnothing 4.0 \times 40$ mm and to concrete base by 2 bolts M12 (see Fig. 3.2b)
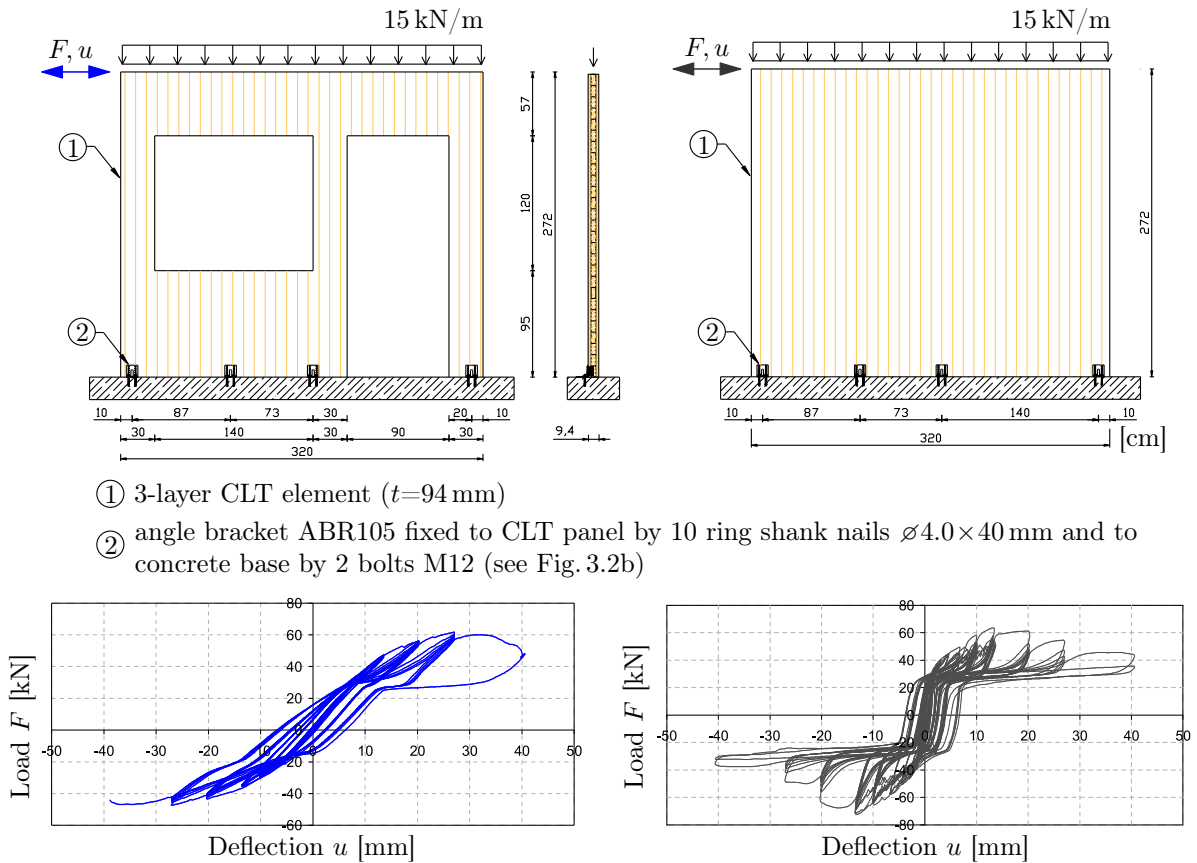
Figure 3.1: Cyclic testing of CLT wall elements at the University of Ljubljana – configurations and test results [Duji06c]

It was found that the loading conditions in terms of centric and eccentric loading affect the load bearing capacity of CLT wall elements. It was observed that openings in CLT elements lead to a significant reduction of stiffness and to a change of the hysteresis shape which affects the energy dissipation capacity (see Fig. 3.1).

Shaking table tests on CLT wall panels

Two specimens of CLT wall panels in the same configuration were tested on a shaking table (see Fig. 3.2a) under a series of ground motions (records of El Centro 1940, Kobe 1995 and others) where the PGA was increased gradually from 0.06 up to 0.38g. Similar to the wall panel tests depicted in Figure 3.1, the wall dimensions were 3.20 by 2.72 m and CLT wall panels were anchored with angle brackets (see Fig. 3.2b). An extra mass of 4.8 t each (stated as representative of a three storey CLT building) were applied on the top of these wall panels via a CLT slab segment.

(a)   **(b)**
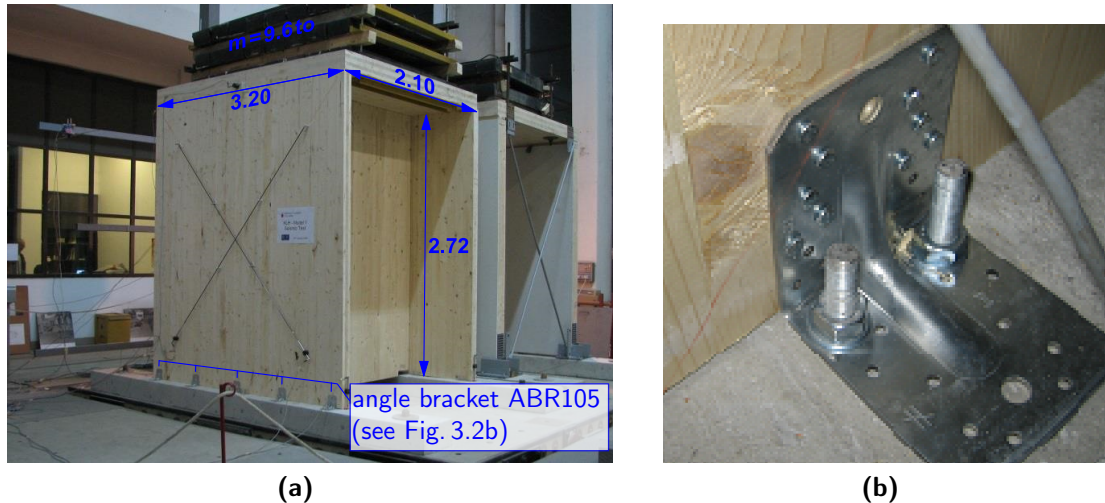
Figure 3.2: Test setup – (a) specimen on the shaking table, (b) angle bracket ABR105 [Simp15] with ten ring shank nails and two anchor bolts M12 (anchoring of specimen) [Duji06a]

A good correlation with results from the cyclic tests was found with respect to the ductile behaviour.

3.1.2 SOFIE – Construction System Fiemme

The research project SOFIE [CNRI] was a comprehensive study of the performance of CLT constructions (2D and 3D). Experimental investigations on were carried out in the scope of this project as follows:

- wall elements in four configurations under monotonic and cyclic loading [Cecc06b],
- a single-storey CLT structure in three configurations under pseudo-dynamic loading [Laur06],
- a three-storey CLT structure under dynamic loading on a shaking table [Cecc06a] and
- a seven-storey CLT building under dynamic loading on a shaking table [Cecc13].

Wall element testing

Wall element tests were performed in preparation for the single-storey and three-storey CLT structure tests. A total of 14 CLT wall elements were tested in different configurations (see Fig. 3.3). All the wall elements had the same dimensions. One configuration had a door opening.
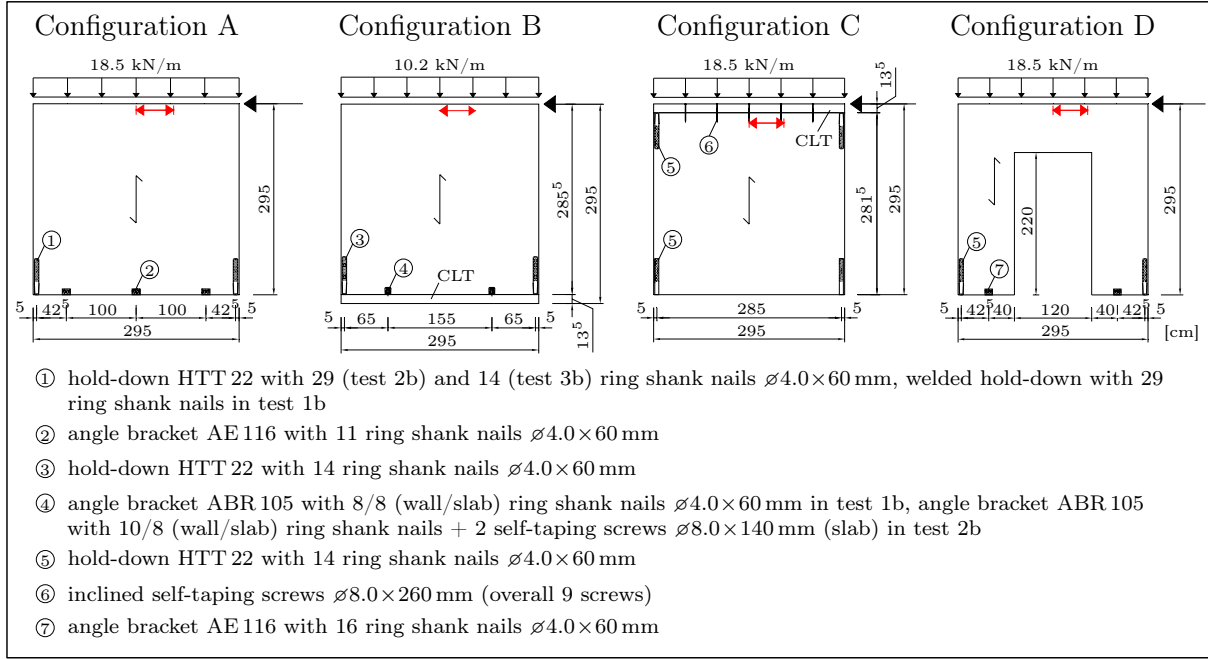
Figure 3.3: Configurations of CLT wall elements tested (cyclic) under the SOFIE project [Cecc06b]
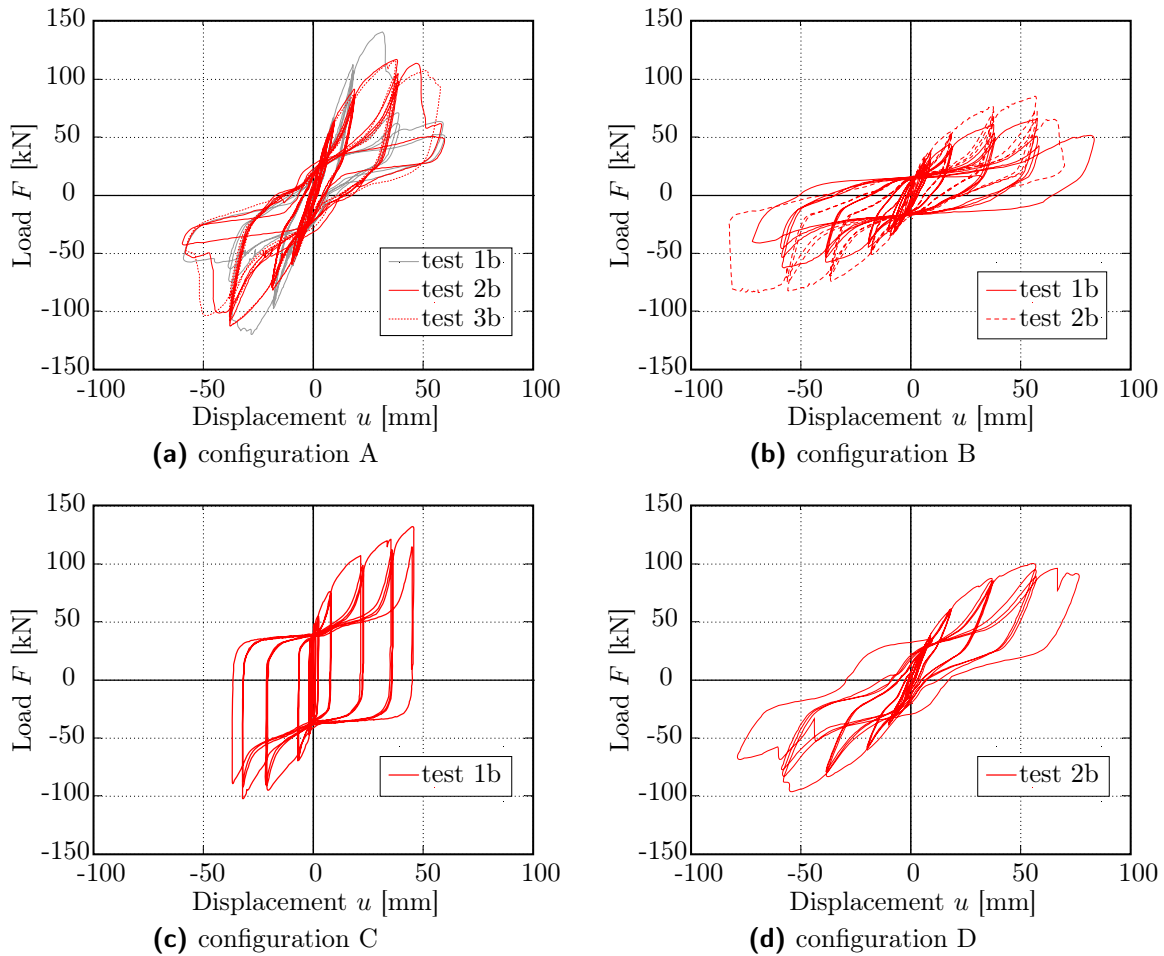
Figure 3.4: Results from cyclic wall element testing under the SOFIE project [Cecc06b]

The uniform vertical load was fixed on the presumed loading of wall elements in vertical direction in a three storey building. Configurations A,C,D and configuration B represent a "first-storey wall" and a "second-storey wall" respectively. The wall elements were anchored by hold-downs and angle brackets (HTT 22, AE 116, ABR 105 [Simp15]) in combination with annular ring shank nails. Hold-downs and angle brackets were fixed with bolts to a steel girder, except configuration B, which had a CLT bases. The connection between wall and CLT on the top (floor-slab-to-lower-wall connection) in configuration C was made by inclined self-tapping screws.

Different hysteretic behaviour was obtained compared to the test results obtained by DUJIC ET AL. (see Fig. 3.1) with reference to the deformation and load-bearing capacity. One reason was the location of hold-downs at wall ends instead of angle brackets. One specimen with welded hold-downs showed higher load-bearing capacity but lower deformation capacity. It was found that support conditions in combination with a modified anchoring detail influenced the hysteretic behaviour significantly (see Fig. 3.4a and 3.4b). However, the wall element with an opening also had a lower stiffness (cf. Fig. 3.4a, 3.4d and 3.1).

Three-storey CLT structure testing

A three-storey CLT structure was tested on a shaking table in one direction in three configurations (see Fig. 3.5). The difference between the three configurations is a different wide opening in the first storey.
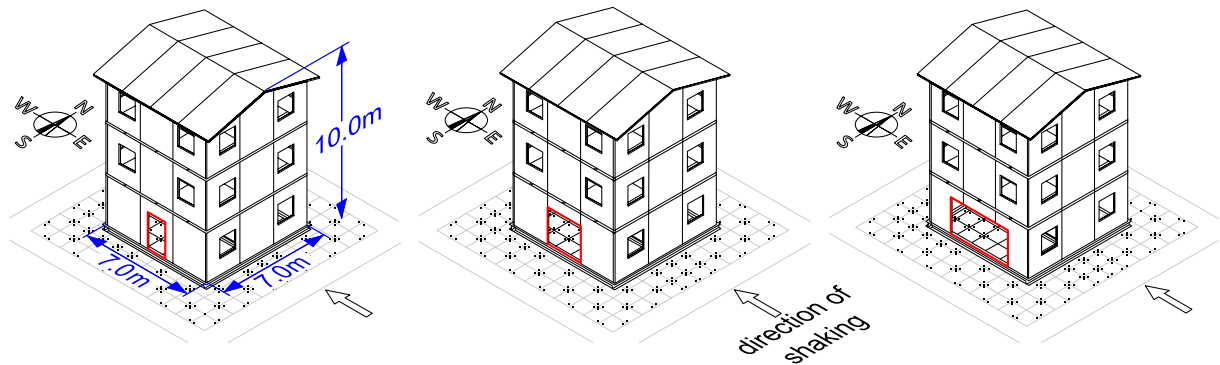
Figure 3.5: Configurations of the three-storey SOFIE structure [Cecc06a]

A mass of 15 t was added to each floor. All wall elements and roof panels had a thickness of 85 mm. The floor panels had a thickness of 142 mm. Walls were anchored with hold-downs and angle brackets as used in the wall element tests. The dimensions of the CLT panels for walls and floors were limited for reasons of transportation. This is one reason why smaller sections of CLT panels were used for setting up the test structure. It was also aimed for more ductility due to segmented CLT wall. Adjacent wall panels and floor panels were connected in-plane by "LVL joints" with self-tapping screws $\varnothing 8 \times 80$ mm and "overlap joints" with self-tapping screws $\varnothing 10 \times 180$ mm respectively (cf. Fig. 3.7). The connection between the perpendicular walls and the floor-to-lower-wall connection were executed, similarly. The spacing of the screws is not documented.

Three ground motion records were applied at different intensities (see Tab. 3.1).

A stiff "box-type" behaviour was generally observed for each configuration [Cecc13]. The structure withstood all tests without significant damage. *Near collapse* – failure of hold-downs – was only reached for the Nocera Umbra earthquake with $1.20g$ resulting in a maximum drift of the first storey of about 37 mm. However, the structure did not tend to twist in any of the three configurations. No permanent deformation occurred.

	PGA in g		
El Centro, California, 1940	0.15	0.30[1)]	0.50
Kobe, Japan, 1995	0.15	0.50	0.82[1)]
Nocera Umbra, Italy, 1997	0.15	0.50[1)]	1.20

[1)] original PGA

Table 3.1: Ground motion records for shaking table tests on three-storey SOFIE structures

Seven-storey CLT building on the shaking table

The final step of this project was to test a seven-storey CLT building on the shaking table. The building consists of wall panels with varying thicknesses – 142 mm in storeys 1 and 2, 125 mm in storeys 3 and 4 and 85 mm in storeys 5 to 7. The floor panels had a thickness of 142 mm. A mass of 30 t was added per floor. Walls were again segmented with a maximum length of an element of 2.3 m. The typical connections are illustrated in Figure 3.7. With this set-up, an initial natural frequency of 2.3 Hz and 3.5 Hz was obtained in the X-direction and Y-direction, respectively.
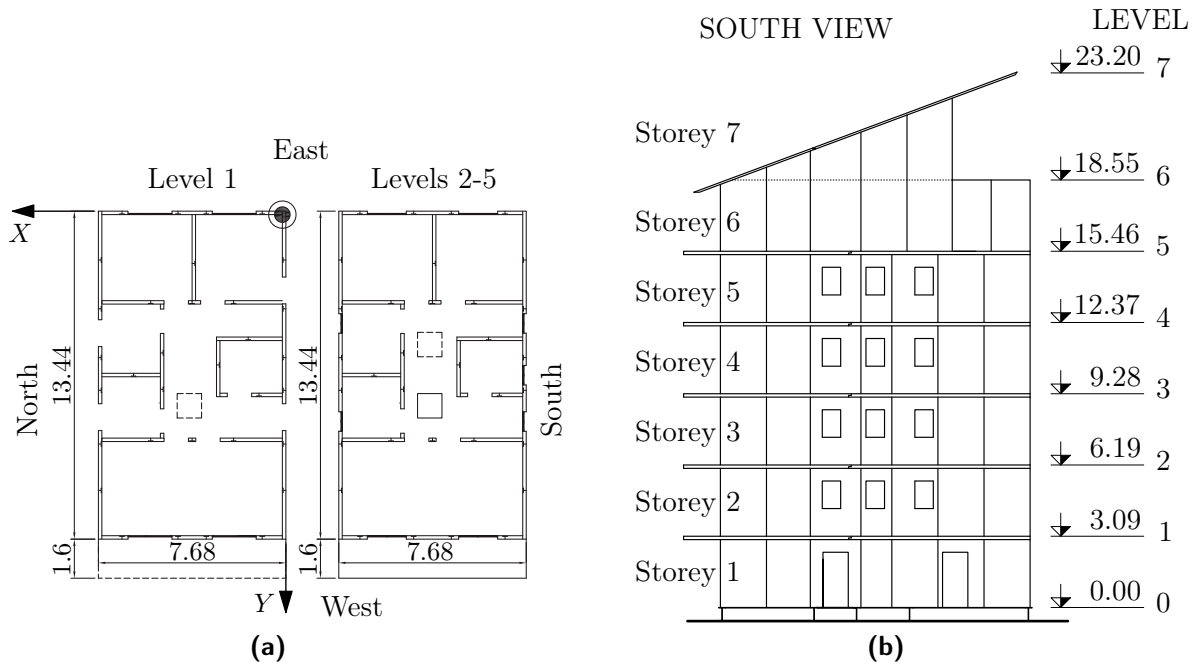
Figure 3.6: Seven-storey SOFIE building; (a) floor plans, (b) elevation [Cecc13]

A test sequence with three different earthquakes (Kobe, Nocera Umbra and Kashiwazaki R1) and increasing intensity were applied. Shaking table tests were performed in all three directions. Results of the shaking table test with the unscaled Kobe earthquake (see Fig. 2.8) can be summarised as follows:

- Accelerations of more than $3g$ were measured at level 6.
- The maximum deflections on the top were about 287 mm and 175 mm in the X- and Y-direction, respectively.
- The maximum inter-storey drift of 67 mm was obtained in the X-direction between the second and the third floors.
- After this test the natural frequency dropped down to 1.7 Hz in the X-direction and 2.7 Hz in the Y-direction.
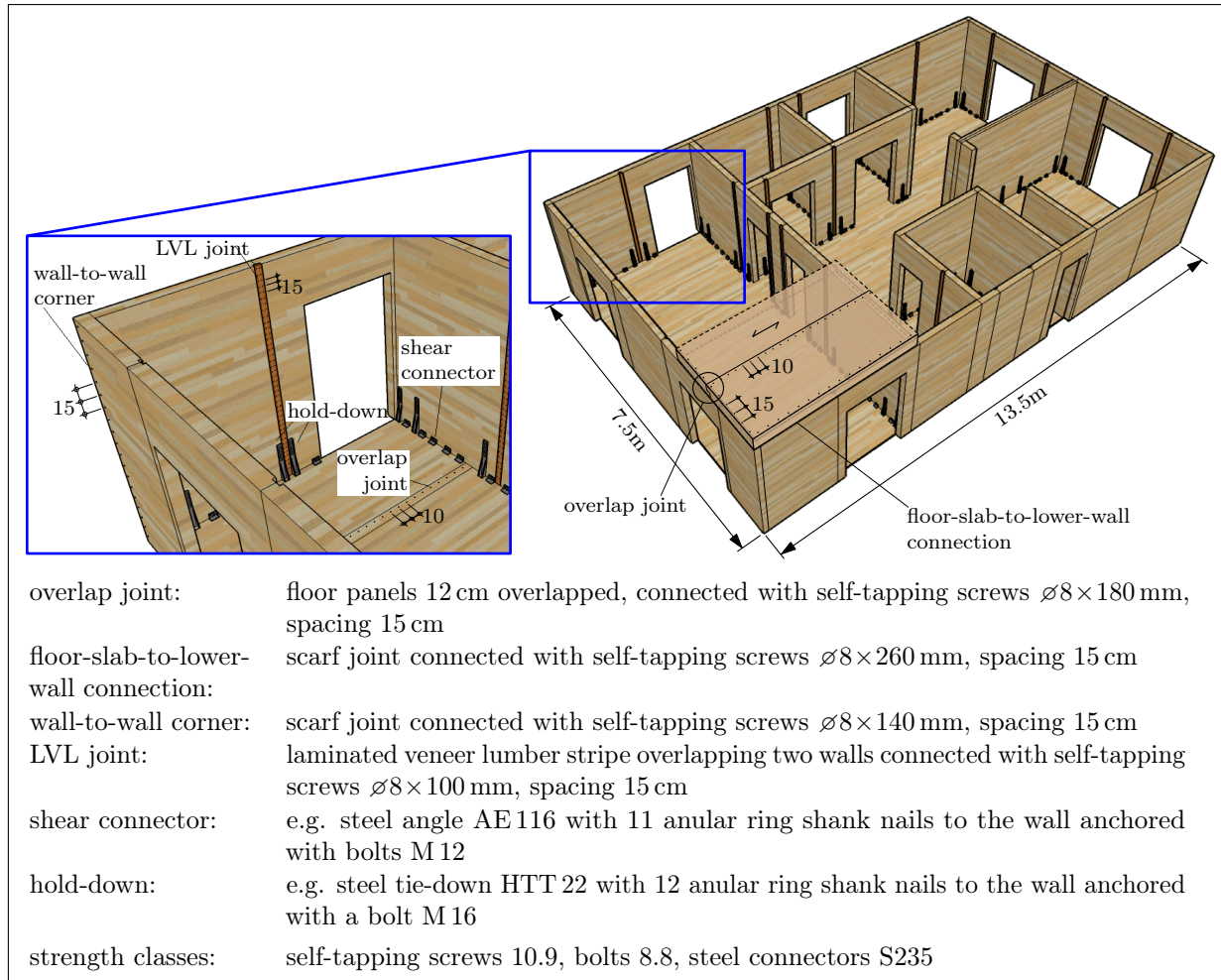
Figure 3.7: Connection between structural elements [Bouk09; Cecc13]

The building did not exhibit any residual lateral deflection after the whole test series. A "box-type" behaviour was detected in the Y-direction similar to the three-storey SOFIE building. The building in the X-direction responded as bending beam which led to heavy loaded tensile anchoring.

For further reading please refer to [Cecc06b; Laur06; Cecc06a; Sand06; Bouk09; Cecc11; Popo11; Sand12; Cecc13].

Connection behaviour

Based on the results from wall element testing and the shaking table tests, it was recognised that the behaviour of connections must be investigated further. Experimental investigations into the behaviour of connections were performed by GAVRIC [Gavr13] which included test series to connections such as those used for the SOFIE buildings. In addition to connections for the anchoring of wall elements, such as hold-downs and angle brackets, different configurations of connections with self-tapping screws were tested. The following configurations of connections with self-tapping screws are of further interest for this thesis:

SC-WC-0 - connection betwen perpendicular walls for shear loading along the joint,
SC-WC-90 - connection between perpendicular walls for shear loading perpendicular to the joint,
SC-WS-0 - connection between slab and wall (top) for shear loading along the joint, and
SC-WS-90 - connection between slab and wall (top) for shear loading perpendicular to the joint

Screws with a diameter of ⌀ 10 mm and a length of 180 mm were used for the connection between perpendicular walls. Screws with the same diameter but a length of 260 mm were taken for the connection between slab and wall. The screws were not inclined. The hysteretic behaviour of the two types of connection is illustrated in Figures 3.8 and 3.9 for a single screw. The hysteresis curve is compared with the load-displacement curve from monotonic testing. It shows that the hysteretic behaviour differs between the two loading directions. However, the load bearing capacity is almost the same for each configuration at about 8 kN.

(a) SC-WS-0

(b) SC-WC-90
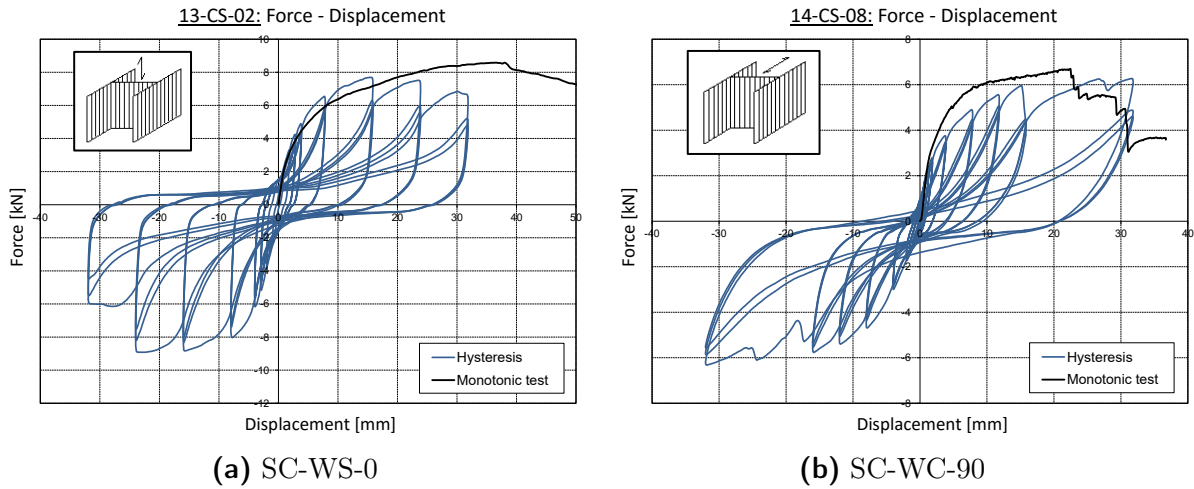
Figure 3.8: Hysteresis and behaviour for monotonic testing of the screw connection between perpendicular walls; (a) shear along the joint, (a) shear perpendicular to the joint, from [Gavr13]

(a) SC-WS-0

(b) SC-WS-90
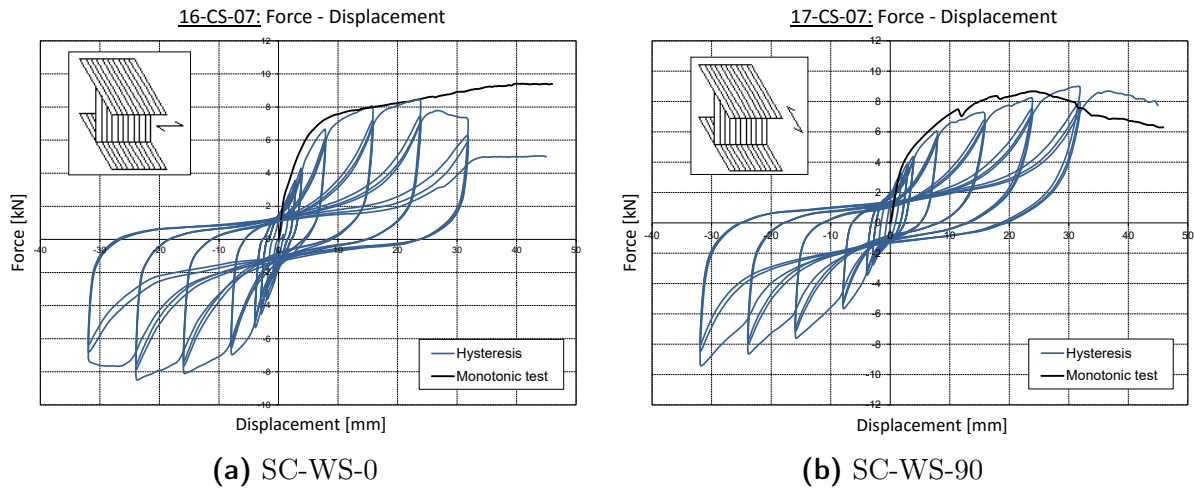
Figure 3.9: Hysteresis and behaviour for monotonic testing of the screw connection between slab and wall (top); (a) shear along the joint, (a) shear perpendicular to the joint, from [Gavr13]

3.1.3 FPInnovations tests

A total of 32 CLT wall elements were tested under monotonic and cyclic loading at the research centre of FPInnovations [Popo11; FPIn].

Twelve main configurations were investigated including

- different length,
- elements with openings and vertical joints,
- multiple number and types of connectors,
- different magnitude of vertical load and
- walls over one and two storeys.
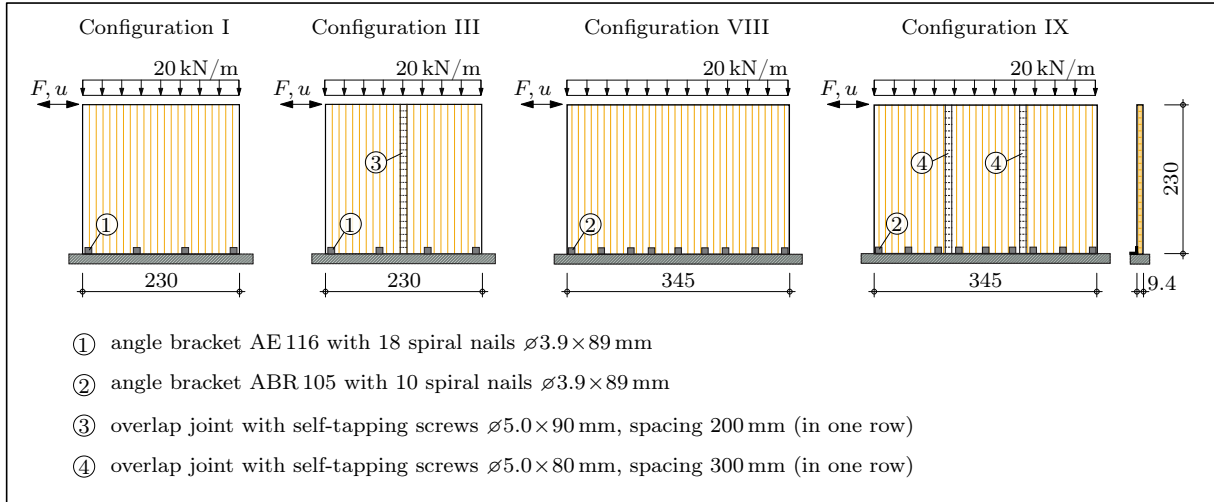
Figure 3.10: For configurations of CLT wall elements tested at FPInnovations [Popo11]

(a) configuration I

(b) configuration III

(c) configuration VIII
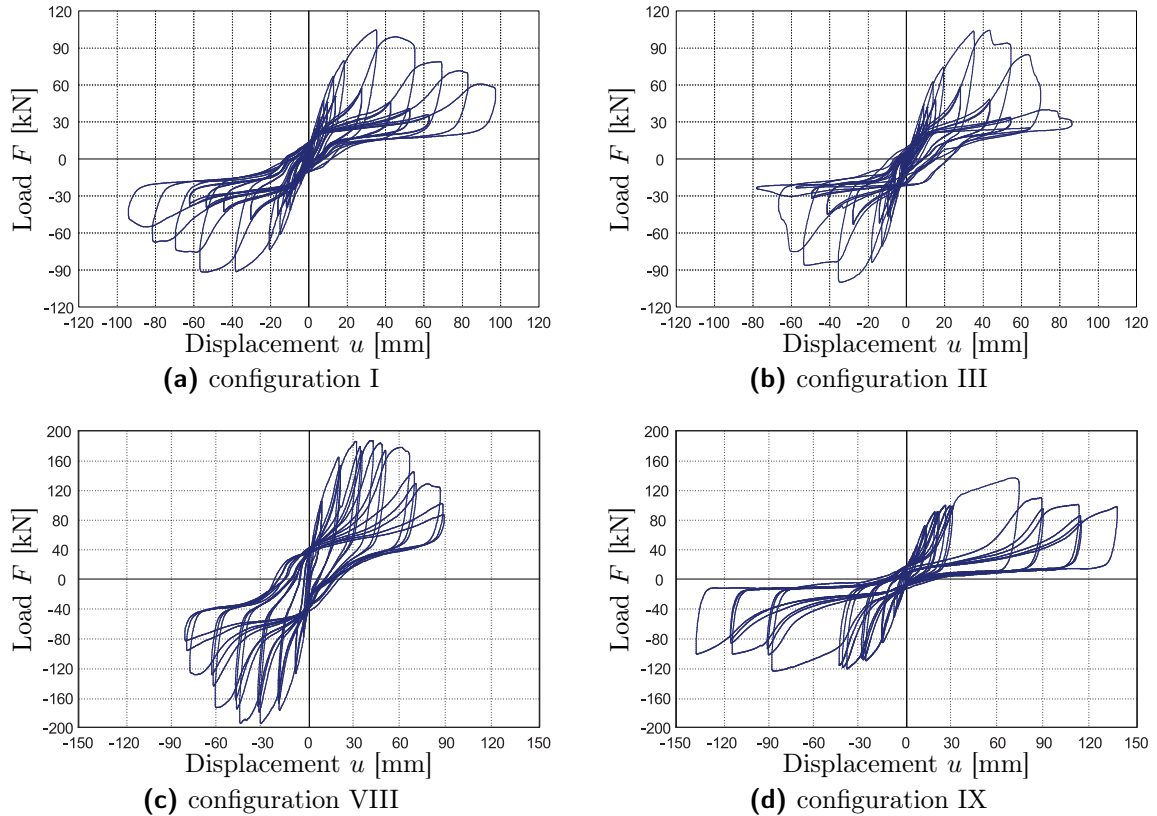
(d) configuration IX

Figure 3.11: Results from cyclic wall element testing [Popo11]

The walls were anchored by angle brackets types AE 116 and ABR 105 in the configurations which are depicted in Figure 3.10 (see above). Angle brackets were fixed to a steel girder. Spiral nails were used mainly for the connection between CLT and the steel angle. Adjacent wall panels were connected by self tapping screws at vertical joints.

It was found by means of these tests that the wall length and vertical joints influence the deformation capacity and the hysteretic behaviour of CLT wall significantly (see Fig. 3.11). The initial stiffness, for example, was reduced for the configuration with vertical joints by 20 to 30 % in comparison to configurations I and VIII [Popo12a; Popo12b].

3.1.4 SERIES – Seismic Engineering Research Infrastructures for European Synergies

Shaking table tests on three types of timber structures were performed in the scope of the SERIES Timber Building project :

- light-frame [Piaz13a; Piaz13b],
- cross laminated timber [Schi13] and
- log house [Lour13].

Each of the test buildings had three storeys. Tests on connections and wall elements were carried by FLATSCHER AND SCHICKHOFER [Flat11; Schi13] in preparation of the shaking table test on the CLT structure.

CLT wall element testing

Five wall configurations were considered at the wall element level (see Fig. 3.12). Similar to the previous investigations on CLT wall elements a uniform vertical load up to 20 kN/m was applied during monotonic and cyclic testing. The wall elements were anchored with hold-downs and angle brackets (see Fig. 3.12). Hold-downs and angle brackets were fixed with bolts to a steel girder.

① angle bracket AE 116 with 14 ring shank nails ⌀4.0×60 mm

② hold down HTT 22 with 15 ring shank nails ⌀4.0×60 mm

③ overlap joint with self-tapping screws ⌀6.0×100 mm, spacing 100 mm (in one row)

④ scarf joint with self-tapping screws ⌀8.0×280 mm, spacing 200 mm (in one row)
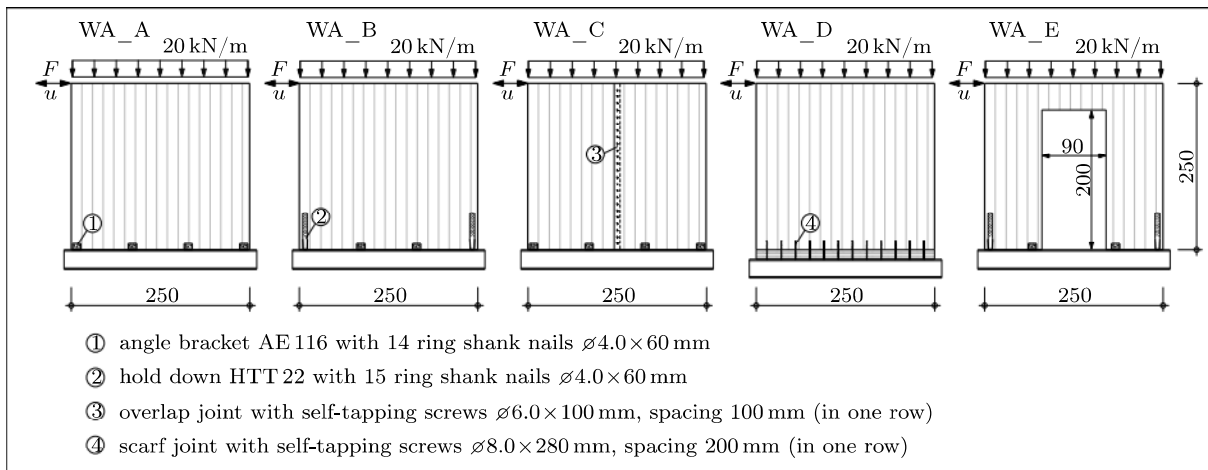
Figure 3.12: Configurations of CLT wall elements [Flat12]

Although the dimensions of the CLT elements differed slightly from the dimensions used in the FPInnovations study, similar effects could be observed. However, the reduction of stiffness caused by the vertical joint could not be confirmed by this test series. The reasons could be different diameters and spacing of screws and different test set-ups (see [Humm13]).

It was found that the total deformation of anchored CLT wall elements is dominated by rocking (in-plane rotation of the element). The following contributions on the overall deflection u of CLT wall elements without vertical joints and openings were stated as follows:

- CLT (bending and shear): 5 – 10%
- slip (translation): 20 – 25%
- rocking (rotation): 65 – 75%

The behaviour of connectors, such as angle brackets, hold-downs and self-tapping screws, was studied in different configurations under monotonic and cyclic loading. The test program consisted of about 180 connections. Characteristic hysteresis curves for two configurations of connections are illustrated in Figure 3.13:

SC-X-0 - connection with inclined screws for shear loading along the joint, and

AB-Ti-T - connection with angle bracket for loading in tension and compression.

Self-tapping screws with a diameter of $\varnothing\,8\,\text{mm}$ and a length of 200 mm were used for configuration SC-X-0. The screws were inclined at an angle of 45°. Regarding configuration AB-Ti-T the angle bracket type AE116 [Simp15] was connected with the CLT wall and CLT slab by 14 and 7 ring shank nails, respectively. Ring shank nails with the dimensions $\varnothing 4.0 \times 60\,\text{mm}$ were used.

(a) SC-X-0   **(b)** AB-Ti-T
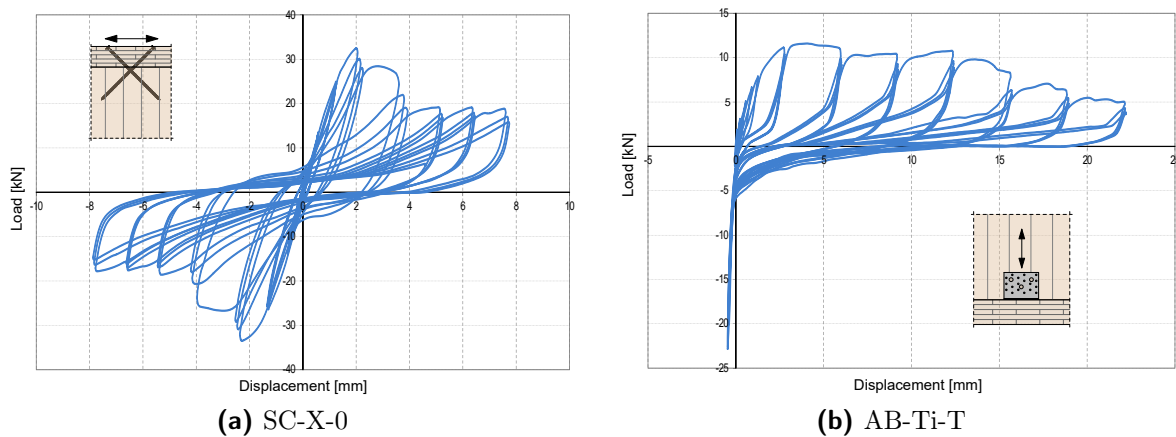
Figure 3.13: Hysteretic behaviour of connections – inclined self-taping screws and angle bracket (from [Flat11])

Figure 3.13 shows that the stiffness of connection with inclined self-tapping screws is much higher in comparison with screw connections without inclination (see Figs. 3.8 and 3.9). Configuration AB-Ti-T exhibits a distinctive nonsymmetric hysteresis with non-linear behaviour for tensile loading and almost elastic behaviour in compression.

Shaking table test on a three-storey CLT building

The test structure was assembled with 100 mm thick wall elements (three layers), 150 mm thick floor-slab elements (five layers) and 99 mm thick roof-slab elements (three layers). The structure had a weight of about 16 t including fasteners and connectors. An additional mass of 72 t, 60 t and 27.7 t were applied on the first floor, the second floor and the roof, respectively. Wall elements were anchored with hold-downs and angle brackets. Adjacent CLT elements were connected with self-tapping screws (see Fig. 3.14).
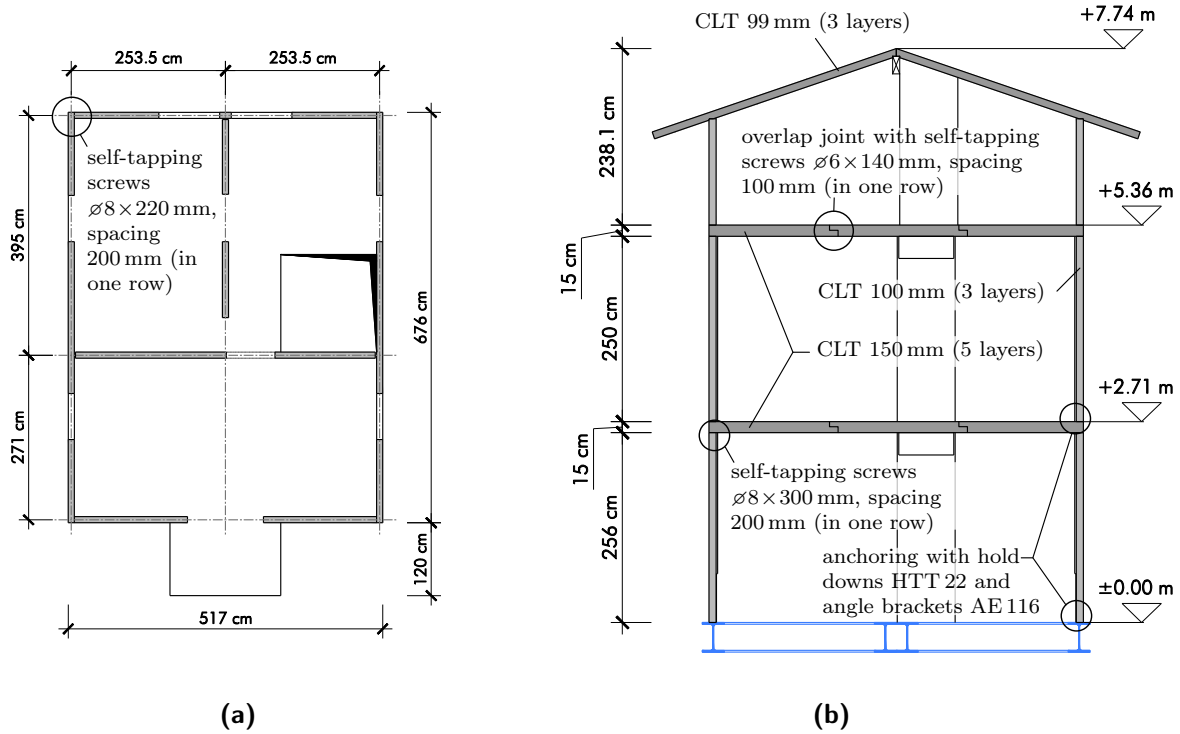
Figure 3.14: Three-storey CLT building – (a) floor plan, (b) elevation [Schi13]

The three-storey CLT building was subjected to a series of ground motions with increasing PGA including records of the Montenegro earthquake (1979) and the Tohoku earthquake (2011). The maximum PGA was $0.5g$. The building withstood a total of 32 seismic tests without significant loss of load bearing capacity. Only minor damage at the structural elements and connections were detected. The natural frequency of the structure remained fairly constant around 4 Hz. This indicates that the test structure exhibited a nearly elastic behaviour. In addition, small inter-storey drifts up to 6.6 mm and low tensile force at the hold-downs up to 2.4 kN were measured.

3.2 Numerical modelling

This section relates to numerical simulations of timber structures under earthquake impact. A review to non-linear static and dynamic studies is given including different scale of modelling and several modelling techniques. Three-dimensional behaviour and the application of DBD will be discussed with reference to multi-storey timber structures.

3.2.1 Filiatrault et al.

FILIATRAULT AND FOLZ [Fili02] modified the DDBD method (see section 2.4.3) for light-frame timber structures. One reason for the modification was that the classic DDBD procedure includes relationships of ductility and equivalent viscous damping which requires the definition of a unique yield point; the latter does not exist for light-frame timber structures [Muño08; FEMA 440]. For that reason FILIATRAULT AND FOLZ proposed a procedure based on the target displacement of the equivalent SDOF system and damping chararcterisation (see Fig. 3.15). To create the damping database an analytical determination of values for hysteretic damping by means of the SAWS hysteretic model (see Fig. 3.16a) was recommended. The SAWS hysteretic model was developed by FOLZ AND FILIATRAULT [Folz04a; Folz04b] for the **S**eismic **A**nalysis of **W**oodframe **S**tructures.
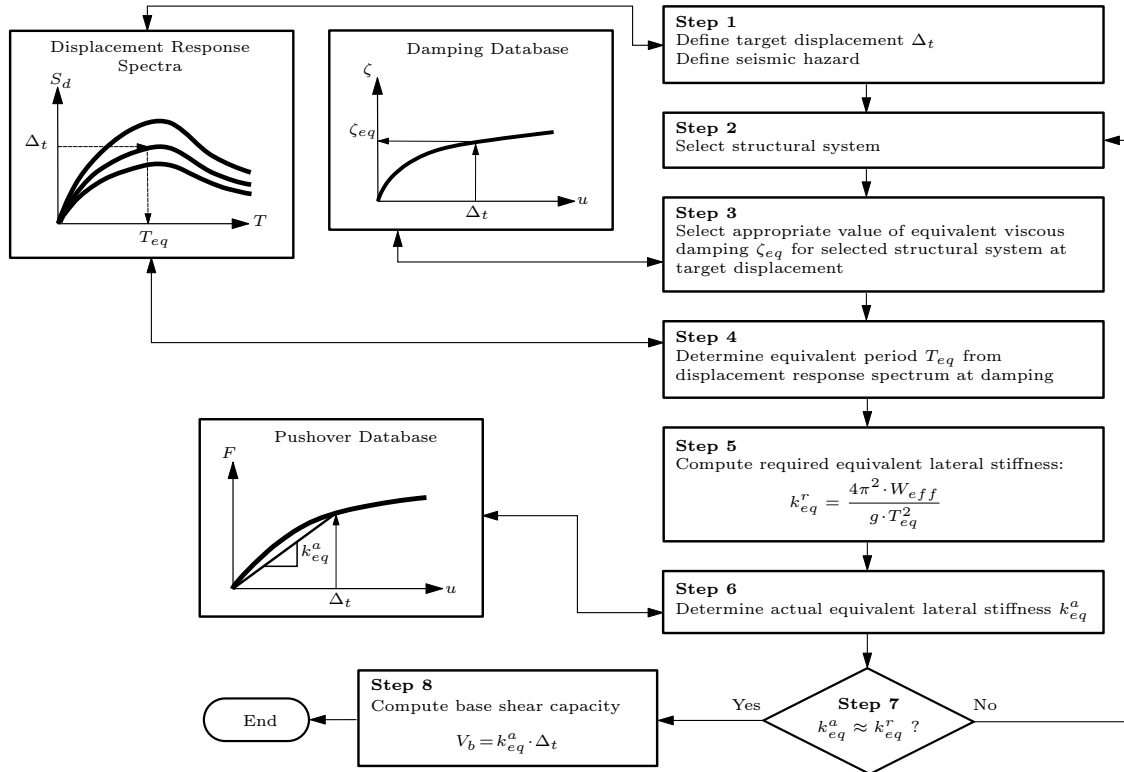
Figure 3.15: PBD procedure according to FILIATRAULT AND FOLZ [Fili02]

The procedure was further simplified by a bilinear relationship for equivalent viscous damping ξ_{eq} over building drift Δ_t (top displacement divided by the height of the building). This relationship was found by a parametric study considering different types of buildings with one to three storeys and several types of light-frame elements or structures [Fili03]. FILIATRAULT ET AL. determined the global hysteretic behaviour – base shear F_b over top displacement d – by means of a "pancake model" [Fisc00; Fili01]. It was stated that

the pancake model predicts the seismic response with sufficient accuracy. However, rigid diaphragms for floor and roof slab with two translational DOFs and one rotational DOF are assumed in the pancake model (cf. Fig. 3.16). Shear wall characteristics are represented by non-linear springs which account for lateral deflection. Spring properties were determined by means of the CASHEW programme which is based on the SAWS model. The $\xi_{eq} - \Delta_t$ relationship was then found by evaluating the global hysteretic behaviour ($F_b - d$ curve).
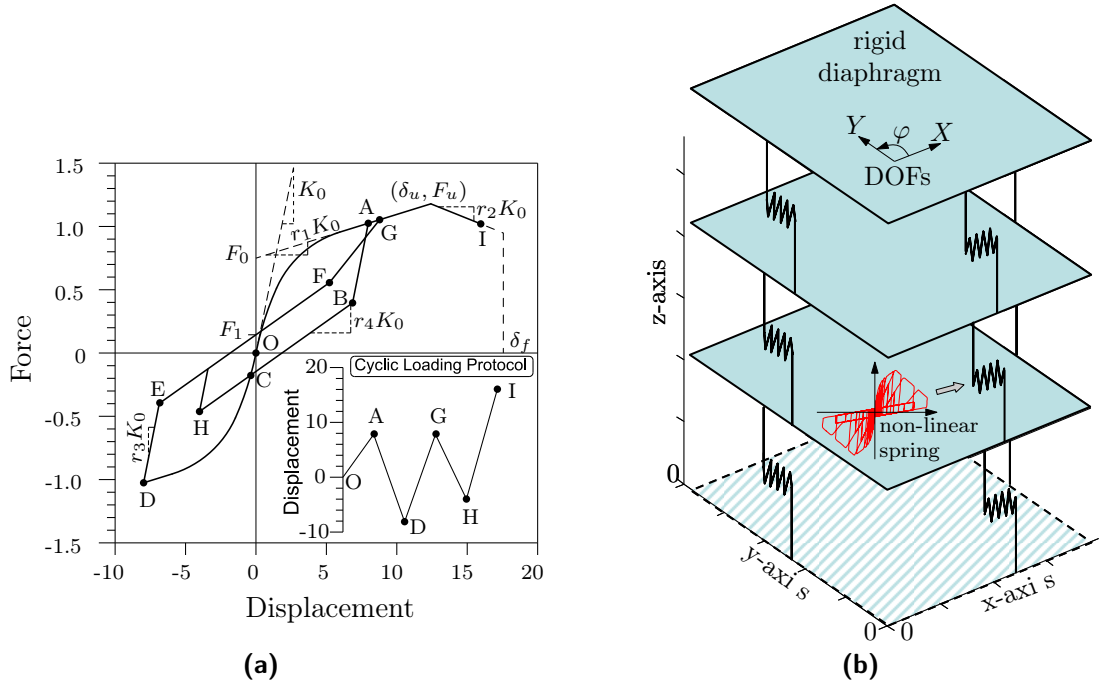
Figure 3.16: (a) SAWS hysteretic model [Folz01b], (b) analysis model – "pancake model" (from [Pang07])

3.2.2 Rosowsky et al.

PANG AND ROSOWSKY [Pang07] extended the PBD procedure according [Fili02] to a direct-displacement-based design procedure of MDOF systems. This method is based on an equivalent linearisation of the non-linear backbone curve of shear walls. Here, the non-linear system is substituted by a linear one with an equivalent stiffness based on equal energy. A database for shear walls is included in the methodology where properties are derived by means of the SAWS model (see Fig. 3.16a).

The method was applied to a three-storey light-frame building and was validated by a non-linear THA using the model depicted in Figure 3.16. A nominal damping ratio of 1% was considered in THA. The PBD procedure was used to design the six-storey timber-frame building which was tested on a shaking table under seismic action in the scope of the NEESWood project [Pang08; Roso08]. Later, a simplified version of the procedure was proposed by PANG ET AL. [Pang10a; Pang10b].
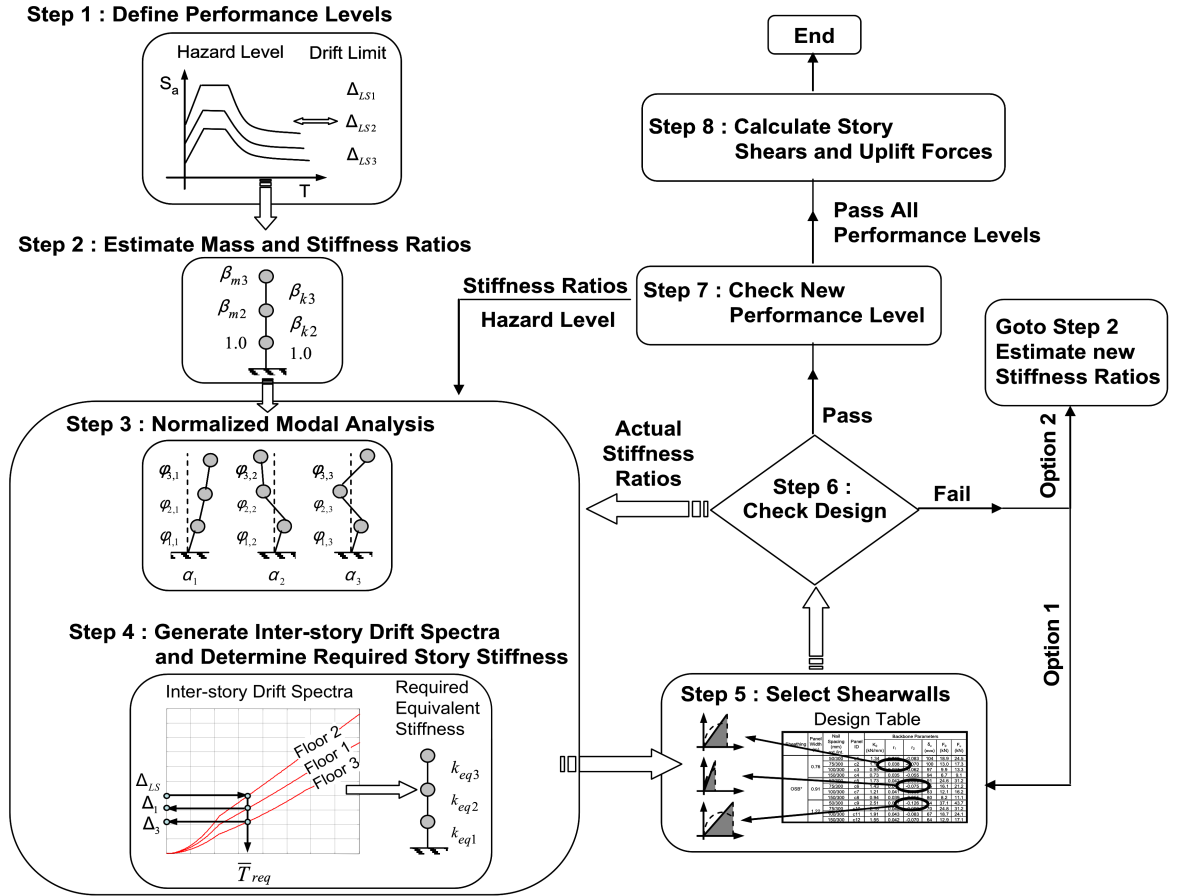
Figure 3.17: PBD procedure according to Pang and Rosowsky (from [Pang07])

$u_i = l_i/H \cdot u$, deformation of connector i
$H =$ height of the wall panel
$L =$ length of the wall panel
$l_i =$ distance between CoR and connector i
$f_i(u_i) =$ load-displacement relationship of connector i
$G =$ resultant gravity force
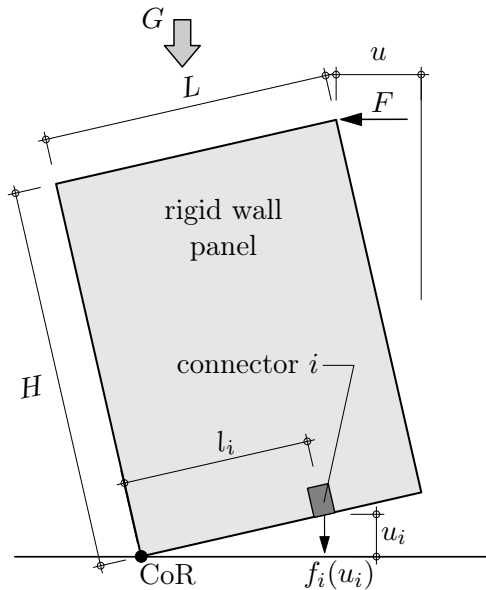
Figure 3.18: Kinematic model of an anchored CLT panel (from [Pei12])

The simplified DBD procedure was applied to a ten-storey CLT building [Pei12]. The kinematic model depicted in Figure 3.18 was applied to create non-linear backbone curves for CLT wall elements which are required within the design procedure proposed. In this kinematic model a rigid body rotation of the CLT panel is assumed where the load-displacement relationship is calculated by Eq. (3.1) considering a uniform vertical load.

$$F(u) = \sum_{i=1}^{n} \frac{l_i}{H} \cdot f_i(u_i) + \frac{L}{2H} \cdot G \tag{3.1}$$

The connector behaviour is represented by non-linear zero length springs using the SAWS model (see Fig. 3.16a). The spring properties were obtained by a "back calibration" procedure on the basis of results from wall element testing [Pei12]. The spring behaviour was varied until the hysteretic behaviour of the wall element fitted sufficiently. Numerical analyses were performed using the software SAPWood [Lind10].

As mentioned by KARACABEYLI [Kara13] several limitations comes with this kinematic model. The model is only valid up to a certain story drift level due to small angle approximation. The length of the wall panel needs to be short enough that the assumed rotation in the model is realistic; panels with large length to height ratios will not be able to rotate as assumed in the model.

It was assumed in the seismic design of the ten-storey CLT building that the global behaviour of the lateral load resisting system is a combination of behaviour of single CLT wall elements. The building was designed for different performance objectives and matched all the drift limits. Furthermore, a response modification factor which is a lateral force reduction factor according to US definitions [ASCE 7] was determined at 4.3. This value may be comparable with a behaviour factor of 2.5 to 3.0. However, it was stated by PEI ET AL. [Pei12] that if the boundary conditions prevent rocking of the wall the results of the study might not apply fully.

3.2.3 Ceccotti et al.

CECCOTTI ET AL. [Cecc08; Bouk09; Duji10] performed numerical investigations on the SOFIE buildings (see section 3.1.2) in order to evaluate the performance of the CLT structures obtained from shaking table testing and to find a somehow general applicable behaviour factor for the CLT construction type. A behaviour factor of 3.0 was proposed based on numerical simulations of the three-storey SOFIE building [Cecc08; Cecc10] and the PGA approach (see section 2.5.1). This behaviour factor was confirmed with the base shear approach [Popo11]. The numerical simulation was carried out using the non-linear dynamic analysis software DRAIN-3DX [Prak93]. Figure 3.19 shows the implementation of the three-storey analysis model. The model incorporates:

- truss elements assembled to rigid braced frames representing CLT panels,
- non-linear spring elements representing the behaviour of hold-downs, angle brackets and screw connections, and
- lumped masses in the nodes.

Viscous damping of 2% was considered added by stiffness proportional damping. The floor slab was modelled completely rigid. Spring properties were calibrated on results from wall element testing (see section 3.1.2).

The seven-storey SOFIE building was modelled in the same manner (see Fig. 3.20a). According to Boukes [Bouk09] good agreement with the results from shaking table testing was achieved. However, some features – such as the interaction of perpendicular walls, wall-slab interaction and influence of vertical load – were not considered in the model or were not addressed. Boukes [Bouk09] stated that the simplified 3D model was chosen for numerical reasons.
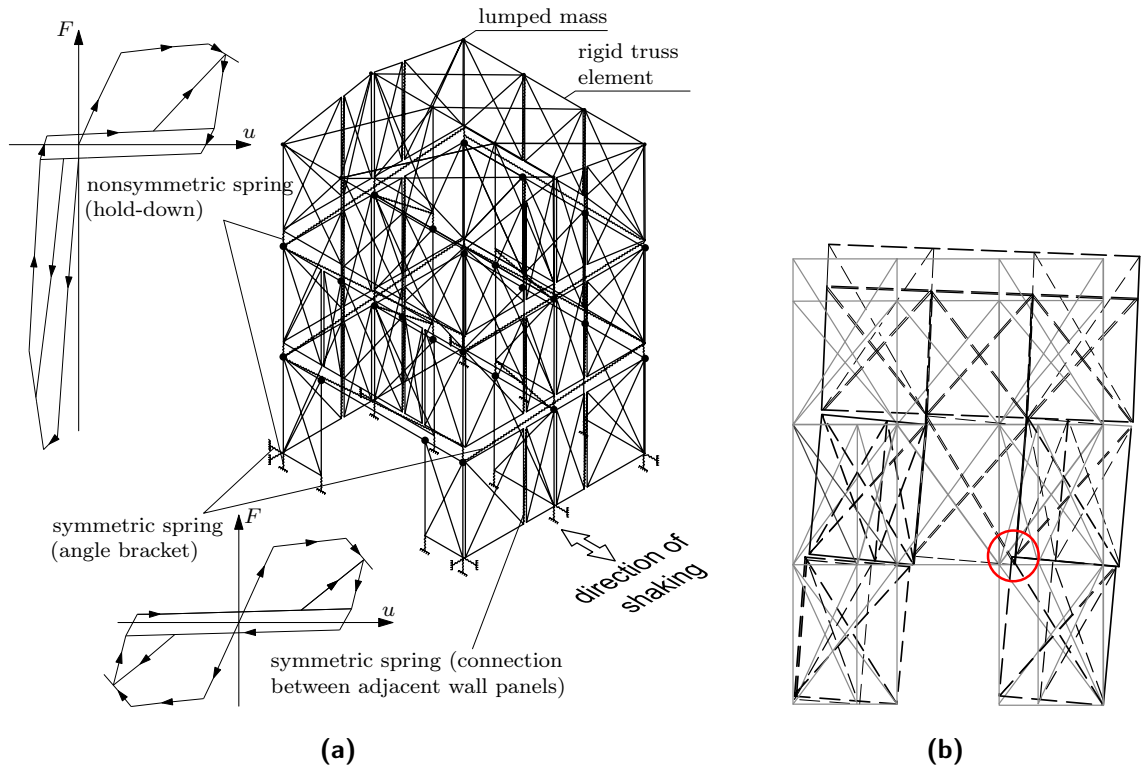
Figure 3.19: Analysis model of the three-storey SOFIE building (DRAIN-3DX) – (a) implementation and (b) deformation shape (from [Cecc08])

Figures 3.19b and 3.20a show deformation shapes of the three-storey and the seven-storey SOFIE building analysed exemplarily. The figures shows that this type of analysis model cannot reproduce all the features of the real building. Figure 3.20a depicts that there is a discontinuity between adjacent wall elements, which is not realistic at the floor level.

Additional numerical simulations were carried out on a model of the seven-storey SOFIE building [Duji10] using the software SAP2000 [Comp00]. Linear THA were performed where the connector behaviour was modelled by link elements with secant stiffness. The secant stiffness of each link element was determined on the basis of single connector behaviour obtained from cyclic testing. An equivalent viscous damping value of 0.15 was considered to account for energy dissipation caused by non-linear deformation of connections. The CLT elements were modelled with shell elements and homogeneous orthotropic material. Only the flexibilities of the anchoring (hold-downs and angle brackets) of wall elements were considered. The results from the numerical simulation matched those from the shaking table test with the original record of the Kobe earthquake (1995) in respect of the top displacement comparatively well. That appears to be reasonable, since the behaviour in the test can be described as nearly elastic.

(a)   **(b)**
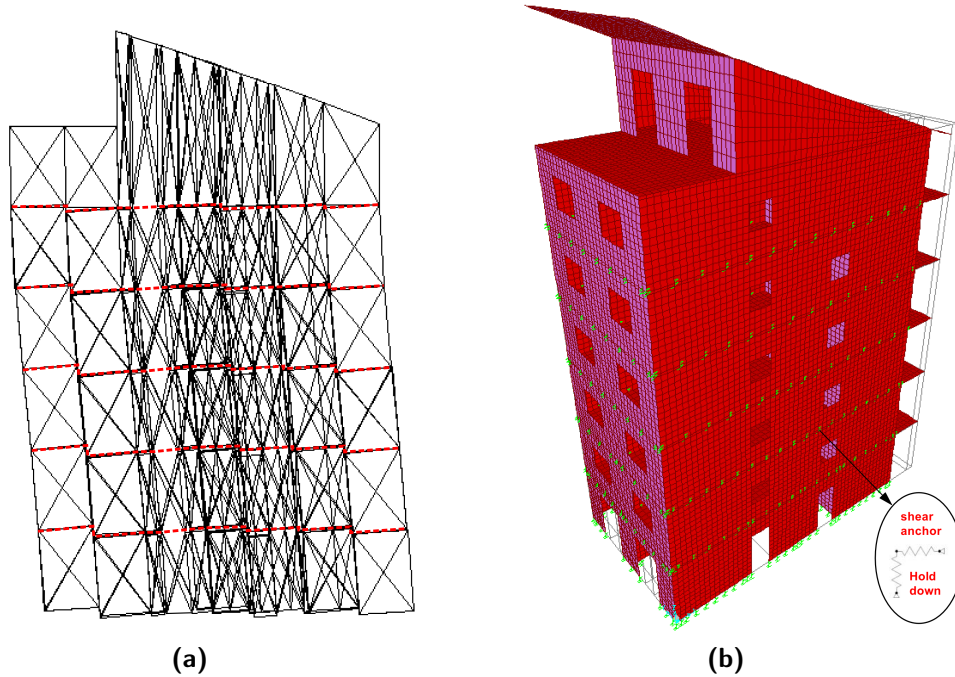
Figure 3.20: Seven-storey SOFIE building models – (a) deformation shape of DRAIN-3DX model
(from [Bouk09]) and (b) implemented SAP2000 model (from [Duji10])

3.2.4 Fragiacomo et al.

Fragiacomo et al. [Frag11; Sust11] performed a case study on a four-storey CLT
building model (see Fig. 3.21) in order to show the influence of the connection properties
in the seismic design of CLT structures. The seismic performance of the four-storey CLT
building was evaluated by FBD and DBD. A conservative behaviour factor of 2.0 was
taken for FBD and the N2 method was applied within DBD. The openings of windows and
doors in the walls were considered. A rigid floor diaphragm was assumed. The connections
between the structural elements – the connection between adjacent wall panels, between
perpendicular walls and between floor slab and wall – were modelled with link elements
which represent the stiffness of connectors such as angle brackets and self-tapping screws.
The stiffness properties of the connections were derived from the results of single connection
tests on angle brackets and self-tapping screws.

In the study a dead load for the floor slab and roof slab assemblies of $3.5\,\text{kN/m}^2$ and
$2.0\,\text{kN/m}^2$ respectively was considered. In addition, a live load of $2.5\,\text{kN/m}^2$ was added to
the floor and a snow load of $2.0\,\text{kN/m}^2$ was applied to the roof. The weight of the walls
was taken as $1.2\,\text{kN/m}^2$.

Analyses were performed with the software SAP2000 [Comp00]. Three variants of the
analysis model were studied. In one model, the connection between perpendicular walls
were considered and in a second model, this connection was neglected. The first period
of both models were about $0.6\,\text{s}$. Based on the fundamental period of the three-storey
SOFIE building (cf. section 3.1.2) the first period of the four-storey analysis model was
expected around $0.4\,\text{s}$. It was stated that the considerable amount of friction might be
the reason for that difference [Frag11]. Friction was not included in the analysis model.
A global ductility between 1.7 and 2.5 was found with the N2 method which is in the
range of the behaviour factor presumed (2.0). Different procedures to idealise non-linear
capacity curves by bilinear ones were demonstrated.
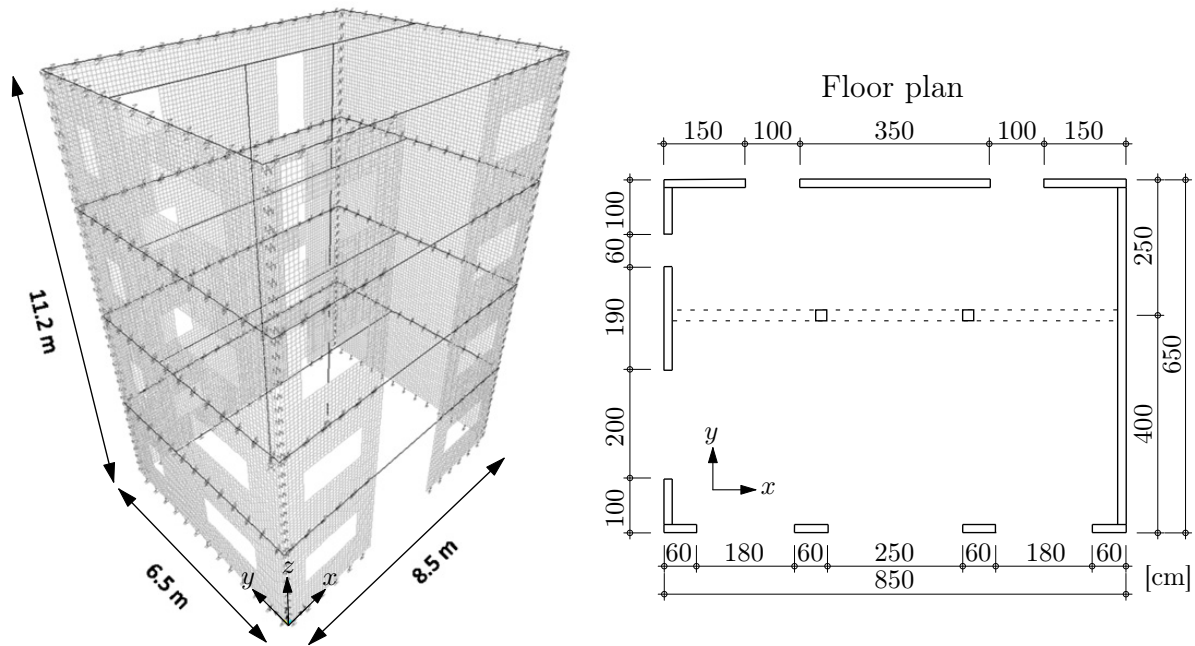
Figure 3.21: Analysis model and floor plan for a four-storey CLT building (from [Frag11])

FRAGIACOMO ET AL. stated that the current formulae of the N2 method do not cover systems where the hysteretic behaviour is dominated by significant pinching and stiffness degradation. This issue was also addressed by other researchers [Nord11; Merg15; Humm15]. It is further noted that NTHA should be carried out including appropriate hysteretic behaviour for connections to show the influence of connections on the global ductility.

RINALDIN AND FRAGIACOMO [Rina16] studied the behaviour of the SOFIE buildings with three and seven storeys by means of the software ABAQUS [Dass]. The CLT elements were modelled as linear elastic using shell elements in combination with an isotropic material model. The hysteretic behaviour of the connections was considered by non-linear springs. A user element (UEL) was implemented in ABAQUS which incorporates the non-linear characteristics of the connections and was developed by RINALDIN [Rina13]. Spring properties were derived from the results of connection and wall element testing. Friction was also considered by means of the UEL. A parametric study was carried out to evaluate the influence of friction and to find a sufficient friction coefficient.

Figure 3.22 shows the analysis models of the three- and seven-storey SOFIE buildings. Springs are denoted by blue dots. It shows that connections of adjacent wall elements and connections between perpendicular walls were considered.

NTHAs were performed using the records which were applied for the shaking table tests (see section 3.1.2). Mass proportional damping was used and 2 % viscous damping was taken into account. Results from the NTHA matched the results from the shaking-table tests comparatively well. Deviations in the top displacement and for the acceleration of about 7 % and 20 % respectively were found.

(a)   **(b)**
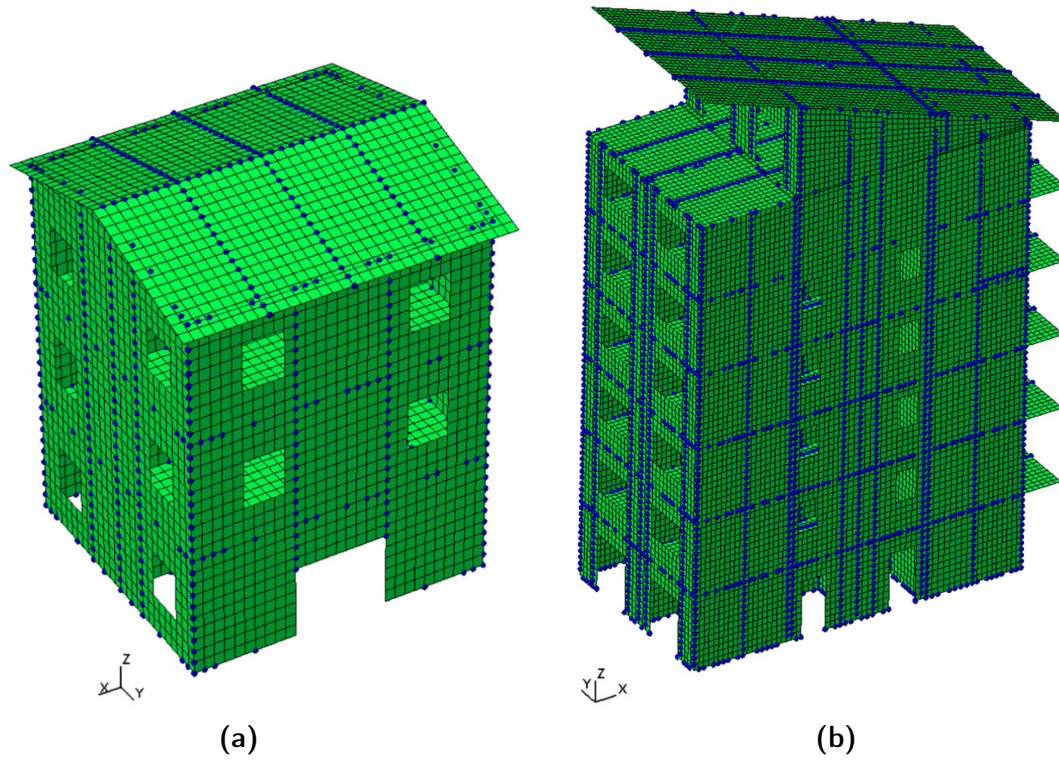
Figure 3.22: Analysis model (ABAQUS) – (a) three-storey SOFIE building, (b) seven-storey SOFIE building (from [Rina16])

3.3 Summary and interim conclusion

This section gives a summary of the experimental and analytical investigations presented in the previous sections. Topics for further research are derived subsequently from this summary.

Experimental investigations

The number of tests on CLT wall elements shows that substructure testing is an important step to evaluate the seismic performance of the CLT construction. Different hysteretic behaviour was obtained which does not only depend on the behaviour of the single connector. The hysteretic behaviour of CLT wall elements is also influenced by vertical load, openings, vertical joints, support conditions and wall dimensions. A uniform vertical load was usually applied which might be representative of three-storey CLT structures. Dujic et al. [Duji06b] also considered an eccentric vertical load. While the effect of openings is comparatively clear contrary results of the influence of vertical joints were obtained by wall element testing. It was found that screw connections can be very stiff or almost rigid. Element tests with walls connected to a CLT base show a reduction of stiffness compared to rigid support conditions connected with lower load-bearing capacity and higher deformation capacity. It was generally confirmed that the main deformation capacity is provided by the connections. The predominant deformation mechanism of single wall elements is rocking. However, deformation characteristics changes from rocking to slip with increasing wall length.

Full scale tests on the shaking table show that CLT buildings can withstand severe earthquakes without significant damage. Scaled and unscaled ground motions records of earthquakes such as Kobe (1995) or El Centro (1940) were applied. The structural response for earthquake excitation is characterised basically by small inter-storey and building drifts, minor change in the eigenfrequency and sometimes high accelerations in the upper levels of the building. The global response was also described as "box-type" behaviour [Cecc13].

Analytical investigations

NTHAs were carried out to predict the seismic performance of multi-storey CLT buildings, to validate DBD procedures and to derive behaviour factors for FBD.

Commercial software, such as DRAIN-3DX, SAP2000 or Abaqus and tools, such as SAPWood or Cashew, were employed to perform non-linear analyses. Ground motions such as those used in shaking table tests were taken for THA. Viscous damping between 1 and 5% was considered and stiffness proportional damping was applied. Only those structural elements which are located in the direction of excitation normally accounted for the lateral load-resisting system for the determination of seismic response. Then, the load-displacement behaviour per storey results only from the combination of the single wall element behaviour in the direction of excitation.

Load-displacement characteristics were modelled by a series of non-linear springs. The SAWS model [Folz01b] is frequently used to describe the behaviour of the non-linear springs. Spring properties were determined on the basis of the single connection behaviour and were calibrated on hysteretic behaviour from wall element testing. In the most cases springs for the anchoring and sometimes springs for in-plane joints of CLT elements were implemented. Two studies included springs for the connection between perpendicular walls [Frag11; Rina16]. However, further influences such as flexural stiffness of slabs and

flexibility of floor-slab-to-lower-wall connections were not considered or not discussed in most cases.

Different PBD procedures have been proposed for timber structures, especially for the light-frame construction type, and were applied to simplified single- and multi-storey timber building models. The procedures are based on or related to the DDBD method and the N2 method.

Conclusion

The performance of CLT buildings observed on the shaking table indicates that the behaviour is dominated by limited inelastic deformations and a considerable contribution of 3D effects. This means that the global behaviour of CLT buildings cannot only be described by an addition of the hysteretic behaviour of single wall elements. Due to wall-slab interaction several features of CLT buildings, such as

- stiffness of the connection between perpendicular walls,
- stiffness of the connection between floor/roof slab and lower wall,
- out-of-plane stiffness of floor slabs and roof slab

can influence the global behaviour significantly [Humm12]. Vertical load and support conditions as well as size of wall elements are among the characteristics of connections affecting the behaviour of a single CLT wall element. There is a lack, even in experimental investigations, with respect to element tests for realistic boundary conditions which should represent the situation of a single wall as substructure of a multi-storey timber building. Vertical loading, which was applied for wall element tests, may reflect the situation of a three-storey CLT building, but it is not valid for higher buildings up to eight storeys and more. Furthermore, the axial load of walls in a building rarely has a uniform shape or acts centrically but appears rather as an eccentric vertical load [Duji06b; Humm12]. The eccentricity might also affect the hysteretic behaviour.

It appears promising to study the substructure behaviour under realistic boundary conditions and to incorporate the relevant characteristics on the element level and 3D effects within advanced numerical models. That leads to a better understanding of the real performance of CLT constructions under seismic action.

Although different PBD procedures have already been proposed for timber structures the application and the validity of DBD should be demonstrated on appropriate multi-storey timber building models. DBD should be validated against NTHA. The comparison of two DBD methods – N2 method and CSM – is a further aim.

To achieve these objectives, analysis models of reference structures will be developed considering the relevant features (see chapter 5). Information for analysis models were obtained by means of experimental investigations on wall elements for realistic boundary conditions (see chapter 4). Displacement-based design of multi-storey CLT buildings will be presented in chapter 6 and results will be compared with results from NTHA (see chapter 5).

4 Experimental Investigations

Tests on connections (90 specimens), light-frame wall elements (20 specimens), moment-resisting frames (10 specimens) and CLT wall elements (15 specimens) were carried out within the scope of the research project OPTIMBERQUAKE [Opti].

Tests on CLT wall elements (see section 4.3) and their connections (see section 4.2) were performed to find data for wall configurations which have not been tested before (cf. Fig. 4.1). These experimental investigations are aimed at reflecting the situation of wall elements which are part of reference structures (see section 5). Reference to real structures under set-up and testing conditions is vitally important to obtain reliable and representative test results.

This applies particularly to detailing, loading conditions and base conditions of CLT wall elements.

(a)

(b) **(c)**
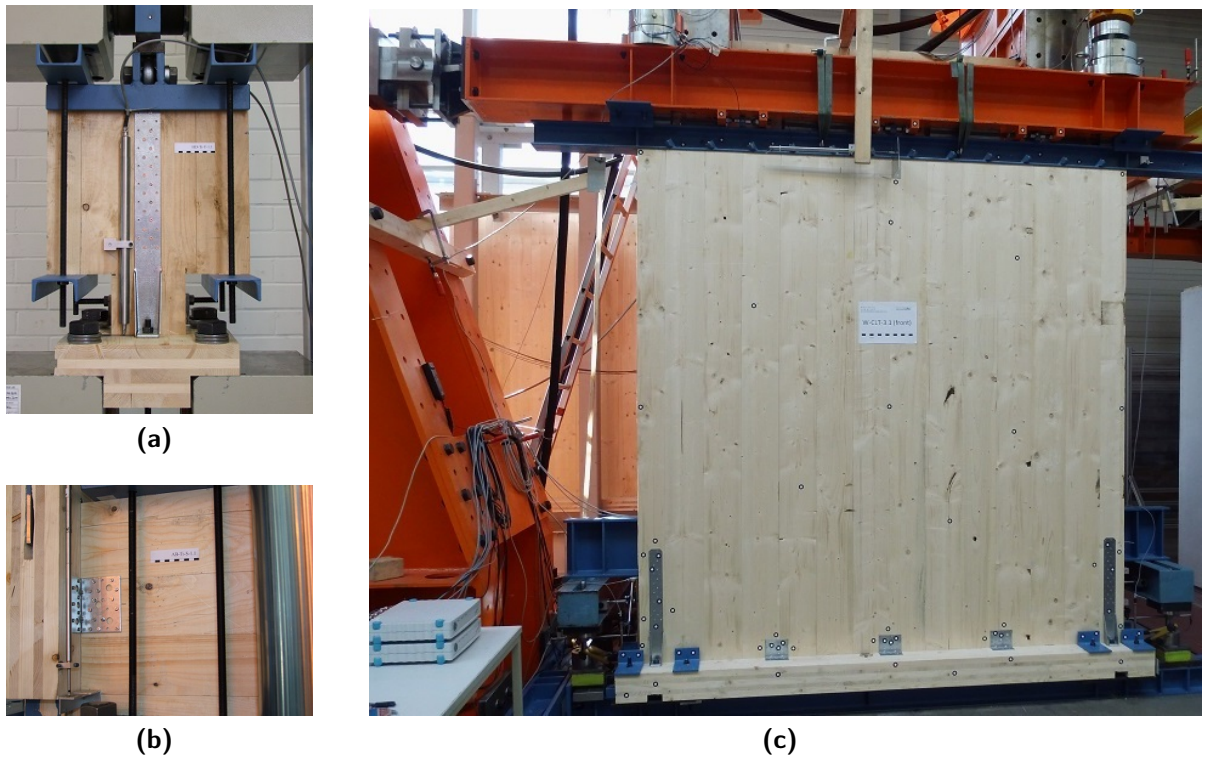
Figure 4.1: Experimental investigations on connections and wall elements related to the CLT construction; (a) wall-to-slab-connection with hold-down for loading in tension and compression, (b) wall-to-slab-connection with angle bracket for shear loading and (c) full-scale wall element on a CLT base

Details about the tests on connections and CLT wall elements and the related test results will be summarised in the following sections. The full documentation about test set-up, test results and data post-processing can be found in the test reports [Seim13b; Seim13a].

4.1 Materials and Basic Definitions

Connections and wall elements were tested under monotonic and cyclic loading. The cyclic tests which are presented here were performed according to [ISO 16670] and [ISO 21581] for connection tests and wall element tests, respectively.

Different configurations were tested. Prefabricated hold-downs HTT 22 and angle brackets AE 116 [Simp15], which are typical for construction practice, were used for connections and wall elements. The steel connectors were connected with a fixed number of ring shank nails to the wooden parts (CLT). Ring shank nails with a diameter of $\varnothing$ 4.0 mm and a length of 60 mm were taken for all tests (see Fig. 4.2a). The mean tensile strength $f_{u,mean}$ of the nails was determined at $763 \, \text{N/mm}^2$ by additional tests [Seim13b].

Two CLT sections were considered in the tests (see Fig. 4.2b and 4.2c). Wall elements or parts of them had a thickness of 105 mm. Sections with a thickness of 138 mm were chosen for slab segments. The CLT was made from spruce board layers with a strength class of C24.
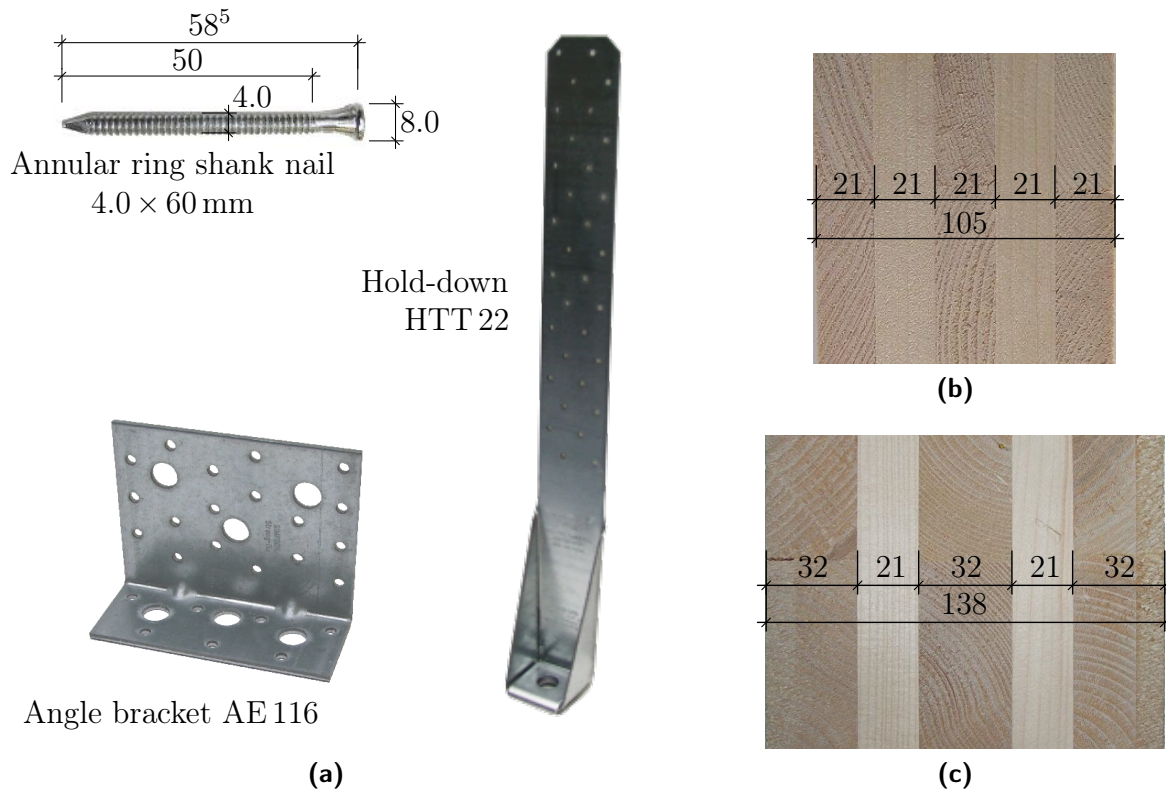
Figure 4.2: Connectors and CLT considered for experimental investigations; (a) ring shank nail and steel connectors, (b) wall cross-section and (c) slab cross-section

The different test configurations of connections and wall elements are documented in section 4.2 and 4.3. Issues such as load application and measuring of quantities (force and displacement) are explained in these sections. A hysteretic load-displacement curve can be drawn by means of the data recorded for force F and displacement u (see Fig. 4.3a).

The envelope curve which wraps the hysteresis curve is utilised to derive spring properties for nonlinear analysis (see chapter 5) and, moreover, to determine the parameters

- initial stiffness k_{ini},
- yield displacement u_y,
- ultimate displacement u_u and
- hysteretic damping ξ_{hyst},

which characterise the performance of a construction under seismic action (see 2.2). Protocols according to [ISO 16670] and [ISO 21581] for the loading. Three envelope curves are obtained where the envelope curve for each cycle can be created by connecting the points of maximum load of each deformation level (see Fig. 4.3a). Values of hysteretic damping ξ_{hyst} can be computed by means of Eq. (2.8) for each hysteresis loop. The first and the third cycle are normally considered. The other parameters are determined on the basis of the backbone curve, which represents the first-cycle behaviour.

In the first step, the backbone curve is idealised by a bilinear elastic-plastic $F - u$ relationship, which is also recommended as a basis to determine pushover curves for DBD. The bilinear curve is described by the initial stiffness k_{ini}, yield displacement u_y and ultimate displacement u_u. The last two parameters are also necessary to calculate the ductility μ (see 2.2). A few procedures were proposed for the definition of the yield point (see e.g. [Muño08]). However, the approach according to KOBAYASHI AND YASUMURA [Koba11] (K & Y approach) and the EEEP approach [ASTM E 2126-11] seem to be most reasonable for the bilinearisation of the nonlinear backbone curve with reference to seismic design and timber structures. The two approaches provide a procedure to define the initial stiffness and yield displacement based on the principle of energy equivalency.

Additionally, an ultimate displacement u_u must be defined as a deformation limit to denote failure. The point where the load is dropped to 80 % of the maximum load F_{max} normally characterises the ultimate displacement. However, in some cases, a significant loss of strength is observed after reaching F_{max}. Then, the displacement at the maximum load is used as ultimate displacement.

(a)   **(b)**
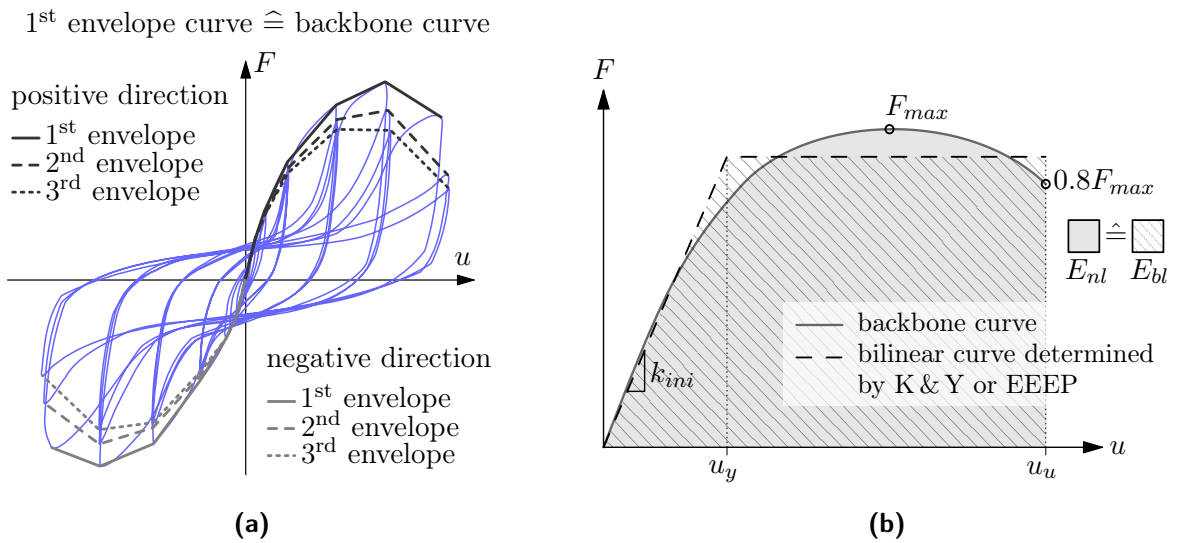
Figure 4.3: (a) Hysteresis – definition of envelope curves and backbone curve, (b) bilinearisation of the backbone curve

4.2 Connections

Details of the wall-to-slab connections' horizontal forces in practical engineering are assigned to angle brackets and tensile forces to hold-downs. However, the steel connectors, especially angle brackets, also have considerable load-bearing capacity in the secondary direction (see Fig. 4.4). It is crucial to consider the secondary direction for seismic design, not only for reasons of load-bearing capacity by loading of connections. The main concern is that the global hysteretic behaviour is influenced and, hence, the energy dissipation capacity of the structure in the secondary direction. In addition to that, the hysteretic behaviour of the connector itself is affected by the conditions of detailing in terms of different materials which form the anchorage base (see Fig. 4.4). Two main reference details are distinguished in the following:

- The joint to the rigid reinforced concrete (RC) base in the first level and
- the joint to the elastic CLT slab in higher levels.

The rigid concrete base is represented by steel components. A 138-mm-thick CLT segment was located beneath the CLT wall element in the configurations with CLT base.

These joints are more or less the only details in CLT structures where energy can be dissipated. Screwed connections might also have a proportion of energy dissipation. However, the energy dissipation capacity of screwed connections is assumed to be considerable lower than that of angle brackets.
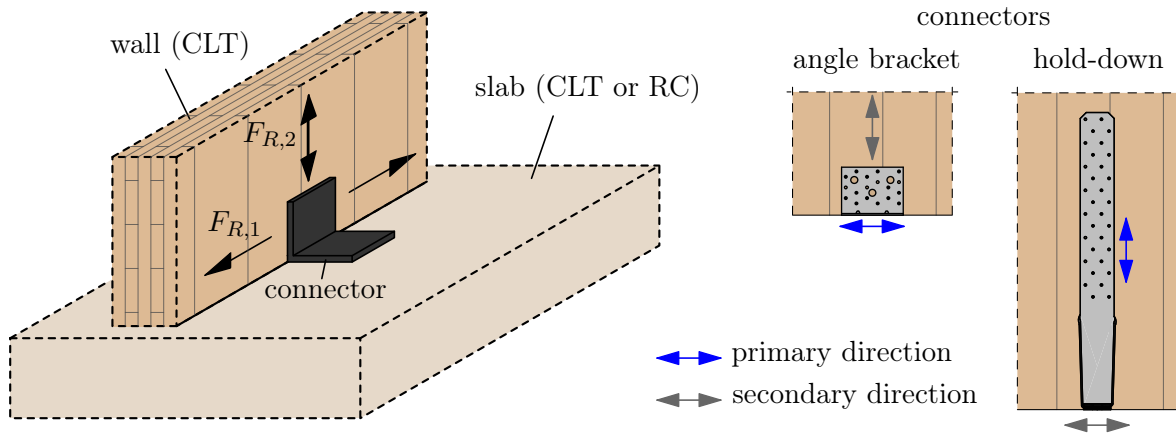
Figure 4.4: Loading directions for connectors at wall-to-slab connection, definition of primary and secondary loading direction

4.2.1 Configurations and specimens

A total of six configurations of connections were tested under cyclic loading. The different configurations are shown in Figure 4.5, where three configurations were equipped with angle brackets and three with hold-downs. The connectors were located on one side of the wall segment. Where the displacement δ and the force F were applied and measured are illustrated. The relative displacement u – displacement between wall and base – was measured with inductive displacement transducers at both sides of the wall segment. A ball bearing was located at the opposite site of the connection to avoid out-of-plane movement of the movable part due to eccentric anchoring. Please refer to SEIM ET AL. [Seim13b] for more details of the test set-up.
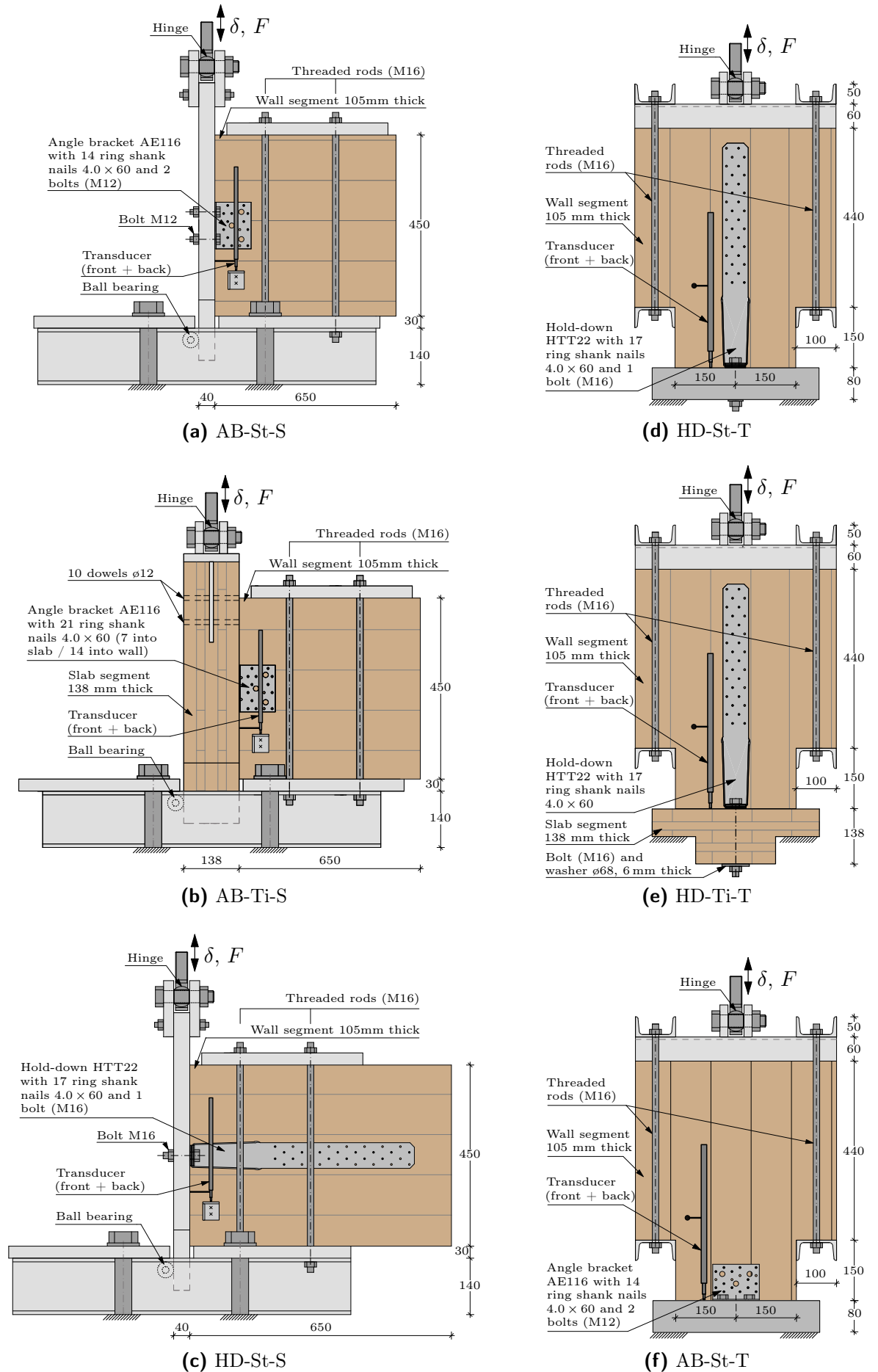
Figure 4.5: Configurations of connections; (a) – (c) connections under shear loading, (d) – (f) connection under loading in tension and compression
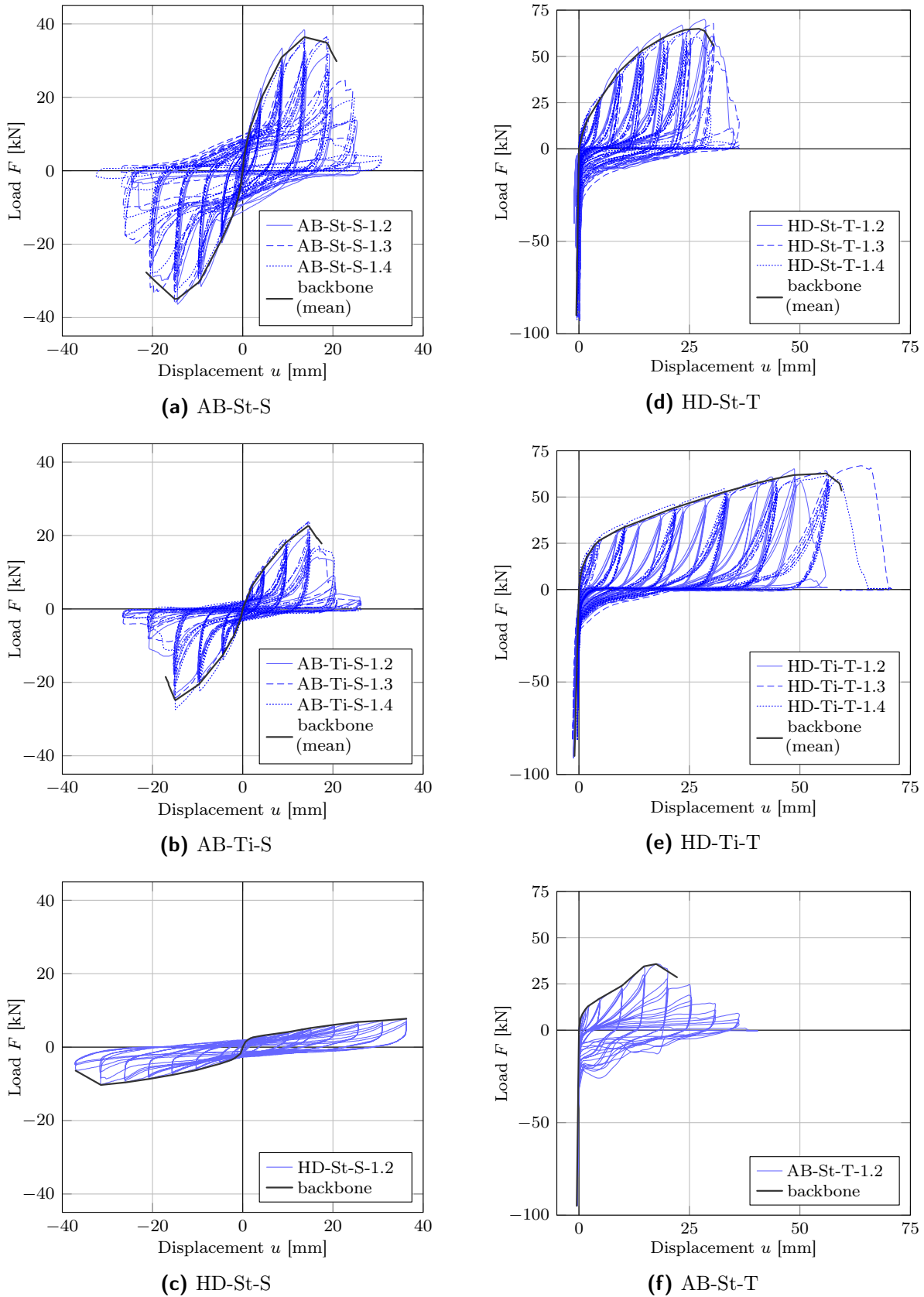
Figure 4.6: Hysteretic curves and backbone curves of connections; (a) – (c) under shear loading, (d) – (f) under loading in tension and compression

4.2.2 Results

With reference to the different configurations, the hysteresis curves which are obtained are depicted in Figure 4.6. More than one test was performed for some configurations. A backbone curve was determined for each test. The backbone curve of each configuration, as depicted in Figure 4.6, is then created as the mean of the several backbone curves. The results, which are given in Table 4.1, relate to the backbone of each configuration. The positive and the negative branch were evaluated separately. Here, the maximum force of the backbone and the ultimate displacement are reported. Furthermore, the initial stiffness and the yield displacement, which were determined with the K & Y [Koba11] and EEEP [ASTM E 2126-11] approaches, are given. In addition, the mean values of hysteretic damping, determined with Eq. (2.8) for the first and the third cycle are provided in Table 4.1.

It can be observed by means of hysteretic damping that angle brackets exhibit a higher potential to dissipate energy compared to hold-downs. On the other hand, the deformation capacity u_u of angle brackets is lower than that of hold-downs for the primary and secondary directions. The deformation capacity of angle brackets is even lower for the configuration with a CLT base. The hold-down anchored on CLT shows the opposite behaviour. Configuration HD-Ti-T shows a higher deformation capacity because of an indentation of the washer on the bottom side of the CLT slab segment.

The test results confirm that the load-bearing capacity of the angle brackets in the secondary direction (AB-St-T) is considerably high and even almost matches the maximum force of the primary direction (AB-St-S). Because of the lower number of nails in the slab segment in configuration AB-Ti-S, the maximum load is lower than in configuration AB-St-S. In contrast to that, the load-bearing capacity of configurations HD-St-T and HD-Ti-T is very similar, whereas the maximum load in the secondary direction (HD-St-S) is comparatively low. Results of each test in terms of maximum force, displacement values, values of initial stiffness and hysteretic damping are given in the documentation.

config- uration	n		F_{max} [kN]	u_u [mm]	K & Y		EEEP		$\xi_{hyst,1}$ [–]	$\xi_{hyst,3}$ [–]
					u_y [mm]	k_{ini} [kN/mm]	u_y [mm]	k_{ini} [kN/mm]		
AB-St-S	3	pos*	36.9	20.6	7.3	4.8	5.8	5.7	0.190	0.148
		neg*	35.2	20.7	7.6	4.2	6.4	4.8		
AB-Ti-S	3	pos*	22.7	17.2	8.9	2.3	7.8	2.5	0.175	0.101
		neg*	24.9	16.8	7.7	2.9	6.8	3.1		
HD-St-S	1	pos	7.7	36.5	12.0	0.5	8.3	0.7	0.274	0.203
		neg	10.3	34.4	10.8	0.8	8.2	1.0		
HD-St-T	3	pos*	66.7	30.8	11.3	5.3	9.9	6.0	0.071	0.035
HD-Ti-T	3	pos*	64.5	59.6	12.8	4.3	9.0	6.0	0.062	0.019
AB-St-T	1	pos	35.8	22.2	6.7	4.4	5.9	4.9	0.136	0.098

n – number of tests
* mean over the number of tests per configuration

Table 4.1: Results for tests on connections – maximum force, displacement values, values of initial stiffness and hysteretic damping

With reference to the derived deformation and stiffness characteristics, it can be observed that higher values of the initial stiffness K_{ini} are obtained by means of the EEEP approach compared to the K & Y approach.

An evaluation of the displacement and stiffness characteristics of connections determined will be given with reference to DBD in chapter 6. Additional information regarding the test results is documented by SEIM ET AL. [Seim13b].

4.3 Wall Elements

A special focus was to test the wall elements under boundary conditions which reflect the situation in a multi-storey CLT building. On the one hand, the two support conditions: rigid base (such as a concrete basement) and elastic base (such as a CLT slab), were considered and, on the other hand, different load levels which represent the conditions of a certain wall in a building in a specific storey. Loading conditions were found by a parametric study on different multi-storey timber buildings [Humm12].

4.3.1 Configurations and specimens

The different configurations which were considered for cyclic testing of wall elements are summarised in Table 4.2. The test labels refer to the ones which were used in the test report [Seim13a]. The first configuration was tested for comparison with wall element tests from other researchers (see section 3.1). The test conditions in this configuration are approximately comparable with an outer wall on the first level of a building with one to two storeys. A higher vertical load was applied in configuration 2 and 3 to account for the axial load of walls (first level) in a building with up to four storeys and eight storeys, respectively. The influence of support conditions depending on the position of the wall element in elevation and different detailing were investigated by means of three more configurations (4 to 6). Finally, the interaction between axial and horizontal loading was studied with the configurations 7 and 8. An eccentric vertical load occurs predominantly in lower levels of buildings with eight or more storeys.

	test[a]	configuration	anchoring	base conditions	vertical load
1	W-CLT-1.2	W-CLT-St-10	2 HD, 3 AB	rigid (steel)	10 kN/m
2	W-CLT-2.2	W-CLT-St-50	2 HD, 3 AB	rigid (steel)	50 kN/m
3	W-CLT-4.3	W-CLT-St-100	2 HD, 3 AB	rigid (steel)	100 kN/m
4	W-CLT-3.2	W-CLT-Ti-10	2 HD, 3 AB	CLT	10 kN/m
5	W-CLT-3.3	W-CLT-Ti-50	2 HD, 3 AB	CLT	50 kN/m
6	W-CLT-3.4	W-CLT-Sy-50	2 HD, 3 AB	CLT + Sylodyn	50 kN/m
7	W-CLT-4.2	W-CLT-Ti-50M	2 HD, 3 AB	CLT	50 kN/m + M[b]
8	W-CLT-4.4	W-CLT-St-100M	2 HD, 3 AB	rigid (steel)	100 kN/m + M[b]

HD – hold-down, AB – angle bracket, Sylodyn – elastomeric interlayer

[a] test labels as used in the test report [Seim13a]

[b] overturning moment on the top of the wall, see Eq. (4.1) and Fig. 4.8

Table 4.2: Configurations of cyclic CLT wall element tests

① Hold-down HTT 22 with 17 ring
shank nails 4.0×60 and bolt
M16

② Angle bracket AE 116 with 14
ring shank nails 4.0×60 and 2
bolts M12

① Hold-down HTT 22 with 17 ring
shank nails 4.0×60 and 1 bolt
M16 + washer ⌀ 68 (5 mm thick)

② Angle bracket AE116 with 21 ring
shank nails 4.0×60 (7 into slab /
14 into wall)

elastomeric interlayer
(Sylodyn NE, t=12.5 mm)

(a) W-CLT-St   **(b)** W-CLT-Ti/W-CLT-Sy
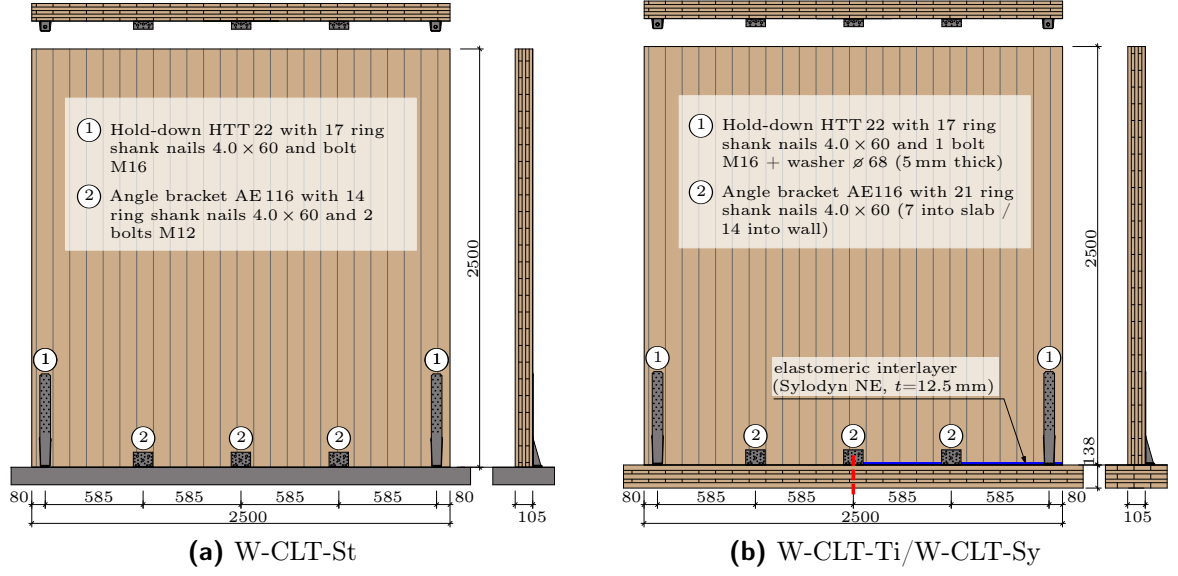
Figure 4.7: Configurations of wall element testing – base conditions and anchoring; (a) rigid
base - anchoring on steel, (b) elastic base - anchoring on CLT without and with
elastomeric interlayer

All wall elements tested had the dimension $2.5 \times 2.5\,\mathrm{m}$ and a thickness of $105\,\mathrm{mm}$ (see
Fig. 4.7). The two main configurations with respect to base conditions and anchoring
are depicted in Figure 4.7. The CLT elements were anchored with two hold-downs and
three angle brackets in all configurations. The same types of steel connectors as those
used for the tests on connections (see section 4.2) were used for the anchoring of the wall
elements.

In addition to the rigid base and the elastic CLT-support, requirements of sound proofing on
support detailing were considered in configuration W-CLT-Sy-50 by adding an elastomeric
interlayer in the contact area between the wall and the CLT slab. The elastomer Sylodyn NE
[Getz11; Teib09] was used as an interlayer material in this configuration. The interlayer
Sylodyn NE has a thickness of $12.5\,\mathrm{mm}$ and a Young's modulus of $6.55\,\mathrm{N/mm^2}$. An
interlayer strip of $100\,\mathrm{mm}$ in width was located underneath the CLT wall.

With respect to load conditions, uniform vertical loads of 10 to $100\,\mathrm{kN/m}$ and a combination
of a uniform vertical load and an overturning moment M were applied. The overturning
moment is a function of the horizontal load F. It was found by means of a preliminary
study on multi-storey reference buildings [Seim11] that the shear span h_0 for certain walls
in a CLT building is significantly higher than the wall height h (see Fig. 4.8). The shear
span for configurations 7 and 8 was fixed at $h_0 = 2.2 \cdot h$, which corresponds to an overturning
moment of

$$M = (h_0 - h) \cdot F = 3\,\mathrm{m} \cdot F \tag{4.1}$$

with M overturning moment on the top of the wall [kNm]
 h_0 shear span, $h_0 = 2.2 \cdot h$ [m]
 h wall height, $h = 2.5\,\mathrm{m}$

The application of the vertical load during the test is described in section 4.3.2. The cyclic
protocols according to [ISO 21581] was applied with a speed of $1.0\,\mathrm{mm/s}$ for loading in
horizontal direction.

4.3.2 Test set-up

A steel girder (HEB 120) which transfers the loads from the upper girder (HEB 300) to the wall is located on the top of the wall. The HEB 120 girder is connected with 24 diagonal self-tapping screws ($\varnothing\, 8.0 \times 160$ mm) to the top of the wall. The horizontal load is transferred by block shear connectors welded to the girders and eccentric bolts (see Fig. 4.9). The vertical load is applied by contact with elastomer bearings between the upper and the lower girder. The steel girder or the CLT section which forms the base of each wall element was fixed to the concrete floor of the laboratory.

Loading is applied by two vertical cylinders (V1 and V2) and one horizontal cylinder (F), as shown in Figure 4.9. Firstly, the vertical load is applied force-controlled by the vertical cylinders. Then, the wall element is loaded in horizontal direction displacement-controlled following the cyclic loading protocol. The resulting vertical load is held constantly during application of the horizontal displacement, except in configurations 7 and 8. The vertical actuators allow uplift of the wall element due to in-plane rotation (rocking).

The application of the combined vertical load – in configurations 7 and 8 – is illustrated in Figure 4.8 for one direction exemplarily. The magnitude and direction of the overturning moment depend on the horizontal load. The overturning moment is applied by the two vertical actuators V1 and V2, as shown in Figure 4.8.
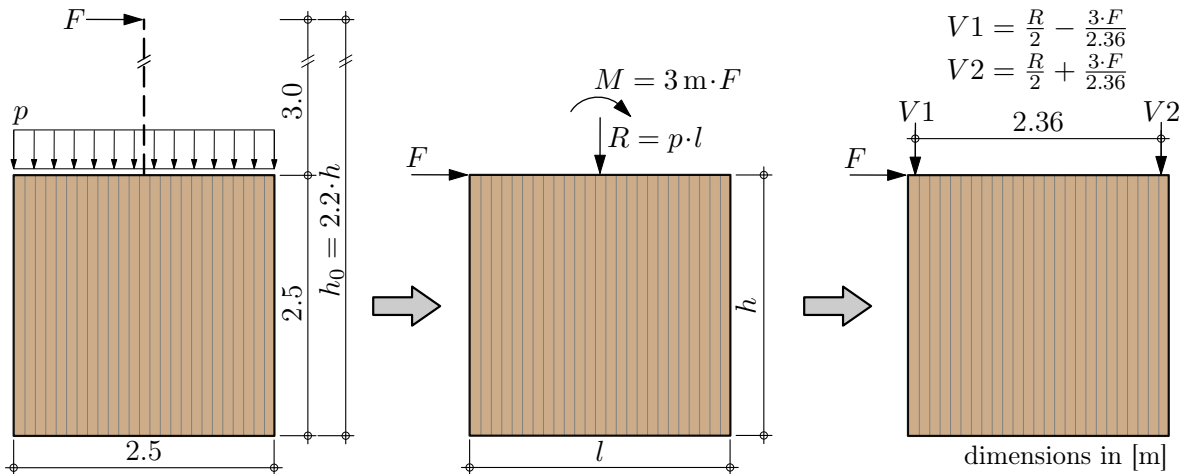
Figure 4.8: Combined vertical loading - application of vertical load for configurations 7 and 8

In order to draw the hysteresis curve, the lateral displacement (W1 + W2) and the corresponding horizontal load (F) are measured at the top the wall element in Figure 4.9. The second transducer (W2) is included to check the displacement of W1. More detailed information for the test set-up is provided in the test report [Seim13a].
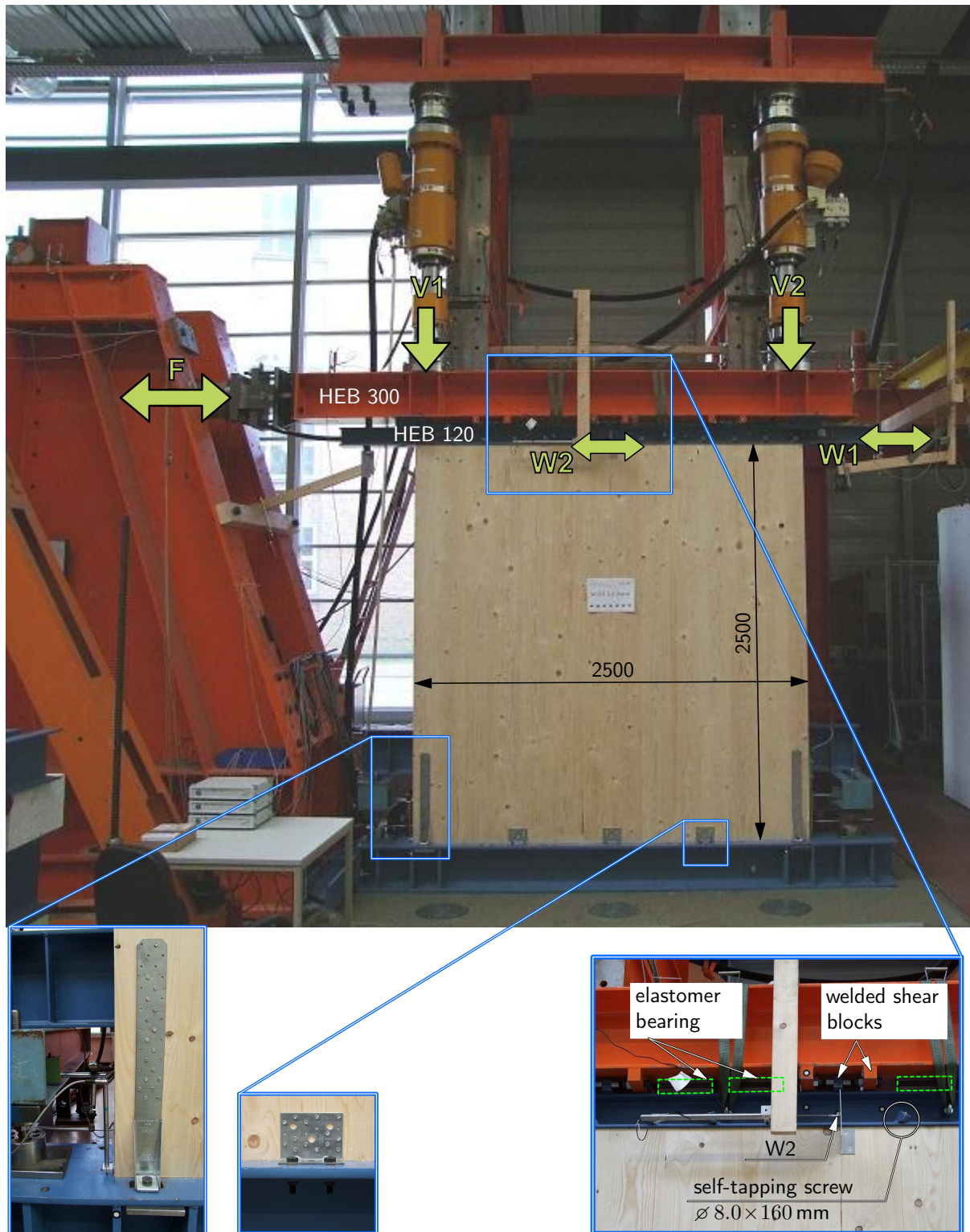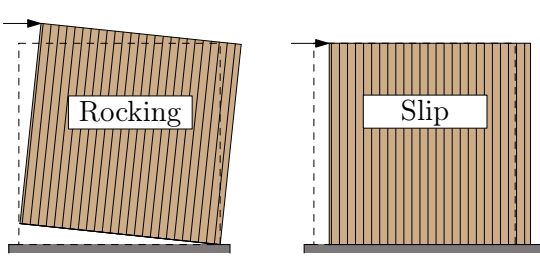
Figure 4.9: Test set-up for CLT wall elements

4.3.3 Test results

Even if the configuration of connectors and the dimensions of the CLT wall elements (see Fig. 4.10) are completely the same, it was found that the results can be significantly different (see Tab. 4.3). This applies to the maximum load F_{max}, displacement and stiffness characteristics (u_u, u_y, k_{ini}), as well as the damping ratio ξ_{hyst} and the hysteretic behaviour in general. It was found that the deformation mechanism of the CLT wall element is the key factor in this context (see Tab. 4.4).

configuration		F_{max} [kN]	u_u [mm]	K & Y		EEEP		$\xi_{hyst,3}$ [–]
				u_y [mm]	k_{ini} [kN/mm]	u_y [mm]	k_{ini} [kN/mm]	
W-CLT-St-10	pos	87.3	54.0	17.8	4.4	13.3	5.6	0.103
	neg	89.1	56.9	17.0	4.6	13.8	5.5	
W-CLT-St-50	pos	116.8	48.5	12.0	8.5	7.7	12.6	0.162
	neg	122.4	47.3	12.6	8.4	8.7	11.5	
W-CLT-St-100	pos	135.2	42.8	8.3	14.6	5.3	22.2	0.218
	neg	140.3	43.8	8.6	14.4	4.5	25.9	
W-CLT-Ti-10	pos	63.2	78.5	14.3	3.9	8.1	6.6	0.084
	neg	73.4	71.8	19.5	3.4	14.6	4.4	
W-CLT-Ti-50	pos	92.5	70.9	8.9	9.7	5.3	16.0	0.089
	neg	96.5	63.4	14.0	6.7	5.0	17.3	
W-CLT-Sy-50	pos	99.0	66.7	16.4	5.3	14.0	6.0	0.085
	neg	94.3	53.3	16.0	5.2	12.2	6.6	
W-CLT-Ti-50M	pos	45.6	57.3	9.5	4.4	6.3	6.5	0.054
	neg	46.7	51.6	7.7	5.6	5.8	7.3	
W-CLT-St-100M	pos	83.4	47.3	6.2	11.8	5.5	13.3	0.109
	neg	85.0	40.9	9.6	8.0	5.0	14.5	

Table 4.3: Results for tests on CLT wall elements – maximum force, displacement values, values of initial stiffness and hysteretic damping (3$^{\mathrm{rd}}$ cycle)

configuration	rocking	slip	CLT	deformation mechanisms
W-CLT-St-10	64 %	30 %	6 %	
W-CLT-St-50	45 %	44 %	11 %	
W-CLT-St-100	35 %	48 %	17 %	
W-CLT-Ti-10	75 %	21 %	4 %	
W-CLT-Ti-50	74 %	17 %	9 %	
W-CLT-Sy-50	70 %	22 %	8 %	
W-CLT-Ti-50M	83 %	8 %	9 %	
W-CLT-St-100M	71 %	19 %	10 %	

"CLT" stands for the inherent deformation of the CLT element due to bending and shear.

Table 4.4: Contributions to the overall deflection from wall element testing – rocking, slip and CLT

Table 4.4 depicts the different contributions of deformation as the mean of the evaluation of the positive and negative backbone curve. The determination of the contributions of deformation refers to the procedure which was presented by FLATSCHER [Flat12]. Reasons

for the different manner of deformation are the various boundary conditions with respect to vertical load and support conditions. Regarding the rigid base the CLT wall elements tend to slip more compared to the configuration with the elastic base. The amount of slip increases with increasing uniform vertical load for the rigid base configuration. The behaviour of wall elements with a timber base or some kind of elastic base is predominantly characterised by rocking. Here, the contribution of rocking to the overall deflection stays almost constant for uniform vertical load, no matter the load level, and it amplifies in the case of an eccentric vertical load.
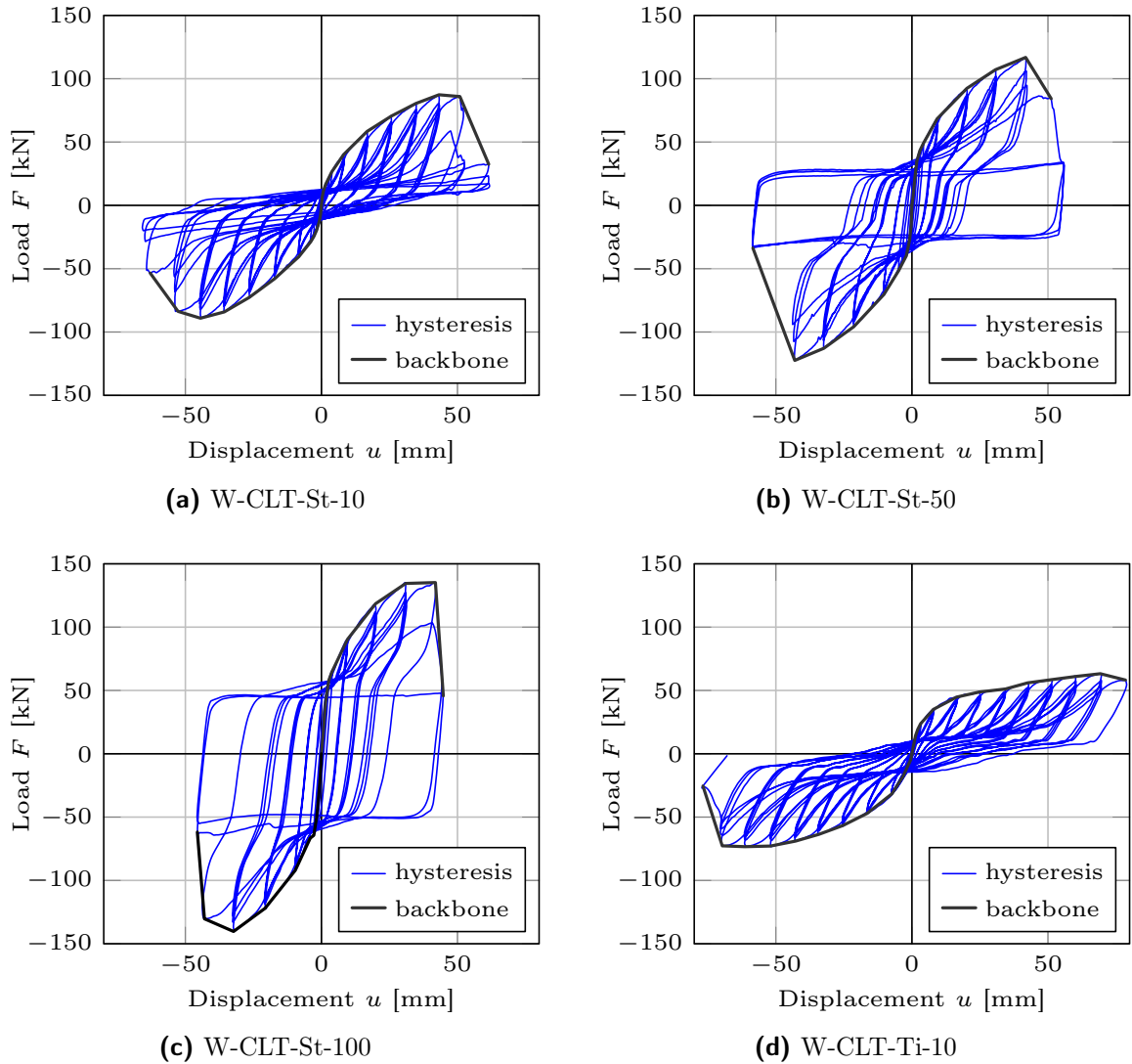
(a) W-CLT-St-10

(b) W-CLT-St-50

(c) W-CLT-St-100

(d) W-CLT-Ti-10

Figure 4.10: Hysteretic curves and backbone curves of the different configurations of CLT wall elements for transducer W1 (part 1)

It was observed that a higher uniform vertical load leads to a clear increase of the maximum load F_{max} and initial stiffness k_{ini}. The eccentric vertical load yields a loss of stiffness and load-bearing capacity. A similar effect can be observed for the configuration with the elastomeric interlayer. Furthermore, the deformation capacity of the CLT wall element is restricted depending on the deformation mechanism. If rocking dominates, the ultimate displacement u_u is higher compared to a situation where the main contribution is slip. However, if rocking is the predominant contribution to deflection, comparatively low damping ratios ξ_{hyst} are obtained. This effect is associated with the behaviour of a single

connector in the primary loading direction: hold-downs exhibit a comparatively high deformation capacity and low hysteretic damping and angle brackets, by contrast, show less deformation capacity and higher damping ratios (see Tab. 4.1).
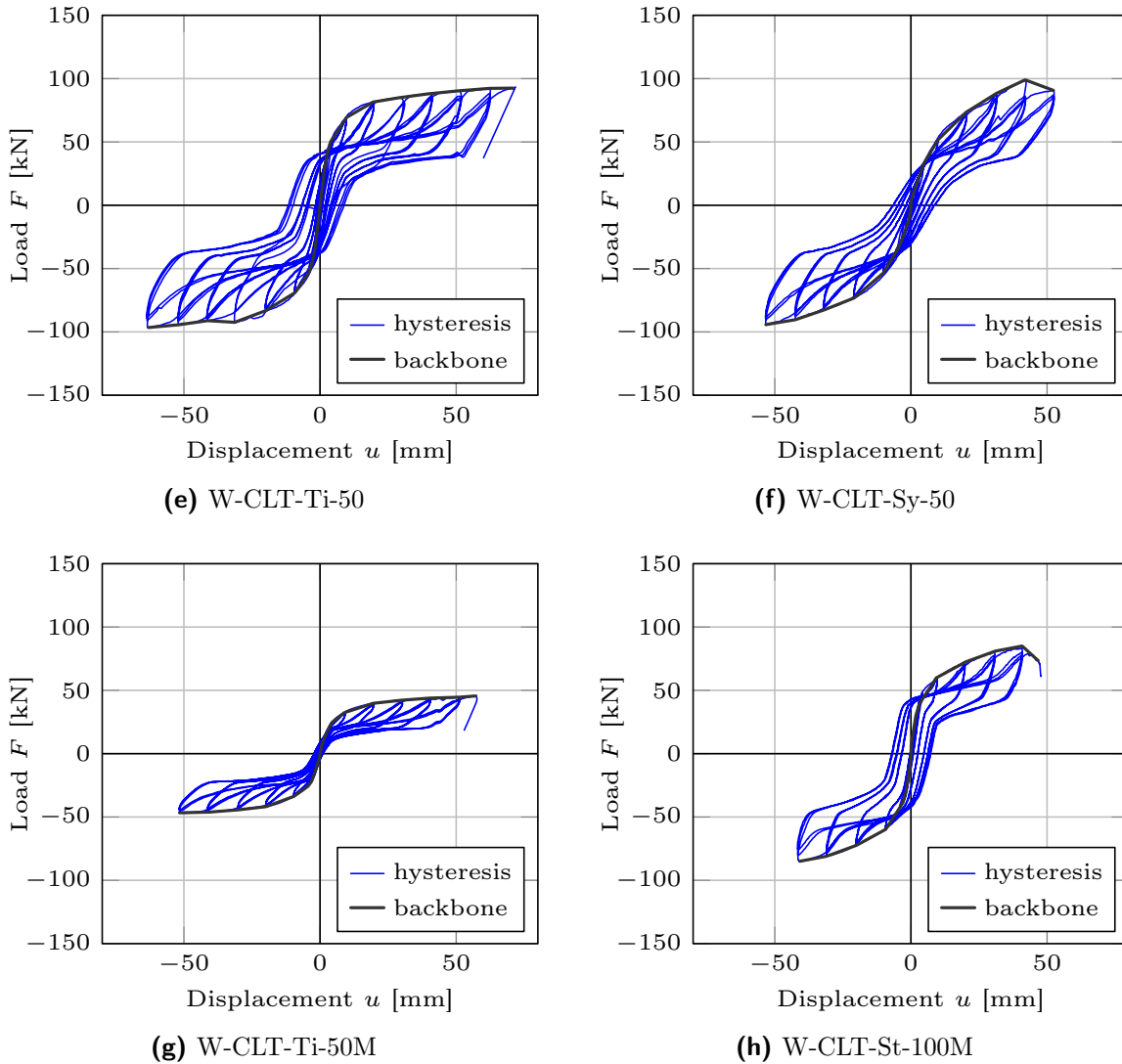
(e) W-CLT-Ti-50

(f) W-CLT-Sy-50

(g) W-CLT-Ti-50M

(h) W-CLT-St-100M

Figure 4.10: Hysteretic curves and backbone curves of the different configurations of CLT wall elements for transducer W1 (part 2)

It must be noted that the rigid base with a steel girder does not fully capture the support conditions of a wall on the first floor realistically. A much higher contribution of friction for a realistic RC support is definitely expected. The supporting steel girder is lacquered, as seen in Figure 4.9. It is known that the friction coefficient of the painted surface is lower than that of the unpainted surface. This issue will be taken up again when analysis models are set up in the following chapter.

The fact that a quantification of hysteretic damping is required in order to perform DBD by means of CSM was addressed in the previous sections 2.3.2 and 2.4.3. Values of hysteretic damping for different displacement amplitudes can be derived from test results on the wall element level. Data of the tests documented in Figure 4.10 and four further cyclic tests on CLT wall elements – which were performed in the scope of the research project OPTIMBERQUAKE [Opti] – have been taken as basis for the evaluation

of hysteretic damping of CLT wall elements. With reference to the test report [Seim13a] the following tests were considered: W-CLT-1.2, W-CLT-1.3, W-CLT-2.2, W-CLT-2.3, W-CLT-3.2, W-CLT-3.3, W-CLT-3.4, W-CLT-3.5, W-CLT-3.6, W-CLT-4.2, W-CLT-4.3 and W-CLT-4.4.

The graphs of hysteretic damping over the displacement amplitude for these 12 cyclic tests can be found in the test report [Seim13a]. From these graphs fairly constant values for hysteretic damping with increasing deformation appear until a drift limit of 50 mm ($0.02 \cdot h$) is reached. This applies especially to the damping ratios of the third cycle. The summary of the 12 graphs and the related histogram are depicted in Figure 4.11.

Since outliers exist for specific amplitudes and certain cycles, the median value is documented in addition to the mean value. The median value seems to be more descriptive than the mean value in this case. However, the median value coincides with the mean value for the first cycle evaluation and is slightly lower than the mean value of the third cycle. The evaluation of the second cycle was not considered here because the difference between the damping ratios of the second and third cycle is quite small (see [Seim13a]).

It becomes clear from Figure 4.11 that the damping values are scattered, even for wall elements with the same constellation of connectors and wall dimensions. However, a strong concentration of the damping ratio in the range of 0.10 to 0.14 can be observed. The median value of the first cycle could be interpreted as the upper limit and the median value of the third cycle might be the lower limit of hysteretic damping for this wall element configuration. The median value is 0.124 and the mean value 0.134 if all values of hysteretic damping of the first and the third cycle are taken together.
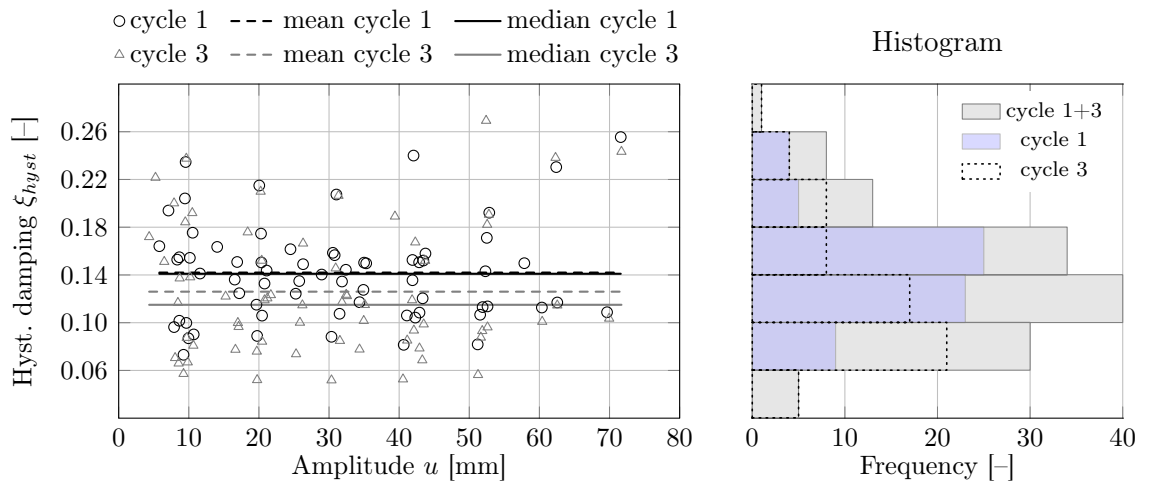
Figure 4.11: Summary of hysteretic damping for CLT wall elements and overall distribution of hysteretic damping for cycle 1 and cycle 3 (based on test results from [Seim13a])

The data obtained for connections and wall elements will be considered as the basis for numerical simulations on the wall level in the first step and on the building level in the second step. Load-displacement characteristics will be taken to determine the properties of different types of springs which will be involved to set up numerical models of wall elements and reference structures (see section 5). The contributions of deflection to each configuration derived (see Tab. 4.4) will be used for the validation of numerical wall element models. The values for hysteretic damping will be incorporated as part of effective damping for DBD (see section 6).

5 Structure and substructure modelling

In this chapter the development of numerical models will be studied on the level of single walls and the building level. These investigations create the basis to validate different design approaches for CLT constructions. The numerical simulations were performed by means of the numerical software OPENSEES [McKe], using the finite element method. With reference to the analysis programme the input data which are required for the implementation of analysis models will be provided in the following subsections. The analysis models developed allow performance of both linear and non-linear dynamic and static analyses.

The test results from section 4.3 of the tests on CLT wall elements are taken for validation of the wall element model (see section 5.2). Reference structures will be defined for modelling on the building level (see section 5.3). Connections are represented by discrete springs and CLT components are modelled with shell elements in both scales of numerical modelling. The set of springs which are incorporated in the analyses and the corresponding input parameters will be presented in section 5.1. The properties of the shell elements will be described in the context with numerical models of walls and structures (see section 5.2 and 5.3).

The following analysis procedures (AP) are distinguished within this study:

- AP1 pseudo-linear dynamic,
- AP2 non-linear dynamic,
- AP3 non-linear static and
- AP4 simplified non-linear static.

Pseudo-linear dynamic refers to the full modal analysis which is used to determine the eigenfrequency of the structure. However, several assumptions have to be met for full linear-elastic analyses. This issue was discussed, for example, by SUSTERSIC ET AL. [Sust11; Sust15]. Springs with asymmetric elasticity in tension and compression were also considered to avoid these assumptions in the development of the analysis model (see section 5.1.1). For that reason, the term *pseudo-linear* is used. The advantage of this type of modelling is that it is consistent with AP2 and AP3 with respect to the initial stiffness.

Non-linear dynamic stands for the non-linear time history analysis (see section 5.4).

Non-linear static analyses will be performed on the level of single wall elements as well as on the building level. For numerical simulations with wall elements cyclic loading is applied which is static. Non-linear static analyses on structural models will be discussed in section 6.3.

Simplified non-linear static refers to non-linear static analyses based on bilinear idealised load-displacement characteristics of connections (see section 6.3).

5.1 Elastic and non-linear springs

In this study, non-linearities which appear in a building during seismic action are represented by non-linear springs. In the numerical simulations discrete springs are represented by zero-length link elements which are implemented between two nodes – Ni and Nj – with the same coordinates. Different characteristics can be assigned to a zero-length link element. The different types of springs and their characteristics are subsumed in the next subsection. The input parameters which are required for the different springs with focus on the plenty of analyses will be derived in section 5.1.3.

5.1.1 Typology of spring elements

Multiple types of springs were considered to account for the characteristic behaviour of the connections which are used within the four analysis procedures. A total of eight types of springs were distinguished. The characteristics of these springs representing different features, respectively, behaviour of connections, are documented in Table 5.1. Springs with elastic behaviour have been considered for pseudo-linear analyses, and also, in a few cases for non-linear analyses (see Tab. 5.1). Inelastic behaviour is taken into account by elastic-plastic load-displacement relationships within simplified non-linear analysis and by the SAWS model (see Fig. 3.16a and [Folz01b]) within realistic non-linear analyses.

Table 5.1 presents the resultant load-displacement characteristics which are in some cases a combination of different spring elements (type d, f, h). This means that the load-displacement characteristics of these types d, f and h are implemented implicitly by defining multiple springs at the same place. The combination of springs elements is illustrated in Table 5.2.

The withdrawal behaviour of the screw connection (positive direction) is assumed to be linear.

Three load-displacement characteristics are distinguished for connections with hold-downs and angle brackets loaded in the positive direction. However, contact is always taken into account by spring type b.

It must be noted that the characteristic behaviour of hold-downs in the primary direction and angle brackets in the secondary direction for non-linear analyses cannot be reproduced sufficiently by combining the "SAWS" spring with the "contact" spring. Therefore an elastic-plastic spring (type e) was introduced which does not affect the backbone curve of the SAWS model. Only the unloading path and the reloading path of the "SAWS" spring are modified by this elastic-plastic spring. Using this modification, the unloading and the reloading path shift vertically into the IV. quadrant of the coordinate system (see Tab. 5.2, type h). A nearly elastic behaviour for negative relative displacement is obtained in combination with the contact element.
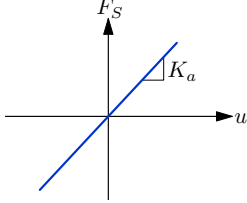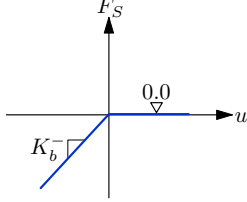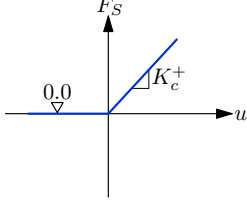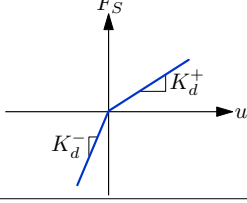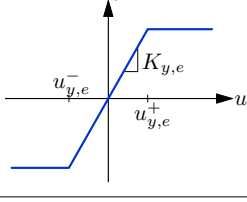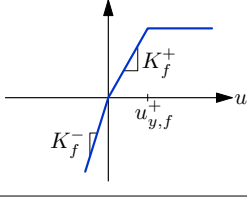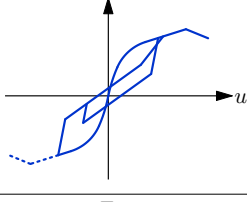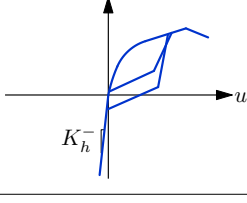
	type of springs		parameters	representing	analysis proc.
a		linear-elastic	K_a	AB primary direction, HD secondary direction, slip behaviour of screw connection	pseudo-linear dynamic
b		zero positive stiffness and linear negative stiffness	K_b^-	contact	pseudo-linear dynamic, non-linear static, non-linear dynamic, simplified non-linear static
c		linear positive stiffness and zero negative stiffness	K_c^+	withdrawal behaviour of screw connection	pseudo-linear dynamic, non-linear static, non-linear dynamic, simplified non-linear static
d*		elastic with different stiffness in positive and negative direction	K_d^+, K_d^-, $|K_d^-| > K_d^+$	HD primary direction, AB secondary direction	pseudo-linear dynamic
				withdrawal behaviour of screw connection in combination with contact	see spring type c
e		elastic-plastic	$K_{y,e}$, $u_{y,e}^+$, $u_{y,e}^-$	AB primary direction, HD secondary direction, slip behaviour of screw connection	simplified non-linear static
f*		elastic-plastic in positive direction and linear in negative direction	K_f^+, $u_{y,f}^+$, K_f^-	HD primary direction, AB secondary direction	simplified non-linear static
g		SAWS model according to FOLZ ET AL. [Folz01a; Folz01b; Uriz10] (10 parameter model)	$F_{0,g}$, $F_{1,g}$, $\delta_{u,g}$, $K_{0,g}$, $r_{1,g}$, $r_{2,g}$, $r_{3,g}$, $r_{4,g}$, α_g, β_g	AB primary direction, HD secondary direction, slip behaviour of screw connection	non-linear static, non-linear dynamic
h*		combined spring, SAWS model in positive direction and linear in negative direction	$F_{0,h}$, $F_{1,h}$, $\delta_{u,h}$, $K_{0,h}$, $r_{1,h}$, $r_{2,h}$, $r_{3,h}$, $r_{4,h}$, α_h, β_h, $K_{y,h}$, $u_{y,h}^+$, $u_{y,h}^-$, $K_{n,h}$	HD primary direction, AB secondary direction	non-linear static, non-linear dynamic
*see Table 5.2				AB – angle bracket, HD – hold-down	

Table 5.1: Types of springs for connections of CLT elements

combination	characteristics of spring ①	characteristics of spring ②	characteristics of spring ③	final characteristics
d by c⊕b	F_S graph, 0.0, slope K_c		F_S graph, 0.0, K_b	$K_d^+ = K_c$ $K_d^- = K_b$
d by a⊕b	F_S graph, slope K_a		F_S graph, 0.0, K_b	$K_d^+ = K_a$ $K_d^- = K_a + K_b$
f by e⊕b	F_S graph, slope K_e, $u_{y,e}^-$, $u_{y,e}^+$, $u_{y,e}^- = u_{y,e}^+$		F_S graph, 0.0, K_b	$K_f^+ = K_e$ $u_{y,f}^+ = u_{y,e}^+$ for $u < 0$ and $u > u_{y,e}^-$: $K_f^- = K_e + K_b$
h by g⊕e⊕b	SAWS model, $\bullet_g = \bullet_h$	$u_{y,h}^+ = 0$, $u_{y,h}^-$, $K_{y,h}$	F_S graph, 0.0, $K_b = K_{n,h}$	for $u < 0$: $F_S(u) = F_1(u) + F_2(u) + F_3(u)$ $K_h^- = \dfrac{F_1 + F_2}{u} + K_{n,h}$ $K_{n,h} \gg \dfrac{F_1 + F_2}{u}$ reload, unload

Table 5.2: Spring types with asymmetric load-displacement characteristics by combining multiple springs

The approach to subdivide the final spring characteristics into prototypes of springs was chosen for reasons of transparency. The main advantages of this approach are that contact conditions only have to be defined once for all types of analyses and that the properties of the several springs can be determined separately. The contact element plays an important role because it

- considers varying contact stiffness due to different support conditions (rigid, non-rigid),
- accounts for asymmetric load-displacement characteristics and
- can capture friction in the contact area.

The relevance of the first point has already been discussed in the previous chapters. The second item is significant for connections with asymmetric hysteretic behaviour regarding energy dissipation. The third issue is indispensable in order to determine the load-bearing capacity and the potential of energy dissipation of structural elements and the whole structure realistically.

5.1.2 Friction element

If friction has not been considered in the analyses the contact element will have been implemented by a zero-length link with the characteristics of spring type b (as mentioned above). The so-called *singleFPBearing element* has been used in addition to the "contact" spring (see Fig. 5.1) to consider friction in the contact area. The singleFPBearing element incorporates a friction model defined previously to determine the friction force F_μ.

$$F_\mu = F_x \cdot \mu' \tag{5.1}$$

A constant friction coefficient μ has been applied. The singleFPBearing element requires the specification of an initial stiffness k_{Init}, which means that the full friction force is achieved after a certain relative displacement d_y, d_z (sliding). The parameter R_{eff} considers the curvature of the sliding surface. The friction force acts in both local directions (y and z). The contact force F_b presents the axial force F_x. However, this element incorporates further features which were not required in this study. These features have been switched off by applying zero stiffness in case of moments action and by using default values (see [Sche14]).
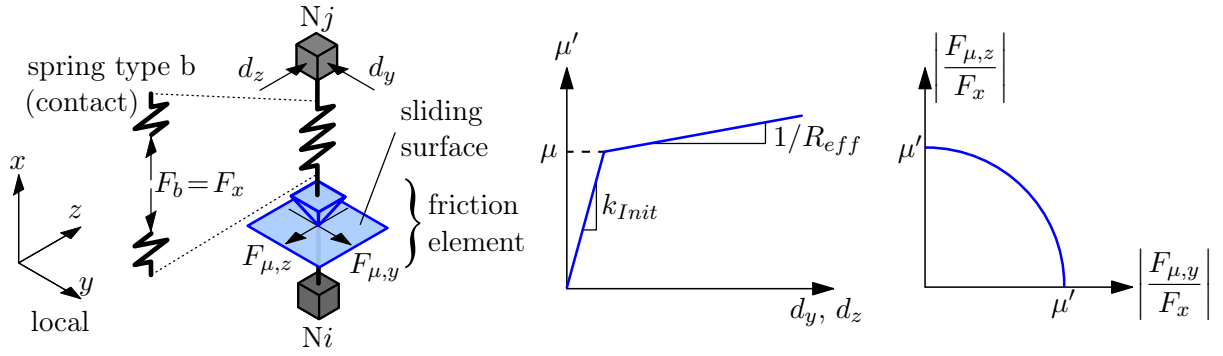
Figure 5.1: Definitions for singleFPBearing element [Sche14]

5.1.3 Derivation of input parameters

Values for the parameters required for numerical modelling will be derived based on the test results of connections (see section 4.2). In addition to that, data which were obtained by the experimental investigations of FLATSCHER [Flat11] and GAVRIC [Gavr13] (see section 3.1) will be included.

Labeling of the configurations of connections refer to sections 3.1.2, 3.1.4 and 4.2. In addition to the different configurations with angle brackets and hold-downs, connections with self-tapping screws are considered. Table 5.3 subsumes the configurations of screw connections which have been distinguished in this study.

config.	connection type	connection between	loading	test results from
SC-WC-0	single screw, not inclined	perpendicular walls	shear along the joint	GAVRIC [Gavr13]
SC-WC-90	single screw, not inclined	perpendicular walls	shear perpendicular to the joint	GAVRIC [Gavr13]
SC-WS-0	single screw, not inclined	slab and wall (top)	shear along the joint	GAVRIC [Gavr13]
SC-WS-90	single screw, not inclined	slab and wall (top)	shear perpendicular to the joint	GAVRIC [Gavr13]
SC-X-0	screw pair, inclined	perpendicular walls, slab and wall (top)	shear along the joint	FLATSCHER [Flat11]

Table 5.3: Configurations of connections with self-tapping screws

The determination of spring properties for the different configurations of hold-downs, angle brackets and self-tapping screws is discussed in the following subsections, based on the definitions in Table 5.1. Firstly, the properties of spring types g and h will be derived, since some of these properties can be used directly for the other types of springs.

Properties of spring types g and h

The backbone curves of the connections tested (see Fig. 4.6) were chosen to calibrate the spring parameters of the SAWS model. The parameters K_0, F_0, δ_u, r_1 and r_2 were modified as long as the error between the "test curve" and the "analytical curve" was a minimum. The error ϵ was defined according to Eq. (5.2).

$$\epsilon = \sum_{i=1}^{n} \left(F_{exp,i} - F_{num,i} \right)^2 \tag{5.2}$$

$F_{exp,i}$ and $F_{num,i}$ stand for the forces obtained experimentally and analytically, respectively, at the same displacement level i. The parameters $r_{3,g}$, $r_{4,g}$, α_g, β_g and $r_{3,h}$, $r_{4,h}$, α_h, β_h, $K_{y,h}$, $u_{y,h}^+$, $u_{y,h}^-$ which account for the hysteretic behaviour were calibrated, so that
  - the spring behaviour reproduce the hysteretic characteristics of the connection as well as possible and
  - the cumulated energy E_{cum} for the spring matches the one for the connection.

The cumulated energy is the summation of the dissipated energy for each displacement amplitude of the hysteresis and is plotted against the corresponding cumulated displacement u_{cum} (see Fig. 5.2). The cumulated displacement is the sum over the displacements u_i.
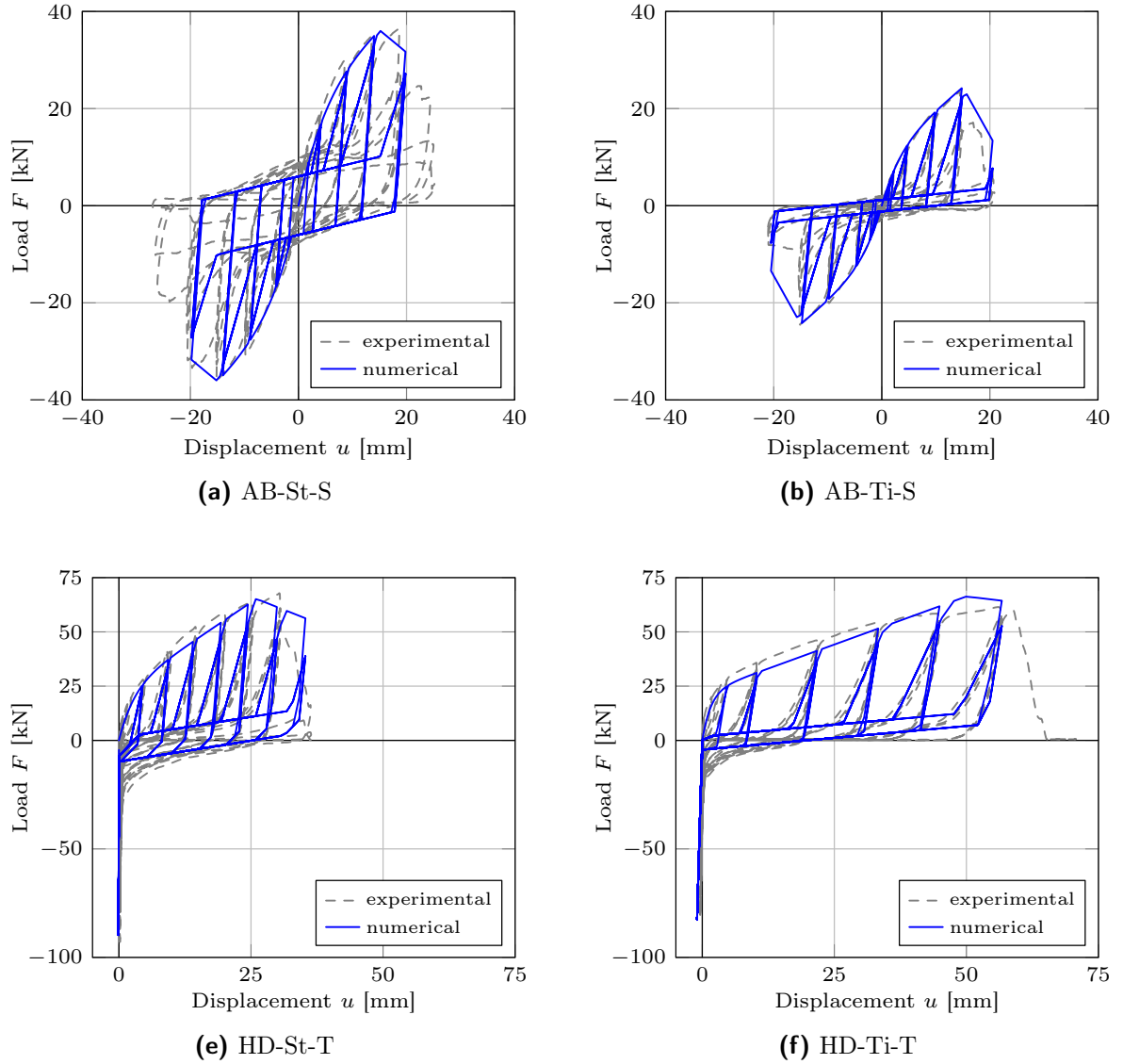
(a) AB-St-S

(b) AB-Ti-S

(e) HD-St-T

(f) HD-Ti-T

Figure 5.2: Hysteretic behaviour of configurations AB-St-S, AB-Ti-S, HD-St-S and HD-St-T, HD-Ti-T, AB-St-T; load-displacement curves and cumulated energy of experimental investigations and numerical model (part 1)

Subsequently, non-linear spring properties for hold-downs, angle brackets and screw connections were determined for different loading directions. The properties, which were found for non-linear springs, are summarised in Tables 5.4 and 5.5. Only the parameters of the SAWS model apply for spring type g, the symmetric non-linear spring. Additional properties are required for spring type h. A bilinear spring was added in order to get a better agreement in the unloading path and in the energy content of the load-displacement curve from testing. The yield displacement of the bilinear spring in the positive direction u_y^+ is always set to zero. The contact stiffness $K_{n,h}$ was adopted based on the stiffness in the negative direction from testing.

The same properties were chosen for the configuration HD-St-S and HD-Ti-S, since anchoring to a different base does not influence the load-displacement characteristics of connections with hold-down for shear loading significantly.
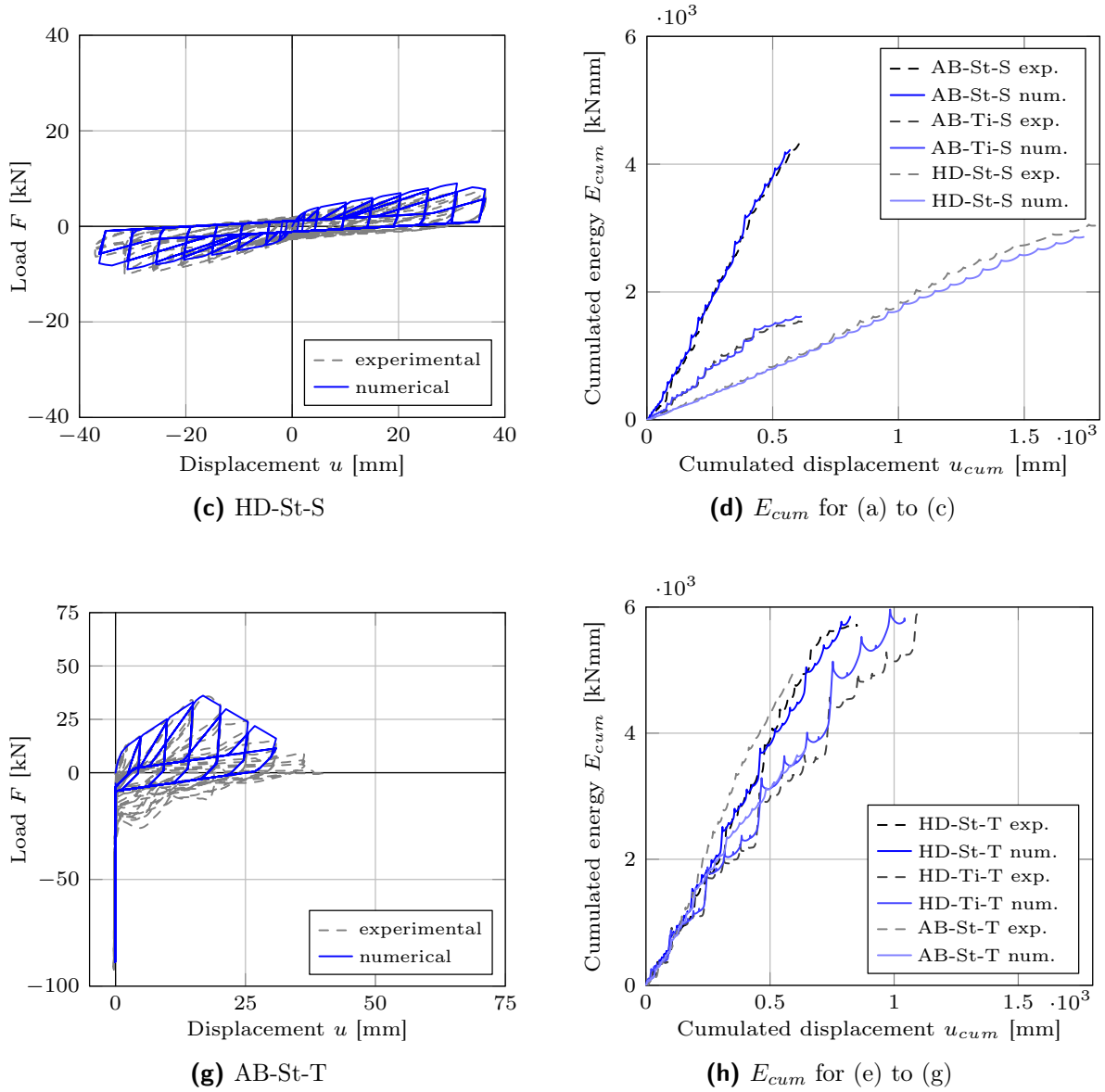
(c) HD-St-S

(d) E_{cum} for (a) to (c)

(g) AB-St-T

(h) E_{cum} for (e) to (g)

Figure 5.2: Hysteretic behaviour of configurations AB-St-S, AB-Ti-S, HD-St-S and HD-St-T, HD-Ti-T, AB-St-T; load-displacement curves and cumulated energy of experimental investigations and numerical model (part 2)

The hysteretic behaviour and the progression of cumulated energy for hold-downs and angle brackets are compared in Figure 5.2. It shows that the fundamental characteristics can be reproduced very well by the SAWS model in combination with the properties derived. The cumulated energy especially, is matched by the analytical model in almost every case. However, the analytical model overpredicts and underpredicts the energy slightly for the configurations HD-Ti-T and AB-St-T, respectively (see Fig. 5.2h).

config.	$K_{0,g}$ [kN/mm]	$F_{0,g}$ [kN]	$F_{1,g}$ [kN]	$\delta_{u,g}$ [mm]	$r_{1,g}$ [–]	$r_{2,g}$ [–]	$r_{3,g}$ [–]	$r_{4,g}$ [–]	α_g [–]	β_g [–]
AB-St-S	5.36	23.2	6.9	15.0	0.170	-0.170	3.00	0.040	0.25	1.05
HD-St-S/HD-Ti-S	2.38	3.1	1.0	31.0	0.080	-0.170	3.00	0.020	0.60	1.10
AB-Ti-S	3.99	10.7	1.2	15.0	0.230	-0.500	3.00	0.030	0.05	1.05
SC-WC-0[1]	2.27	7.9	0.8	23.3	0.010	-0.100	2.50	0.020	0.90	1.15
SC-WC-90[1]	1.29	5.6	0.5	32.0	0.015	-0.100	1.50	0.030	0.80	1.20
SC-WS-0[1]	1.83	7.6	1.1	23.3	0.024	-0.075	2.50	0.020	0.80	1.15
SC-WS-90[1]	1.52	5.6	1.2	31.2	0.076	-0.070	2.00	0.035	0.55	1.14
SC-X-0[2]	31.00	24.5	3.0	2.0	0.180	-0.120	1.00	0.020	0.80	1.10

[1] based on the test results of GAVRIC [Gavr13]
[2] based on the test results of FLATSCHER [Flat11]

Table 5.4: Parameters for spring type g

config.	$K_{0,h}$ $[\frac{kN}{mm}]$	$F_{0,h}$ [kN]	$F_{1,h}$ [kN]	$\delta_{u,h}$ [mm]	$r_{1,h}$ [–]	$r_{2,h}$ [–]	$r_{3,h}$ [–]	$r_{4,h}$ [–]	α_h [–]	β_h [–]	$K_{y,h}$ $[\frac{kN}{mm}]$	$u_{y,h}^-$ [2] [mm]	$K_{n,h}$ $[\frac{kN}{mm}]$
AB-St-T	14.29	9.3	0.8	16.8	0.112	-0.100	3.00	0.025	0.45	1.05	2.50	-3.7	10^3
HD-St-T	9.64	21.4	1.2	26.0	0.180	-0.200	3.00	0.040	0.03	1.05	2.14	-4.0	10^3
AB-Ti-T[1]	11.79	6.9	0.5	3.0	0.130	-0.020	1.00	0.015	0.40	1.03	0.95	-2.5	70
HD-Ti-T	14.52	22.0	1.8	50.0	0.060	-0.071	1.00	0.015	0.40	1.04	0.83	-6.0	70

[1] based on the test results of FLATSCHER [Flat11]
[2] yield displacement in the positive direction $u_y^+ = 0$ (see Tab. 5.2)

Table 5.5: Parameters for spring type h

The non-linear hysteretic behaviour of an angle bracket which is anchored on CLT must also be considered in the secondary loading direction (tension). The test data of FLATSCHER [Flat11] were used to find spring properties for configuration AB-Ti-T. The test configuration is comparable with the one of the connectors presented in section 4.2. The behaviour obtained is illustrated in Figure 5.4a.

The test results of GAVRIC [Gavr13] were taken for the calibration of connections with not inclined self-tapping screws. The comparison of experimental and numerical results is depicted in Figure 5.3. Furthermore, the test results from FLATSCHER [Flat11] were taken to calibrate the spring behaviour for connections with inclined self-tapping screws. Figures 5.4c and 5.4d illustrate that the spring behaviour is almost equivalent to the real behaviour. Details concerning these tests are given in sections 3.1.2 and 3.1.4. The hysteretic behaviour can be reproduced excellently, even for the connections with self-tapping screws, by the SAWS model in combination with the properties derived.
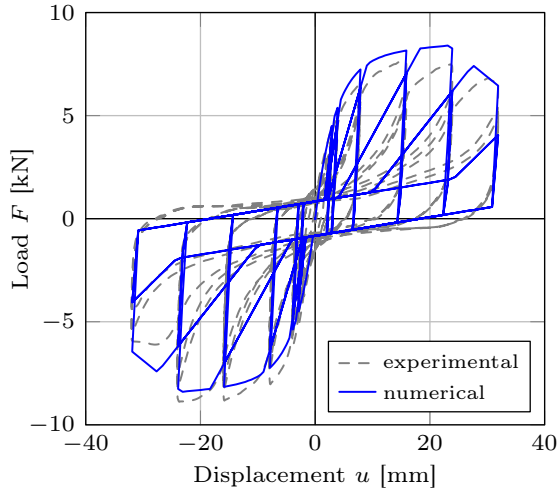
(a) SC-WC-0
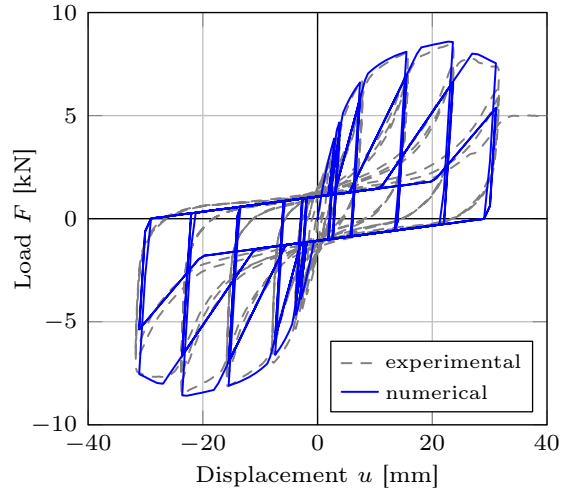
(d) SC-WS-0
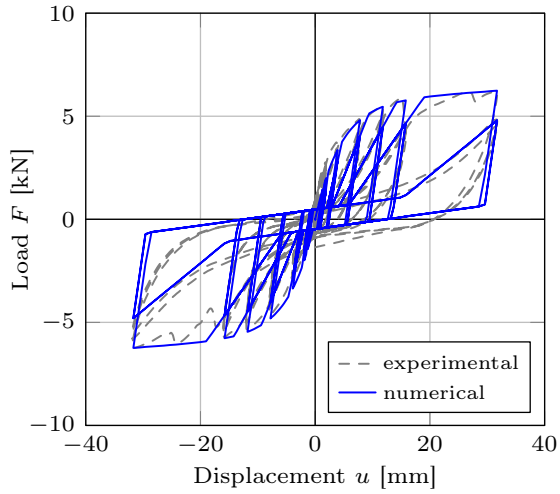
(b) SC-WC-90
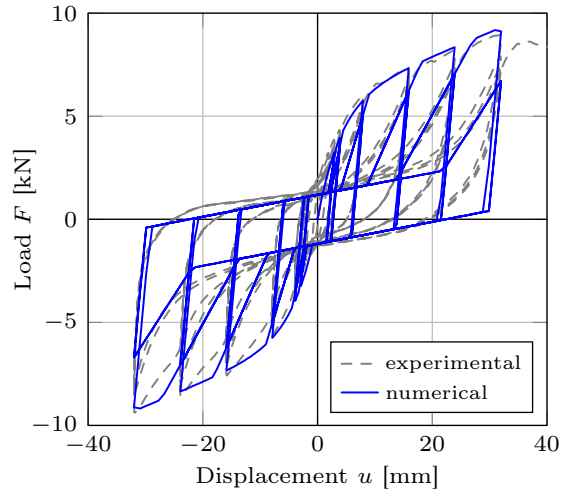
(e) SC-WS-90
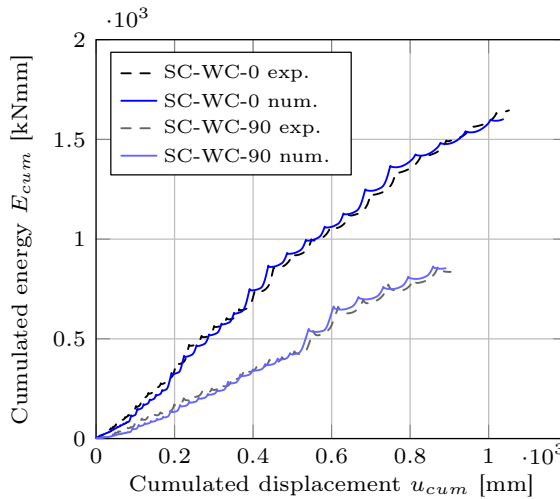
(c) E_{cum} for (a) and (b)
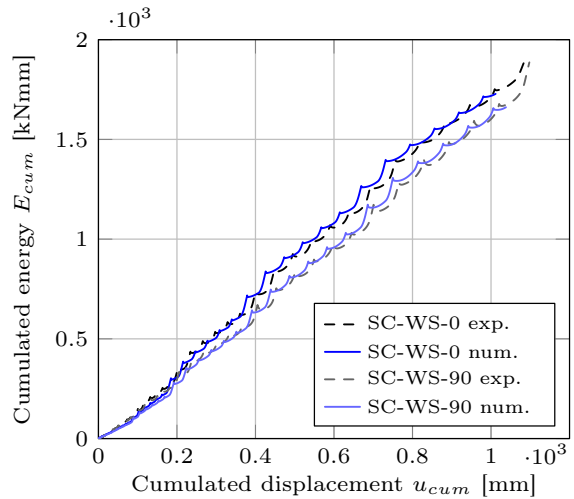
(f) E_{cum} for (d) and (e)

Figure 5.3: Hysteretic behaviour of configurations SC-WC-0, SC-WC-90 and SC-WS-0, SC-WS-90; load-displacement curves and cumulated energy of experimental investigations and analytical numerical model; test results from [Gavr13]

(a) AB-Ti-T

(b) E_{cum} for (a)

(c) SC-X-0

(d) E_{cum} for (c)
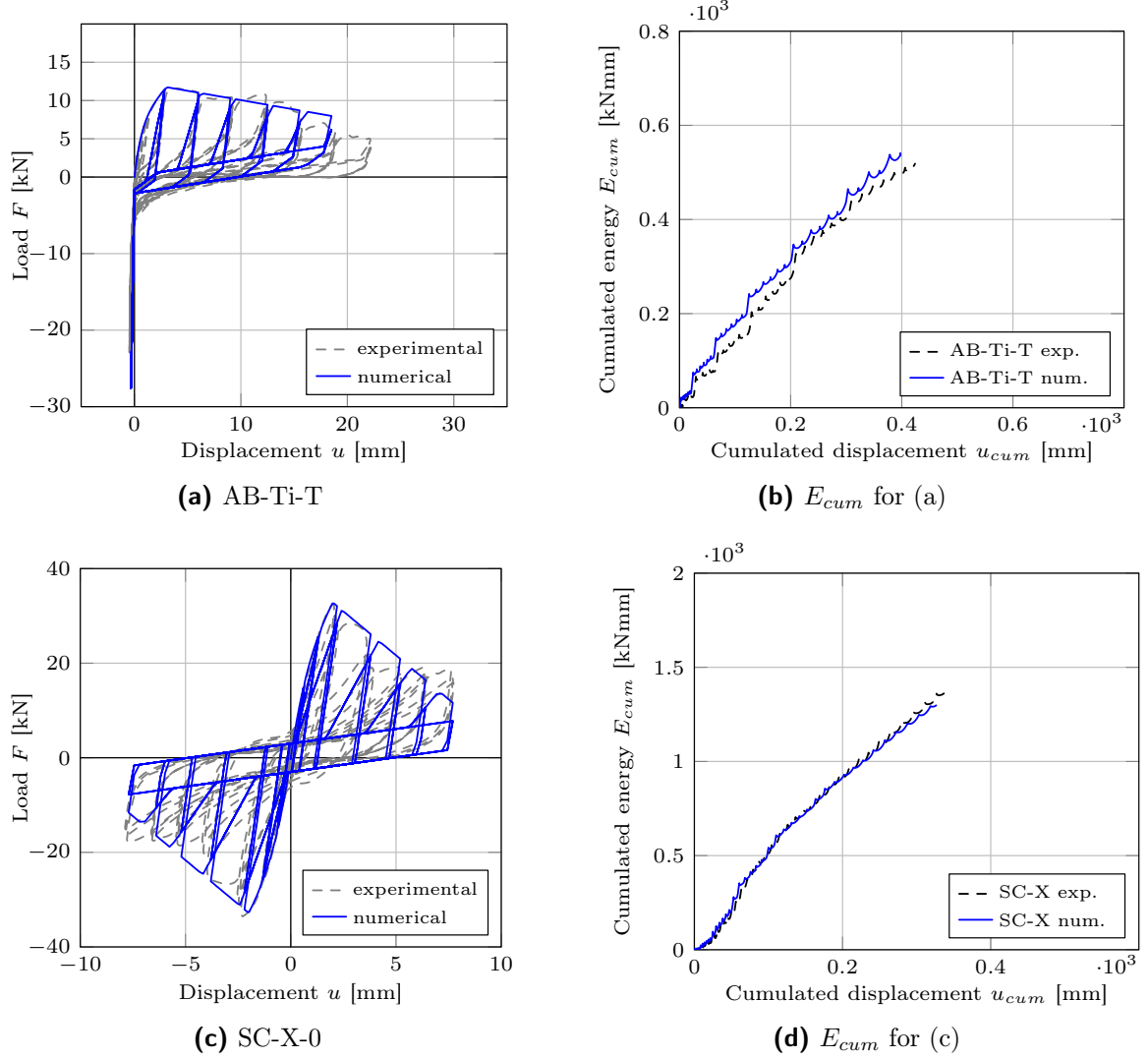
Figure 5.4: Hysteretic behaviour of configurations AB-Ti-T and SC-X-0; load-displacement curves and cumulated energy of experimental investigations and numerical model; test results from [Flat11]

Properties of spring types e and f

Parameters of springs with elastic-plastic behaviour were found by consistent bilinearisation as described in section 4.1. Again, the K & Y and EEEP approaches were used to obtain the initial stiffness k_{ini}, the yield displacement u_y and the ultimate displacement u_u. The parameters are already given in Table 4.1 for the connections which were presented in section 4.2.

The properties which were found for AB-Ti-T – the angle bracket in the secondary loading direction with elastic support conditions – and connections with self-tapping screws are summarised in Table 5.6. Spring type e is described by the parameters $K_{y,e}$, $u_{y,e}^+$ and $u_{y,e}^-$ (see Tab. 5.1) where a symmetric behaviour is assumed ($u_{y,e}^+ = |u_{y,e}^-|$). Therefore, the mean value of the positive and negative backbone of k_{ini} and u_y were taken to specify $K_{y,e}$, and $u_{y,e}^+$, respectively. However, the ultimate displacement u_u is not used for the elastic-plastic spring, but is required to denote failure. The properties derived serve as input data for DBD (see section 6).

config.		u_u [mm]	K & Y		EEEP	
			u_y [mm]	k_{ini} [kN/mm]	u_y [mm]	k_{ini} [kN/mm]
AB-Ti-T[1]	pos	14.5	1.5	7.1	1.3	8.0
SC-X-0[1]	pos	3.7	1.5	20.2	1.3	23.5
	neg	3.5	1.4	21.4	1.2	24.1
SC-WC-0[2]	pos	31.8	4.9	1.5	4.0	1.8
	neg	25.8	4.9	1.7	4.3	1.9
SC-WC-90[2]	pos	32.0	4.7	1.2	3.2	1.7
	neg	32.0	9.0	0.7	7.3	0.8
SC-WS-0[2]	pos	32.0	8.1	1.0	6.3	1.2
	neg	31.9	5.8	1.3	4.4	1.7
SC-WS-90[2]	pos	45.4	8.3	1.0	5.1	1.5
	neg	32.0	11.1	0.7	9.3	0.9

[1] based on the test results of FLATSCHER [Flat11]
[2] based on the test results of GAVRIC [Gavr13]

Table 5.6: Parameters for spring type e – stiffness and deformation characteristics

In addition to the properties of spring type e the contact stiffness K_b (spring type b) is required to define spring type f (see Tab. 5.2). The contact stiffness is the same as for spring type h (see Tab. 5.5).

$$K_b = K_{n,h} \tag{5.3}$$

Spring type f is applied for the configurations HD-St-T, HD-Ti-T, AB-St-T and AB-Ti-T (see Tables 5.6 and 4.1) which exhibit an asymmetric behaviour in tension and compression.

Properties of spring types a to d

The stiffness $K_{g,0}$ of spring type g (see Tab. 5.4) is applied for the definition of spring type a. Again, the contact stiffness K_b is defined by Eq. (5.3) for spring type b.

An elastomeric interlayer (Sylodyn, see section 4.3.1) was considered for one wall element test. For this configuration, the contact stiffness was determined with Eq. (5.4).

$$K_b = \frac{E_{il} \cdot b_{il}}{t_{il}} \cdot l_{cont,test} = \frac{6.55 \cdot 100}{12.5} \cdot 300 = 15720 \, [\text{N/mm}] \tag{5.4}$$

with E_{il} Young's modulus of the interlayer [N/mm²]
      b_{il} width of the interlayer [mm]
      t_{il} thickness of the interlayer [mm]
      $l_{cont,test}$ contact length used for connection tests, $l_{cont,test} = 300$ mm

The data for the interlayer are given in section 4.3.1. The same contact length as that used in the test configurations HD-St-T, HD-Ti-T and AB-St-T (see Fig. 4.5) was taken into account.

Spring type c accounts for the withdrawal behaviour of self-tapping screws. Since, self-tapping screws exhibit almost no energy dissipation capacity for recurrent loading in

the axial direction (see [Gavr13]), the withdrawal behaviour of the screw connection was considered by an elastic spring. The withdrawal stiffness K_{ax} was determined according to BLASS ET AL. [Blaß06] with Eq. (5.5).

$$K_c^+ = K_{ax} = 234 \cdot (\rho \cdot d)^{0.2} \cdot l_{ef}^{0.4} \tag{5.5}$$

with ρ density of the timber section (CLT) [kg/m^3]
           d diameter of the screw [mm]
           l_{ef} embedment length [mm]

Both connections with inclined self-tapping screws and those not inclined were considered within numerical investigations (see Tab. 5.3). The dimensions which are given in Table 5.7 correspond to the test configurations used by FLATSCHER [Flat11] and GAVRIC [Gavr13]. Only the length of the inclined screws was adapted to obtain a sufficient embedment length. The original length is 200 mm. The wood density was taken into account at 420 kg/m^3.

config.	angle [°]	d [mm]	l_{SC} [mm]	l_{ef} [mm] [2]	K_{ax} [N/mm]
SC-WS-ax	90	10	260	122	8480
SC-X-ax	45	8	320[1]	125	2×8189

[1] screw length modified
[2] determined with a slab thickness of 138 mm

Table 5.7: Withdrawal stiffness of self-tapping screws

not inclined screws   inclined screws (screw pair)
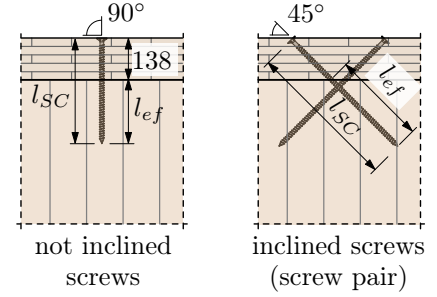
Figure 5.5: Connections with self-tapping screws

Properties for spring type d do not have to be defined. The behaviour of spring type d results from the combination of

- spring types a and b for hold-downs and angle brackets loaded in tension and compression, and
- spring types b and c for connections with self-tapping screws loaded in tension and compression,

as illustrated in Table 5.2.

The properties of spring types g and h for hold-downs and angle brackets are used to predict the hysteretic behaviour of CLT wall elements in the following section. Subsequently, the further properties are incorporated additionally for simulations on the building level (see sections 5.4 and 6.3).

5.1.4 Definition of friction properties

It was mentioned in section 4.3.3 that friction contributes to the load-displacement characteristics of CLT wall elements. The singleFPBearing element (see section 5.1.2) was used for this purpose.

The singleFPBearing element requires the definition of the parameters k_{Init}, R_{eff} and μ. However, it is difficult to find the first two parameters by means of experimental investigations. The parameter k_{Init} only defines at which point of sliding the predefined

friction coefficient is reached but should be carefully selected for numerical reasons. If k_{Init} is chosen too high, convergence problems may occur during analysis due to a rapid change of stiffness. The parameter R_{eff} account for the curvature of the sliding surface. However, the surface in the contact area can be considered as plane for experimental and analytical investigations in this thesis. For that reason, the parameter R_{eff} was set at 10^8.

Values which are proposed by PETERSEN [Pete96] were adopted to specify the friction coefficient μ. Kinematic friction is presumed as the behaviour of CLT wall elements is characterised by a considerable amount of sliding. PETERSEN [Pete96] proposes ranges of kinematic friction coefficient μ_k for different contact conditions (see Tab. 5.8). The contact conditions: steel-to-timber, timber-to-timber and concrete-to-timber are distinguished with reference to numerical simulations on the level of CLT wall elements and CLT buildings. *Timber* is representative of CLT. The proposed range of the friction coefficient for steel-to-timber contact relates to raw steel. However, the bearing beam in the test set-up of CLT wall elements was a coated steel girder (see section 4.3.2). It becomes clear from Table 5.8 that the friction coefficient μ_k is significantly higher for raw steel than for smooth steel. For that reason a reduced friction coefficient of 0.1 is assumed for the contact between coated steel and CLT. The friction coefficients which were proposed by PETERSEN [Pete96] are taken into account for timber-to-timber and concrete-to-timber connections.

The preselected properties for steel-to-timber and timber-to-timber contact conditions (see Tab. 5.8) will be validated in section 5.2. The friction coefficient for concrete-to-timber contact is required for numerical simulations on the building level. Here, the lower bound of the range of friction coefficient, $\mu_k = 0.3$, is chosen as an approximation.

ref. name	contact conditions	k_{Init} [N/mm]	R_{eff} [mm/N]	μ_k [−]
	steel-to-steel, raw			0.4[1]
	steel-to-steel, smooth			0.1[1]
	steel-to-timber, raw steel			0.3 to 0.5[1]
FM-1	steel-to-timber, coated steel	10^3	10^8	0.1[2]
FM-2	timber-to-timber	10^3	10^8	0.2 to 0.4[1]
FM-3	concrete-to-timber	10^3	10^8	**0.3** to 0.4[1]

[1] according to PETERSEN [Pete96]
[2] assumed friction coefficient for coated steel

Table 5.8: Specification of the parameters k_{Init}, R_{eff} and μ_k

5.2 Prediction of the Hysteretic Behaviour of CLT Wall Elements

The hysteretic behaviour of the eight configurations of CLT wall elements for the validation of the spring properties, as presented in section 4.3 are predicted by means of a non-linear static analysis in this section. Therefore, a plain model of the CLT wall was developed by means of the analysis software OPENSEES. Non-linear static analyses are performed for multiple displacement steps. The same loading protocol as that used in the different tests is applied in each configuration. A NEWTON-RAPHSON iteration was chosen to solve the non-linear static problem.

5.2.1 Analysis model and configurations

The CLT element is considered as fully elastic. The layered cross section of the CLT element is taken into account by means of effective material properties. An isotropic material is assigned to the shell elements. The material properties for isotropic shell elements are given in Table 5.9. The Young's modulus E was determined for in-plane loading. The board layers have a Young's modulus of $11000\,\mathrm{N/mm^2}$ parallel to the grain (C 24, see section 4.1). The effective Young's modulus E_{ef} was determined with Eq. (5.6).

$$E_{ef} = E_{0,mean,CLT} \cdot \frac{d_{ef}}{d} = 11000 \cdot \frac{3 \cdot 21}{105} = 6600\,[\mathrm{N/mm^2}] \tag{5.6}$$

The three vertical layers of the CLT element were considered for the effective thickness d_{ef}. The horizontal layers can be neglected (see e.g. [Wall13]). A reasonable value of the Poisson's ratio for timber was chosen of 0.3.

material	Young's modulus $E_{ef}\,[\mathrm{N/mm^2}]$	Poisson's ratio $\nu\,[-]$
isotropic	6600	0.3

Table 5.9: Properties of the isotropic material for shell elements representing the CLT wall
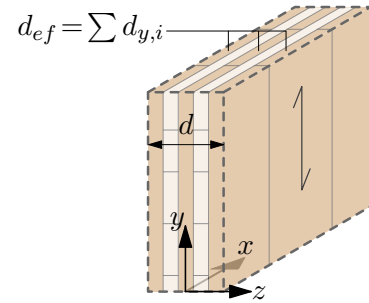
Figure 5.6: Nominal and effective thickness of the CLT

In this context it must be noted that the hysteretic behaviour of single CLT wall elements is dominated by the load-displacement characteristics of the connections. Bending and shear deformations of the CLT elements do not contribute significantly to the overall deflection (see section 4.3.2). Thus, the global behaviour – which is important in this study – do not really change whether an isotropic or an orthotropic material is used to represent the stiffness characteristics of the CLT wall section. The isotropic material was chosen to make the model as simple as possible with respect to the numerical effort for three-dimensional analyses on the building level (see section 5.3). The same applies to the mesh size. It was set to 250 by 250 mm (see Fig. 5.7). Shell elements from type MITC4 (Mixed Interpolation of Tensorial Components) were used to model the CLT section. The number 4 refers to the number of nodes by which the shell element is defined. The MITC4 element was developed by DVORKIN AND BATHE [Dvor84]. It incorporates linear isoparametric interpolation functions for the mathematical formulation of membrane and plate quantities. Only the behaviour in-plane (membrane direction) is considered for the simulation on the wall level.

The analysis model is illustrated in Figure 5.7. Support and load conditions of the different configurations were considered as documented in section 4.3.1. A rigid beam with a height h^* was implemented for application of a eccentric vertical load on the top of the wall. For configurations with a uniform vertical load, h^* is set to zero. If a eccentric vertical load is applied, the rigid beam has a height of 3.0 m.
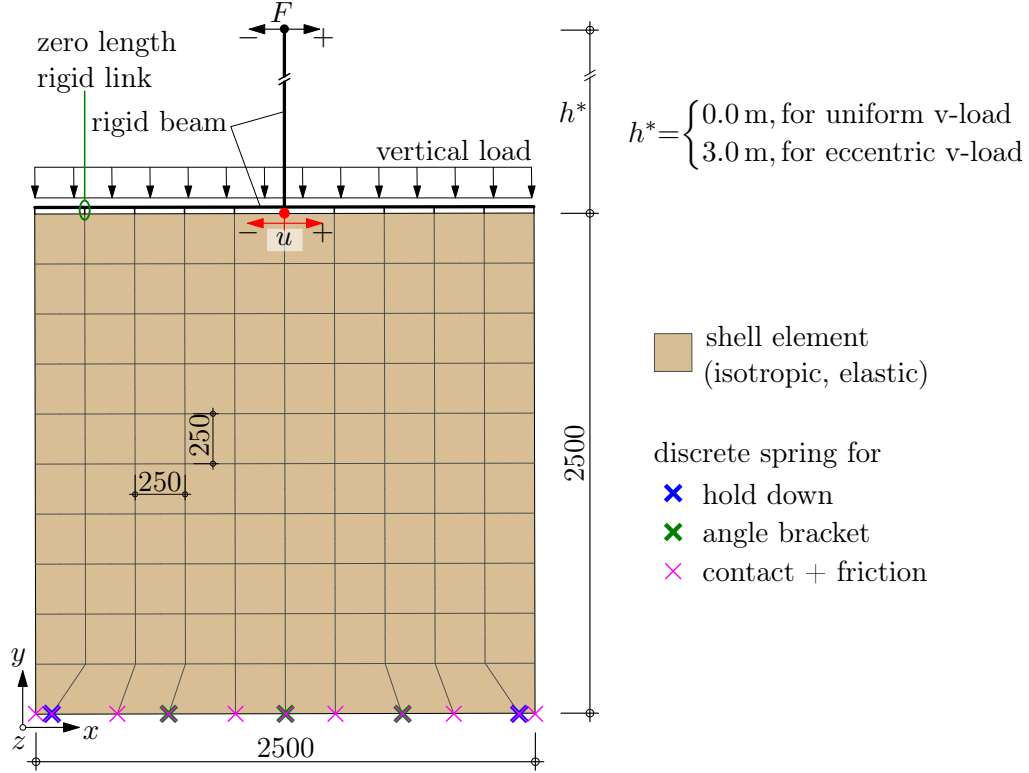
Figure 5.7: Analysis model for CLT wall elements

The non-linear load-displacement characteristics are attributed to discrete springs including friction, as illustrated in Figure 5.7. Spring types, spring properties and the properties for friction which were applied for numerical simulations on the wall level for different configurations are specified in Table 5.10. The spring properties were derived based on test results which were found for loading in one direction. However, hold-downs and angle brackets used for the anchoring of CLT wall elements exhibit a different load-bearing capacity for loading in multiple direction. That is well-known from wall element tests and was stated by other researchers, for example, GAVRIC [Gavr15]. RINALDIN AND FRAGIACOMO [Rina16] showed that a quadratic interaction

$$\left(\frac{V}{F_{R,1}}\right)^2 + \left(\frac{N}{F_{R,2}}\right)^2 \leq 1 \tag{5.7}$$

matches the experimental results for biaxial loaded connections sufficiently.
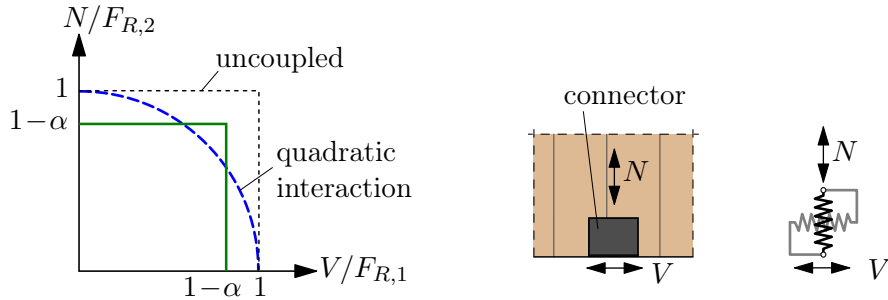
Figure 5.8: Force interaction for bidirectional loading

Some additional considerations are necessary because the programme OpenSees does not provide an inelastic spring with different strength interaction for multiple loading directions. The discretisation of springs by zero-length link elements includes an uncoupled behaviour. A comparatively simple approach was taken to consider strength degradation due to force interaction by reducing the strength in both direction ($F_{R,1}$ and $F_{R,2}$, see Fig. 4.4) by means of a constant factor α. The factor α was iteratively determined by calibrating calculations on the wall level and was found to be 15 % ($\alpha = 0.15$).

The spring properties derived (see Tabs. 5.4 to 5.5) were modified by the "force interaction factor" α according to Eq. (5.8).

$$Q_{mod} = (1 - \alpha) \cdot Q \qquad\qquad\qquad \text{with } \alpha = 0.15 \qquad\qquad (5.8)$$

The following quantities (Q) were modified: K_0, F_0, F_1 and K_y. The modified quantities Q_{mod} (spring properties) were applied to predict the hysteretic behaviour of the different configurations of CLT wall elements.

The location of the springs for hold-downs and angle brackets is equivalent to the test configurations. A continuous contact is created by distributing the "contact" springs along the wall length (see Fig. 5.7). The different support conditions (rigid, elastic) are considered by means of the contact springs. The contact force which is required to determine the friction force is also provided by the contact spring. It must be noted that contact stiffness was determined based on the test results for the configurations HD-St-T, HD-Ti-T and AB-St-T (see Fig. 4.5) where the contact area had a length of 300 mm. However, a different contact length accounts for each contact spring in the wall model (see Fig. 5.9). Therefore, the stiffness K_b was adapted for each contact spring in proportion to the corresponding contact length $l_{cont,i}$ with Eq. (5.9).

$$K_b^* = K_b \cdot \frac{l_{cont,i}}{l_{cont,exp}} \qquad\qquad\qquad\qquad\qquad\qquad (5.9)$$

with K_b contact stiffness [kN/mm]
 $l_{cont,i}$ contact length for spring i [mm]
 $l_{cont,exp}$ contact length as used for tests on connections, $l_{cont,exp} = 300$ mm
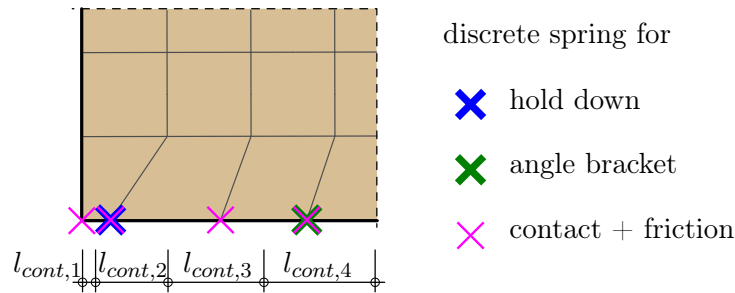
Figure 5.9: Contact length for contact springs

The specifications for friction which are given in Table 5.10 for the different configurations refer to the definitions as made in section 5.1.4. It is assumed that the same friction properties apply for the configuration with elastomeric interlayer (Sylodyn) as for the configuration with timber-to-timber contact which means the elastic support conditions. The friction coefficient μ_k was given in the range of 0.2 to 0.4 for the timber-to-timber connection (FM-2). As a first attempt, the friction coefficient was set to 0.4 for the configurations with an elastic support. However, it was found by the validation with test results (see section 5.2.2) that the friction coefficient should be slightly reduced to 0.38. The friction coefficient for the steel-to-timber connection (rigid support) was considered at 0.1, as has already been defined in section 5.1.4.

spring symbol	connector/ behaviour	support conditions	spring type x	spring type y	spring properties x	spring properties y	friction	for wall configurations
✖	hold-down	rigid	g	h	HD-St-S[1]	HD-St-T[2]	singleFP Bearing, FM-1	W-CLT-St-10, W-CLT -St-50, W-CLT-St-100, W-CLT-St-100M
✖	angle bracket	rigid	g	h	AB-St-S[1]	AB-St-T[2]		
✕	contact			b		$K_b = K_{n,h}$		
✖	hold-down	elastic, CLT	g	h	HD-Ti-S[1]	HD-Ti-T[2]	singleFP Bearing, FM-2	W-CLT-Ti-10, W-CLT-Ti-50, W-CLT-Ti-50M
✖	angle bracket		g	h	AB-Ti-S[1]	AB-Ti-T[1]		
✕	contact			b		$K_b = K_{n,h}$		
✖	hold-down	elastic, CLT+ Sylodyn	g	h	HD-Ti-S[1]	HD-Ti-T[2],[3]	singleFP Bearing, FM-2	W-CLT-Sy-50
✖	angle bracket		g	h	AB-Ti-S[1]	AB-Ti-T[2],[3]		
✕	contact			b		$K_b = K_{n,h}$[3]		

[1] $K_{0,g}$, $F_{0,g}$, $F_{1,g}$ modified by Eq. (5.8)

[2] $K_{0,h}$, $F_{0,h}$, $F_{1,h}$, $K_{y,h}$ modified by Eq. (5.8)

[3] contact stiffness according to Eq. (5.4)

Table 5.10: Specification of input parameters for numerical simulations on the wall level for different configurations

5.2.2 Results from analyses on the wall model

Figure 5.11 shows the diagrams of load vs. displacement and cumulated energy vs. cumulated displacement obtained by the numerical simulation in comparison to the test results. Analogous to the experimental investigations, the displacement was recorded in the middle of the top of the wall (see Fig. 5.7).

In addition to the comparison of load-displacement characteristics and cumulated energy, the contributions to the overall deflection were evaluated. The hysteretic behaviour is dominated by the two contributions rocking and slip. If the contributions of deformations from the numerical simulation fit the experimental ones this would be an additional validation for the model and for the parameters which describe connections, contact and friction. The contributions of deformation were determined from the backbone curve (cf. Fig. 5.11k). Figure 5.10 shows the deformed shape of the wall element. The several contributions of deformation were calculated by Eqs. (5.10) to (5.12). The average over the several displacement steps are given in Table 5.11 in proportion to the top displacement u.

The contributions of deformation obtained analytically are compared with the experimental ones as given in Table 4.4. Table 5.11 shows that the deformation contributions from the numerical simulation are fairly close to those from the wall element testing. Only in configurations W-CLT-St-100 and W-CLT-Ti-50 could the deformation characteristics from testing not be fully reproduced. In both cases the contribution of slip is considerably higher and as a consequence the contribution of rocking is lower than the test results. That might be caused by a higher impact of friction in the test.

Even, the deformations of the CLT element are close to the ones from testing. The absolute deviation from the experimental values is less than 10 %, except for configuration W-CLT-St-100.

$$\text{Slip:} \qquad u_s = \frac{u_{1,x} + u_{2,x}}{2} \qquad (5.10)$$

$$\text{Rocking:} \quad u_\varphi = \frac{(u_{1,y} - u_{2,y}) \cdot h}{l} \qquad (5.11)$$
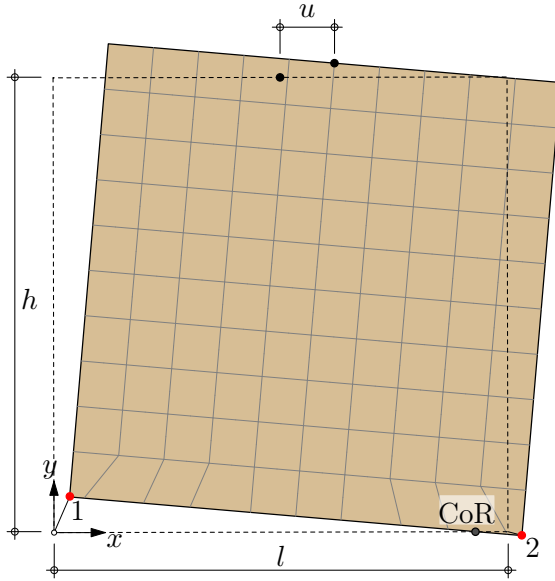
$$\text{CLT:} \qquad u_{CLT} = u - u_s - u_\varphi \qquad (5.12)$$

Figure 5.10: Deformed wall element and points for recording displacements

configuration	numerical			experimental		
	rocking	slip	CLT	rocking	slip	CLT
W-CLT-St-10	67 %	28 %	4 %	64 %	30 %	6 %
W-CLT-St-50	47 %	47 %	6 %	45 %	44 %	11 %
W-CLT-St-100	16 %	78 %	6 %	35 %	48 %	17 %
W-CLT-Ti-10	72 %	24 %	4 %	75 %	21 %	4 %
W-CLT-Ti-50	55 %	39 %	6 %	74 %	17 %	9 %
W-CLT-Sy-50	70 %	26 %	5 %	70 %	22 %	8 %
W-CLT-Ti-50M	71 %	14 %	13 %	83 %	8 %	9 %
W-CLT-St-100M	61 %	19 %	18 %	71 %	19 %	10 %

"CLT" stands for the inherent deformation of the CLT element due to bending and shear.

Table 5.11: Contributions to the overall deflection – rocking, slip and CLT; comparison of numerical and experimental results
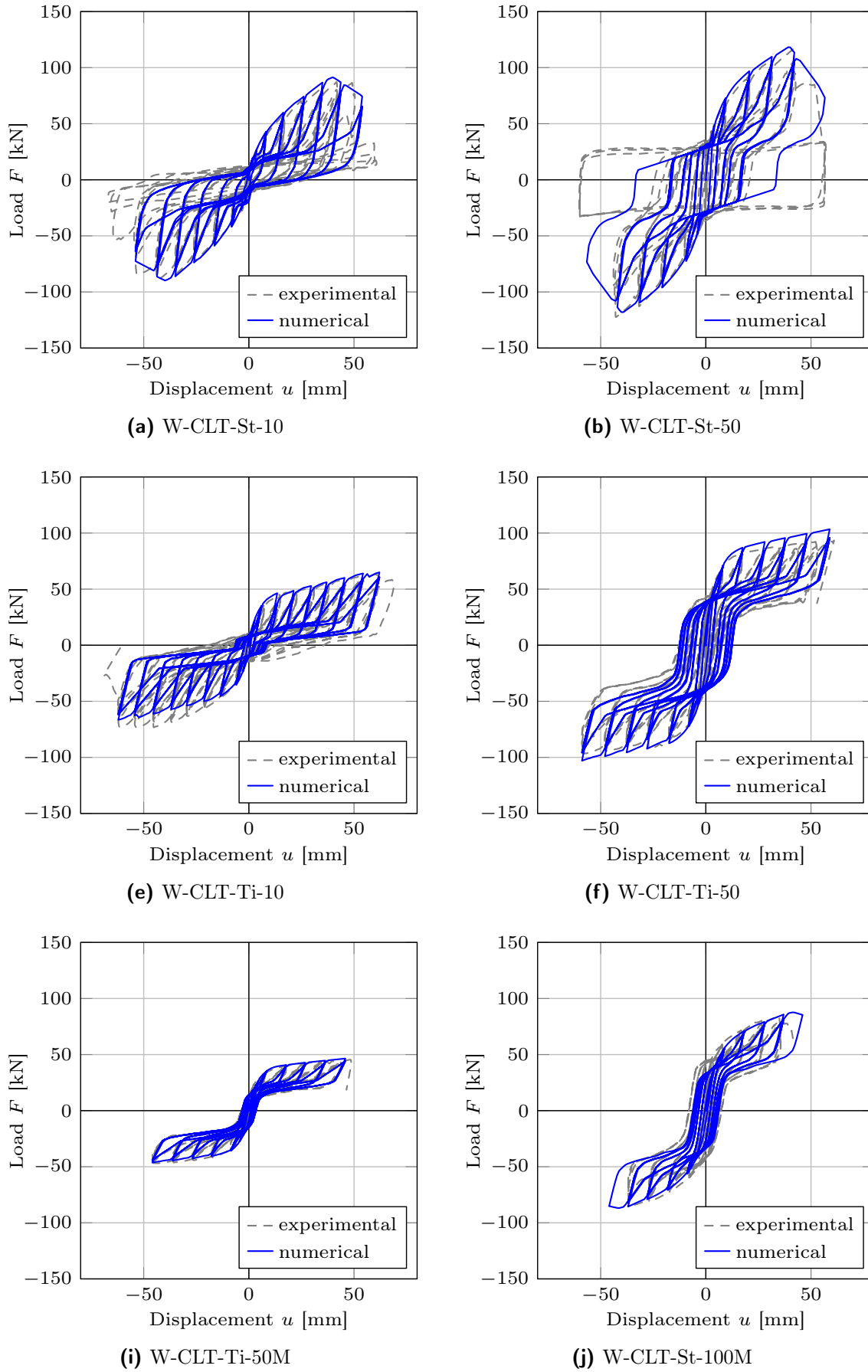
Figure 5.11: Behaviour of CLT wall elements; load-displacement curves and cumulated energy of experimental investigations and numerical model (part 1)
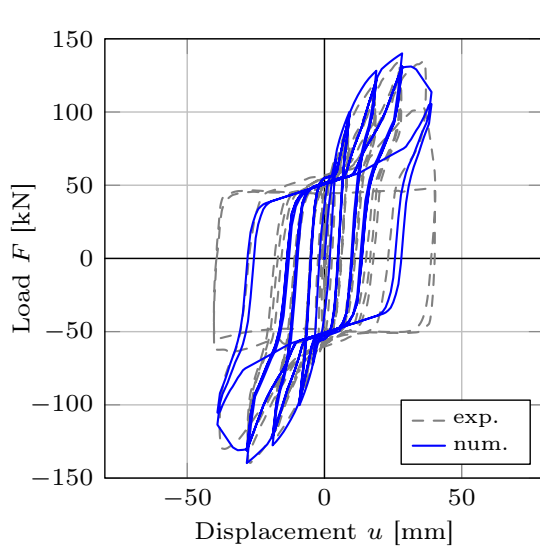
(c) W-CLT-St-100
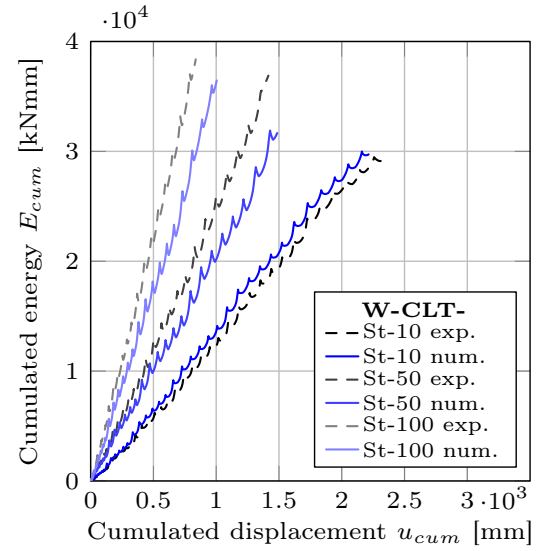
(d) E_{cum} for (a) to (c)
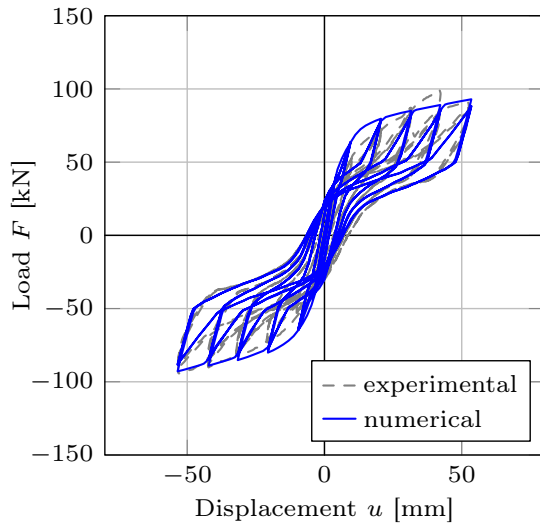
(g) W-CLT-Sy-50
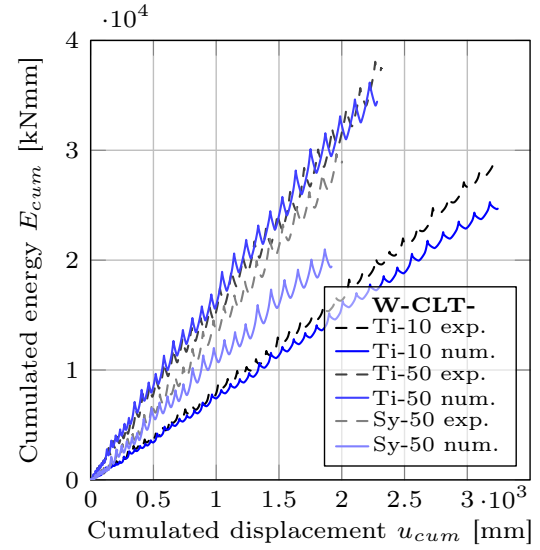
(h) E_{cum} for (e) to (g)
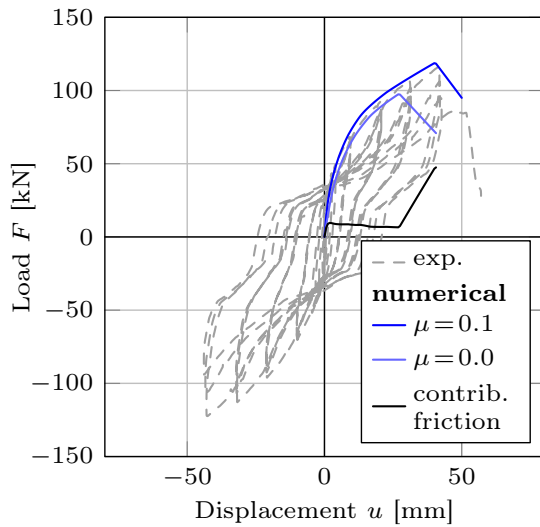
(k) W-CLT-St-50 and friction
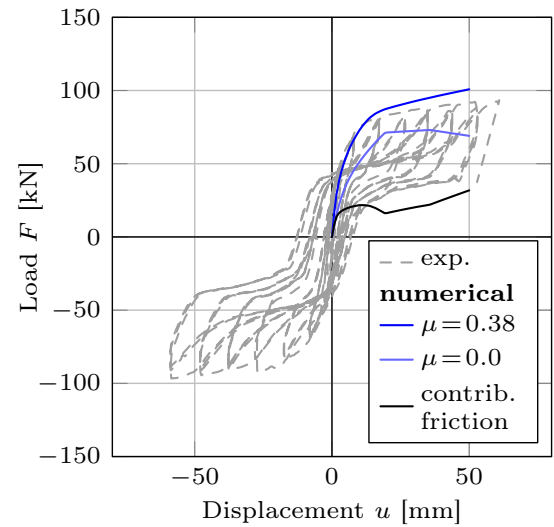
(l) W-CLT-Ti-50 and friction

Figure 5.11: Behaviour of CLT wall elements; load-displacement curves and cumulated energy of experimental investigations and numerical model (part 2)

Furthermore, the influence of friction is illustrated in Figures 5.11k and 5.11l for the configurations W-CLT-St-50 and W-CLT-Ti-50. The backbone curves which were obtained with and without considering friction are depicted. The contribution of friction is the difference between the two backbone curves. For W-CLT-St-50, both backbone curves are almost equivalent to the "experimental" curve until a displacement of about 25 mm is reached. This is approximately the displacement level where the load bearing capacity of an angle bracket for shear loading (AB-St-S) is reached. This indicates that the contribution of slip is close to 100 % for zero friction. If friction is considered the contribution of rocking increases because of higher resistance to shear. That leads to higher deformation capacity and load-bearing capacity of the wall element.

Similar effects can be observed for the configuration W-CLT-Ti-50. However, the load-bearing capacity without friction is significantly underpredicted. The difference between the two backbone curves is more pronounced than in configuration W-CTL-St-50 because of the higher friction coefficient.

It must be noted that the presumed friction coefficient for the steel-to-timber connection of 0.1 yields reasonable results for the configurations W-CLT-St-10, W-CLT-St-50, W-CLT-St-100 and W-CLT-St-100M with respect to the load-displacement characteristics (see Figs. 5.11a to 5.11c and 5.11j). The friction coefficient of 0.38 for the timber-to-timber connection provides the best agreement with the test results of the configurations with elastic support conditions (see Figs. 5.11e to 5.11g and 5.11i). The hysteresis curve could be predicted sufficiently, even for the configuration with an interlayer. However, the load-bearing capacity in W-CLT-Ti-50 is slightly overestimated.

Figure 5.11 shows that the load-displacement behaviour of CLT wall elements can be predicted in a reasonable way. More particularly, the deformation characteristics (see Tab. 5.11) and the load-bearing capacity obtained by the numerical simulation coincided with results from experimental investigations in most cases. That also implies that the isotropic material model and the material properties defined account for the stiffness of the CLT wall section sufficiently. Most importantly, the hysteretic behaviour of the CLT wall elements can be predicted for different boundary conditions. The friction coefficients 0.1 and 0.38 could be confirmed for steel-to-timber and timber-to-timber contact, respectively. Effects of force interaction were incorporated by a constant factor α which accounts for strength degradation and decreasing energy dissipation capacity. However, this led to an underestimation of the energy dissipation capacity in some cases.

Based on these results, it appears to be obvious that the data set of spring properties is definitely appropriate for simulations on the building level.

5.3 Reference Structures and Analysis Models

5.3.1 Engineering pre-design

A reference structure was developed as basis for numerical simulations on the building level. The floor plan is illustrated in Figure 5.12. The floor plan proposed is aimed at representing a building to be used for apartments or offices. The dimensions are oriented towards common modular dimensions in Europe. The beam and the two columns are only considered for the vertical load transfer. The floor plan was used to set up a CLT building with two, four and eight storeys, respectively.
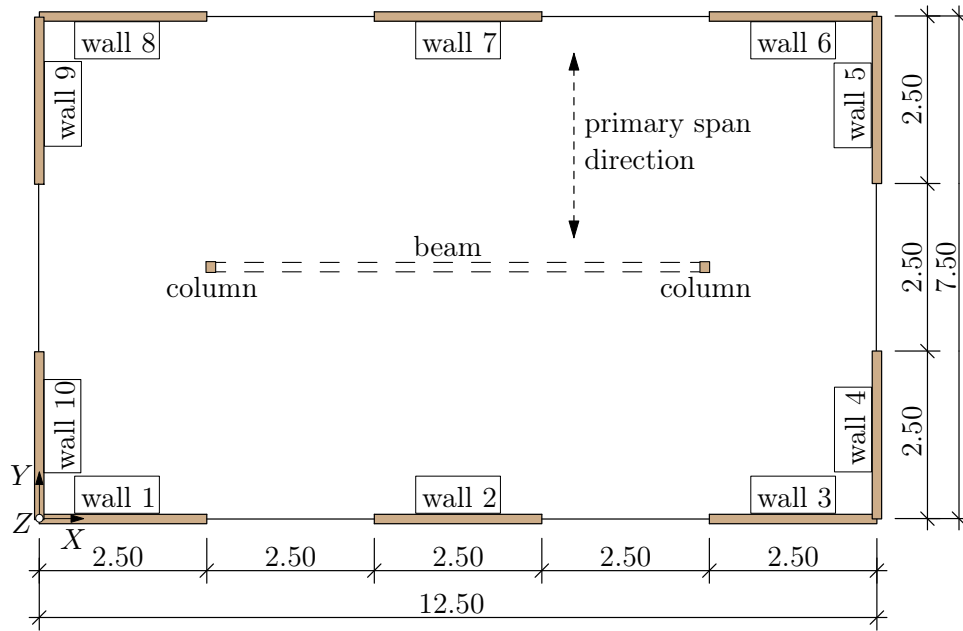
Figure 5.12: Floor plan of the reference structure

The reference structure was developed according to [FEMA P695] and considers aspects of buildings physics, fire safety and usage with respect to gravity loads. Figure 5.13 shows the assemblies and details which were chosen as reference.

The data of the reference structures are summarised in Table 5.12. The storey height was set to 2.75 m, which is common for residential buildings. The live load at the floor slabs is chosen at $1.5\,\mathrm{kN/m^2}$ in terms of usage in category A (residential buildings) [EN 1991-1-1].

	in X-direction	in Y-direction	storey height
Dimensions [m]	12.5	7.5	2.75
Number of walls × wall length [m]	6×2.5	4×2.5	
Number of storeys	2	4	8
Gravity loads [kN/m²]	roof slab	floor slab	walls
dead load	1.0	3.0	1.5
live load	–	1.5	–

Table 5.12: Data for reference structures

Different constellations of shear walls were considered in the study on the building level. There is a distinction between "shear wall type" and "box type" in plan and between single
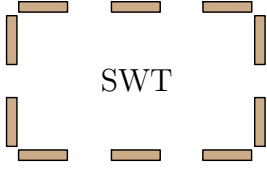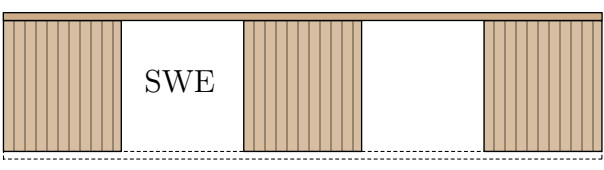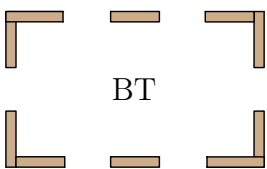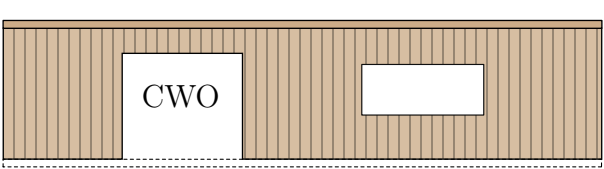
wall elements and continuous walls with openings in elevation (see Tab. 5.13). Shear wall type (SWT) means that perpendicular walls are not connected to each other. Perpendicular walls at the wall corner are joined together in the box type (BT) model. The configuration with single wall elements (SWE) represents the idealised situation where sections around openings are neglected. The consideration of such "non-structural" sections is taken into account by the continuous wall with openings (CWO).

Roof slab

–	water proofing
200 mm	insulation
138 mm	cross laminated timber
40 mm	insulation/lathing
25 mm	gypsum plasterboard (2×12^5 mm)

Exterior Wall

20 mm	plaster system
200 mm	insulation
105 mm	cross laminated timber
60 mm	insulation/lathing
25 mm	gypsum plasterboard (2×12^5 mm)

Floor Slab

–	floor finish
50 mm	screed flooring
30 mm	impact sound insulation
60 mm	fill within a honeycombed mould
138 mm	cross laminated timber
60 mm	insulation/lathing
25 mm	gypsum plasterboard (2×12^5 mm)

Figure 5.13: Reference details and assemblies of the CLT construction

The thickness of the slab was designed based on the service limit state. The primary span direction is depicted in Figure 5.12. The same cross-sections as those used in the tests on connections and wall elements (see section 4.1) were taken for floor slabs, roof slab and CLT shear walls of the reference structure (see Fig. 5.13).

in plan	in elevation
SWT	SWE
shear wall type	single wall elements
BT	CWO
box type	continuous wall with openings

Table 5.13: Constellations of shear walls for three-dimensional analyses

Define seismic zone and response spectrum

Estimate the structural period with $T_1 = 0.05 \cdot H^{3/4}$

Determine base shear and equivalent lateral forces

Determine number of connectors required

Define 3D model using elastic stiffness of connectors

Compute eigenfrequency of the structure by modal analysis

Structural period confirmed?

Set last period to structural period

NO

YES

Prelaminary seismic design completed

Figure 5.14: Procedure of preliminary seismic design and determination of structural period

A preliminary seismic design is necessary when preparing of non-linear analyses to guarantee an adequate distribution of strength. The outcome of preliminary seismic design is the number of connectors required which is used to set up the analysis model (see section 5.3.2). The design procedure is illustrated in Figure 5.14 and refers to the lateral force method (see section 2.4.2). In the initial step the structural period was estimated by an empirical formula (see Fig. 5.14) as proposed in [EN 1998-1].

Base shear and equivalent lateral forces

Base shear F_b and equivalent lateral forces F_i are calculated with Eqs. (2.12) and (2.13), respectively. Therefore, the design spectrum and the masses of the structure were specified as given in Table 5.14. The elastic response spectrum type 1, soil class B [EN 1998-1] and a ground acceleration of $a_g = 0.25$ g were taken as reference, for example, for a building in Italy. A behaviour factor of 2.0 was chosen to create the design spectrum (see Fig. 5.16). Seismic masses are determined by Eq. (5.13) using the dead load G_k and the live load Q_k as given in Table 5.12.

$$m = (G_k \text{ "+" } \psi_E \cdot Q_k) / g \tag{5.13}$$

with

$$\psi_E = \varphi \cdot \psi_2 = 0.8 \cdot 0.3 \tag{5.14}$$

The combination coefficients φ and ψ_2 were chosen in accordance to [EN 1998-1] and [EN 1990].

response spectrum:	type 1, soil class B ($S = 1.2$)	
ground acceleration:	$a_g = 0.25$ g, $PGA = S \cdot a_g = 0.3$ g	
behaviour factor:	$q = 2.0$	
level of	roof slab	floor slab
lumped mass m_i	14.9 t	42.6 t

Table 5.14: Seismic action and lumped masses m_i

The determination of masses, base shear and equivalent lateral forces is demonstrated in detail in annex A.

Design of connections

The number of connectors required was determined based on the SWT-SWE configuration of the reference structure. Lateral and vertical loads for the calculation of reactions – shear and tensile forces - were taken into account according to [EN 1990] with Eq. (5.15).

$$E_{d,AE} = G_k \text{ "+" } A_{Ed} \text{ "+" } \psi_2 \cdot Q_k \tag{5.15}$$

with $E_{d,AE}$ action effect due to seismic action
   A_{Ed} seismic action, lateral loads
   ψ_2 combination coefficient, $\psi_2 = 0.3$

This implies that the full dead load and 30 % of the live load have been applied as vertical loads together with the lateral seismic action A_{Ed}. The seismic action is represented by the equivalent lateral forces.

Wall elements have been anchored by hold-downs and angle brackets of the same type as those presented in sections 4.3. The connection between slab and wall at the top of each wall element is executed by self-tapping screws. The load-bearing capacity of the connectors from testing (see sections 4.2 and 5.1.3) is reduced by the "force interaction factor" α, see Eq. (5.8).

It is worth pointing out that principles of capacity design for CLT structures have been considered within seismic preliminary design. Overstrength and potential overdesign were taken into account by means of Eq. (5.16).

$$E_d = E_{d,G} \text{ "+" } \gamma_{Rd} \cdot \Omega \cdot E_{d,AE} \qquad (5.16)$$

with $E_{d,G}$ action effect due to non-seismic action, quasi-permanent combination
γ_{Rd} overstrength factor
Ω overdesign factor
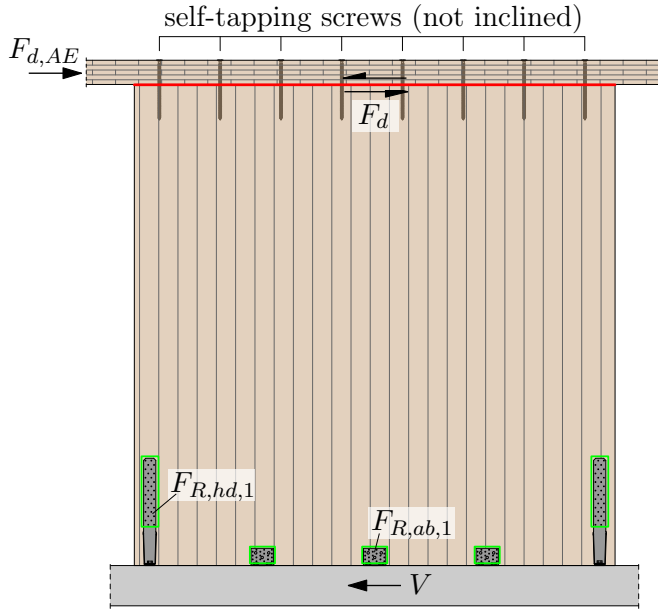
$$F_d = \gamma_{Rd} \cdot \Omega \cdot F_{d,AE} \qquad (5.17)$$

$$\text{with } \Omega = \frac{\sum F_{R,i,1}}{V}, \quad F_{d,AE} = V$$

— connection with self-tapping screws, with overstrength $\gamma_{Rd} = 1.3$

□ ductile connection

Figure 5.15: Action effect F_d for capacity design of the connection with self-tapping screws

According to the recommendations of FOLLESA ET AL. [Foll11] the screw connection between slab and wall were designed with an overstrength factor of 1.3. However, in this study the structure is designed by means of the resistance obtained experimentally (Tabelle A.1), not by the characteristic strength. These values of the resistance have been used to be consistent with the input parameters for nonlinear static and dynamic analyses. As a consequence a conservative behaviour factor ($q = 2.0$) has been applied. It must be noted that this procedure differ from the one which is used from engineers in practice. Here, design values of the strength have to be applied in order to design the structure according to the lateral force method.

The capacity design guarantees that the connectors of the anchoring – hold-downs and angle brackets – exhibit ductile behaviour, even for structural behaviour which deviates from SWT and SWE. Figure 5.15 illustrates which action is applied to design the screw connection. The effects of friction were not considered here.

The determination of shear and tensile forces and the design of connections is demonstrated in the annex A.

Analysis model and eigenfrequency

A three-dimensional model of the reference structure (SWT-SWE configuration) has been defined which is described in the next section in detail. However, only elastic springs – spring types a to d (see Tab. 5.1) – were implemented. The input data applied are summarised in Table 5.16 in conjunction with the discretisation of the analysis model. Full modal analyses were carried out to determine the eigenfrequencies of the structure. It was considered that gravity loads may lead to an increase of global stiffness and, consequently, to an increase of the eigenfrequency. According to Eq. (5.15) the gravity loads P are included with

$$P = G_k \text{ "+" } 0.3 \cdot Q_k. \tag{5.18}$$

Gravity loads are applied to slabs and walls. Lumped masses (see Tab. 5.14) are located at the centre of roof slab and floor slab. Gravity loads and masses must be specified separately, since the analysis programme OPENSEES does not support a takeover of masses from gravity loads.

The first eigenfrequency, respectively fundamental period, which was found by means of three-dimensional modal analyses and a few iterations according to the procedure in Figure 5.14 is illustrated in Figure 5.16. The fundamental period for the SWT-SWE structure for two, four and eight storeys in both the X- and Y-direction was separately computed.
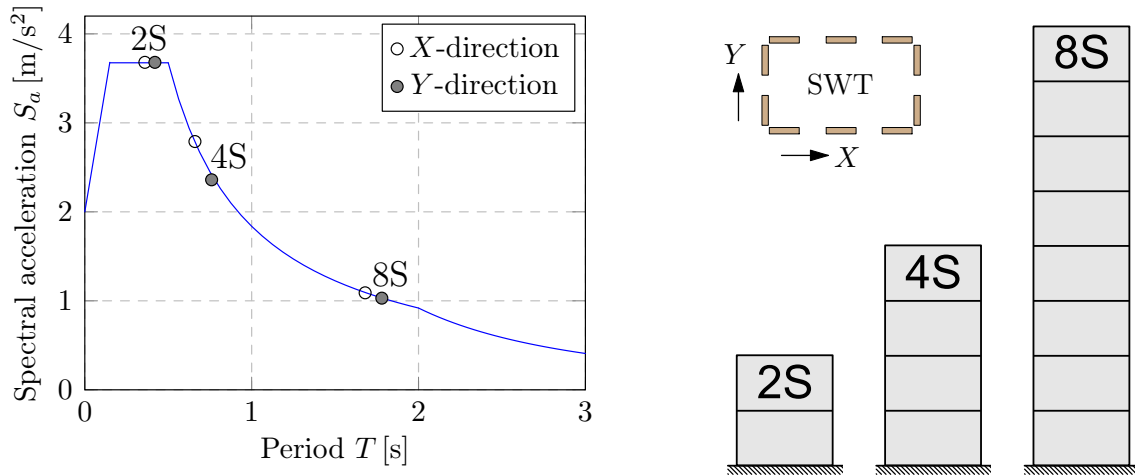
Figure 5.16: Design spectrum for soil class B, $a_g = 0.25$ g and $q = 2.0$ and fundamental periods of the two-storey (2S), four-storey (4S) and eight-storey (8S) building for the SWT-SWE configuration

5.3.2 Numerical discretisation

In this section, the discretisation of analysis models is described with reference to the analysis software OPENSEES applied. For this purpose, the input parameters required are depicted in this section. The data which accompany displacement-based design will be explained in section 6.

The analysis model was implemented with shell elements and discrete springs, as described in section 5.2. Shell elements for slabs and springs for screw connections were included in addition to shell elements for walls and springs for hold downs and angle brackets (see

Fig. 5.18). Similar to the definitions for CLT wall elements, effective material properties were used to consider the layered cross-section of the slab. An elastic orthotropic material model was applied to account for the different bearing behaviour of the slab in both the X- and Y-direction (see Figs. 5.12 and 5.17). The out-of-plane stiffness of the slab is significant for the distribution of gravity loads and for wall-slab interaction (see section 3.3).

Effective material properties were determined by a "back-calculation" from the effective bending and shear stiffness of the layered cross-section. Firstly, the components of the stiffness matrix D_{ij} for out-of-plane stress were determined, according to AUGUSTIN ET AL. [Augu10; Thie13; Wall13], considering the assembly of the CLT section – two layers in the X-direction, each 21 mm, and three layers in the Y-direction, each 32 mm. Subsequently, the effective material properties as listed in Table 5.15 were found by using the plate theory of MINDLIN AND REISSNER in combination with orthotropic material. The Poisson's ratio was set to 0.3 for all directions.

E_x	E_y	E_z	G_{xy}	G_{yz}	G_{zx}	ν_{xy}	ν_{yz}	ν_{zx}
[N/mm^2]						[−]		
1540	9460	11000	70	70	150	0.3	0.3	0.3

Table 5.15: Effective elastic, orthotropic material properties for CLT slab, $d\!=\!138$ mm
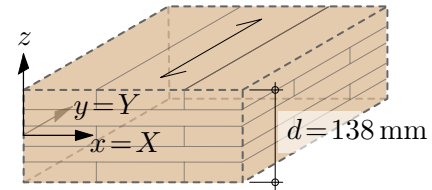
Figure 5.17: Local and global reference axis for CLT slab

The type of shell elements and the elastic properties for shear walls are identical to those used for numerical simulations on the wall level. It was shown in section 5.2 that the isotropic material model is adequate to represent the stiffness of the CLT wall section.

The same shell elements – MITC4 elements – have been applied for the slab. The mesh size was set to 250 by 250 mm for walls and slabs in order to get a proper balance between accuracy and computation time. A finer mesh would lead to a significant increase of the computation time.

Figure 5.18 shows the discretisation of the two storey reference structure. In addition to discrete springs at the bottom of the wall, springs for the connection between the top of the wall and slab and between perpendicular walls were implemented in the analysis model. Springs for hold-downs, angle brackets and contact to the base were considered in the 3D model in the same way as described in section 5.2.

Analyses with and without friction were performed. For analyses without friction spring type b has been used in the contact area. If friction was considered the singleFPBearing element (see section 5.1.2) would be implemented.

It must be noted that springs between perpendicular walls were only implemented in the BT configuration. Here, self-tapping screws (SC-WC) with a spacing of 250 mm were considered. The spacing of the springs is oriented on the mesh size. The number of connectors – hold-downs, angle brackets and self-tapping screws between slab and wall – were determined by preliminary seismic design (see section 5.3.1). Springs for hold-downs were located at the end of walls. Springs for angle brackets and self-tapping screws were distributed uniformly along the length of the wall.

"Contact" springs were defined at each point along the length of the wall to create a continuous contact in the wall-slab joint at the top and the bottom of the wall. A rigid support was assumed in the ground floor and an elastic support condition (CLT) in higher floors.
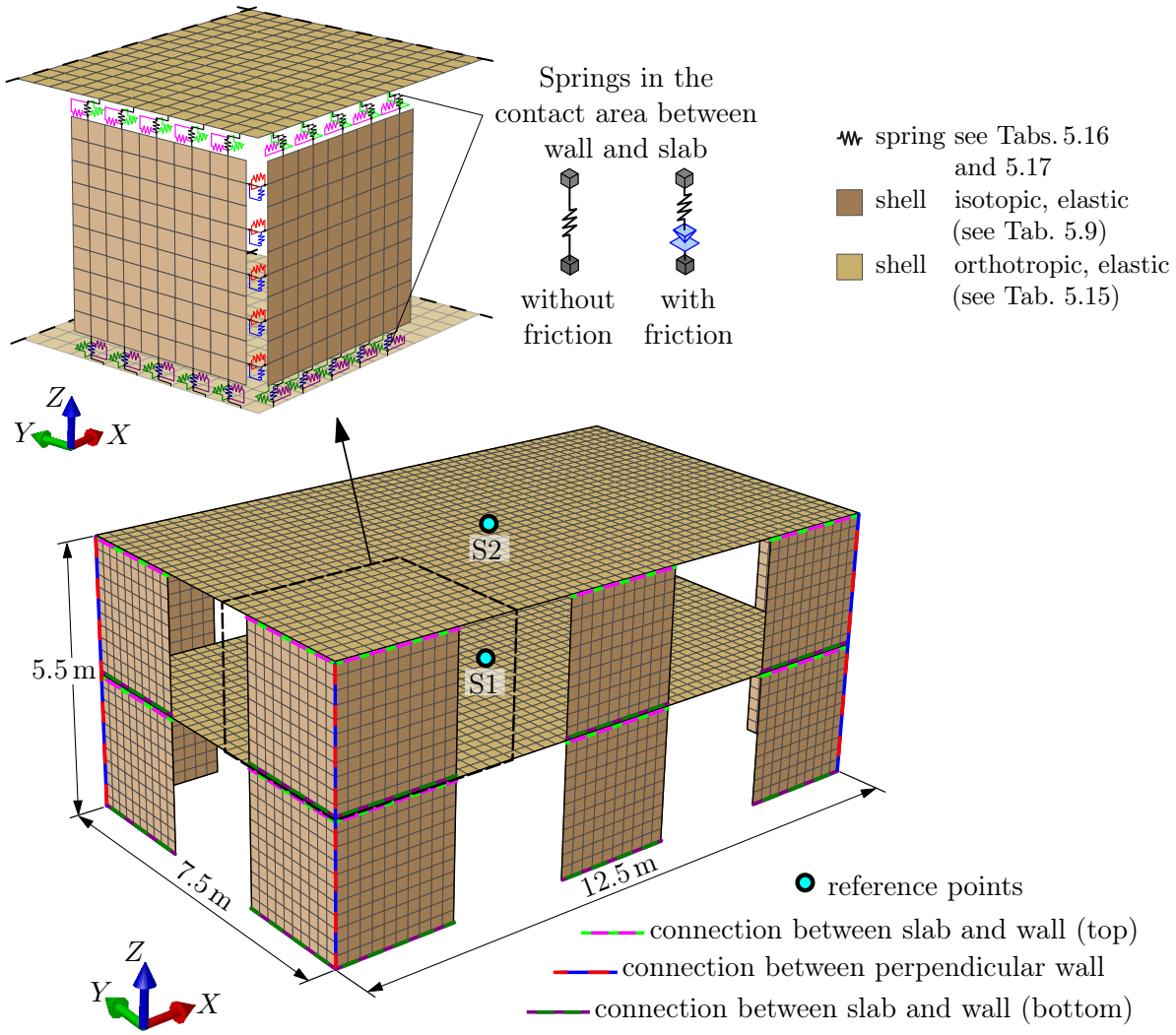
Figure 5.18: Model of a two-storey CLT building with single wall elements, implementation of shells and springs

Linear-elastic springs – spring type a – were implemented at the bottom in the local z-direction to prevent shear walls from out-of-plane movement (cf. Fig. 5.6). However, a comparatively low stiffness ($K_a = 1\,\text{kN/mm}$) was chosen. The influence of this stiffness was investigated by varying it from 1 to 100 kN/mm and was found to be less significant for the global response.

A legend of the implemented springs is given in Table 5.16 which depicts the different type of springs and the spring properties used for analysis with screws which were not inclined and without friction. The types of springs and the corresponding spring properties were changed depending on the analysis procedures (AP). The different analysis procedures were specified at the beginning of this chapter. For the spring properties, refer to section 5.1.3.

The spring properties $K_{0,g}$, $F_{0,g}$, $F_{1,g}$ and $K_{0,h}$, $F_{0,h}$, $F_{1,h}$, $K_{y,h}$ are again modified by Eq. (5.8) to account for force interaction. And the contact stiffness K_b is adapted according to Eq. (5.9).

	config.	type			properties		
		AP1	AP2+3	AP4	AP1	AP2+3	AP4
⎌	SC-WS-0	a	g	e	$K_a = K_{0,g}$	$\bullet_g$ (Tab. 5.4)[1]	$\bullet_e$ (Tab. 4.1, 5.6)
⎌	SC-WS-90	a	g	e	$K_a = K_{0,g}$	$\bullet_g$ (Tab. 5.4)[1]	$\bullet_e$ (Tab. 4.1, 5.6)
⎌	SC-WS-ax	d	d	d	$K_c = K_{ax},\ K_b = K_{n,h}$		
		b	b	b	$K_b = K_{n,h}$		
⎌		a	a	a	$K_a = 1\,\mathrm{kN/mm}$		
⎌	HD-∗-S/ AB-∗-S	a	g	e	$K_a = K_{0,h}$	$\bullet_g$ (Tab. 5.4)[1]	$\bullet_e$ (Tab. 4.1, 5.6)
⎌	HD-∗-T/ AB-∗-T	d	h	f	$K_a = K_{0,h},$ $K_b = K_{n,h}$	$\bullet_h$ (Tab. 5.5)[2]	$\bullet_f$ (Tab. 4.1, 5.6)[3]
		b	b	b	$K_b = K_{n,h}$		
⎌	SC-WC-0	a	g	e	$K_a = K_0$	$\bullet_g$ (Tab. 5.4)[1]	$\bullet_e$ (Tab. 4.1, 5.6)
⎌	SC-WC-90	a	g	e	$K_a = K_0$	$\bullet_g$ (Tab. 5.4)[1]	$\bullet_e$ (Tab. 4.1, 5.6)

∗ St – ground floor, Ti – first and higher floors [1] $K_{0,g}$, $F_{0,g}$, $F_{1,g}$ modified by Eq. (5.8)
• all parameters of this spring type [2] $K_{0,h}$, $F_{0,h}$, $F_{1,h}$, $K_{y,h}$ modified by Eq. (5.8)
[3] combination of spring type e and b (see p. 87)

Table 5.16: Specification of types and properties of springs for analysis procedure AP1 to AP4 without friction using screws which were not inclined

	config.	inclined screws		inclined screws + friction	
		type	properties	type	properties
⎌	SC-X-0	g	$\bullet_g$ (Tab. 5.4)[1]	g	$\bullet_g$ (Tab. 5.4)[1]
⎌	SC-WS-90	g	$\bullet_g$ (Tab. 5.4)[1]	g	$\bullet_g$ (Tab. 5.4)[1]
⎌	SC-X-ax	d	$K_c = K_{ax},$ $K_b = K_{n,h}$	d + FP	$K_c = K_{ax},$ $K_b = K_{n,h}$
		b	$K_b = K_{n,h}$	b + FP	$K_b = K_{n,h}$ + FM-2, $\mu_k = 0.20$
⎌		a	$K_a = 1\,\frac{\mathrm{kN}}{\mathrm{mm}}$	a	$K_a = 1\,\frac{\mathrm{kN}}{\mathrm{mm}}$
⎌	HD-∗-S/ AB-∗-S	g	$\bullet_g$ (Tab. 5.4)[1]	g	$\bullet_g$ (Tab. 5.4)[1]
⎌	HD-∗-T/ AB-∗-T	h	$\bullet_h$ (Tab. 5.5)[2]	h + FP	$\bullet_h$ (Tab. 5.5)[2]
		b	$K_b = K_{n,h}$	b + FP	$K_b = K_{n,h}$ + FM-3, $\mu_k = 0.30$ (floor 1) FM-2, $\mu_k = 0.38$ (floor >1)
⎌	SC-X-0	g	$\bullet_g$ (Tab. 5.4)[1]	g	$\bullet_g$ (Tab. 5.4)[1]
⎌	SC-WC-90	g	$\bullet_g$ (Tab. 5.4)[1]	g	$\bullet_g$ (Tab. 5.4)[1]

∗ St – ground floor, Ti – first and higher floors [1] $K_{0,g}$, $F_{0,g}$, $F_{1,g}$ modified by Eq. (5.8)
• all parameters of this spring type [2] $K_{0,h}$, $F_{0,h}$, $F_{1,h}$, $K_{y,h}$ modified by Eq. (5.8)
FP – singleFPBearing element

Table 5.17: Specification of types and properties of springs for non-linear dynamic analyses (AP2) using inclined screws and considering friction

The influence of inclined self-tapping screws and friction will be studied in some analyses. The input data which are applied for the springs and friction are given in Table 5.17. The spring properties of screws which were not not inclined will just be replaced by the ones of inclined screws for analyses with inclined self-tapping (SC-X-0). Due to a lack of experimental data for inclined screws for shear in the perpendicular direction (SC-X-90), the spring properties of the screws which were not not inclined are taken into account.

Input parameters for friction were given in section 5.1.4. A friction coefficients of 0.38 for the timber-to-timber connection was found from the numerical simulations on the wall level. This friction coefficient is applied in the connection between slab and wall at the bottom. For the connection between the slab and wall on the top the fact that a considerable share of the compressive force is directly transferred over the screw (in axial direction) must be considered. The compressive force is not gathered completely by contact. Effects of friction would be overpredicted if the whole compressive force is taken into account for friction. To capture this influence within three-dimensional analyses in a simple way, a lower friction coefficient was applied in the connection between slab and wall on the top. The friction coefficients is taken into account with 0.2 for this connection. The CLT walls on the ground floor are supported on a concrete basement (see Fig. 5.13). The parameters for concrete-to-timber contact conditions (FM-3) are used here (see section 5.1.4).

Some CLT sections were added to the SWE configuration for the CWO configuration of the structure, as shown exemplarily in Figure 5.19, for the four-storey analysis model. Adjacent wall sections are rigidly linked by each other. There are no joints between. Openings were left over the complete length of 2.5 m for reasons of consistency with the SWE configuration and had to be oriented on the mesh size. Openings for windows always have the dimensions 2.5×1.0 m. It must be noted that the number of connectors was not changed for CWO configuration. However, contact springs were added in the connection zone between wall and slab.

The reference points which are shown in Figures 5.19 and 5.18 are defined at the centre of the mass of the slab. Lumped masses will be fixed to reference points for dynamic analyses (see section 5.4) and horizontal load will be applied at reference points for pushover analysis (see section 6.3). Furthermore, lateral displacements will be recorded at the reference points.
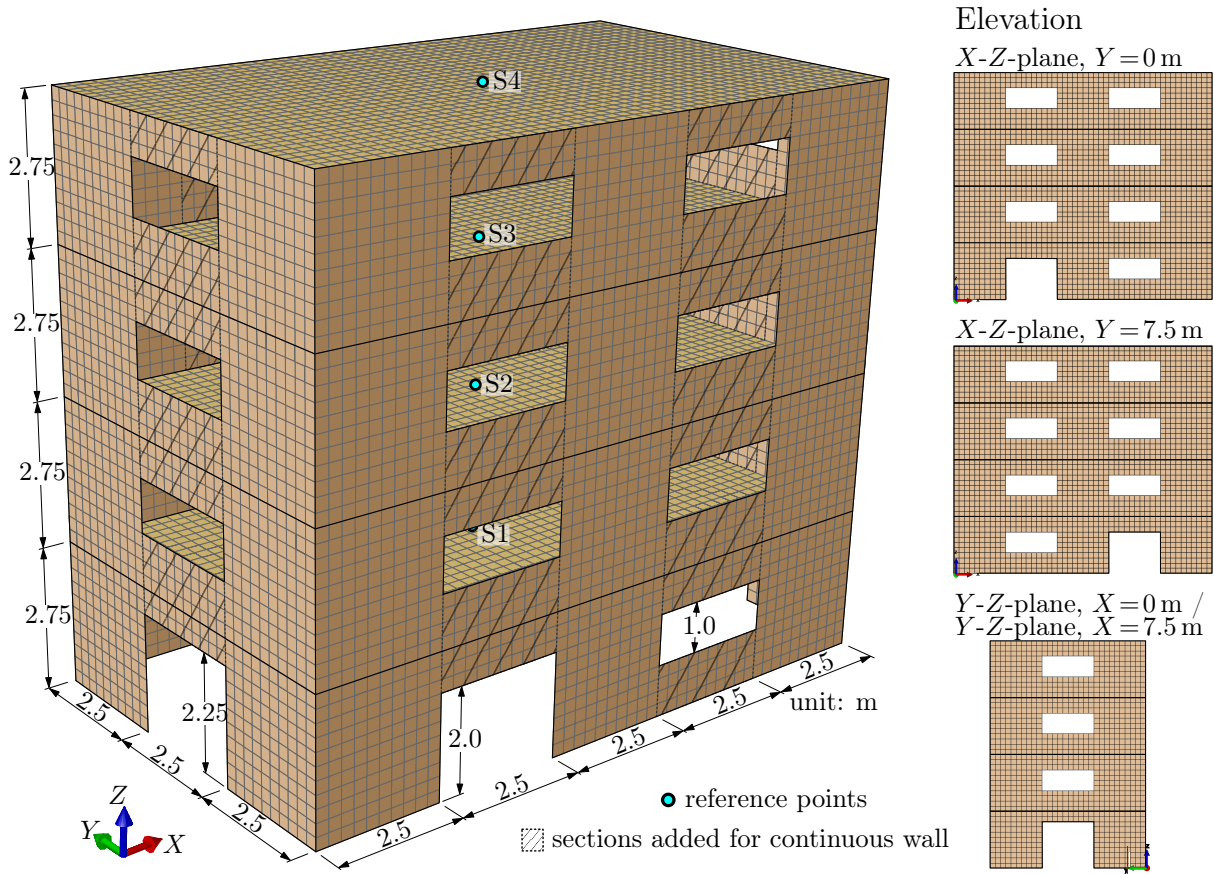
Figure 5.19: Three-dimensional analysis model of the four-storey CLT building with continuous walls

5.4 Dynamic response analyses

In this section the dynamic response of the structure under earthquake excitation will be investigated. For this purpose, NTHAs will be carried out including the structural models as presented in section 5.3. Specifications which are required for full dynamic analyses will be provided in section 5.4.1. Results from NTHA will be given in section 5.4.2. These results will be used to validate the results from DBD (see chapter 6).

5.4.1 Specifications and records

The analysis models developed from section 5.3 capture aspects of stiffness distribution and non-linear hysteretic behaviour of structural components. Uniform gravity loads have been applied to walls and slabs, see Table 5.12 and Eq. (5.15).

As the mass distribution with lumped masses is a basic assumption of DBD, structural masses are applied as lumped masses (see Tab. 5.16) within NTHA for consistency. Lumped masses are located at the reference points (see section 5.3.2).

Stiffness and mass proportional damping have been included. The damping approach refers to Eq. (2.33). However, the initial stiffness matrix $\boldsymbol{K}_{ini}$ has been used to define the damping matrix $\boldsymbol{C}$, see Eq. (5.19).

$$\boldsymbol{C} = \alpha_m \boldsymbol{M} + \alpha_k \boldsymbol{K}_{ini} \tag{5.19}$$

The proportionality factors α_m and α_k were determined with Eqs. (5.20) and (5.21), respectively.

$$\alpha_m = \frac{2 \cdot \xi \cdot \omega_1 \cdot \omega_2}{\omega_1 + \omega_2} \tag{5.20}$$

$$\alpha_k = \frac{2 \cdot \xi}{\omega_1 + \omega_2} \tag{5.21}$$

The first and the second circular frequencies ω_1, ω_2 are determined by full modal analysis. Results are depicted exemplarily for configurations SWT-SWE and BT-SWE in Table 5.18. It is assumed here that the dynamic response is dominated by the first two vibration modes. The damping ratio was taken into account at 5 %, as it is included in the elastic response spectrum.

	SWT–SWE				BT–SWE			
	X-direction		*Y*-direction		*X*-direction		*Y*-direction	
	ω_1	ω_2	ω_1	ω_2	ω_1	ω_2	ω_1	ω_2
2S	17.62	27.36	14.94	22.54	17.83	27.75	15.09	22.78
4S	9.56	20.64	8.24	16.21	9.67	20.86	8.34	16.40
8S	3.75	11.88	3.53	10.51	3.78	12.02	3.56	10.63

Table 5.18: First and second circular frequency (in [rad/s]) from modal analysis for configurations SWT-SWE and BT-SWE

Ground motion records

Ground motion records compatible with the elastic response spectrum type 1, soil class B (see Tab. 5.14) were applied. Seven records were taken for statistical reasons, as is requested in [EN 1998-1]. The spectra of the ground motion records selected are depicted in Figure 5.20. The records were chosen in that way so that the tolerance of the average spectrum – mean over the spectra of the ground motion records – from the target spectrum (elastic response spectrum) is in the range of $\pm\,10\,\%$ within the period domain of 0.01 to 2.0 s. Therefore, the spectra were scaled to the peak ground acceleration $PGA = 0.3$ g. The scale factors (SF) are given in Figure 5.20. The compatible ground motion records were found by means of the tool REXEL [Ierv10]. Details concerning each of the seven records are given in Table 5.19. More information regarding the ground motion records considered, including the accelerogram of each record, are given in the annex B.

Solution strategy and convergence

The NEWMARK [Newm59] method in combination with the KRYLOV-NEWTON algorithm [Scot10] were used as solution strategy. The weighting factors γ and β for time integration with NEWMARK were set to 0.6 and 0.3, respectively, for reasons of convergence. The KRYLOV-NEWTON algorithm is a modification of the classic NEWTON-RAPHSON iteration and speeds up non-linear analyses incorporating the SAWS hysteretic model. The convergence of the iteration is checked by an energy-based criterion, see Eq. (5.22).

$$\tfrac{1}{2}|\Delta \boldsymbol{u} \cdot \Delta \boldsymbol{R}| \leq \eta_E \tag{5.22}$$

with $\Delta \boldsymbol{u}$ vector of incremental displacements

         $\Delta \boldsymbol{R}$ vector of residual forces (unbalance)

         η_E convergence tolerance

ID	Station ID	Earthquake Name	Date	comp.	$PGA\,[\text{g}]^{1)}$
IN0075y	KGS004	NW Kagoshima Prefecture	02.04.1997	NS	0.10
IN0114x	BUI	Friuli (3rd shock)	15.09.1976	EW	0.09
IN0278y	NIG022	MID NIIGATA PREF	11.03.2011	NS	0.06
IN0312x	MOG0	EMILIA Pianura Padana	29.05.2012	NS	0.17
IN0317y	HEC	Hector Mine	16.10.1999	EW	0.34
IN0412x	ST108	South Iceland	17.06.2000	EW	0.13
IN0426x	MRN	EMILIA Pianura Padana	29.05.2012	EW	0.23

[1] *PGA* of the unscaled record

NS – north-south component, EW – east-west component

Table 5.19: Specification of ground motion records
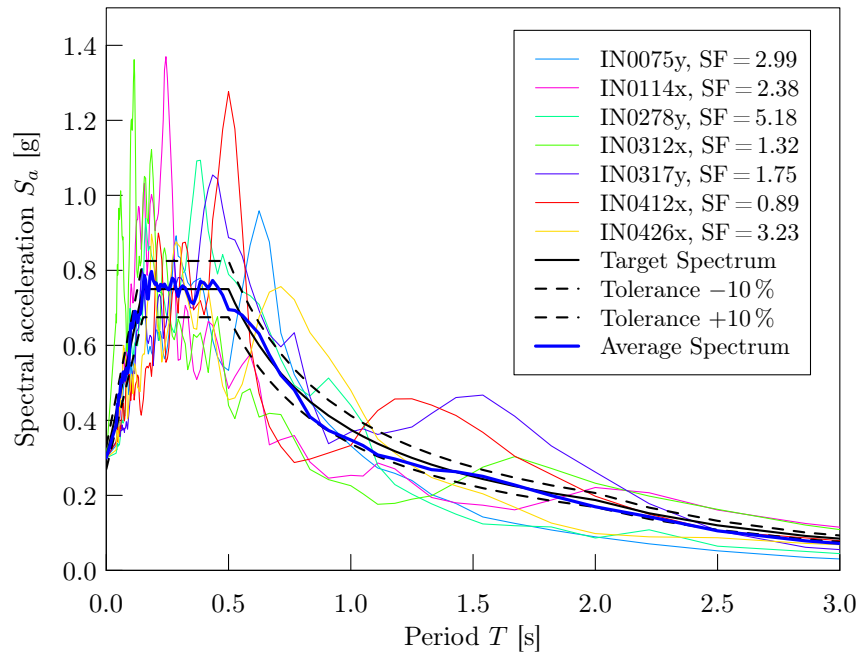
Figure 5.20: Spectra of the ground motion records selected, average spectrum and target spectrum

The convergence tolerance η_E was set to 10^{-4}, as recommended by DE BORST ET AL. [de B14]. This criterion must be fulfilled within a maximum number of iterations of 1000.

Analysis procedure and output

The software OPENSEES was applied for NTHA. The entire analysis procedure includes the following steps:

1. The structural model is set-up including masses and gravity loads.
2. Full modal analysis is carried out to find the first and the second circular frequency.
3. The proportionality factors α_m and α_k are determined.
4. The damping matrix is built.
5. The ground motion record is read and scaled.
6. The analysis model is subjected to the scaled ground motion record in the direction considered.
7. The dynamic response is computed and recorded for each time step of the ground motion record.

All ground motion records are applied separately for the *X*- and *Y*-direction at the base of the structural model. For purposes of seismic design, it should be considered that the excitation might differ from the main two directions. However, for this study, the results from the time history analysis are used as reference for validation.

5.4.2 Analysis results

The results from NTHA are summarised in Tables 5.20 and 5.21. NTHAs for the eight-storey building were performed for the configurations SWT-SWE and BT-SWE. The minimum, maximum and mean value of the absolute values of the base shear over the set of seven records were documented for each configuration of the analysis model. The corresponding summary for the top displacement is given in Table 5.21. These analysis results are obtained without considering friction and for connection with screws which have not been inclined.

Configuration			2S model			4S model			8S model		
Plan	Elevation	Dir	Min	Mean	Max	Min	Mean	Max	Min	Mean	Max
SWT	SWE	X	135.1	195.8	241.7	195.9	272.4	355.7	243.4	315.9	377.9
BT	SWE	X	137.0	202.7	254.1	200.9	281.1	374.8	261.6	329.0	398.2
SWT	CWO	X	140.6	210.6	243.7	202.2	309.2	372.0			
BT	CWO	X	139.8	219.5	263.9	229.1	322.5	396.5			
SWT	SWE	Y	124.0	185.2	218.0	174.3	226.4	274.5	235.2	296.0	348.8
BT	SWE	Y	126.2	192.1	236.0	176.4	239.6	301.5	244.3	306.6	361.1
SWT	CWO	Y	126.4	188.5	224.0	193.5	246.6	280.9			
BT	CWO	Y	130.4	196.8	245.0	198.6	264.4	312.0			

Table 5.20: Results of non-linear time history analyses without friction – base shear (in kN)

Configuration			2S model			4S model			8S model		
Plan	Elevation	Dir	Min	Mean	Max	Min	Mean	Max	Min	Mean	Max
SWT	SWE	X	13	32	56	22	63	108	1	114	219
BT	SWE	X	12	32	56	25	62	104	3	111	220
SWT	CWO	X	10	25	42	11	45	74			
BT	CWO	X	10	25	40	16	46	79			
SWT	SWE	Y	16	36	55	28	79	146	15	108	230
BT	SWE	Y	16	35	55	26	79	139	13	112	227
SWT	CWO	Y	13	30	49	34	59	98			
BT	CWO	Y	13	29	49	31	60	95			

Table 5.21: Results of non-linear time history analyses without friction – top displacements (in mm)

The range of the base shear for the different configurations of analysis models is shown in Figure 5.21. The box plots represent the summary of absolute values of the base shear from NTHA for the set of ground motions. It shows that connecting of perpendicular walls (BT) and adding of wall sections with openings (CWO) lead to an increase of the base

shear. The opposite is true for the deformation characteristics (see Tab. 5.21 and 5.22). The lateral displacements decrease from the SWT–SWE configuration to the BT–CWO structure. Figure 5.22 illustrates that for the X-direction. The deflection shape depicted corresponds to the maximum value of the base shear (see Tab. 5.20). The associated lateral displacements at the reference points are documented in Table 5.22. It can be observed that the top displacement, which relates to the maximum base shear, is always between the mean and maximum values or equals to the maximum value as depicted in Table 5.21.

(a) 2S in X-direction

(c) 4S in X-direction

(b) 2S in Y-direction

(d) 4S in Y-direction
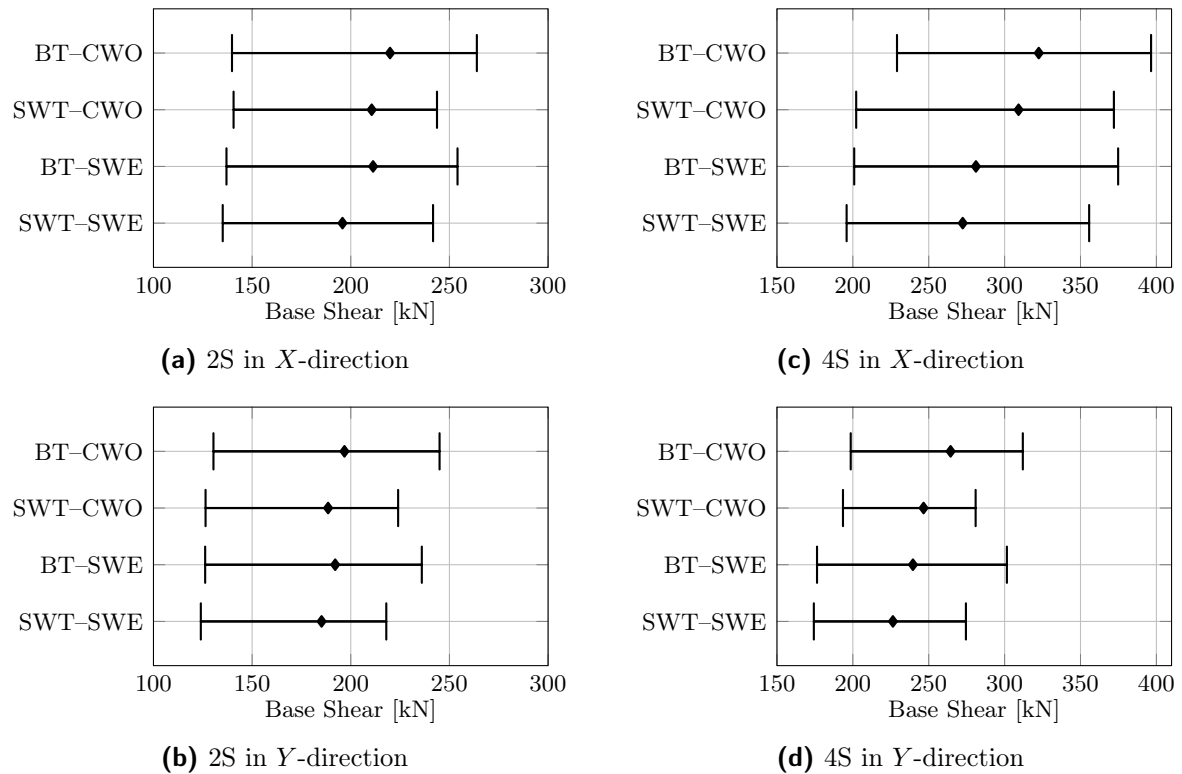
Figure 5.21: Base shear for two- and four-storey structures – minimum, maximum and mean values

Configuration			2S model		4S model				8S model							
Plan	Elevation	Dir	U1	U2	U1	U2	U3	U4	U1	U2	U3	U4	U5	U6	U7	U8
SWT	SWE	X	33	56	34	57	81	90	27	53	75	96	117	141	161	180
BT	SWE	X	29	46	33	56	79	90	27	54	75	95	115	138	156	173
SWT	CWO	X	31	42	28	52	69	74								
BT	CWO	X	29	40	28	50	68	79								
SWT	SWE	Y	46	55	46	74	93	84	24	45	65	88	111	142	179	206
BT	SWE	Y	46	55	47	79	102	109	24	47	68	92	116	146	181	208
SWT	CWO	Y	45	48	40	63	78	88								
BT	CWO	Y	45	48	43	61	69	74								

Table 5.22: Lateral displacements at the reference points for the maximum value of the base shear (in mm)

111

(a) 2S

(b) 4S

(c) 8S
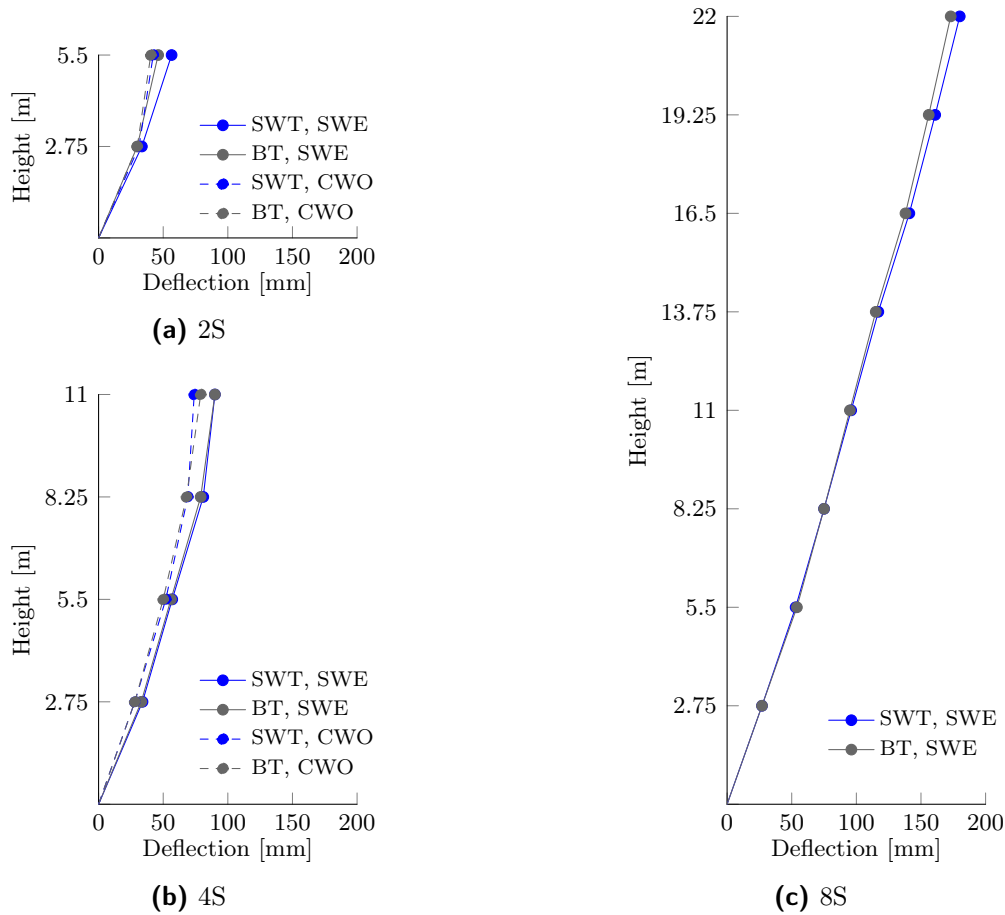
Figure 5.22: Deflection shapes for earthquake excitation in the X-direction, lateral displacements at the reference points corresponding to the maximum base shear

In order to show the different characteristics in the dynamic response base shear over displacement curves are provided in Figure 5.23 for the ground motion record with ID IN0075y (see Tab. 5.19 and annex B). The graphs show that the global hysteretic behaviour is changed from the SWT-SWE configuration to the SWT-CWO configuration significantly: the base shear increases and the lateral displacements decrease. However, it can also be observed that the top displacement is not always proportional to the base shear. This indicates that higher mode effects contribute to the dynamic response. Nevertheless, the deflection at the point of maximum base shear is comparable to those depicted in Figure 5.22.

The influence of friction and of the use of inclined self-tapping screws instead of those which are not inclined in the connection between perpendicular walls and the connection between floor slab and wall (top) were studied in a further step. How the hysteretic behaviour is changed if these modifications are considered is illustrated exemplarily in Figure 5.24. While the usage of inclined self-tapping screws does not change the dynamic behaviour significantly, friction has a vast impact on the dynamic response in terms of global stiffness, load-bearing capacity and energy dissipation capacity. The behaviour for the two-storey building is almost linear in combination with a slightly higher initial stiffness. The base shear also increases. The influence of friction in combination with connections with inclined self-tapping screws might be responsible for the behaviour which was found by shaking table tests of entire CLT structures (see section 3.1).
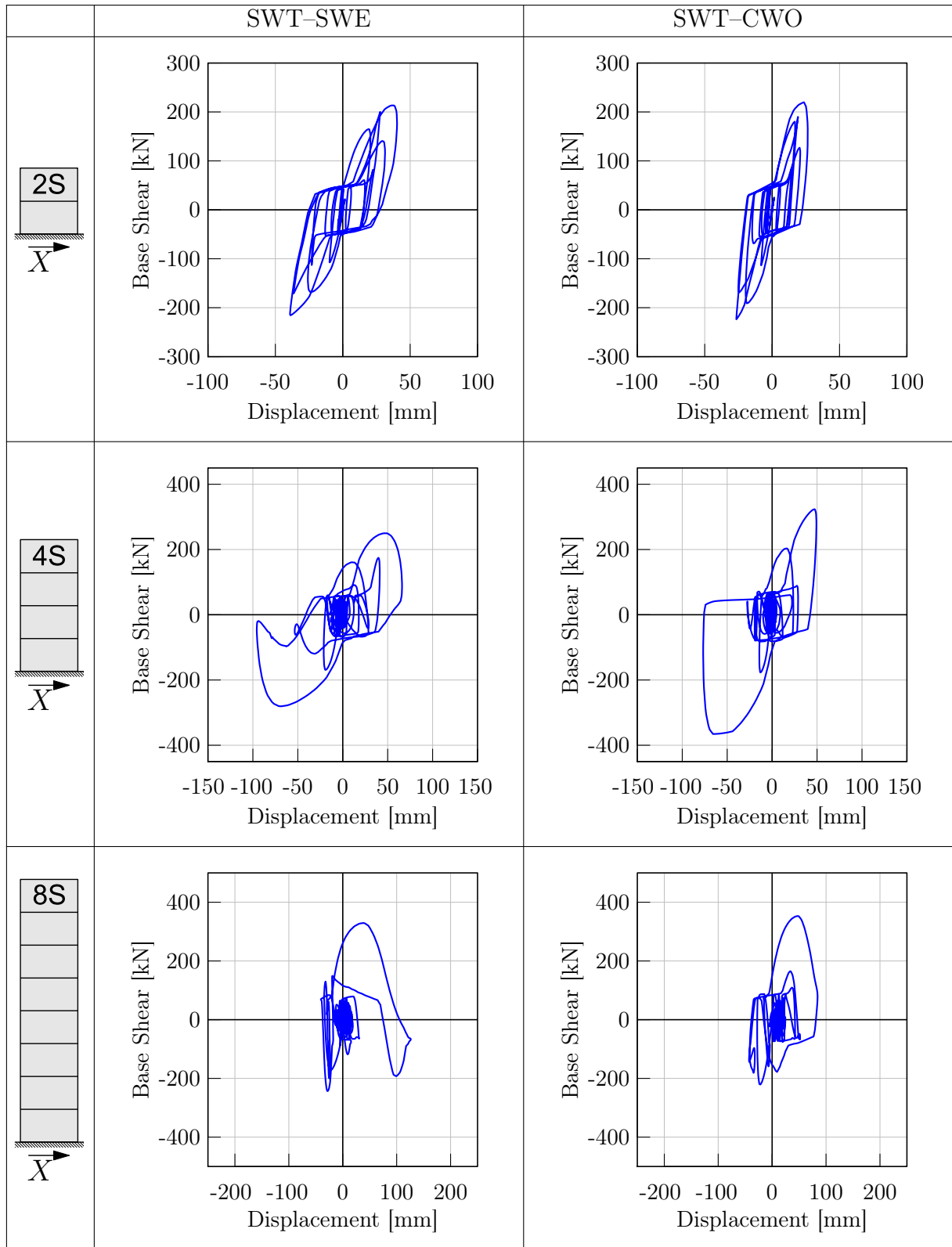
Figure 5.23: Dynamic response for seismic excitation with record IN0075y – lateral displacement over base shear in the X-direction, without friction
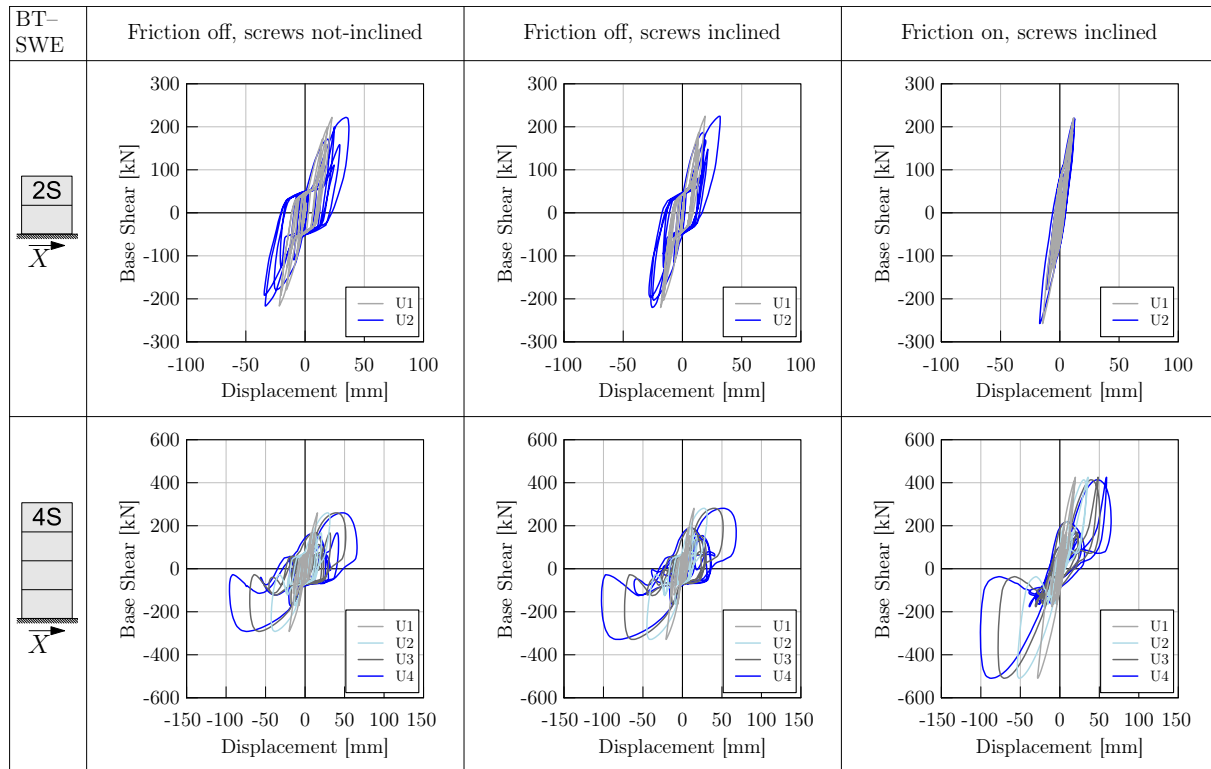
Figure 5.24: Dynamic response for seismic excitation with record IN0075y – lateral displacement over base shear in the *X*-direction, with friction and inclined screws, BT-SWE configuration

6 Displacement-based design for CLT structures

The fundamentals of DBD have already been presented in section 2.4.3 in the context of the capacity spectrum method and the N2 method. From sections 2.5.2, it becomes clear that the current formulation for the definition of the demand spectrum may not fully cover the requirements of CLT constructions. In the first section of this chapter, a new approach to transfer the elastic response spectrum into the demand spectrum will be presented with reference to the N2 method. This approach will be compared with other procedures transferring the elastic response spectrum. Results from DBD will be validated against the full dynamic analysis in section 5.4. The new approach will be evaluated on the level of the SDOF system and the building level.

6.1 $R_\mu - \mu - T$ relationship for CLT structures

6.1.1 Procedure and input data

The procedure to find a transfer relationship for CLT structures is based on the investigations of VIDIC ET AL. [Vidi94] and MERGOS AND BEYER [Merg15]. A set of inelastic SDOF systems (see Fig. 6.1) is considered to represent the hysteretic behaviour of CLT constructions.
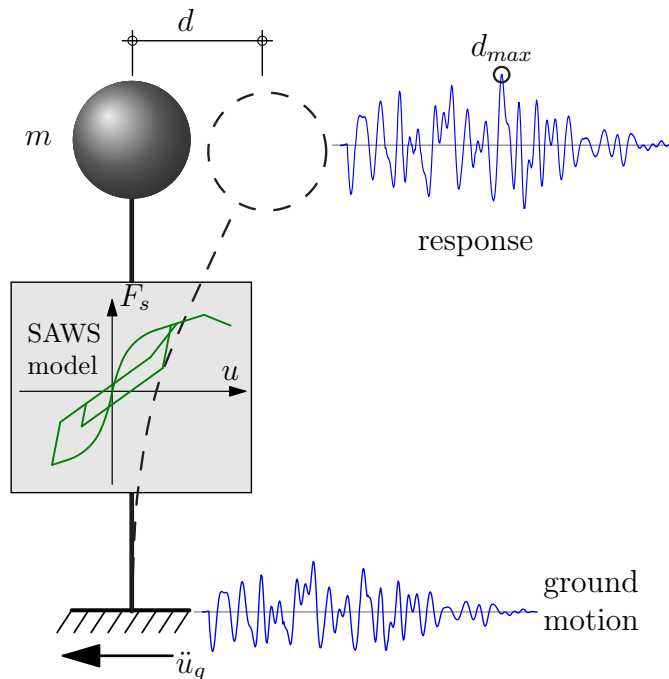
Figure 6.1: Inelastic SDOF system subjected to a specific ground motion

The SAWS hysteretic model is again used to describe the inelastic behaviour. The properties for the hysteretic model will be determined based on the global dynamic response of the reference structure (see section 5.4.2). The hysteretic properties are defined as a function of strength demand F_y, initial stiffness k_{ini} and displacement demand d_m (see below). The quantities F_y, k_{ini} and d_m are determined for the input parameters predefined: reduction factor R_μ, period T and mass m. The SDOF system is subjected to a set of ground motion records. The maximum displacement response d_{max} is computed by means of the NTHA. The displacement d_{max} is used to define the ductility (see section 6.1.3).

Ground motion records

Accelerograms of real earthquakes which are compatible to the elastic response spectrum type 1, soil B were used as seismic action (see Fig. 6.2). A total of 30 records were incorporated into the study. The set of ground motion records as already described in section 5.4.1 was found by comparing the average spectrum of all record with the target spectrum (elastic response spectrum). The tolerance between the average spectrum and target spectrum is less than 10 %.
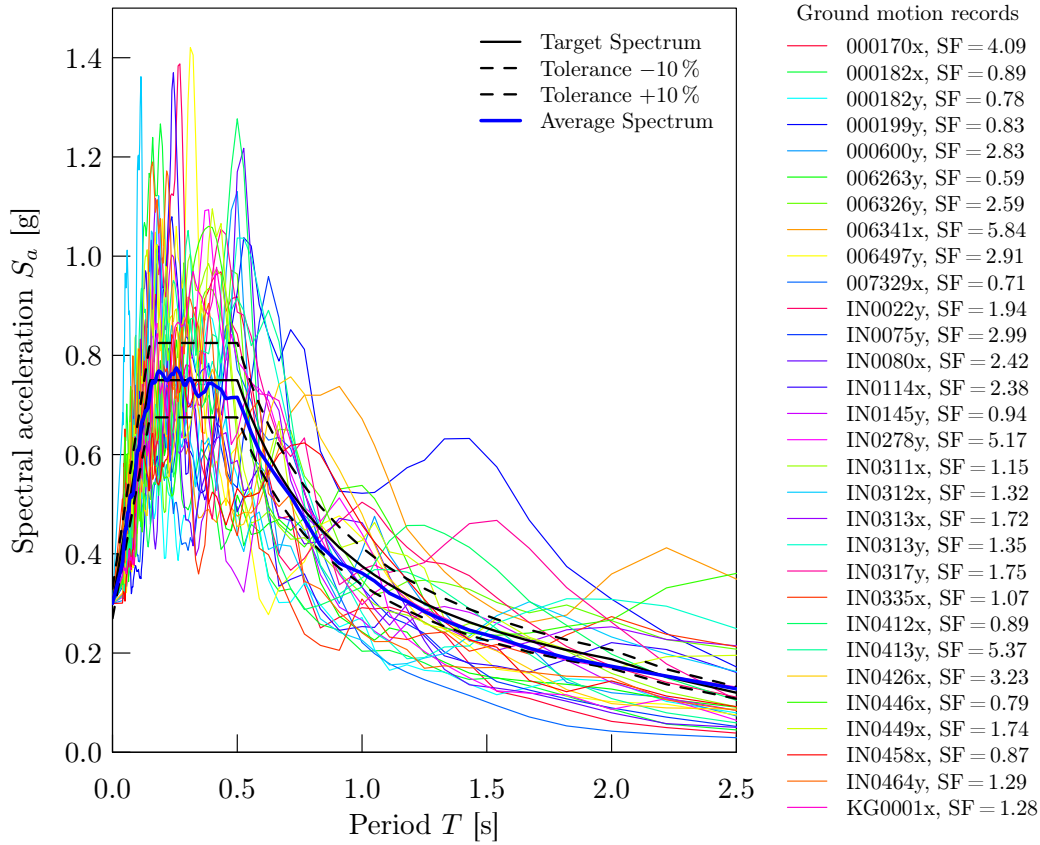
Figure 6.2: Spectra of the ground motion records selected for use in the SDOF study, average spectrum and target spectrum

Details of the ground motion records selected are given in the annex B. Each record was scaled to the PGA of $0.3\,\text{g}$ (cf. Tab. 5.14). The PGA is equal to the acceleration at the zero period. As a period of $0.0\,\text{s}$ is not possible and spectra of ground motion records usually start with a period of $0.01\,\text{s}$, the scale factor SF was determinate by Eq. (6.1).

$$SF = \frac{S_{ae}(T=0.01\,\text{s})}{S_{a,rec}(T=0.01\,\text{s})} \tag{6.1}$$

S_{ae} stands for the spectral acceleration of the elastic response spectrum and $S_{a,rec}$ for the spectral acceleration of the spectrum of the record. The scale factors are given in Figure 6.2.

Strength demand, initial stiffness and displacement demand

Strength demand, initial stiffness and displacement demand are defined based on the input parameters reduction factor R_μ, period T and mass m. The strength demand F_y is calculated by means of the design spectrum. To create the design spectrum (cf. Fig. 5.16), the elastic response spectrum type 1, soil B, was applied, which is scaled by the reduction factor R_μ, where R_μ is set equal to the behaviour factor q. Finally, the strength demand F_y is computed with Eq. (6.2).

$$F_y = S_a(q, T) \cdot m \tag{6.2}$$

The initial stiffness of the SDOF system is determined by Eq. (6.3).

$$T = 2 \cdot \pi \cdot \sqrt{\frac{m}{k_{ini}}} \qquad \rightarrow k_{ini} = \frac{4 \cdot \pi^2}{T^2} \cdot m \tag{6.3}$$

The elastic displacement demand is found using Eq. (6.4) from the elastic response spectrum based on Eq. (2.10).

$$d_m = S_d(T) = \frac{1}{\omega^2} \cdot S_a(T) = \frac{T^2}{4 \cdot \pi^2} \cdot S_a(T) \tag{6.4}$$

The quantities F_y, k_{ini} and d_m are used to define the hysteretic behaviour of the SDOF system.

Inelastic characteristics of the SDOF system

The properties to describe the hysteretic behaviour of the SDOF system were determined based the on results of non-linear time history analyses (see section 5.4) for the two-storey SWE–SWT structure. The dynamic behaviour of the two storey structure is less affected by higher mode effects which show the results from NTHA (see section 5.4.2). Thus, it is assumed that the dynamic response can also be reproduced by an equivalent SDOF system.

Therefore, the global dynamic response of the structure (base shear F_b over top displacement d) is transformed into the response of an equivalent SDOF system using the same relationships as given in section 2.4.3. Again, the basic assumption is that the global response is dominated by one vibration mode. The modal parameters m^* and Γ are computed by Eqs. (2.15) and (2.16) for each time step. Then, the $F^* - d^*$ curve is obtained by the relationships given in Figure 2.15. This is illustrated exemplarily in Figure 6.3 for the SWT-SWE configuration in the Y-direction.

However, it shows that the transformation has some limitations in the range of small lateral displacements. Here, the dynamic response appears to be influenced by higher modes. Nevertheless, the inelastic characteristics are reasonable.
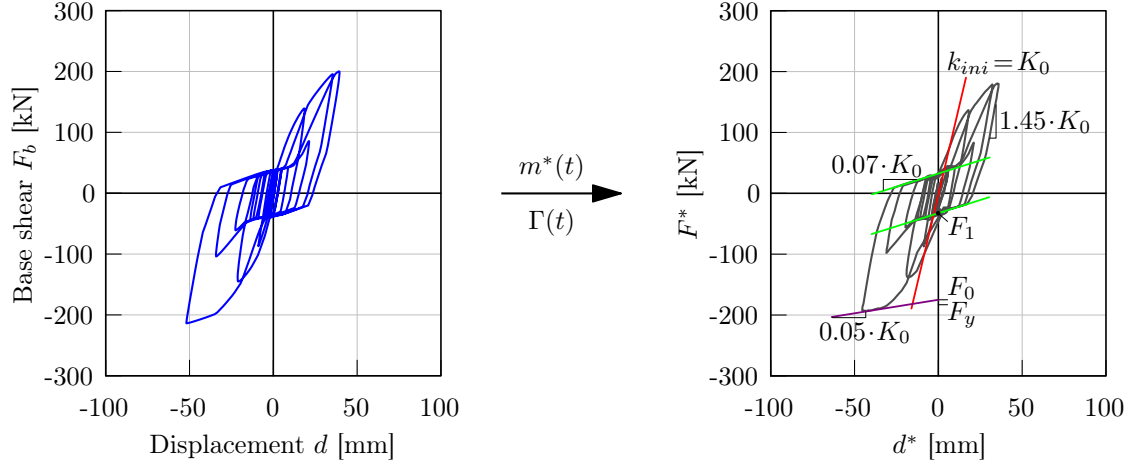
Figure 6.3: Transformation of the global hysteretic response (left) to the response of an equivalent SDOF (right) for the two-storey SWT–SWE structure, excitation in the Y-direction with record IN0075y

Properties for the hysteretic model were determined by means of the $F^* - d^*$ curve, as illustrated in Figure 6.3. The properties which were found are given in Table 6.1. Here the parameters K_0 and F_0 depend on the initial stiffness k_{ini} and the strength demand F_y, respectively. The initial stiffness was determined by Eq. (6.3) and the first period of $T = 0.42$ s for the two-storey SWT-SWE structure in the Y-direction as computed by modal analysis (see sections 5.3.1 and A.3). The mass m is taken into account at 52.5 t, which is the average equivalent mass m^*. The strength demand was obtained by Eq. (6.2), where the spectral acceleration S_a results at 3.68 m/s² (see section A.4) for the first period and $q = 2.0$. This behaviour factor q was used for the preliminary seismic design of CLT structures.

The displacement δ_u is assumed equal to the inelastic displacement demand $q \cdot d_m$. A post-yield stiffness ratio r_1 of 0.05 was derived from the $F^* - d^*$ curve (see Fig. 6.3). It is presumed that the same ratio applies to the post-failure stiffness ($r_2 = -0.05$).

Furthermore, the pinching ratio F_1/F_0 and the parameters for unloading and reloading, r_3 and r_4, could be determined directly with 0.18, 1.45 and 0.07, respectively, from the $F^* - d^*$ curve as illustrated in Figure 6.3. The parameters α and β have been carefully chosen at 0.85 and 1.15, respectively, based on the behaviour of the equivalent SDOF system to account for stiffness and strength degradation.

K_0 [kN/mm]	F_0 [kN]	F_1 [kN]	δ_u [mm]	r_1 [–]	r_2 [–]	r_3 [–]	r_4 [–]	α [–]	β [–]
k_{ini}	$F_y \cdot (1 - r_1)$	$0.18 \cdot F_0$	$q \cdot d_m$	0.05	-0.05	1.45	0.07	0.85	1.15

Table 6.1: Properties of the hysteretic model (SAWS) for CLT structures

It must be noted that VIDIC ET AL. [Vidi94] and MERGOS AND BEYER [Merg15] used a post-yield stiffness ratio r_1 of 0.1. AL-SULAIMANI AND ROESSETT [AlSu85] applied a pinching ratio F_1/F_0 of 0.2 and MERGOS AND BEYER [Merg15] used 0.25 within inelastic SDOF studies. Similar values for r_3 and r_4 were proposed by FILIATRAULT ET AL. [Fili03] and STEWART [Stew87].

The hysteretic properties which were determined based on the behaviour of the equivalent SDOF system will be validated in the following subsection.

Input parameters

The reduction factor R_μ, the period T and the mass m are predefined as input parameters for the study on inelastic SDOF systems. The mass is held constant and was taken into account at $50\,\mathrm{t}$. The parameters R_μ and T were varied as follows:

- reduction factor $R_\mu = 1.0, 1.5, 2.0, 2.5, 3.0, 3.5$ and 4.0, and
- period $T = 0.15, 0.2, 0.3, 0.4, 0.5, 0.6, 0.7, 0.8, 0.9, 1.0, 1.25, 1.5, 1.75$ and $2.0\,\mathrm{s}$.

6.1.2 Validation of inelastic behaviour of the SDOF system

In order to validate the inelastic behaviour of the SDOF system, the input parameters were applied consistently with the analysis on the building level and modal transformation for the two-storey SWE-SWT structure: $q=2.0$, $T=0.42\,\mathrm{s}$ and $m=m^*=52.5\,\mathrm{t}$. The hysteretic properties were determined using the definitions in Table 6.1. The same ground motion record – ID IN0075y – was used to compute the dynamic response. Mass proportional damping was incorporated to account for viscous damping, see Eq. (2.5). The damping ratio was set to $5\,\%$, as commonly included in the elastic response spectrum. The inelastic responses of the SDOF system were recorded in terms of displacement amplitude d and reaction force F.

It can be observed from Figure 6.4 that the properties derived can basically reproduce the global hysteretic behaviour. However, the deflection is slightly underestimated. That difference can be traced back to the damping model. Stiffness and mass proportional damping was applied in the analyses on the building level. Only stiffness or mass proportional damping can be considered for the SDOF system. Mass proportional damping has been chosen for the SDOF study, because stiffness proportional damping leads to a significant overestimation of the displacement capacity. However, mass proportional damping causes a stronger reduction of the displacement amplitudes. In terms of energy conservation, the SDOF system performs quite well, but underpredicts the cumulated energy slightly for reasons aforementioned.

Overall, the damping and hysteretic model chosen in combination with the properties derived yield a conservative estimate of the inelastic behaviour of an equivalent SDOF system.

6.1.3 Results of the SDOF study

Non-linear time history analyses of the SDOF system were carried for each set of parameters. The combination of ground motion record, predefined reduction factor and period are depicted in Table 6.2. Again, $5\,\%$ viscous damping is taken into account using mass proportional damping.

The absolute displacement amplitude was taken from the results of NTHA as maximum displacement d_{max} (cf. Fig. 6.4a) to determine the displacement ductility μ with Eq. (6.6). The yield displacement d_y is computed by Eq. (6.5).

$$d_y = \frac{F_y}{k_{ini}} \tag{6.5}$$

$$\mu = \frac{d_{max}}{d_y} \tag{6.6}$$

119
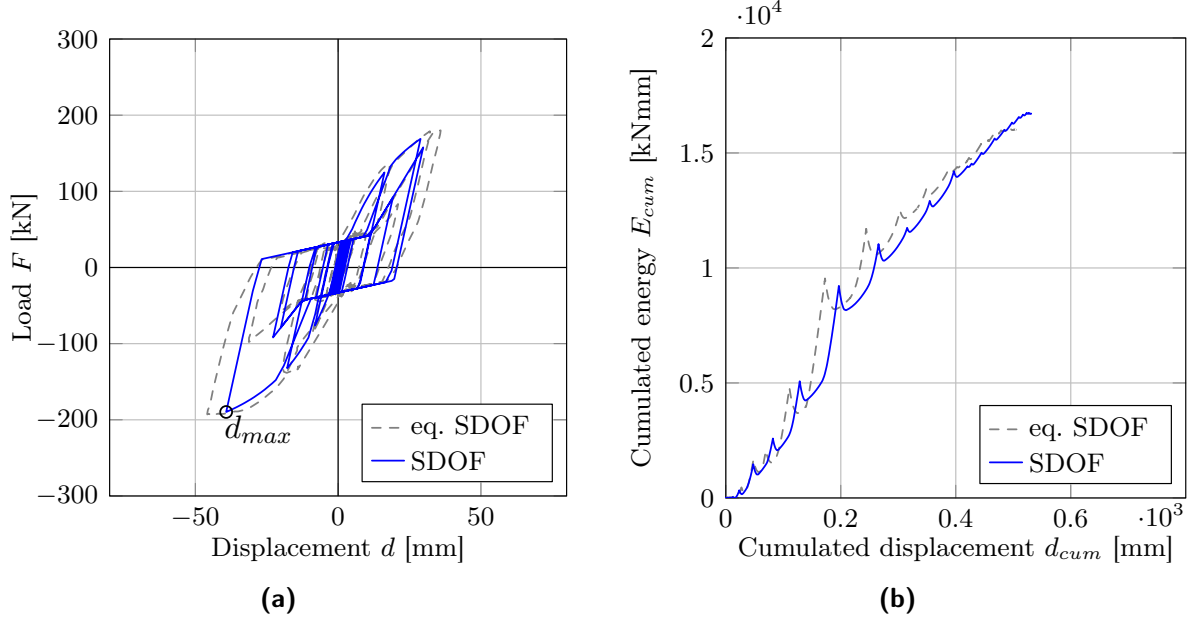
Figure 6.4: Comparison of the inelastic behaviour of the equivalent SDOF system and the SDOF system – (a) hysteresis and (b) cumulated energy

number of records	30
number of reduction factors R_μ	7
number of periods T	14
total	2940

Table 6.2: Combination of parameters

In total, a database of 2940 ductility values was obtained. The mean and median value for each $R_\mu - T$ combination over the corresponding 30 ductility values from the 30 ground motion records were determined. Based on the median values, an analytical relationship between reduction factor R_μ, period T and ductility μ was derived. It was aimed at a similar format of the formula as that which was proposed by VIDIC ET AL. [Vidi94] (see section 2.5.2). However, different coefficients were introduced to account for the characteristics of CLT constructions. The inverse form of the $R_\mu-\mu-T$ relationship is given in Eqs. (6.7) to (6.9).

$$\mu = 1 + c_1 \cdot (R_\mu - 1)^{c_2} \cdot \frac{T_0}{T} \qquad\qquad \text{for } T < T_0 \tag{6.7}$$

$$\mu = 1 + c_1 \cdot (R_\mu - 1)^{c_2} \qquad\qquad \text{for } T \geq T_0 \tag{6.8}$$

$$T_0 = c_3 \cdot T_C \tag{6.9}$$

The coefficients c_1, c_2 and c_3 are empirical parameters which had been iteratively determined. The period T_C is the "corner period" of the elastic response spectrum (cf. Fig. 6.2) and T_0 represents the transient period similarly defined by VIDIC ET AL. [Vidi94] (see section 2.5.2). The coefficients which produce the best correlation with the ductility values provided by the SDOF study are given in Table 6.3. Two sets of coefficients are provided. Why a second coefficient set might be reasonable is discussed below. The $R_\mu-\mu-T$ relationship of the N2 method according to [EN 1998-1] used currently was included in

Table 6.3 for comparison. The formula of [EN 1998-1] is equivalent to Eqs. (6.7) to (6.9) if the coefficients c_1, c_2 and c_3 are set to 1.0. The approaches are compared by means of the mean and median values of the ratio μ_{SDOF}/μ_{approx}. The factor μ_{SDOF} corresponds to the ductility values from the SDOF study and μ_{approx} relates to the approximation according to Eqs. (6.7) to (6.9). The mean and median values are closer to 1.0 for coefficient sets 1 and 2 than for the EC 8 formula. The first set even yields a median value of 1.0 and gives the best coefficient of determination. By means of the coefficient of variation – which is standard deviation divided by the mean value – it is observed that dispersion of the ratio μ_{SDOF}/μ_{approx} is slightly lower for coefficient sets 1 and 2 than for the EC 8 formula.

coeff. set	coefficients			mean	median	standard deviation	coefficient of variation	coefficient of determination
	c_1	c_2	c_3	$\dfrac{\mu_{SDOF}}{\mu_{approx}}$	$\dfrac{\mu_{SDOF}}{\mu_{approx}}$	$\dfrac{\mu_{SDOF}}{\mu_{approx}}$	$\dfrac{\mu_{SDOF}}{\mu_{approx}}$	R^2
1	0.45	1.45	1.45	0.98	1.00	0.15	0.15	0.98
2	0.80	1.20	1.00	0.86	0.88	0.13	0.15	0.96
EC 8	1.00	1.00	1.00	0.81	0.81	0.13	0.16	0.96

Table 6.3: Values derived for coefficients c_1 to c_3 and summary for the ratio of ductility from the SDOF study and empirical formula

(a) coefficient set 1   **(b)** coefficient set 2
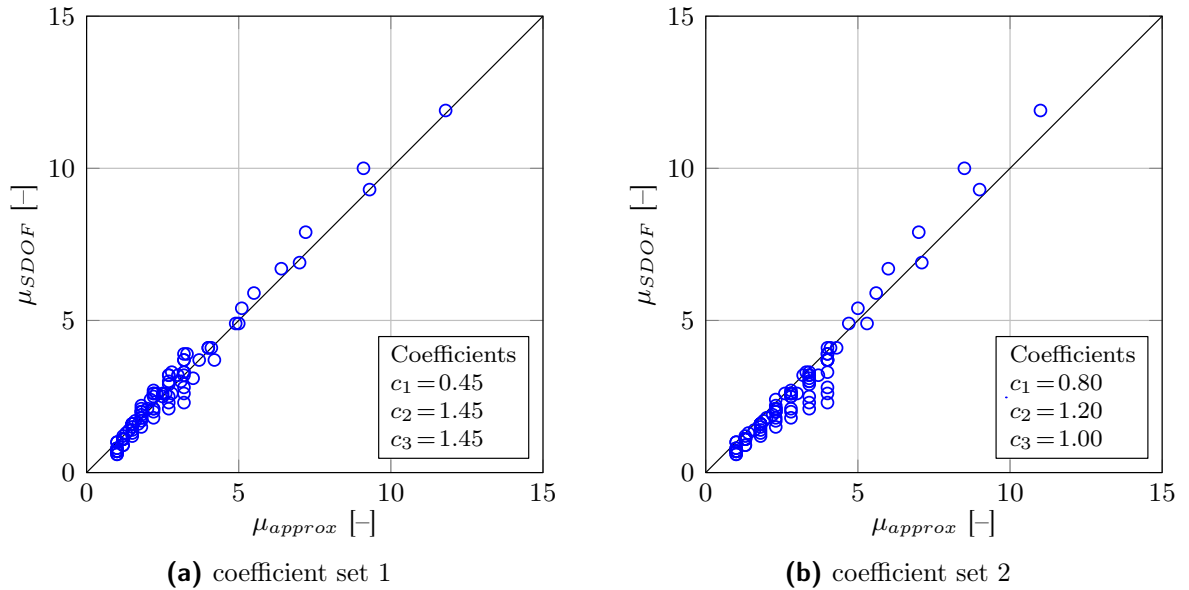
Figure 6.5: Correlation between ductility values from the SDOF study and the empirical approximation

Figure 6.5 depicts the correlations for the two sets of coefficients. The correlations appear reasonable for both sets. However, the first coefficient set yields a better agreement with the ductility values of the SDOF system, especially in the ductility range of 0 to 5. In this ductility range, only the maximum ductility values can be reproduced by means of coefficient set 2 (see Fig. 6.5b). This implies that the ductility available might be overpredicted. The mean and median values of the ratio μ_{SDOF}/μ_{approx} also indicates this (see Tab. 6.3).

However, it was noticed that the inelastic SDOF model applied slightly underpredicts the deformation capacity available (see Fig. 6.4a). It can be expected that maximum displacement d_{max} is indeed higher. As a consequence the displacement ductility would also be increased. Thus, it is deemed uncritical that the second set of coefficients leads to slightly higher values in the ductility range of 0 to 5 in comparison to the values from the SDOF study.

To obtain the reduction factor R_μ for a given ductility, Eqs. (6.7) and (6.8) can be rewritten as follows:

$$R_\mu = 1 + \left[\frac{\mu - 1}{c_1} \cdot \frac{T}{T_0} \right]^{1/c_2} \qquad \text{for } T < T_0 \qquad (6.10)$$

$$R_\mu = 1 + \left[\frac{\mu - 1}{c_1} \right]^{1/c_2} \qquad \text{for } T \geq T_0. \qquad (6.11)$$

The transition period T_0 is determined using Eq. (6.9).

(a) coefficient set 1   **(b)** coefficient set 2
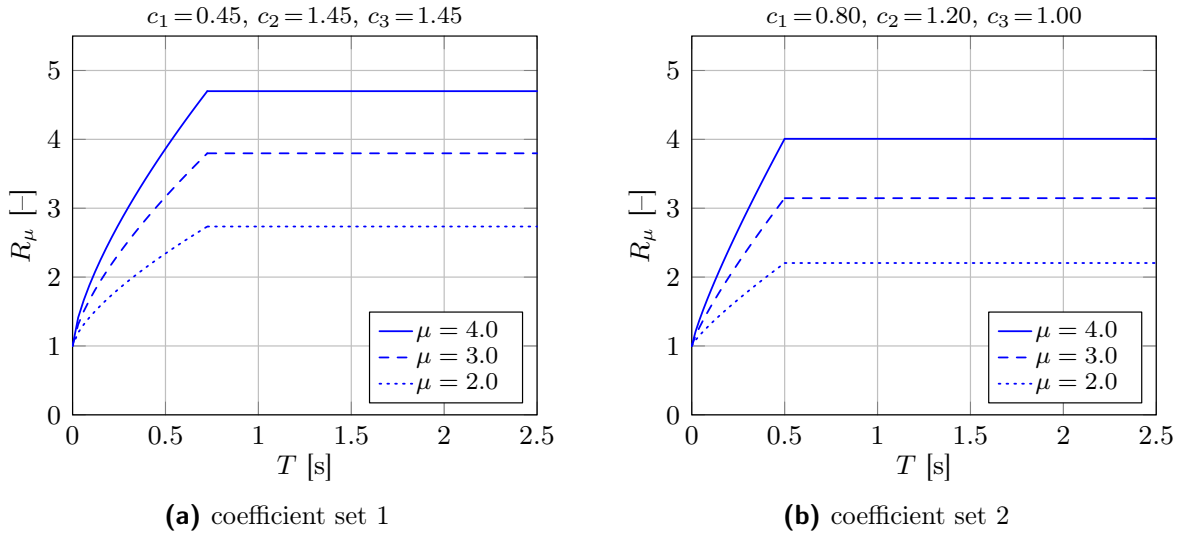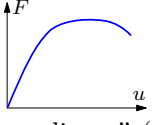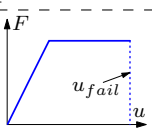
Figure 6.6: Spectra of the reduction factor R_μ for three ductility levels

Figure 6.6 shows the spectra of the reduction factor for different ductility values. It can be noticed that the reduction factor even exceeds the ductility ratio at a certain period. However, it is a physical condition that the reduction factor becomes equal to the ductility for high periods T – equal displacement approach $R_\mu = \mu$ [Mira94]. For that reason, it should be suitable to use the formula with the coefficients $c_1 = 0.8$, $c_2 = 1.2$ and $c_3 = 1.0$. Figure 6.6b shows that the equal displacement approach is nearly fulfilled. A further advantage might be that this formulation is more consistent with the formula as proposed in [EN 1998-1] annex B, since the transition period T_0 becomes equal to the "corner" period T_C. Only two parameters would be needed to adopt the current $R_\mu - \mu - T$ relationship.

The new $R_\mu - \mu - T$ relationship, as depicted in Figure 6.6b, will be used to carry out DBD of CLT structures (see section 6.5). The performance of the new approach will be compared with the N2 method according to [EN 1998-1] and the capacity spectrum method (CSM) according to [ATC-40].

6.2 Structural model

The reference structures, as presented in section 5.3, form the basis for non-linear pushover analysis. The same structural models were taken with respect to shell elements, contact conditions and gravity loads. However, two main spring characteristics were considered to account for the inelastic connector behaviour (see Tab. 6.4). The notation of the spring types relates to the section 5.1.1.

analysis procedure	notation	spring types				properties
non-linear static	F ⟋ "non-linear" (nl) pushover curve	g	h			$\underbrace{K_0,\ F_0}$, δ_u, r_1, r_2 from Tables 5.4 and 5.5 modified by Eq. (5.8)
				d	b	
simplified non-linear static	F u_{fail} "bilinear" (bl) pushover curve	e[1]	f[1]			K_y, $u_y^+ = |u_y^-|$ as mean of k_{ini}, u_y of positive and negative backbone from Tables 4.1 and 5.6
[1] deformation limit u_{fail} defined by a min-max barrier with u_u from Tables 4.1 and 5.6						

Table 6.4: Specification of analysis types and input parameters for pushover analysis

The SAWS model is adopted here to provide non-linear load-displacement characteristics for monotonic loading. The non-linear backbone curve is described by the parameter K_0, F_0, δ_u, r_1 and r_2. The related properties are given in Tables 5.4 and 5.5. Bilinear springs were implemented for simplified non-linear analysis . The properties of the bilinear springs are given in Tables 4.3b and 5.6. Stiffness and deformation characteristics, which were derived by the two approaches K & Y and EEEP, have been included for further evaluation. In order to account for deformation limits of connectors, a "min-max barrier" was defined for each spring using the ultimate displacement values u_u, as given in Tables 4.3b and 5.6. If the relative displacement of a certain spring reaches the displacement limit, the strength drops down to zero.

Average values are used for configurations which provide stiffness and displacement values of the positive (pos) and the negative (neg) backbone curve (see Tabs. 4.3b and 5.6).

$$K_y = \frac{k_{ini,pos} + k_{ini,neg}}{2} \tag{6.12}$$

$$u_y^+ = \frac{u_{y,pos} + u_{y,neg}}{2} \tag{6.13}$$

$$u_{fail} = \frac{u_{u,pos} + u_{u,neg}}{2} \tag{6.14}$$

Non-linear static analyses are performed to have a clear basis for comparison with results from NTHA. Static analyses with bilinear springs are adopted with a focus on the application in engineering practice. Whether the integration of comparatively simple load-displacement relationships for the connectors can also lead to a proper displacement-based design is investigated here. That would ease DBD significantly for engineers in practice. Both "non-linear" pushover curves (obtained with non-linear spring behaviour)

and 'bilinear' pushover curves (obtained with bilinear spring behaviour) are incorporated for DBD (see section 6.3).

It was demonstrated in section 5.4.2 that the consideration of friction changes the dynamic response of CLT structures significantly. However, it must be noted that only the amount of friction in the connection between CLT slab and CLT wall at the bottom could be quantified (see section 5.2). Reasonable friction coefficients were chosen for the connection between concrete basement and the CLT wall (ground floor) and for the connection between CLT slab and the CLT wall on the top. These friction coefficients applied could not be validated by means of test results. A validation of these friction properties would be necessary to be able to understand the main effects and to draw some general conclusions. On the other hand, friction is not usually considered when designing a structure, since the amount of friction is hardly quantifiable. Detailing aspects – for example, the location of interlayers in the contact area between wall and slab for reasons of building physics – can lead to a significant reduction of friction.

With reference to the $R_\mu - \mu - T$ relationships, it is extremely difficult to capture a varying magnitude of friction throughout the building within a single formulation. Thus, the contribution of friction was not further evaluated within DBD.

6.3 Pushover analysis

This section deals with pushover analyses which were carried out as the first step of DBD. Pushover analyses have been performed to obtain the global non-linear load-displacement characteristics. The global behaviour is represented by the capacity curve with the base shear F_b over the top displacement d as described in section 2.4.3.

6.3.1 Load pattern

The capacity curve is determined for external horizontal forces which should represent the inertia forces under earthquake excitation. Since the multiple distributions of inner forces of the height of a building are possible (see section 5.4.2) the two lateral load distributions – uniform pattern and linear pattern – have been applied (see section 2.4.3).

$$F_i = \frac{s_i \cdot m_i}{\sum s_j \cdot m_j} F_b \qquad \begin{array}{ll} \text{uniform:} & s_{i/j} = 1 \\ \text{linear:} & s_{i/j} = z_{i/j} \end{array} \qquad (6.15)$$

with $m_{i/j}$ lumped mass in level i/j (see Fig. 6.8)
          $z_{i/j}$ height in level i/j of the building

The uniform load pattern is representative if the global response is dominated by the deformations shear and slip of the shear walls. The linear load pattern accounts for combined deformation characteristics – bending, rocking, shear and slip.

The lateral loads are applied at the reference points (see section 5.3.1) in the main directions X and Y separately (see Fig. 6.8).
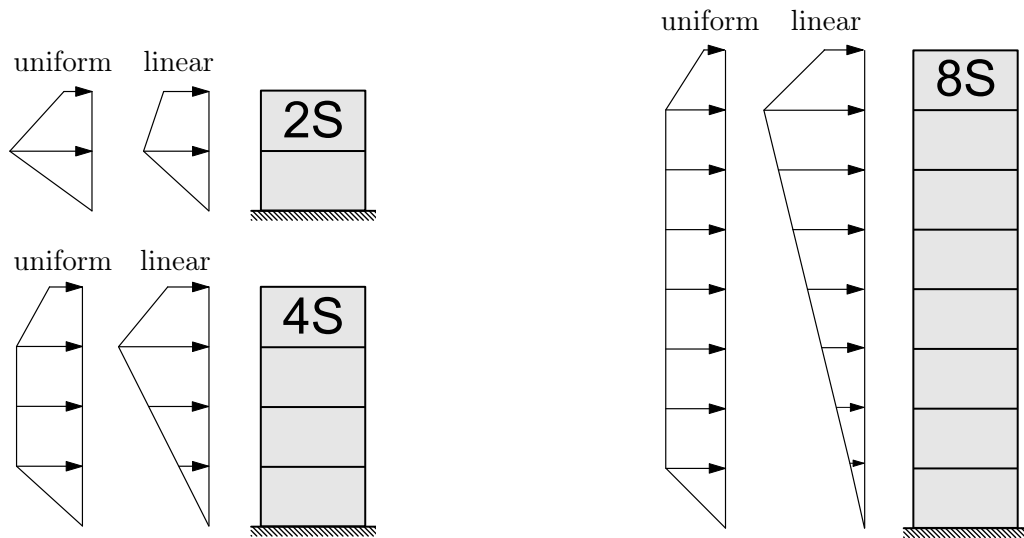
Figure 6.7: Load patterns for pushover analysis of the two-, four- and eight-storey building
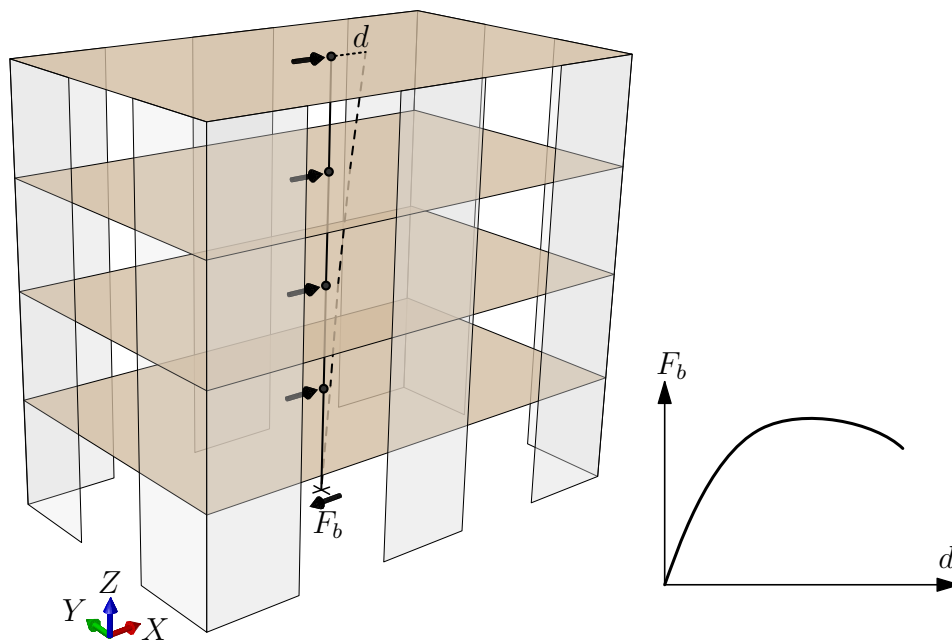
Figure 6.8: Illustration of the application of lateral loads at the reference points in the X-direction of the four-storey building

6.3.2 Controlling and recording loads and displacements

Similar to the THA, the gravity loads were again applied first and were held constantly during the application of lateral loads. Lateral loads were applied displacement controlled. This means that the lateral loads are increased in proportion to the predefined load pattern until a specific displacement at the control node is reached. The reference point at the roof slab was chosen as control node. Adaptive displacement steps were defined to optimise the speed and convergence behaviour of the analysis. The analysis starts with larger displacement steps of 5 to 10 mm depending on the height of the building and decrease down to 1 mm per step when the base shear is in the range of the load-bearing capacity or even beyond that. The convergence tolerance η_E was set to 10^{-4} and must be reached within 1000 iteration steps (see section 5.4.1). The analysis stopped automatically when the base shear dropped down to nearly 80 % of the maximum load after reaching the load bearing capacity or when a deformation limit of a connector is achieved.

The base shear F_b and the lateral displacements u_i at reference points in each level were recorded during the analysis. The base shear was determined as the sum of all reactions forces in the direction of load application. The top displacement $d = u_n$ is used to create the capacity curve (see Fig. 6.8). The horizontal displacements in lower levels are used for modal transformation of the capacity curve (see section 6.6.1).

6.3.3 Results of pushover analysis

Figures 6.9 and 6.10 present the results from the pushover analysis with full non-linear behaviour. Friction was not considered in the determination of the capacity curves. Furthermore, only screws which were not inclined were used for the screw connections.

The capacity curves illustrate the influence of the load patterns and the different configurations on the global non-linear behaviour. The application of the uniform load pattern leads to a higher maximum base shear associated with lower deformation capacity in comparison to the linear load pattern. This effect is more pronounced for the four-storey and the eight-storey building particularly in the X-direction. In the case of the two-storey building the influence of the load pattern is less significant. That is also true for the different structural configurations. With increasing number of storeys, the use of continuous walls with openings (CWO) yields a significantly lower deformation capacity for the buildings with four and eight storeys but not really to an increase of the load-bearing capacity. However, the load-bearing capacity is higher if perpendicular walls are connected to each other (BT). Even the deformation capacity is increased against the SWT configuration.

The bilinear load-displacement relationship (see Tab. 6.4) has been applied for pushover analysis for a potential simplification of DBD. Exemplarily, results from "non-linear" and "bilinear" pushover analyses which were derived for the linear load pattern are compared in Figure 6.11. As mentioned above the two approaches, K & Y and EEEP, which were used for consistent bilinearisation (see sections 4.1, 4.2 and 5.1.3) have been included. It shows that reasonable capacity curves could be achieved, even for simple bilinear spring behaviour, which almost match the "non-linear" pushover curves. However, it is noticeable that the deformation capacity is lower. Nevertheless, the application of bilinear springs with properties which were derived by the K & Y approach leads to a better agreement with "non-linear" pushover curves referring to load bearing capacity and deformation capacity compared to the EEEP approach.
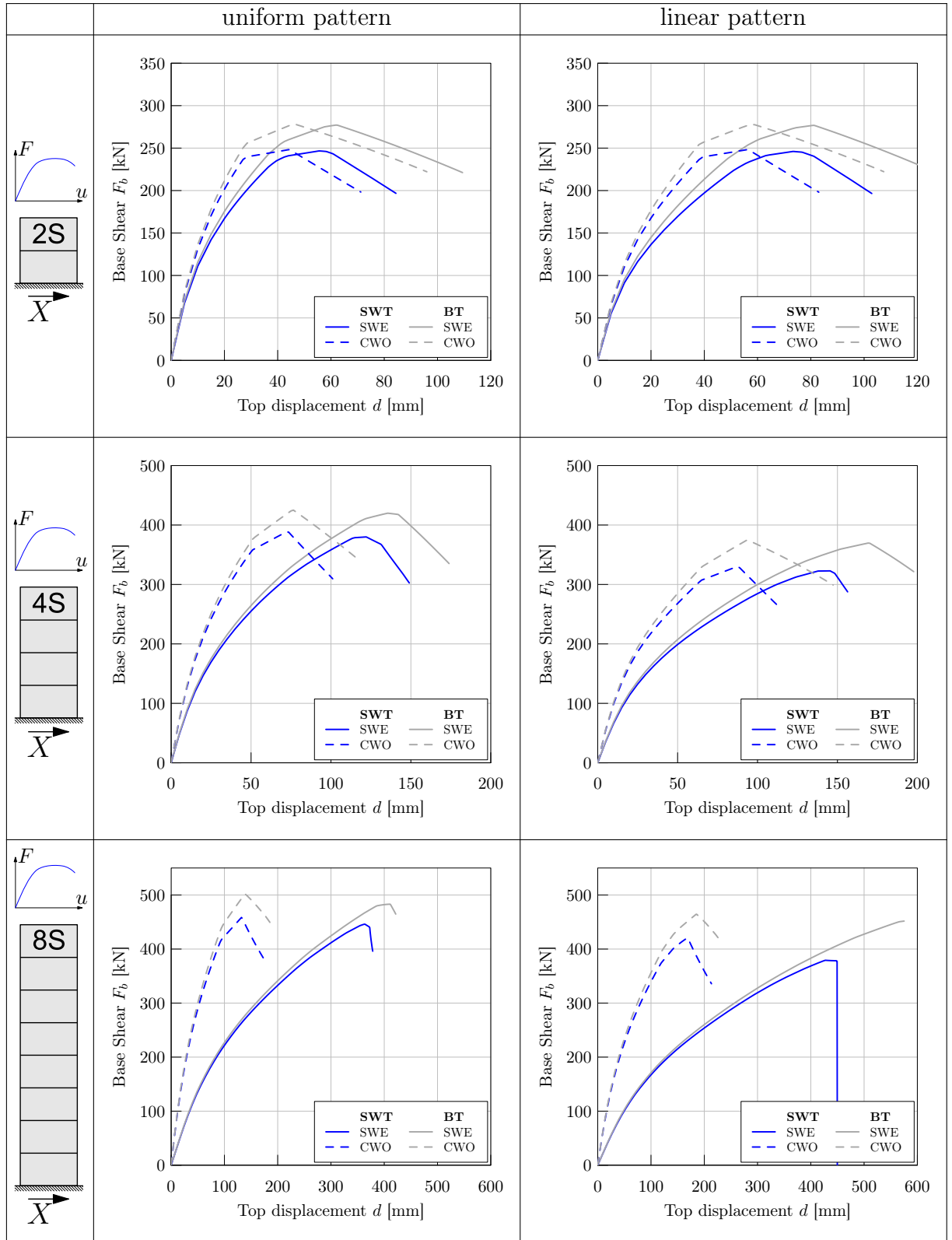
Figure 6.9: Capacity curves from non-linear pushover analysis in the X-direction, without friction
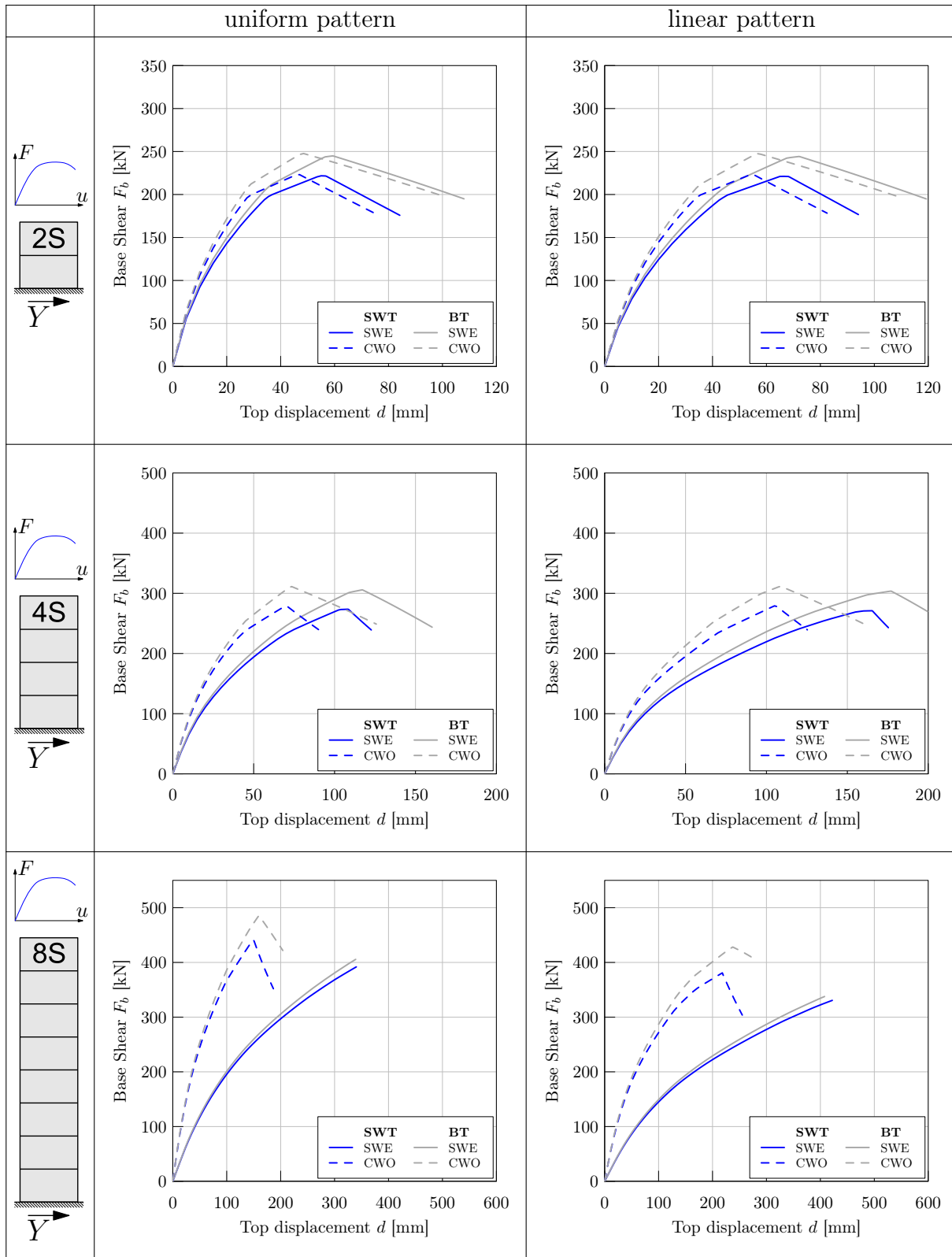
Figure 6.10: Capacity curves from non-linear pushover analysis in the Y-direction, without friction
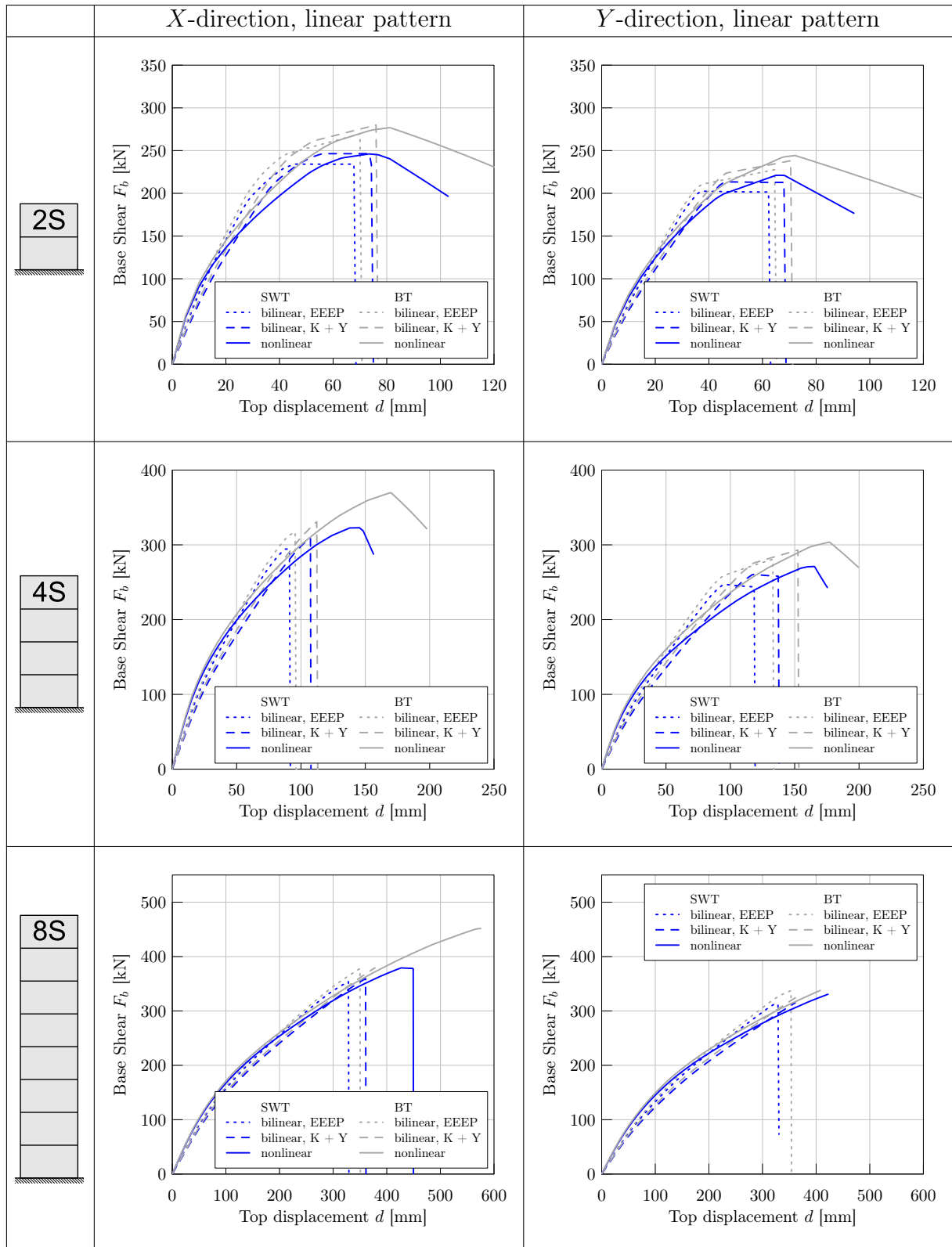
Figure 6.11: Capacity curves – comparison of "non-linear" and "bilinear" pushover curves, without friction

6.4 Transformation of capacity curves

An important step in DBD is the transformation of the capacity curve into a capacity spectrum. This transformation is required to draw the capacity curve into the S_a–S_d diagram (see section 2.4.3). The procedure of the transformation is illustrated in Figure 2.15. The deflection shape – horizontal displacements u_i in level i – corresponding to the load pattern chosen is used to drive the modal parameters m^* and Γ according to Eqs. (2.15) and (2.16). Exemplarily, the deflection shape of the four-storey building (see Fig. 6.8) is shown in Figure 6.12. The deflection shape is normalised by means of Eq. (6.16).

$$\phi_i = \frac{u_i}{d} \tag{6.16}$$

The lumped masses as documented in Table 5.14 are applied to determine the mass of the equivalent SDOF system m^* and the participation factor Γ (see Fig. 6.12).

$$m^* = 14.9{\cdot}1.00 + 42.6{\cdot}0.77 + 42.6{\cdot}0.41 + 42.6{\cdot}0.19 = 73.3$$

$$\Gamma = \frac{73.3}{14.9{\cdot}1.00^2 + 42.6{\cdot}0.77^2 + 42.6{\cdot}0.41^2 + 42.6{\cdot}0.19^2} = 1.52$$
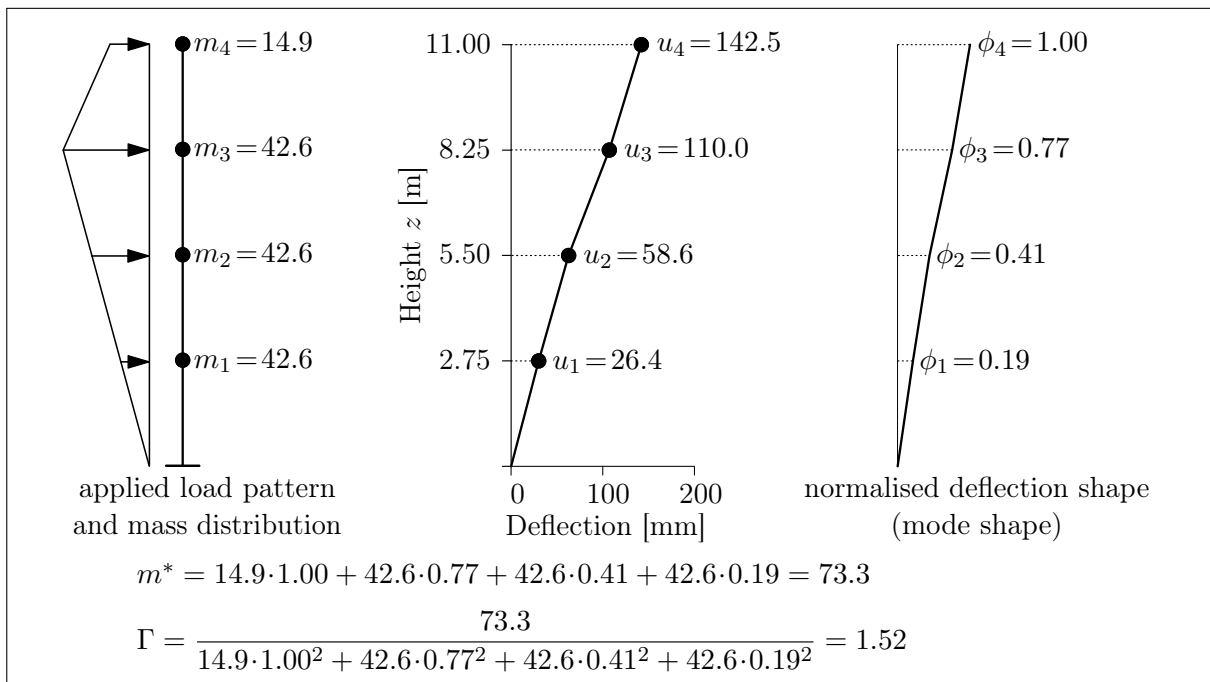
Figure 6.12: Determination of modal parameters for the four-storey SWT–SWE structure (see Fig. 6.8) in the X-direction and linear load pattern

The spectral values of acceleration S_a and displacement S_d were computed with Eqs. (2.18) and (2.19), respectively.

It must be noted that the transformation has been based on the deflection shape at maximum base shear F_b. However, the modal parameters can vary throughout several strength levels due to different deformation characteristics. Consequently, the capacity spectra derived were used in the initial step of DBD. If the strength demand required differs significantly from $F_{b,max}$ or the normalised deflection shape changes, modal parameters were recalculated and the capacity spectrum was revised with the design process (see section 6.5).

The non-linear capacity spectrum is idealised to a bilinear one for the application of the N2 method, as illustrated in Table 2.5. The yield displacement d_y^* is found by using Eq. (2.28). The bilinear idealisation is connected with the determination of the performance point (see section 6.5). The non-linear capacity spectrum does not have to be idealised for the capacity spectrum method.

6.5 Demand spectra and performance points

The determination of the performance point depends on the generation of the demand spectrum and vice versa. The basic steps of this procedure have already been presented in section 2.4.3 with reference to CSM and N2 method. Overall, four different ways to determine the performance point were incorporated for the evaluation of DBD for CLT structures (see Tab. 6.5).

method	demand spectrum	relationship	ref.
N2	inelastic spectrum	$R_\mu - \mu - T$ relationship EC 8	Table 2.5
N2	inelastic spectrum	$R_\mu - \mu - T$ relationship CLT	Section 6.1
CSM	damped spectrum	effective damping ξ_{eff} [ATC-40]	Table 2.5
CSM	damped spectrum	constant effective damping ξ_{eff}[1]	Section 4.3

[1] constant hysteretic damping derived from results of wall element testing

Table 6.5: Overview of the methods considered for the definition of the demand spectrum and the determination of the performance point

Both the N2 method representing the approach with inelastic spectra and CSM using damped spectra were included in the study. In addition to the "standard" procedures according to [EN 1998-1] and [ATC-40], two additional relationships to build the demand spectrum were considered.

As an alternative to the $R_\mu - \mu - T$ relationship which is used in [EN 1998-1], the new approach presented in section 6.1 is adopted. This relationship accounts for the characteristic hysteretic behaviour of CLT structures in terms of pinching as well as stiffness and strength degradation. The [ATC-40] document provides an effective damping relationship for the application of CSM, where the contribution of hysteretic damping ξ_{hyst} (equivalent viscous damping) depends on the spectral displacement (see Tab. 2.5). It might be an acceptable simplification to apply constant hysteretic damping for DBD of low- or mid-rise buildings.

Inelastic spectra

The inelastic spectrum is determined following the procedure illustrated in Figure 6.13. Initially, a reasonable value of the displacement of an equivalent SDOF system at plastic mechanism d_m^* is chosen for the capacity spectrum. The yield displacement of an equivalent SDOF system d_y^* is then determined to idealise the non-linear capacity spectrum by an equivalent bilinear one. The reduction factor R_μ and the ductility μ are calculated next. The ductility μ available results from the $R_\mu - \mu - T$ relationship applied. The formulae (6.7) to (6.9) with the coefficients $c_1 = 0.8$, $c_2 = 1.2$ and $c_3 = 1.0$ were applied to account for the characteristics of CLT structures (see section 6.1). Finally, whether the displacement d_m^* is consistent with the target displacement d_t^* as the product of yield displacement and ductility available must be checked. The procedure was repeated as long as the displacement d_m^* differs more than $5\,\%$ from the target displacement d_t^*. This procedure is equivalent to the iterative method proposed in annex B of [EN 1998-1].

$$\boxed{\text{Chose displacement } d_m^*}$$

$$\downarrow$$

$$\boxed{\text{Determine yield displacement } d_y^* \text{ with Eq. (2.28)}} \longleftarrow$$

$$\downarrow$$

$$\boxed{\text{Determine reduction factor } R_\mu \text{ with Eqs. (2.27) and (2.29)}}$$

$$\downarrow$$

$$\boxed{\begin{array}{c} \text{Determine ductility } \mu \text{ for} \\ \text{N2M, EC8: with Eqs. (2.30) and (2.31)} \\ \text{N2M, CLT: with Eqs. (6.7) to (6.9)} \end{array}} \quad \begin{array}{c} \text{Set} \\ d_m^* = d_t^* \end{array}$$

$$\downarrow$$

$$\boxed{\text{Determine target displacement } d_t^* = d_y^* \cdot \mu}$$

$$\downarrow$$

$$\left\langle \begin{array}{c} 0.95 \cdot d_m^* \leq d_t^* \leq 1.05 \cdot d_m^* \\ ? \end{array} \right\rangle \quad \text{NO}$$

YES $\downarrow$

$$\boxed{\text{Determine inelastic spectrum with Eqs. (2.25) and (2.26)}}$$
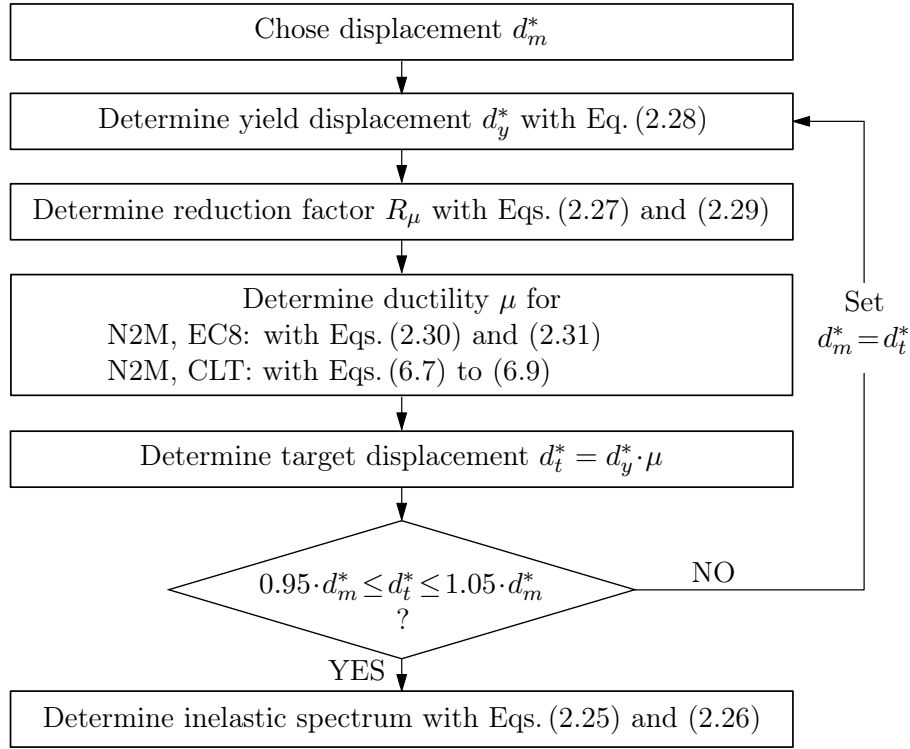
Figure 6.13: Procedure to create the inelastic spectrum, N2 method

Damped spectra

The fundamentals given in Table 2.5 has been used for the determination of the damped spectrum according to [ATC-40]. A transition curve was created first to avoid iteration while finding the performance point. The transition curve represents the damped spectrum which is built by calculating damped values of spectral acceleration S_a for multiple spectral displacements S_d of the capacity spectrum with Eqs. (2.20) to (2.23). The procedure refers to the one presented by HOLTSCHOPPEN [Holt09] and was adapted for application to timber structures as illustrated in Figure 6.14.

The following steps are required for each sampling point P_i:

- The non-linear capacity spectrum is idealised by a bilinear one as illustrated in Table 2.5.
- The yield point – defined by the spectral values $S_{a,y}$ and $S_{d,y}$ – results from the energy equivalency of the bilinear curve with the non-linear capacity curve.
- Equivalent viscous damping $\xi_{eq,i}$ is calculated with Eq. (2.24).
- Effective damping $\xi_{eff,i}$ is determined with Eq. (2.23).
- The damping correction factor η_i is calculated with Eq. (2.23) and $\xi = \xi_{eff,i} \, [\%]$.
- The spectral values of the damped spectra $S_{a,i}$ and $S_{d,i}$ are determined with Eqs. (2.20) and (2.21).

A definition of the initial stiffness respectively initial period is required for the determination of the yield point. It is commonly assumed for timber structures that the behaviour is fairly elastic until 40 % of the maximum load-bearing capacity is reached [EN 12512; EN 26891; ISO 16670; ISO 21581]. This approach has been used to define the initial period T_{ini}, as illustrated in Figure 6.14.

The modification factor κ was set to 0.33 to account for hysteretic behaviour with pinching according to [ATC-40] for the determination of effective damping ξ_{eff}. Again, 5 % nominal damping ξ_0 was applied (cf. section 5.4.1).

The points of spectral acceleration of each damped spectrum that corresponds to the spectral displacements $S_{d,Pi}$ were connected to the transition curve.

$$\xi_{eq,i} = \frac{2}{\pi} \cdot \frac{S_{a,y} \cdot S_{d,Pi} - S_{d,y} \cdot S_{a,Pi}}{S_{a,Pi} \cdot S_{d,Pi}} \quad \Longrightarrow \quad \eta_i = \sqrt{\frac{10}{5 + \xi_{eff,i}}} \geq 0.55 \quad \Longrightarrow \quad \begin{aligned} S_{a,i} &= S_{ae}(\eta_i), \\ S_{d,i} &= \frac{T^2}{4 \cdot \pi^2} S_{ae}(\eta_i) \end{aligned}$$

$$\xi_{eff,i} = \xi_0 + \kappa \cdot \xi_{eq,i}, \quad \kappa = 0.33$$
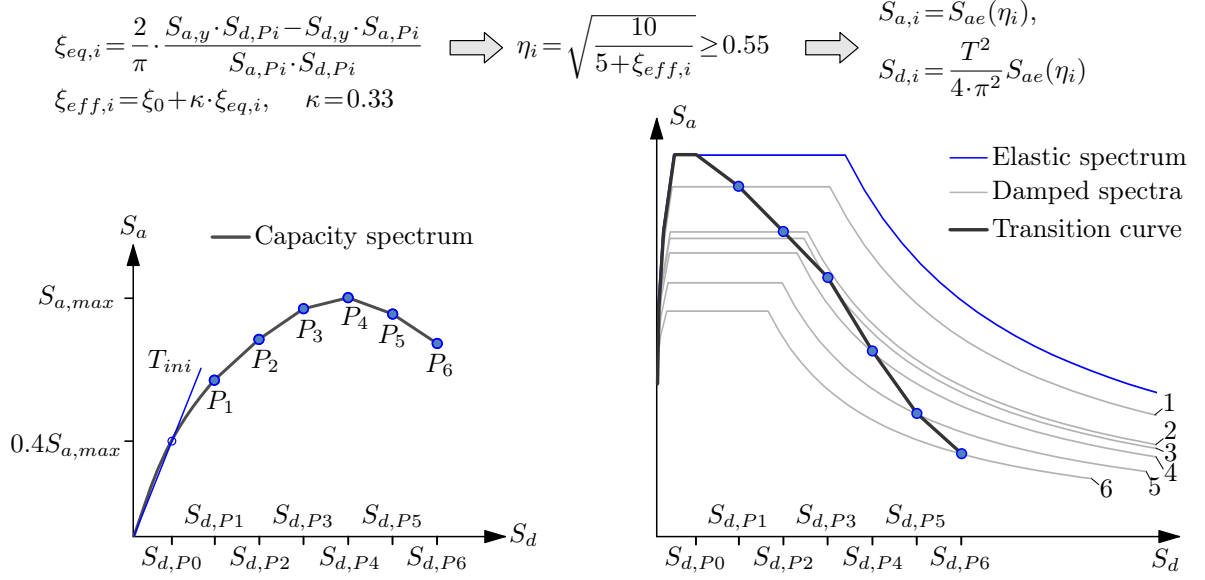
Figure 6.14: Determination of the damped spectrum as transition curve; example with six sampling points

The values of hysteretic damping for the constant damping approach were derived from testing of CLT wall elements (see section 4.3). As constant hysteretic damping cannot account for all characteristics of CLT structures a conservative damping value for hysteretic damping was applied. With reference to damping values from wall element testing (see section 4.3) it seems reasonable to take 10 % hysteretic damping into account. Thus, constant effective damping is 15 % considering 5 % viscous damping and the demand spectrum is determined with $\xi = 0.15$ and Eq. (2.22).

Application

The four procedures were applied to the reference building for different configurations. The capacity curves, as given in Tables 6.9 and 6.10, have been used for DBD where the two load patterns are considered for comparison. The determination of the performance point as an intersection between the demand spectrum and the capacity spectrum is illustrated in Figures 6.15 to 6.17. The performance points are highlighted by coloured circles. There are cases where a performance point could not be found and then the circular mark was assigned with "fail" in the legend.

The determination of performance points is illustrated for some selected examples. Performance points for all configurations of the reference structure and the two load patterns are documented in annex C in Figures C.1 to C.8.
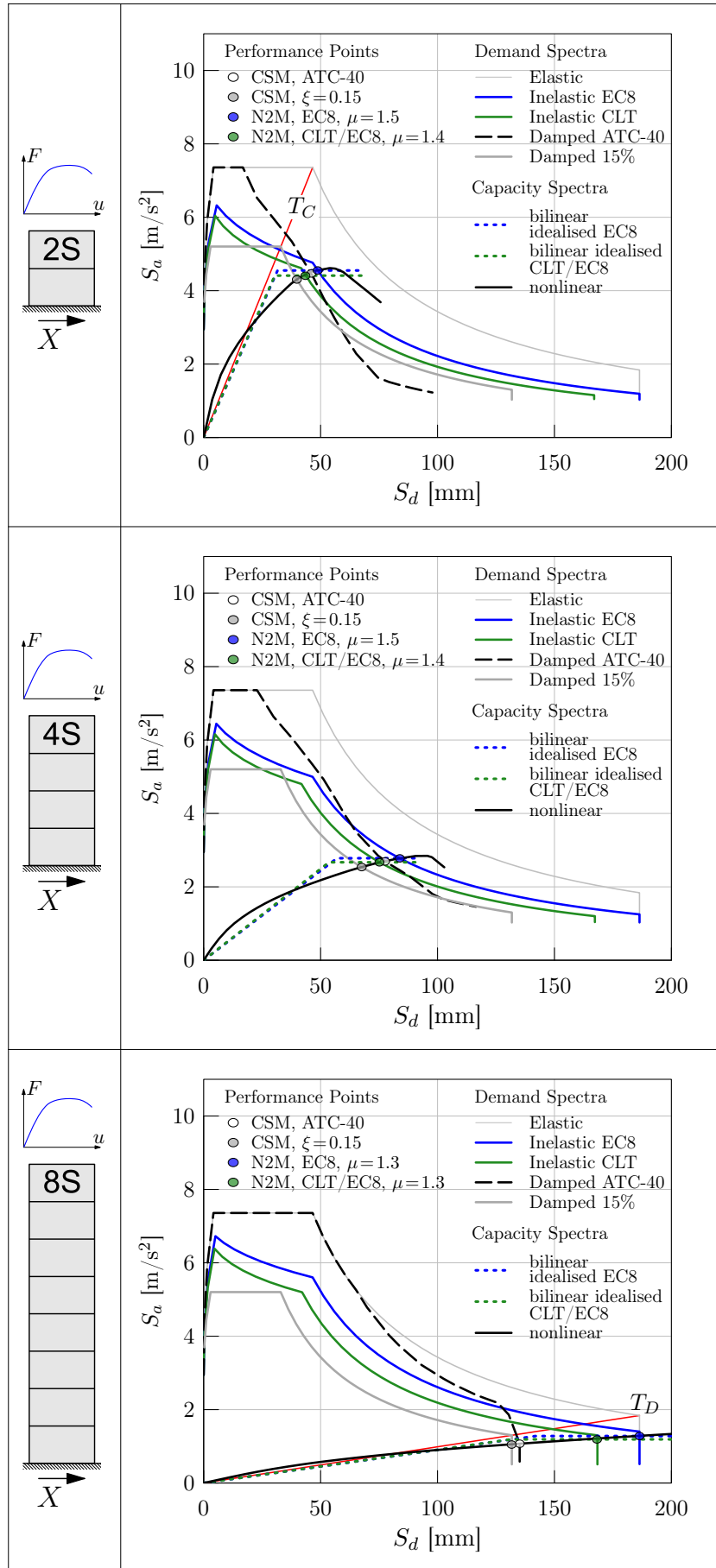
Figure 6.15: Determination of performance points for the SWT–SWE configuration in the X-direction for the linear load pattern

Results

It is observed that reasonable performance points were found for every configuration of the reference structure and both load patterns in the loading direction X by the four DBD procedures. Almost in every case, CSM with constant damping provides the lowest and the N2 method according to [EN 1998-1] the highest spectral values in terms of displacement and acceleration. The N2 method with the new $R_\mu - \mu - T$ relationship and CSM according to [ATC-40] yield performance points which are between those points found by the other two procedures.

Figure 6.15 illustrates that for the SWT–SWE configuration and the linear load pattern. Further characteristics can be observed by means of Figure 6.15 which apply for all configurations and both load patterns. It is noticeable that the performance points in almost any case are located in a range where the period is higher than the "corner" period T_C. Performance points for the two-storey structure were found in the spectral displacement range of about 40 to 60 mm. That is approximately the point where the inelastic spectra (EC 8, CLT) has a knee. The performance points of the four-storey structure are located in the sloping branch within a spectral displacement between 50 and 100 mm. Performance points for the eight-storey structure were mainly detected in the branch with constant spectral displacement. That corresponds to a period which is higher than T_D. Significantly higher values of the spectral displacement in that range are obtained by the N2 method compared to CSM. That is because spectral displacements are more strongly reduced in the case of damped spectra than for inelastic spectra. This indicates that the difference between the two approaches – inelastic spectra and damped spectra – becomes more and more apparent with increasing spectral displacements.

Basically, the same applies for the Y-direction. However, the determination of the performance point failed for very few constellations. It is shown in Figure 6.16 that performance points could not be found by CSM for the four-storey building and uniform load pattern. However, the performance points which were obtained by the N2 method are already far in the post-failure branch of the capacity spectrum. Here, it would be necessary to revise seismic design of the building. It must be remembered that the structure was designed for the linear load pattern. However, even for the linear load pattern critical performance points were found for the SWT-CWO configuration of the four-storey building (see Fig. 6.16). Again, all performance points lie in the post-failure branch and no design point could be obtained for CSM with constant damping.

This might display a weakness of the design with the lateral force method. Each structure was preliminarily designed for a behaviour factor of 2.0 and a distribution of lateral loads which is equivalent to the linear load pattern based on the SWE–SWT configuration. The resulting distribution of strength might not fully cover the strength demand for the uniform load pattern. Moreover, the SWT-CWO configuration exhibits the lowest deformation capacity compared to the other configurations with four storeys (see Figs. 6.10). The level of ductility is also decreased in this case due to lower deformation capacity. This indicates that the preselected behaviour factor might be assumed to be too high for this configuration.
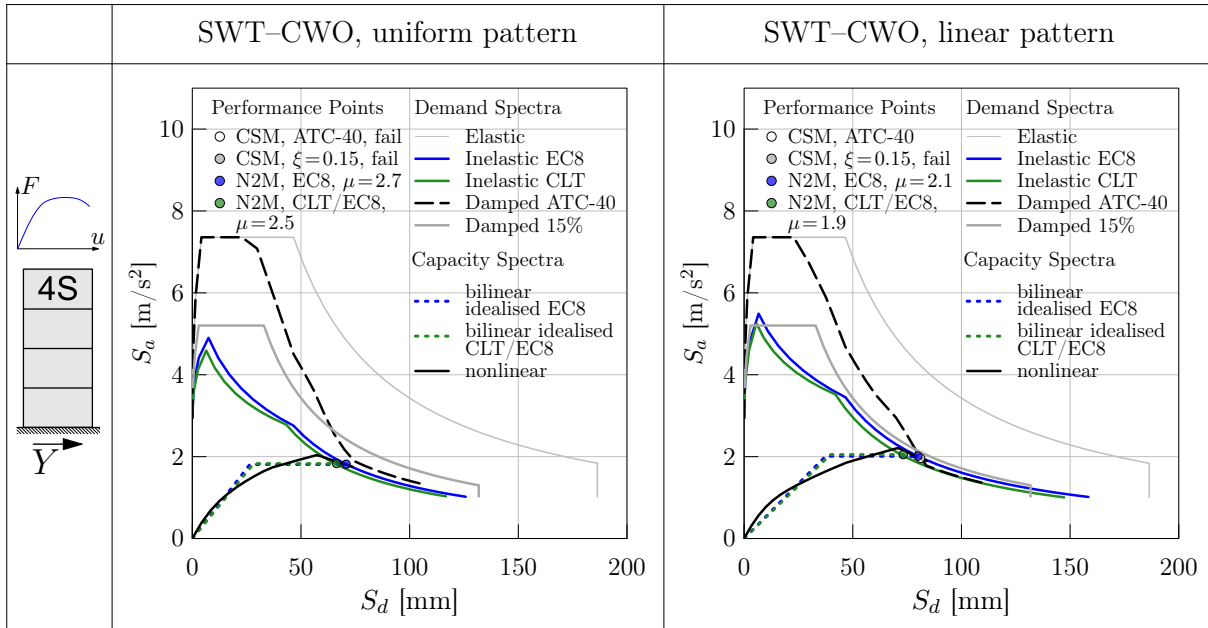
Figure 6.16: Determination of performance points for the four-storey SWT–CWO structure in the Y-direction

In addition to DBD with "non-linear" pushover curves, "bilinear" pushover curves (see Fig. 6.11) were applied. The determination of the performance point with these capacity curves is illustrated in Figure 6.17. Exemplarily, the configurations SWT-SWE and BT-SWE are compared for loading in the X direction and the linear load pattern. Figure 6.17 shows that performance points could only be found for CSM with constant damping for all numbers of storeys. In the case of the other procedures, the performance point determination worked for the two-storey and the eight-storey building, but not for the four-storey building. That has to do with the lower deformation capacity provided by the simplified capacity curve which is obviously a limitation of bilinear spring properties.

| configuration | | | 2S | | 4S | | 8S | |
plan	elevation	Method	$\dfrac{S_{d,nl}}{S_{d,bl}}$	$\dfrac{S_{a,nl}}{S_{a,bl}}$	$\dfrac{S_{d,nl}}{S_{d,bl}}$	$\dfrac{S_{a,nl}}{S_{a,bl}}$	$\dfrac{S_{d,nl}}{S_{d,bl}}$	$\dfrac{S_{a,nl}}{S_{a,bl}}$
SWT	SWE	CSM, ATC-40	0.96	0.99			0.92	0.95
BT	SWE	CSM, ATC-40	0.96	0.96			0.94	0.98
SWT	SWE	CSM, $\xi=0.15$	1.02	0.98	1.04	0.96	1.00	1.02
BT	SWE	CSM, $\xi=0.15$	1.04	0.97	1.03	0.97	1.00	1.04
SWT	SWE	N2M, EC8	0.98	1.01			1.00	0.97
BT	SWE	N2M, EC8	1.01	0.99			1.00	0.99
SWT	SWE	N2M, CLT/EC8	0.98	0.98			0.98	0.96
BT	SWE	N2M, CLT/EC8	1.01	0.97			0.99	0.99
Mean			1.00	0.98	1.04	0.96	0.98	0.99

Table 6.6: Comparison of the spectral values of the performance point for "non-linear" (nl) and "bilinear" (bl) capacity curves – ratio for spectral displacement S_d and spectral acceleration S_a
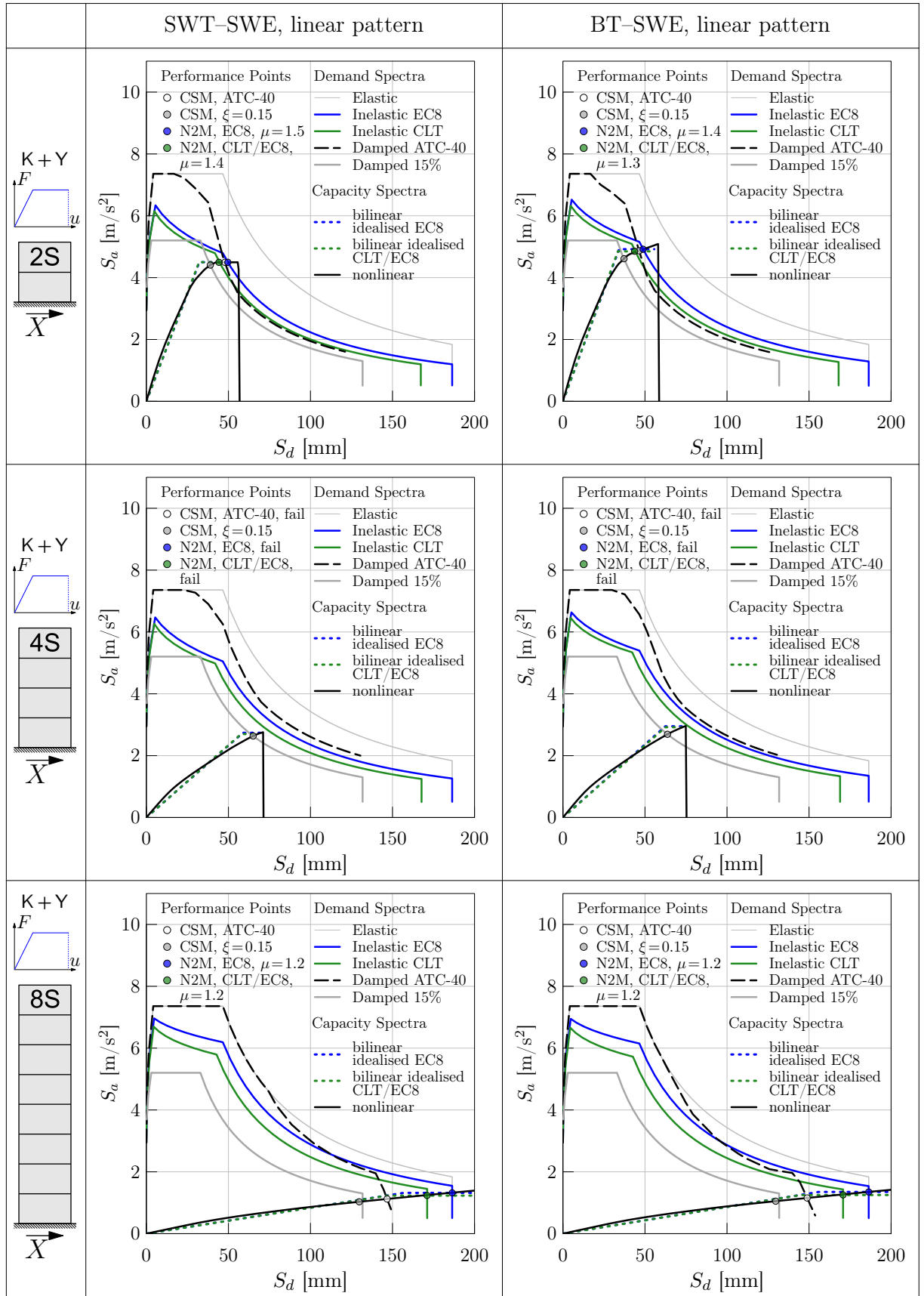
Figure 6.17: Determination of performance points for configurations SWT-SWE and BT-SWE in the X-direction for the linear load pattern considering "bilinear" pushover curves derived by the K + Y approach

137

However, it becomes clear from Table 6.6 that the "bilinear" pushover curves can lead to similar performance points as those found by using "non-linear" capacity curves. Table 6.6 presents the ratios of the spectral displacement S_d and spectral acceleration S_a for the performance points considering full non-linear relationships (see Figs. 6.15 and C.2) and the corresponding points from Figure 6.17 which were found with "bilinear" capacity curves. The mean value of the ratios indicate that the difference between the two approaches for the capacity curve is quite small.

Since performance points were found for almost every configuration and load pattern, it is basically confirmed by DBD that the structures were properly designed with a behaviour factor of 2.0. A final evaluation of the different procedures is conducted in section 6.6.2.

6.6 Comparison of DBD with NTHA

6.6.1 Strength and displacement demand

Finally, the strength and displacement demand of the building are determined with the spectral values – spectral acceleration S_a and spectral displacement S_d – of the performance point and by means of modal transformation (see Fig. 2.15). For back transformation, Eqs. (2.18) and (2.19) can be rewritten as

$$F_b = S_a \cdot m^* \cdot \Gamma \tag{6.17}$$
$$d = S_d \cdot \Gamma. \tag{6.18}$$

The lateral displacement u_i in level i can be calculated from the global displacement response d by means of the normalised deflection shape with the reversed form of Eq. (6.16).

$$u_i = d \cdot \phi_i \tag{6.19}$$

The strength and displacement demand in terms of base shear F_b and lateral displacements u_i are shown and discussed exemplarily for the SWT-SWE configuration in the X-direction. The performance points provide Figure 6.15 for the linear load pattern. The performance points of the uniform load patterns are also considered for comparison (see Fig. C.1). The spectral values of the performance points are documented in annex C together with base shear F_b and the lateral displacements u_i.

In Figure 6.18 the base shear F_b from NTHA are compared with the ones which were found by the different DBD procedures. The same findings which were made at the basis of the spectral accelerations in the previous section apply to the base shear. The N2 method according to [EN 1998-1] yields the highest and CSM with constant damping the lowest values of the base shear. Furthermore, the base shear of the four-storey and eight-storey structures is of a similar order which basically confirms the preliminary seismic design (see section A). However, there is a considerable difference in the base shear which was found for the two load pattern, especially in comparison to the base shear F_b from NTHA.

Figure 6.18a shows that the uniform load pattern leads to a base shear which rather matches the maximum base shear from NTHA for almost all DBD procedures. CSM provides a base shear which is close to the mean base shear from NTHA only for the eight-storey structure. Whereas the linear load pattern leads to similar results in comparison to the uniform load in terms of the base shear of the two-storey structure (see Fig. 6.18b). The base shear obtained by each DBD procedure and linear load pattern lies more or less between
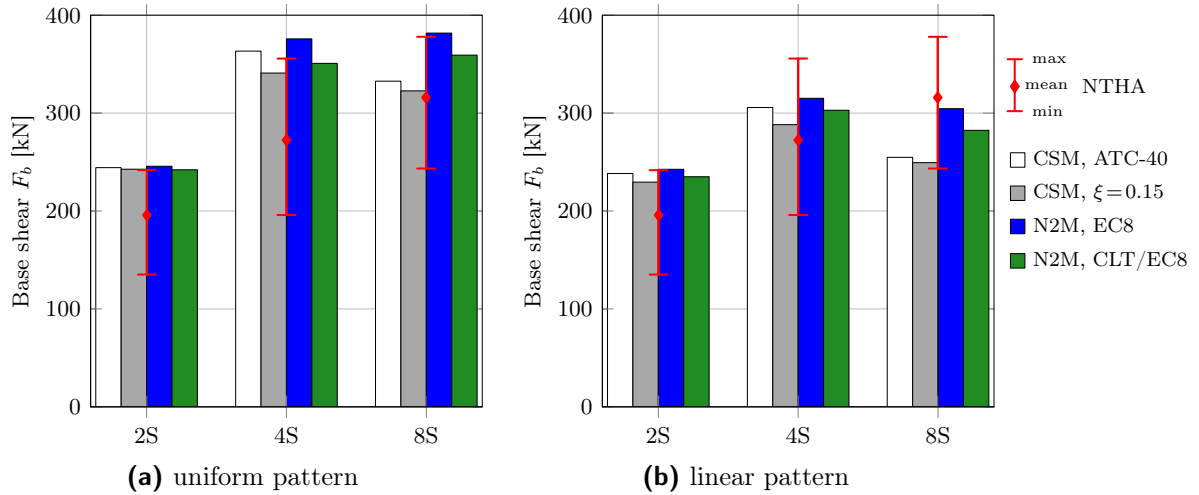
Figure 6.18: Base shear for SWT-SWE configuration in the X-direction – comparison of NTHA and DBD procedures

the mean and maximum base shear from NTHA for the four-storey structure. However, all DBD procedures underpredict the mean base shear of the eight-storey building from NTHA if the linear load pattern is considered. This might indicate that the linear load pattern does not reflect the distribution of inertia forces of the eight-storey SWT-SWE structure under earthquake excitation in the X-direction properly.

In Figure 6.19, the deflection shapes of the two-, four- and eight-storey SWT-SWE structures from DBD and NTHA are compared. The lateral displacements u_i as provided in Table 5.22 have been taken as basis for the evaluation of the displacement demand, since the base shear from DBD corresponds rather to the maximum base shear of NTHA in most cases (see Fig. 6.18). As already stated with reference to the spectral displacement the N2 method according to [EN 1998-1] yields the highest and CSM with constant damping the lowest displacement demand. The modified N2 method and CSM according to [ATC-40] are somehow in between. That correlates with the strength demand.

Furthermore, it can be observed that either the uniform or the linear load pattern returns the deformation characteristics better from NTHA depending on the number of stories. The lateral displacement from NTHA is lower than for DBD in the most cases, although the maximum base shear from NTHA is almost equal or even higher than the base shear from DBD.

Good agreement with the results of NTHA is obtained for the two-storey SWT-SWE structure by the linear load pattern. The new approaches – modified N2 method and CSM with constant damping – fit the deformation characteristics from NTHA best. The same applies to the four-storey building in the context of the uniform load pattern. Only CSM with constant damping in combination with the uniform load pattern reveals a good correlation with the results from NTHA for the eight-storey building.

Similar correlations in the results – base shear and lateral displacements – of NTHAs and the four DBD procedures in combination with the two load patterns were found for the other configurations of structures and for the Y-direction too.
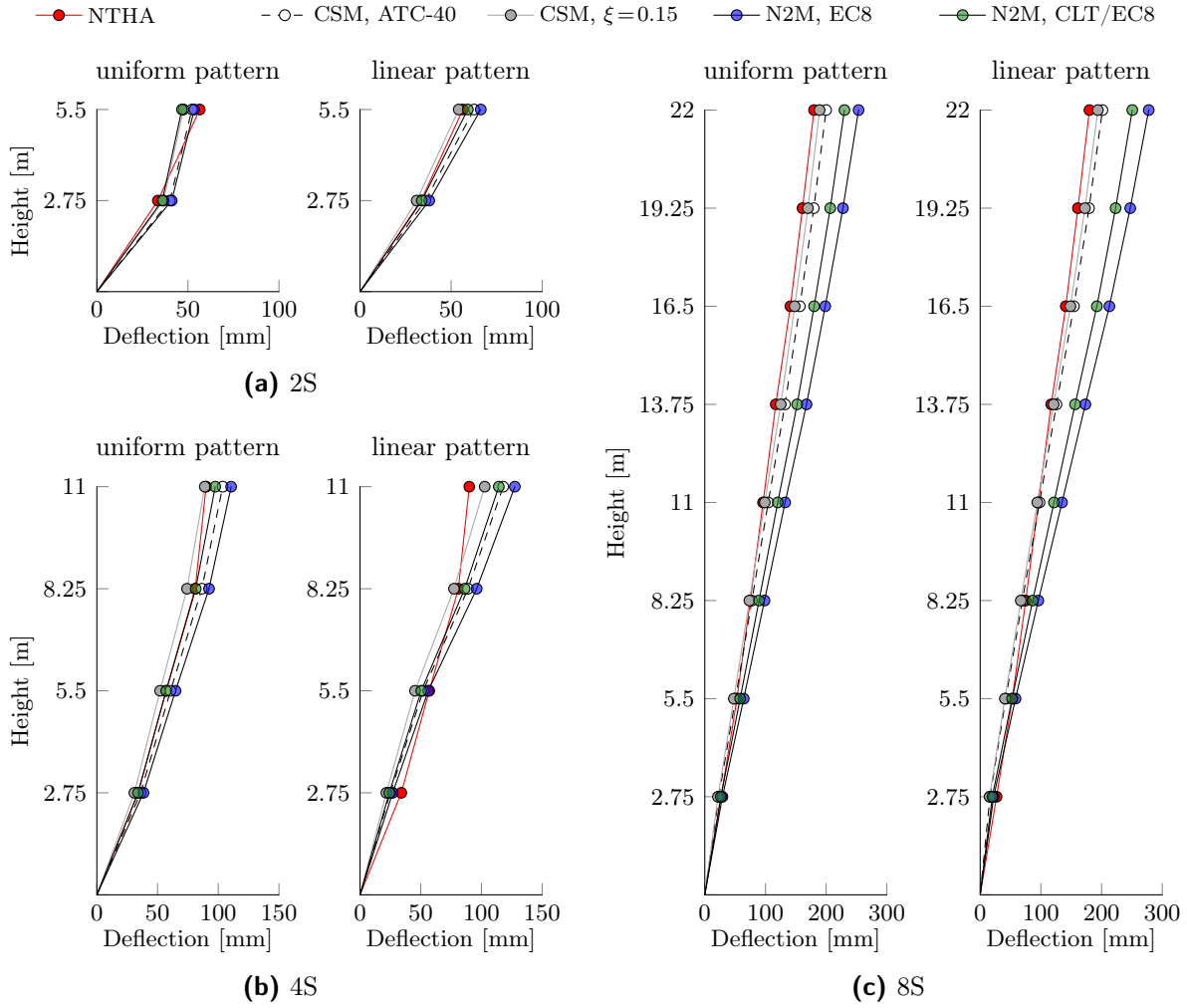
Figure 6.19: Deflection shapes for the SWT-SWE configuration in the X-direction – comparison of NTHA and DBD procedures

All results from DBD with the four procedures are documented in annex C. The documentation includes the spectral values of the performance point (spectral acceleration S_a and spectral displacement S_d), the modal parameters m^* and Γ, the base shear F_b and the lateral displacement at the reference points u_i. Base shear and lateral displacements are incorporated into the evaluation of DBD procedures in the next section.

6.6.2 Evaluation of displacement-based design procedures

The base shear F_b and lateral displacements u_i from NTHA were taken to evaluate the different DBD procedures by means of statistical quantities. The mean values of the base shear (see Tab. 5.20) and the lateral displacements from Table 5.21 will be taken as the basis for comparison. Results from DBD which were found for the two load patterns (see annex C) will be considered in parallel. However, only results which were obtained without considering friction were used as the basis for comparison and validation (see section 6.2).

All results were summarised to one population. The combinations are subsumed in Table 6.7. Four combinations are considered for the eight-storey structure, since results from NTHA are only available for the configurations SWT–SWE and BT–SWE for excitation in the directions X and Y.

n_j	Configurations			Number of storeys		
	Plan	Elevation	Direction	2S	4S	8S
1	SWT	SWE	X	×	×	×
2	BT	SWE	X	×	×	×
3	SWT	CWO	X	×	×	
4	BT	CWO	X	×	×	
5	SWT	SWE	Y	×	×	×
6	BT	SWE	Y	×	×	×
7	SWT	CWO	Y	×	×	
8	BT	CWO	Y	×	×	
Combinations				8	8	4

Table 6.7: Combinations of structural configurations and loading directions

In order to evaluate the base shear the ratio $F_{b,NTHA}/F_{b,DBD}$ was defined. *DBD* stands for the DBD procedure considered. The mean value for each DBD procedure and load pattern is defined as

$$\bar{x} = \frac{1}{n} \sum_{k=1}^{n} \frac{F_{b,NTHA,k}}{F_{b,DBD,k}} \qquad \text{with } n = 8{+}8{+}4 = 20 \qquad (6.20)$$

The same data basis has been used to determine the statistical values median, standard deviation (std. dev.) and coefficient of variation (var. coeff.). The summary is depicted in Table. 6.8.

	$F_{b,NTHA}/F_{b,DBD}$, uniform pattern				$F_{b,NTHA}/F_{b,DBD}$, linear pattern			
	CSM, ATC-40	CSM, $\xi{=}0.15$	N2M, EC8	N2M, CLT/EC8	CSM, ATC-40	CSM, $\xi{=}0.15$	N2M, EC8	N2M, CLT/EC8
Median	0.82	0.84	0.83	0.85	0.87	0.91	0.86	0.88
Mean	0.85	0.87	0.83	0.85	0.95	0.98	0.90	0.92
Std. dev.	0.08	0.09	0.06	0.06	0.18	0.19	0.11	0.12
Var. coeff.	0.10	0.10	0.08	0.07	0.19	0.19	0.12	0.13

Table 6.8: Summary of the base shear ratio $F_{b,NTHA}/F_{b,DBD}$ for the different DBD procedures

It has already been demonstrated in section 6.6.1 that the prediction of the lateral displacements depends on the load pattern. The influence of the load patterns on the lateral displacement is evaluated by means of the ratio $u_{i,NTHA}/u_{i,DBD}$. Here, the lateral displacement from NTHA $u_{i,NTHA}$ in level i is divided by the corresponding lateral displacement from DBD. The mean value is calculated with Eq. (6.21) for the two, four and eight-storey buildings separately.

$$\bar{x} = \frac{1}{n_j \cdot n_i} \sum_{j=1}^{n_j} \sum_{i=1}^{n_i} \frac{u_{i,NTHA,j}}{u_{i,DBD,j}} \qquad (6.21)$$

with n_j number of combinations, Table 6.7
         n_i number of storeys

It appears to be better to use the mean values in combination with the maximum and the minimum values for the evaluation of the lateral displacements. The statistical values median, standard deviation and coefficient of variation are not really convincing for this purpose. The summaries for the deflection ratio $u_{i,NTHA}/u_{i,DBD}$ for the two, four and eight-storey structures are depicted in Table 6.9.

	$u_{i,NTHA}/u_{i,DBD}$, uniform pattern				$u_{i,NTHA}/u_{i,DBD}$, linear pattern			
	CSM, ATC-40	CSM, $\xi=0.15$	N2M, EC8	N2M, CLT/EC8	CSM, ATC-40	CSM, $\xi=0.15$	N2M, EC8	N2M, CLT/EC8
Two-storey structure								
Max	1.07	1.19	1.05	1.20	1.00	1.17	0.96	1.06
Mean	0.92	1.02	0.90	1.02	0.88	1.00	0.83	0.94
Min	0.73	0.80	0.71	0.79	0.77	0.85	0.70	0.79
Four-storey structure								
Max	1.03	1.16	1.02	1.09	1.37	1.57	1.26	1.41
Mean	0.89	0.98	0.87	0.95	0.94	1.08	0.90	0.99
Min	0.53	0.57	0.53	0.58	0.56	0.65	0.53	0.59
Eight-storey structure								
Max	1.36	1.43	1.03	1.15	2.03	2.16	1.52	1.67
Mean	0.98	1.03	0.76	0.85	1.10	1.17	0.82	0.90
Min	0.86	0.91	0.65	0.73	0.83	0.90	0.62	0.69

Table 6.9: Summary of the deflection ratio $u_{i,NTHA}/u_{i,DBD}$ for the different DBD procedures

(a) uniform pattern

(b) linear pattern
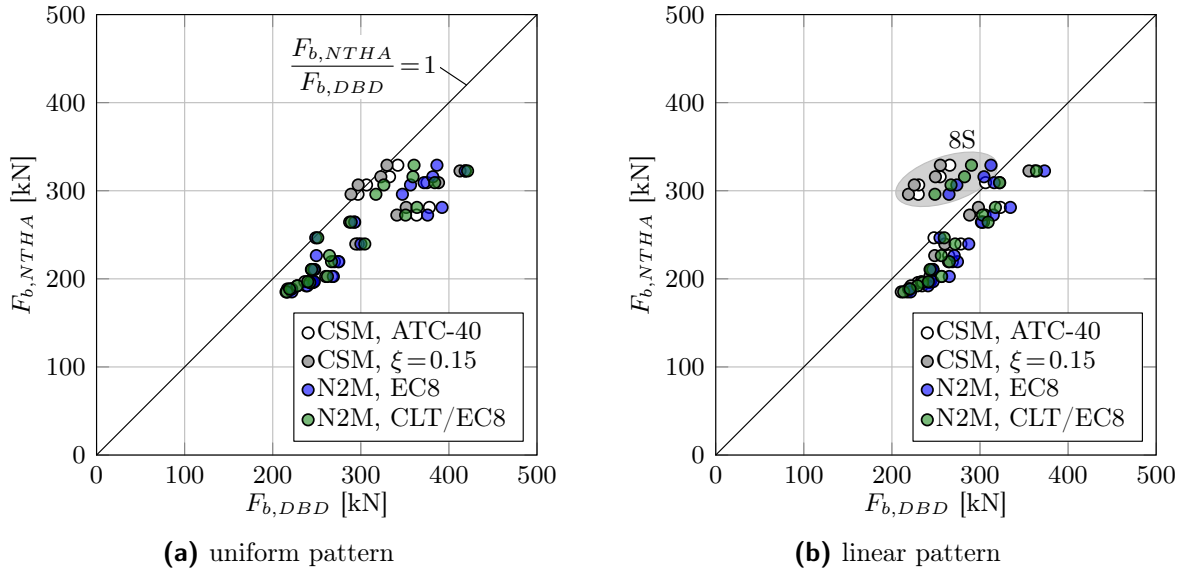
Figure 6.20: Correlation between quantities from NTHA and DBD – base shear F_b

In addition to the basic statistical evaluation, correlations were created for the base shear and the lateral displacements by plotting the quantity from NTHA over the corresponding quantity from DBD. The pairs of values relate to each other with respect to the configuration of the building, the number of storeys and loading direction (see Tab. 6.7). The lateral

displacement u_i in level i from NTHA is plotted over the corresponding lateral displacement from DBD. The same data basis as that considered for the statistical evaluation was used to generate the correlations. The correlations for the base shear and the lateral displacements are presented in Figures 6.20 and 6.21.

Discussion

The main characteristics will be discussed based on the statistical evaluation (see Tabs. 6.8 and 6.9) and the correlations (see Figs. 6.20 and 6.21). The diagonal lines in the correlations are equivalent to the ratios $F_{b,NTHA}/F_{b,DBD}$ and $u_{i,NTHA}/u_{i,DBD}$ equal to 1, as illustrated in Figures 6.20a and 6.21a respectively.
Results which are below that line overpredict quantities from NTHA and will be considered as conservative. With reference to the summaries that corresponds to a mean value which is lower than 1. Mean values higher than 1 indicate an underprediction of the results from NTHA.

In the first step the, influence of the load patterns is evaluated. The evaluation of the different DBD procedures is conducted next.

Figures 6.20a and 6.20b show the correlation of the base shear. It can be observed that the application of the uniform load pattern leads to a conservative strength demand, since the base shear of NTHA is overpredicted in almost all cases. Regarding the linear load pattern the mean values of the base shear ratio are closer to 1.0. However, there are cases where the linear load pattern leads to an underprediction of the base shear from NTHA; the base shear is underestimated by the DBD for the eight-storey structure (see Fig. 6.20b). The difference in the coefficient of variation (see Tab. 6.8) indicates that the base shear ratio scatter more for the linear load pattern.

Similar effects can be observed for the lateral displacements by means of the summaries in Table 6.9 and the correlations in Figure 6.21. Maximum, mean and minimum values do not differ significantly between uniform and linear load pattern for the two-storey structure. However, Figure 6.21b shows that the linear load pattern reproduces the deformation characteristics from NTHA more effectively than the uniform load patter. By contrast, the uniform load pattern leads to a better correlation with the results from NTHA for the four- and eight-storey structure. This also indicates the mean and the maximum values of deflection ratio $u_{i,NTHA}/u_{i,DBD}$. Mean values above 1.0 appear more often for the linear load pattern and the maximum values are higher for the linear than for the uniform load pattern which implies an underestimation of the lateral displacements considering Figures 6.21c to 6.21f.

All in all it can be stated that strength demand and deformation characteristics from NTHA were considered more effective by the linear load pattern for the two-storey structure and by the uniform load pattern for the four- and eight-storey structures.

The four DBD procedures provide a strength demand which is higher than the mean base shear from NTHA in almost any case (see Fig. 6.20). The strength demand is underpredicted only for the eight-storey building and the linear load pattern (see Fig. 6.20b). The underestimation can be traced back to the load pattern and not to the DBD procedures.

(a) 2S, uniform pattern

(b) 2S, linear pattern

(c) 4S, uniform pattern

(d) 4S, linear pattern

(e) 8S, uniform pattern

(f) 8S, linear pattern
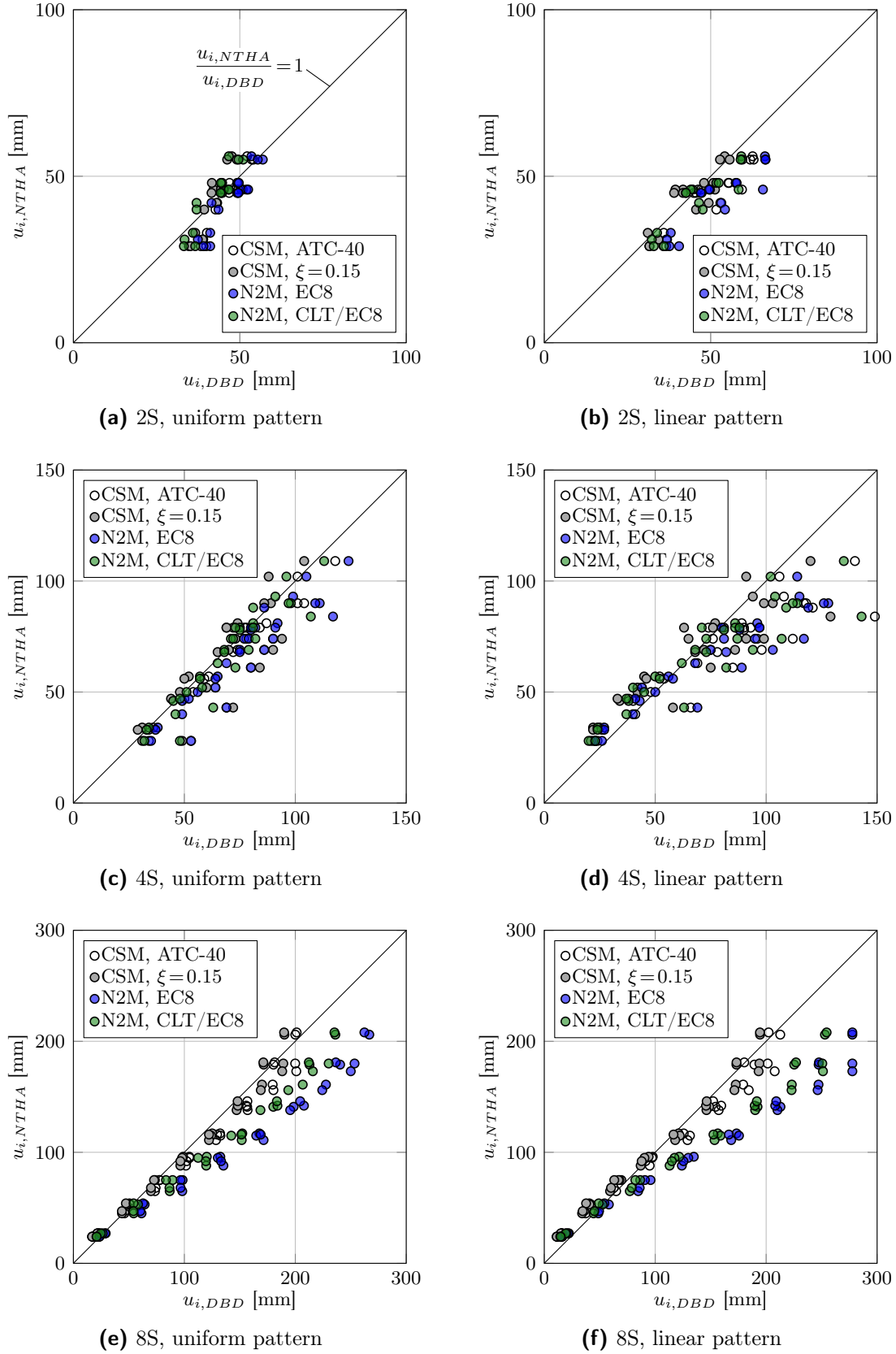
Figure 6.21: Correlation between quantities from NTHA and DBD – lateral displacements u_i

Based on the mean and median values of base shear ratio the N2 method according to [EN 1998-1] can be identified as the most conservative DBD procedure. As has already been noticed on the basis of the performance points, the mean and median values for CSM according to [ATC-40] and the modified N2 method are more or less between CSM with constant damping and the N2 method according to [EN 1998-1]. The coefficient of variation indicates that the base shear ratio scatters more for CSM than for the N2 method.

The N2 method according to [EN 1998-1] also leads to the highest displacement demand. The mean values of the deflection ratio are always lower than 1.0 and lower than the other DBD procedures (see Tab. 6.9) which means that the N2 method according to [EN 1998-1] overpredicts the lateral displacements more than the other DBD procedures. The modified N2 method and CSM with constant damping lead to the best agreement with the lateral displacements from NTHA for the two- and four-storey structures and linear and uniform load patterns, respectively. The mean values of the deflection ratio are between 0.94 and 1.00. The CSMs in combination with the uniform load pattern provide a good agreement with the lateral displacements of NTHA for the eight-storey structure – mean values between 0.98 and 1.03. This is illustrated in Figure 6.21e. Surprisingly, the best correlation was found by CSM with constant damping. Figures 6.21e and 6.21f show that there is a deviation of the lateral displacement from the N2 methods which increase systematically proportional to the height of the building.

It has already been noted with reference to the evaluation of the performance points that the spectral displacement is significantly higher for N2 method compared to CSM for the eight-storey structure which can be traced back to the different nature of the inelastic and damped spectra in the range of constant spectral displacement.

Summary and Conclusion

A better correlation with results from NTHA was found by the uniform load pattern for the four- and eight-storey structures. The characteristics of the two-storey structure were matched more effectively by the linear load pattern.

With reference to the four DBD procedures the following can be concluded:

- The N2 method according to [EN 1998-1] leads to the most conservative results for the base shear and lateral displacements.
- CSM with constant damping predicts the results from NTHA best.
- Similar results can be found by CSM according to [ATC-40] and the N2 method using the new $R_\mu - \mu - T$ relationship for CLT structures. Base shear and lateral displacements are close to those obtained by NTHA but are more conservative than CSM with constant damping.
- The N2 methods exhibit systematically higher lateral displacements than the CSMs for the eight-storey structure.

It is confirmed that both load patterns – uniform and linear – have to be considered for DBD of multi-storey CLT structures. Based on the statistical evaluation of the DBD procedures and the discussion of the results, CSM according to [ATC-40] and the N2 method in combination with the new $R_\mu - \mu - T$ relationship can be recommended for the seismic design of multi-storey CLT structures. However, CSM with 15 % constant damping allows a good estimation of the seismic strength and displacement demand for CLT structures up to eight-storeys.

7 Summary and Outlook

This thesis deals with the subject of displacement-based seismic design for multi-storey CLT structures. The work aims at the development of improved DBD procedures for CLT structures. Two new and completely different DBD procedures are proposed. Focus is placed on a systematic development of reference structures and realistic structural models. Experimental investigations on connections and CLT wall elements and the evaluation of the test results are intended to build the basis for DBD and structural modelling.

In a first step, the fundamentals of the dynamic action "earthquake" and its impact on structures are discussed generally. Analytical formulations to characterise dynamic processes are presented and established analysis methods are introduced. Two existing DBD methods - the CSM according to [ATC-40] and the N2 method according to [EN 1998-1] – are elaborated and featured.

An overview of experimental and analytical investigations regarding the topic of timber structures under seismic action is given in chapter 3 with the focus on the characteristics of multi-storey CLT constructions together with a review of different approaches for numerical modelling of multi-storey CLT structures and the application of DBD to CLT structures.

It has been noticed that load and support conditions and connections, which are characteristic for CLT constructions in construction practice, are not completely consistent with conditions in experimental investigations and in analysis models. Furthermore, it could not be stated whether the DBD methods presented in chapter 2 can be applied for multi-storey CLT buildings or not. Among others, the characterisation of the hysteretic behaviour which is incorporated in the N2 method differ significantly from experimental results which have been derived for CLT structures.

For these reasons, a study including experimental and analytical investigations was carried out considering the issues above stated. At first, a test series was undertaken with typical connections of the CLT construction and CLT wall elements considering of realistic boundary conditions. That applies for the detailing of connections as well as for the vertical loading of wall elements. By means of the wall element tests, the amount of hysteretic damping - which is an important parameter for the capacity spectrum method - is found to be in a range of 10 to 14 %.

The results of the experimental study are also used to determine properties for nonlinear spring elements for 3D simulations on the building level. The spring properties are validated on the wall element level. The modelling approach results in a conservative estimate of the energy dissipation capacity. A comparatively simple reference structure is developed for numerical simulations on the building level which considers the essential peculiarities of the CLT construction. The building is designed with the lateral force method – frequently used by engineers in practice – and a behaviour factor of 2.0. Multiple types of reference structures are modelled for a different number of storeys to cover a wide range of variants for this construction type. The structural configurations shear wall type, box type, single wall elements and continuous wall with openings are considered.

Full dynamic analyses have been performed using specific nonlinear characteristics of wall elements and connections. The influence of the different structural configurations and the impact of friction on the dynamic response are ascertained and discussed. The results of NTHA are used to validate the applicability of the different DBD methods for CLT buildings.

A new formulation of the reduction factor R_μ is developed for the application of the N2 method to CLT structures. The new $R_\mu - \mu - T$ relationship incorporates the characteristic hysteretic behaviour of the CLT construction. In addition to the adapted N2 method three further DBD procedures are considered. On the one hand, the N2 method according to [EN 1998-1] and CSM according to [ATC-40] are included. On the other hand a simplified version of CSM is integrated for which the effective damping is constantly taken into account at 15 %. Here, the share of hysteretic damping is fixed to a conservative value of 10 % in accordance with results from wall element testing.

Simplified bilinear and full nonlinear load-displacement relationships are involved for the determination of the capacity curve. The suitability of both approaches are confirmed. However, a lower deformation capacity is detected when bilinear springs are used.

The results of DBD are validated against the results of NTHAs. The influence of the load pattern on strength demand and deformation characteristics is demonstrated. It is found that the two load patterns – uniform and linear – are relevant for DBD of CLT structures. It is noticed that the N2 method according to [EN 1998-1] yields considerable higher values for the strength and displacement demand than all other DBD procedures and the time history analysis. Surprisingly, it is determined that the simplest approach – CSM with constant damping – leads to the best correlation with the results from NTHAs. Conservative results and good agreement with results from NTHAs are achieved for the CSM according to [ATC-40] and the N2 method in combination with the new formulation of reduction factor R_μ.

It is demonstrated that the new approach for the reduction factor R_μ is considerably more favourable for DBD of CLT structures with the N2 method as the one according to [EN 1998-1]. Adequate predictions of the strength and the displacement demand are confirmed for the different configurations of the CLT construction.

Consequently, the N2 method in combination with the new formulation of reduction factor R_μ will be recommended for displacement-based seismic design of multi-storey CLT buildings. The usage of the new $R_\mu - \mu - T$ relationship would only imply a minimal modification of the N2 method according to [EN 1998-1]. However, the approach with 15 % constant damping might also be a suitable method for the seismic design of CLT structures up to eight storeys. The procedure could be further simplified if bilinear load-displacement relationships are used for the connection behaviour.

Both the uniform and the linear load pattern should be considered within DBD of CLT structures. The two load patterns account implicitly for the different deformation characteristics – bending, rocking, shear and slip – which are inherent for CLT structures. Different deformation characteristics appear depending on the structural configuration.

A clear definition of the element properties would be required for the application of DBD in engineering practice. With reference to non-linear analyses, [EN 1998-1] asks for utilising bilinear load-displacement relationships, as a minimum, which are based on the mean values of material properties. Appropriate analytical approaches for the stiffness, the strength and the deformation capacity are required with respect to the connections of CLT constructions. In this context, a guideline for the application of DBD to timber structures which is oriented on European Standards would be helpful for practicing engineers. In this guideline, effects of irregularities of the structure and the contribution of higher vibration modes which are not covered by this work should be discussed. A systematic study of the influence of friction would be necessary in future experimental and numerical investigations regarding the response of multi-storey CLT structures under earthquake impact.

8 Zusammenfassung

Diese Dissertation befasst sich mit dem Thema der verhaltensbasierten Erdbebenbemessung mehrgeschossiger Brettsperrholzkonstruktionen (BSP-Konstruktionen). Das Ziel dieser Arbeit ist die Entwicklung verbesserter verhaltensbasierter Verfahren für BSP-Konstruktionen. Zwei neuartige, eigenständige verhaltensbasierte Bemessungsansätze werden vorgeschlagen. Der Schwerpunkt wird auf eine systematische Entwicklung von Referenzgebäuden und die Berechnungsgrundlagen gelegt. Experimentelle Untersuchungen an Verbindungen und BSP-Wandelementen und die Auswertung der Versuchsergebnisse bilden die Basis für die verhaltensbasierte Bemessung und Modellierung.

Zuerst werden die Grundlagen der dynamischen Einwirkung „Erdbeben" und die Auswirkungen auf Gebäude im Allgemeinen erörtert. Mathematische Formulierungen zur Beschreibung dynamischer Prozesse werden vorgestellt. Die verfügbaren Berechnungsmethoden werden in diesem Zusammenhang eingeführt. Der Schwerpunkt liegt hier auf der verhaltensbasierten Berechnung. Zwei bestehende verhaltensbasierte Methoden – die Kapazitätsspektrummethode nach [ATC-40] und die N2-Methode nach [EN 1998-1] – werden ausführlich beschrieben. Jedoch konnte zunächst keine abschließende Aussage darüber getroffen werden, ob die verhaltensbasierten Methoden für mehrgeschossige BSP-Konstruktionen angewendet werden können oder nicht. Unter anderem ist das Hystereseverhalten, welches der N2-Methode zugrunde liegt, nicht typisch für BSP-Konstruktionen.

Ein Überblick über die im Fachschrifttum dokumentieren experimentellen und analytischen Untersuchungen von Holzkonstruktionen unter Erdbebeneinwirkung wird in Kapitel 3 gegeben, wobei der Schwerpunkt auf die Eigenschaften von mehrgeschossigen BSP-Konstruktionen gelegt wird. Dieses Kapitel beinhaltet auch einen Überblick über die verschiedenen Vorgehensweisen bei der Modellierung von mehrgeschossigen BSP-Konstruktionen und die Anwendung der verhaltensbasierten Berechnung. Es wird festgestellt, dass bei den bisherigen Untersuchungen die Randbedingungen hinsichtlich Auflast und Lagerung sowie der Verbindungen, die typisch für BSP-Konstruktionen sind, nicht immer mit den Gegebenheiten in der Baupraxis übereinstimmen.

Aus diesen Gründen wurden umfassende experimentelle und analytische Untersuchungen durchgeführt, welche die zuvor genannten Punkte berücksichtigen. Zuerst wurde eine Versuchsreihe mit typischen Verbindungen von BSP-Konstruktionen und BSP-Wandelementen unter realistischen Randbedingungen konzipiert. Dies betrifft die Verbindung am Wandfuß und die Vertikallast am Wandkopf. Anhand der Untersuchungen der Wandelemente wird festgestellt, dass die hysteretische Dämpfung – die ein wichtiger Parameter für die Kapazitätsspektrummethode ist – im Bereich von 10 - 14 % liegt.

Die Ergebnisse der experimentellen Untersuchung werden zur Bestimmung der Kennwerte von nichtlinearen Federn für die 3D-Simulation auf Bauwerksebene genutzt. Die Federelemente werden systematisiert und auf der Ebene der Wandelemente validiert. Der verwendete Modellierungsansatz und die Federkennwerte führen zu einer geringfügig konservativen Abschätzung der Energiedissipationskapazität. Eine vergleichsweise einfache Referenzkonstruktion, welche die grundlegenden Besonderheiten der BSP-Konstruktion beachtet, wird

für die numerische Simulationen auf Bauwerksebene entwickelt. Das Gebäude wird mit dem Ersatzkraftverfahren und einem Verhaltensbeiwert von 2,0 bemessen. Mehrere Typen von Referenzkonstruktionen werden für eine unterschiedliche Anzahl von Stockwerken modelliert, um möglichst viele Konstruktionsvarianten abzudecken. Die Konstruktionstypen „shear wall type", „box type", „single wall elements" und „continuous wall with openings" werden berücksichtigt.

Umfassende dynamische Untersuchungen werden mit realistischen Ansätzen durchgeführt. Der Einfluss der verschiedenen Konstruktionstypen und von Reibungseffekten auf die dynamische Antwort werden aufgezeigt und diskutiert. Mit den Ergebnissen der Zeitverlaufsberechnung wird die Anwendbarkeit der verschiedenen verhaltensbasierten Methoden für BSP-Konstruktionen bewertet.

Für die Anwendung der N2-Methode für BSP-Konstruktionen wird eine neue Formulierung zur Ermittlung des Reduktionsfaktors R_μ entwickelt. Die neue $R_\mu - \mu - T$-Beziehung berücksichtigt das charakteristische Hystereseverhalten von BSP-Konstruktionen. Zusätzlich zu der angepassten N2-Methode werden drei weitere verhaltensbasiete Verfahren berücksichtigt. Zum einen werden die N2-Methode nach [EN 1998-1] und die Kapazitätsspektrummethode nach [ATC-40] betrachtet. Zum anderen wird eine vereinfachte Version der Kapazitätsspektrummethode angewendet, bei der die effektive Dämpfung anhand der Ergebnisse der Versuche an Wandelementen auf den konservativen Wert von 10 % festgelegt wird.

Vereinfachte bilineare und vollständig nichtlineare Kraft-Verformungsbeziehungen werden zur Bestimmung der Kapazitätskurve verwendet. Die Eignung beider Vorgehensweisen wird bestätigt. Jedoch ergibt sich rechnerisch eine geringere Verformungsfähigkeit bei der Verwendung von bilinearen Federn.

Die Ergebnisse der verhaltensbasierten Berechnung werden den Ergebnissen der Zeitverlaufsberechnung gegenübergestellt. Der Einfluss der Lastverteilung auf den Widerstand und die Verformungseigenschaften wird aufgezeigt. Es wird deutlich, dass die beiden Lastverteilungen – konstant und linear – für die verhaltensbasierte Bemessung von BSP-Konstruktionen bedeutsam sind. Außerdem wird festgestellt, dass die N2-Methode nach [EN 1998-1] wesentlich höhere Werte beim erforderlichen Widerstand und den zugehörigen Verformungen ergeben als alle anderen verhaltensbasierten Verfahren und als die Zeitverlaufsberechnung. Überraschenderweise zeigt sich, dass die einfachste Methode, die Kapazitätsspektrummethode mit konstanter Dämpfung, die beste Übereinstimmung mit den Ergebnissen der Zeitverlaufsberechnung liefert. Konservative Ergebnisse und gute Übereinstimmungen mit den Ergebnissen der Zeitverlaufsberechnung werden für die Kapazitätsspektrummethode nach [ATC-40] und die N2-Methode in Kombination mit der neuen Formulierung für den Reduktionsfaktor R_μ erzielt.

Es wird gezeigt, dass der neue Ansatz für den Reduktionsfaktor R_μ wesentlich besser für die verhaltensbasierte Bemessung der BSP-Konstruktionen mit der N2-Methode geeignet ist als die Formulierung nach [EN 1998-1]. Die angemessene Prognose des erforderlichen Widerstands und der zugehörigen Verformungen kann für die verschiedenen Konfigurationen der BSP-Konstruktion bestätigt werden.

References

[AlSu85]   Al-Sulaimani, G.; Roessett, J.: *Design spectra for degrading systems. Journal of Structural Engineering* 111.12 (1985), pages 2611–2623.

[Ambr02]   Ambraseys, N.; Smit, P.; Sigbjornsson, R.; Suhadolc, P.; Margaris, B.: *Internet-Site for European Strong-Motion Data.* Edited by E. European Commission RESEARCH-DIRECTORATE GENERAL; C. Programme. 2002. URL: http://www.isesd.hi.is/ESD_Local/frameset.htm.

[Anch14]   Ancheta, T. D.; Darragh, R. B.; Stewart, J. P.; Seyhan, E.; Silva, W. J.; Chiou, B. S.; Wooddell, K. E.; Graves, R. W.; Kottke, A. R.; Boore, D. M.; Kishida, T.; Donahue, J. L.: *PEER Ground Motion Database.* Edited by S. Mazzoni; J. Way. 2014. URL: http://peer.berkeley.edu/products/strong_ground_motion_db.html.

[Asch00]   Aschheim, M.; Black, E. F.: *Yield point spectra for seismic design and rehabilitation. Earthquake Spectra* 16.2 (2000), pages 317–336.

[Asch03]   Aschheim, M.; Montes, E. H.: *The representation of P-Δ effects using Yield Point Spectra. Engineering Structures* 25.11 (2003), pages 1387–1396.

[Asch99]   Aschheim, M.: *Yield Point Spectra: A simple alternative to the capacity spectrum method. Proceedings of 1999 SEAOC Convention, Reno, Nevada, USA (preprint).* 1999.

[Augu10]   Augustin, M.; Blaß, H. J.; Bogensperger, T.; Ebner, H.; Ferk, H.; Fontana, M.; Frangi, A.; Hamm, P.; Jöbstl, R. A.; Moosbrugger, T.; Richter, A.; Schickhofer, G.; Thiel, A.; Traetta, G.; Uibel, T.: *BSPhandbuch, Holz- Massivbauweise in Brettsperrholz: Nachweise auf Basis des neuen europäischen Normenkonzepts.* 2., überarbeitete Auflage. Verlag der Technischen Universität Graz, 2010.

[Augu84]   Augusti, G.; Baratta, A.; Casciati, F.: *Probabilistic methods in structural engineering.* Chapman and Hall, 1984.

[Aydi03]   Aydinoğlu, M.: *An incremental response spectrum analysis procedure based on inelastic spectral displacements for multi-mode seismic performance evaluation. Bulletin of Earthquake Engineering* 1.1 (2003), pages 3–36.

[Bach02]   Bachmann, H.: *Erdbebensicherung von Bauwerken.* 2., überarbeitete Auflage. Birkhäuser Verlag Basel, Boston, Berlin, September 2002.

[Blaß06]   Blaß, H. J.; Bejtka, I.; Uibel, T.: *Tragfähigkeit von Verbindungen mit selbstbohrenden Holzschrauben mit Vollgewinde.* Karlsruher Berichte zum Ingenieurholzbau, Band 4. Universität Karlsruhe (KIT), 2006.

[Bouk09]   Boukes, J.: *A computer model for a seven storey timber building constructed with X-lam panels and an experiment on the Kerto-Q laminated Veneer lumber connection. M. Sc. Report, TU Delft* (2009).

[Brun11]   Brunner, R.; Jung, P.; Steiger, R.; Wenk, T.; Wirz, N.: *Erdbebengerechte mehrgeschossige Holzbauten.* Technischer Bericht. Lignum, 2011.

References

[Cecc02]   Ceccotti, A.; Karacabeyli, E.: *Validation of seismic design parameters for wood-frame shearwall systems. Canadian Journal of Civil Engineering* 29.3 (2002), pages 484–498.

[Cecc06a]   Ceccotti, A.; Follesa, M.: *Seismic behaviour of multi-storey X-lam buildings. COST E29 International Workshop on Earthquake Engineering on Timber Structures.* 2006, pages 81–95.

[Cecc06b]   Ceccotti, A.; Follesa, M.; Lauriola, M.; Sandhaas, C.: *Sofie Project – Test results on the lateral resistance of cross-laminated wooden panels. Proceedings of the First European Conference on Earthquake Engineering and Seismicity.* Volume 3. 2006.

[Cecc08]   Ceccotti, A.: *New technologies for construction of medium-rise buildings in seismic regions: the XLAM case. Structural Engineering International* 18.2 (2008), pages 156–165.

[Cecc10]   Ceccotti, A.; Sandhaas, C.: *A proposal for a standard procedure to establish the seismic behaviour factor q of timber buildings. Proceedings of the 11th World Conference on Timber Engineering, Riva del Garda, Italy.* 2010.

[Cecc11]   Ceccotti, A.; Sandhaas, C.; Yasumura, M.: *Seismic behaviour of cross-lam timber buildings. 9.Grazer Holzbau-Fachtagung, TU Graz, Austria* (2011).

[Cecc13]   Ceccotti, A.; Sandhaas, C.; Okabe, M.; Yasumura, M.; Minowa, C.; Kawai, N.: *SOFIE project – 3D shaking table test on a seven-storey full-scale cross-laminated timber building. Earthquake Engineering & Structural Dynamics* 42.13 (2013), pages 2003–2021. URL: http://dx.doi.org/10.1002/eqe.2309.

[Chop01]   Chopra, A. K.; Goel, R. K.: *Direct displacement-based design: use of inelastic vs. elastic design spectra. Earthquake Spectra* 17.1 (2001), pages 47–64.

[Chop95]   Chopra, A. K.: *Dynamics of Structures: Theory and Applications to Earthquake Engineering.* Edited by W. J. Hall. Prentice hall international series in civil engineering and engineering mechanics. Prentice Hall Englewood Cliffs, New Jersey, 1995.

[Chop99a]   Chopra, A. K.; Goel, R. K.: *Capacity-demand-diagram methods based on inelastic design spectrum. Earthquake spectra* 15.4 (1999), pages 637–656.

[Chop99b]   Chopra, A. K.; Goel, R. K.: *Capacity-demand-diagram methods for estimating seismic deformation of inelastic structures: SDF systems. Civil and Environmental Engineering* (1999), pages 1–73.

[Clou93]   Clough, R. W.; Penzien, J.: *Dynamics of structures.* 2nd edition. McGraw-Hill, 1993.

[CNRI]   CNR-IVALSA: National Research Council of Italy – Trees and Timber Institute: *The SOFIE project.* last access 08.07.2016. URL: http://www.ivalsa.cnr.it/en/current-projects/edilizia-e-architettura/progetto-sofie.html.

[Comp00]   Computers & Structures: *SAP2000 – integrated finite element analysis and design of structures.* 2000.

[Dass]   Dassault Systemes: *Abaqus FEA – a software suite for finite element analysis and computer-aided engineering.* version 6.12. URL: www.simulia.com.

[de B14]   de Borst, R.; Crisfield, M. A.; Remmers, J. J. C.; Verhoosel, C. V.: *Nichtlineare Finite-Elemente-Analyse von Festkörpern und Strukturen*. 1. Auflage. Wiley-VCH Verlag, 2014.

[Deie10]   Deierlein, G. G.; Reinhorn, A. M.; Willford, M. R.: *Nonlinear structural analysis for seismic design – A Guide for Practicing Engineers. NEHRP Seismic Design Technical Brief No.* 4 (2010).

[Duji04]   Dujic, B.; Pucelj; Janez; Zarnic, R.: *Testing of racking behaviour of massive wood wall panels. Meeting 37 of the Working Commission W18-Timber Structures (CIB W18), Edinburgh, Scotland*. CIB-W18/37-15-2. 2004.

[Duji06a]   Dujic, B.; Aicher, S.; Zarnic, R.: *Racking behaviour of light prefabricated cross-laminated massive timber wall diaphragms subjected to horizontal actions. Otto-Graf-Journal* 17 (2006), pages 125–142.

[Duji06b]   Dujic, B.; Aicher, S.; Zarnic, R.: *Testing of wooden wall panels applying realistic boundary conditions. Proceedings of the 9th World Conference on Timber Engineering, Portland, Oregon, USA*. 2006.

[Duji06c]   Dujic, B.; Klobucar, S.; Zarnic, R.: *Influence of openings on shear capacity of masive cross-laminated wooden walls. COST E29 International Workshop on Earthquake Engineering on Timber Structures*. 2006.

[Duji06d]   Dujic, B.; Zarnic, R.: *Study of lateral resistance of massive X-lam wooden wall system subjected to horizontal loads. COST E29 International Workshop on Earthquake Engineering on Timber Structures*. 2006.

[Duji08]   Dujic, B.; Klobcar, S.; Zarnic, R.: *Shear capacity of cross-laminated wooden walls. Proceedings of the 10th World Conference on Timber Engineering, Miyazaki, Japan*. 2008.

[Duji10]   Dujic, B.; Strus, K.; Žarnić, R.; Ceccotti, A.: *Prediction of dynamic response of a 7-storey massive XLam wooden building tested on a shaking table. Proceedings of the 11th World Conference on Timber Engineering, Riva del Garda, Italy*. 2010.

[Dvor84]   Dvorkin, E. N.; Bathe, K.-J.: *A continuum mechanics based four-node shell element for general non-linear analysis. Engineering computations* 1.1 (1984), pages 77–88.

[ESEC]   ESECMaSE: *Enhanced Safety and Efficient Construction of Masonry Structures in Europe*. last access 08.07.2016. URL: http://www.esecmase.org.

[Fajf00]   Fajfar, P.: *A nonlinear analysis method for performance-based seismic design. Earthquake spectra* 16.3 (2000), pages 573–592.

[Fajf05]   Fajfar, P.; Kilar, V.; Marusic, D.; Perus, I.; Magliulo, G.: *The extension of the N2 method to asymmetric buildings. Proceedings of the 4th European workshop on the seismic behaviour of irregular and complex structures*. 41. 2005.

[Fajf88]   Fajfar, P.; Fischinger, M.: *N2 – A method for non-linear seismic analysis of regular buildings. Proceedings of the 9th World Conference in Earthquake Engineering, Kyoto, Japan*. 1988.

[Fajf94]   Fajfar, P.; Vidic, T.: *Consistent inelastic design spectra: hysteretic and input energy. Earthquake Engineering and Structural Dynamics* 23 (1994), pages 523–437.

References

[Fajf96]   Fajfar, P.; Gašperšič, P.: *The N2 method for the seismic damage analysis of RC buildings. Earthquake Engineering & Structural Dynamics* 25.1 (1996), pages 31–46.

[Fajf99]   Fajfar, P.: *Capacity spectrum method based on inelastic demand spectra. Earthquake Engineering and Structural Dynamics* 28 (1999), pages 979–993.

[Fehl08]   Fehling, E.; Stürz, J.; Aldoghaim, E.: *Identification of suitable behaviour factors for masonry members under earthquake loads (deliverable 7.3)*. Technical report. Technical report of the collective research project: Enhanced Safety and Efficient Construction of Masonry Structures in Europe (ESECMaSE). University of Kassel, 2008.

[Ferr12]   Ferraioli, M.; Lavino, A.; Mandara, A.: *Behaviour Factor for seismic design of moment-resisting steel frames. Proceedings of 15th World Conference on Earthquake Engineering, Lisbon, Portugal.* 2012.

[Fili01]   Filiatrault, A.; Fischer, D.; Folz, B.; Uang, C.; Seible, F.: *Shake Table Tests of a Two-Story Woodframe House*, pages 1–8. 2001.

[Fili02]   Filiatrault, A.; Folz, B.: *Performance-based seismic design of wood framed buildings. Journal of Structural Engineering* 128.1 (2002), pages 39–47.

[Fili03]   Filiatrault, A.; Isoda, H.; Folz, B.: *Hysteretic damping of wood framed buildings. Engineering Structures* 25.4 (2003), pages 461–471.

[Fisc00]   Fischer, D.; Filiatrault, A.; Folz, B.; Uang, C.; Seible, F.: *Shake Table Tests of a Two-Story Woodframe House*. Structural Systems Research Report No. SSRP 2000/15. Department of Structural Engineering, University of California, San Diego, 2000.

[Flat11]   Flatscher, G.; Schickhofer, G.: *Verbindungstechnik in BSP bei monotoner und zyklischer Beanspruchung – Statusbericht TU Graz. 9.Grazer Holzbau-Fachtagung, TU Graz, Austria* (2011).

[Flat12]   Flatscher, G.: *Versuchstechnische Betrachtung zyklisch beanspruchter Wandelemente in der Holz-Massivbauweise. 18. Internationales Holzbau-Forum, Garmisch-Partenkirchen.* 2012.

[Foll11]   Follesa, M.; Fragiacomo, M.; Lauriola, M. P.: *A proposal for revision of the current timber part (Section 8) of Eurocode 8 Part 1. Meeting 44 of the Working Commission W18-Timber Structures (CIB W18), Alghero, Italy.* CIB-W18/44-15-1. 2011.

[Folz01a]   Folz, B.; Filiatrault, A.: *SAWS - Version 1.0, A Computer Program for the Seismic Analysis of Woodframe Structures*. Structural Systems Research Project Report No. SSRP-2001/09. Department of Structural Engineering, UCSD, La Jolla, CA, 2001.

[Folz01b]   Folz, B.; Filiatrault, A.: *Cyclic analysis of wood shear walls. Journal of Structural Engineering* 127.4 (2001), pages 433–441.

[Folz04a]   Folz, B.; Filiatrault, A.: *Seismic analysis of woodframe structures. I: Model formulation. Journal of Structural Engineering* 130.9 (2004), pages 1353–1360.

[Folz04b]   Folz, B.; Filiatrault, A.: *Seismic analysis of woodframe structures. II: Model implementation and verification. Journal of Structural Engineering* 130.9 (2004), pages 1361–1370.

[FPIn]   FPInnovations: *A Canadian non-profit member organization for scientific research and technology transfer.* last access 08.07.2016. URL: https://fpinnovations.ca.

[Frag11]   Fragiacomo, M.; Dujic, B.; Sustersic, I.: *Elastic and ductile design of multi-storey crosslam massive wooden buildings under seismic actions. Engineering Structures* 33.11 (2011). Modelling the Performance of Timber Structures, pages 3043–3053.

[Free04]   Freeman, S. A.: *Review of the development of the capacity spectrum method. ISET Journal of earthquake technology* 41.1 (2004), pages 1–13.

[Free75]   Freeman, S.; Nicoletti, J.; Tyrell, J.: *Evaluations of existing buildings for seismic risk–A case study of Puget Sound Naval Shipyard, Bremerton, Washington. Proceedings of the 1st US National Conference on Earthquake Engineering.* Earthquake Engineering Research Institute Oakland, CA. 1975, pages 113–122.

[Free78]   Freeman, S. A.: *Prediction of response of concrete buildings to severe earthquake motion. ACI Special Publication* 55 (1978).

[Free98]   Freeman, S. A.: *The capacity spectrum method as a tool for seismic design. Proceedings of the 11th European conference on earthquake engineering.* 1998, pages 6–11.

[Gavr13]   Gavric, I.: *Seismic behaviour of cross-laminated timber buildings.* Ph.D. Thesis. University of Trieste, Italy, 2013.

[Gavr15]   Gavric, I.; Fragiacomo, M.; Ceccotti, A.: *Cyclic behavior of cross-laminated timber (CLT) wall systems: experimental tests and analytical prediction models. Structural Engineering* 141 (2015).

[Getz11]   Getzner the good vibrations company: *Übersicht Sylodyn.* 2011. URL: http://www.getzner.com.

[Ghob01]   Ghobarah, A.: *Performance-based design in earthquake engineering: State of development. Engineering Structures* 23.8 (2001), pages 878–884.

[Giar03]   Giardini, D.; Grünthal, G.; Shedlock, K.; Zhang, P.: *International Handbook of Earthquake & Engineering Seismology, International Geophysics Series 81 B.* chapter: *The GSHAP Global Seismic Hazard Map,* pages 1233–1239. Academic Press, Amsterdam, 2003. URL: http://www.gfz-potsdam.de/GSHAP.

[Gupt98]   Gupta, A.; Krawinkler, H.: *Effect of stiffness degradation on deformation demands for SDOF and MDOF structures. Proceedings of the 6th US National Conference on Earthquake Engineering.* 1998.

[Holt09]   Holtschoppen, B.: *Beitrag zur Auslegung von Industrieanlagen auf seismische Belastungen.* Dissertation. Lehrstuhl für Baustatik und Baudynamik, RWTH Aachen, 2009.

[Hris05]   Hristovski, V.; Stojmanovska, M.: *Experimental and Analytical Evaluation of the Racking Strength of Massive Wooden Wall Panels – Preliminary Project Phase. EE21C, Skopje-Ohrid, Macedonia* (2005).

[Hris12]   Hristovski, V.; Dujic, B.; Stojmanovska, M.; Mircevska, V.: *Full-scale shaking-table tests of XLam panel systems and numerical verification: Specimen 1. Journal of Structural Engineering* 139.11 (2012), pages 2010–2018.

[Humm12]   Hummel, J.; Seim, W.: *Wall-slab interaction of multi-storey timber buildings under earthquake impact. Proceedings of the 12th World Conference on Timber Engineering, Auckland, New Zealand.* 2012.

[Humm13]   Hummel, J.; Flatscher, G.; Seim, W.; Schickhofer, G.: *CLT wall elements under cyclic loading – details for anchorage and connection. The State-of-the-Art in CLT Research. COST Action FP1004: Focus Solid Timber Solutions – European Conference on Cross Laminated Timber (CLT), Graz, Austria.* 2013.

[Humm15]   Hummel, J.; Seim, W.: *Performance-based seismic design of light-frame structures – Proposed values for equivalent damping. INTER - International Network on Timber Engineering Research, Šibenik.* 48-15-1. 2015.

[Ierv10]   Iervolino, I.; Galasso, C.; Cosenza, E.: *REXEL: computer aided record selection for code-based seismic structural analysis. Bulletin of Earthquake Engineering* 8.2 (2010), pages 339–362.

[Kapp99]   Kappos, A.: *Evaluation of behaviour factors on the basis of ductility and overstrength studies. Engineering Structures* 21.9 (1999), pages 823–835.

[Kara13]   Karacabeyli, E.; Douglas, B.: *CLT Handbook - Cross laminated timber.* chapter: *Seismic performance of cross-laminated timber buildings.* 2013.

[Kawa99]   Kawai, N.: *Application of capacity spectrum method to timber houses. Meeting 32 of the Working Commission W18-Timber Structures (CIB W18), Graz, Austria.* CIB-W18/32-15-2. 1999.

[Kein67]   Keintzel, E.: *Die Berechnung der Schwingungen von Vielgeschossbauten mit Hilfe von kontinuierlichen Ersatzstrukturen. Die Bautechnik* (December 1967), pages 420–427.

[Koba11]   Kobayashi, K.; Yasumura, M.: *Evaluation of plywood sheathed shear walls with screwed joints tested according to ISO 21581. Meeting 44 of the Working Commission W18-Timber Structures (CIB W18), Alghero, Italy.* CIB-W18/44-15-8. 2011.

[Kraw01]   Krawinkler, H.; Parisi, F.; Ibarra, L.; Ayoub, A.; Medina, R.: *Development of a Testing Protocol for Woodframe Structures.* Technical report. CUREE Publication No. W-02. 2001.

[Kraw98]   Krawinkler, H.; Seneviratna, G.: *Pros and cons of a pushover analysis of seismic performance evaluation. Engineering structures* 20.4 (1998), pages 452–464.

[Kres11]   Kreslin, M.; Fajfar, P.: *The extended N2 method taking into account higher mode effects in elevation. Earthquake Engineering & Structural Dynamics* 40.14 (2011), pages 1571–1589.

[Kres12]   Kreslin, M.; Fajfar, P.: *The extended N2 method considering higher mode effects in both plan and elevation. Bulletin of Earthquake Engineering* 10.2 (2012), pages 695–715.

[Laur06]   Lauriola, M. P.; Sandhaas, C.: *Quasi-static and pseudo-dynamic tests on XLAM walls and buildings. COST E29 International Workshop on Earthquake Engineering on Timber Structures, Coimbra, Portugal.* 2006.

[Lind10]   Lindt, J. W. van de; Pei, S.: *SAPWood – Seismic Analysis Package for Woodframe Structures*. Version 2.0.1. 2010. URL: https://nees.org/resources/sapwood.

[Lour13]   Lourenco, P. B.; Branco, J. M.; Aranha, C.; Costa, A. C.; Candeias, P. X.; Bartolucci, C.: *Seismic Performance Of Multi-storey Timber Buildings – LegnoCase building. Timber Building Project*. Technical report. SERIES – Seismic Engineering Research Infrastructures For European Synergies, 2013.

[McKe]   McKenna, F.; Fenves, G. L.: *OpenSees – Open System for Earthquake Engineering Simulation, an object-oriented software framework*. Version 2.4.6. URL: http://opensees.berkeley.edu/.

[Merg15]   Mergos, P.; Beyer, K.: *Displacement based seismic design of symmetric single-storey wood-frame buildings with the aid of N2 method. Frontiers in Built Environment* 1.10 (2015).

[Mesk11]   Meskouris, K.; Hinzen, K.-G.; Butenweg, C.; Mistler, M.: *Bauwerke und Erdbeben*. 3. Auflage. Vieweg+Teubner Verlag Wiesbaden, 2011.

[Mira94]   Miranda, E.; Bertero, V. V.: *Evaluation of strength reduction factors for earthquake-resistant design. Earthquake Spectra* 10.2 (1994), pages 357–379.

[Mist06]   Mistler, M.: *Verformungsbasiertes seismisches Bemessungskonzept für Mauerwerksbauten*. Dissertation. Lehrstuhl für Baustatik und Baudynamik, RWTH Aachen, 2006.

[Müll84]   Müller, F.; Keintzel, E.: *Erdbebensicherung von Hochbauten*. 2., überarbeitete und erweiterte Auflage. Ernst und Sohn Verlag, Berlin, 1984.

[Muño08]   Muñoz, W.; Salenikovich, A.; Mohammad, M.; Quenneville, P.: *Determination of yield point and ductility of timber assemblies: in search for a harmonised approach. Proceedings of the 10th World Conference on Timber Engineering, Miyazaki, Japan*. 2008.

[Nass91]   Nassar, A. A.; Krawinkler, H.: *Seismic demands for SDOF and MDOF systems*. 95. John A. Blume Earthquake Engineering Center, Department of Civil Engineering, Stanford University, 1991.

[Newm59]   Newmark, N. M.: *A method of computation for structural dynamics. Journal of the engineering mechanics division* 85.3 (1959), pages 67–94.

[Newm82]   Newmark, N. M.; Hall, W. J.: *Earthquake Spectra and Design*. Engineering monographs on earthquake criteria, structural design, and strong motion records. Earthquake Engineering Research Institute, June 1982.

[Nord11]   Norda, H.; Butenweg, C.: *Möglichkeiten und Grenzen der Anwendbarkeit statisch nichtlinearer Verfahren nach DIN EN 1998-1. Bauingenieur* 86 (2011), pages 13–21.

[Opti]   Optimberquake: *Optimization of Timber Multi-storey Buildings against Earthquake impact*. last access 17.11.2015. URL: http://www.optimberquake.eu/.

[Pang07]   Pang, W.; Rosowsky, D. V.: *Direct displacement procedure for performance-based seismic design of multistory woodframe structures. Development of a Performance-Based Seismic Design Philosophy for Mid-Rise Woodframe Construction*. NEESWood Rep. No. NW 2. Zachry Department of Civil Engineering, Texas A&M University, 2007. URL: www.engr.colostate.edu/NEESWood.

[Pang08]   Pang, W.; Rosowsky, D.: *Performance-based seismic design of six-story wood-frame structure. Structural Engineering International* 18.2 (2008), pages 179–185.

[Pang10a]   Pang, W.; Rosowsky, D. V.; Pei, S.; van de Lindt, J. W.: *Simplified direct displacement design of six-story woodframe building and pretest seismic performance assessment. Journal of Structural Engineering* 136.7 (2010), pages 813–825.

[Pang10b]   Pang, W.; Rosowsky, D. V.; van de Lindt, J. W.; Pei, S.: *Simplified direct displacement design of six-story NEESWood Capstone Building and pre-test seismic performance assessment. Proceedings of the 11th World Conference on Timber Engineering, Riva del Garda, Italy.* 2010.

[Park89]   Park, R.: *Evaluation of ductility of structures and structural assemblages from laboratory testing. Bulletin of the New Zealand National Society for Earthquake Engineering* 22.3 (1989), pages 155–166.

[Paul90]   Paulay, T.; Bachmann, H.; Moser, K.: *Erdbebenbemessung von Stahlbetonhochbauten.* Birkhauser Basel-Bosten-Berlin, 1990.

[Paul92]   Paulay, T.; Priestley, M. J. N.: *Seismic design of reinforced concrete and masonry buildings.* A Wiley-Interscience publication. Wiley, New York, 1992.

[Pei10]   Pei, S.; van de Lindt, J. W.; Pryor, S. E.; Shimizu, H.; Isoda, H.: *Seismic Testing of a Full-Scale Mid-Rise Building: The NEESWood CapstoneTest - Development of a Performance-Based Seismic Design Philosophy for Mid-Rise Woodframe Construction.* Technical report. Report NW-04. Colorado State University, 2010.

[Pei12]   Pei, S.; Popovski, M.; van de Lindt, J. W.: *Seismic design of a multi-story cross laminated timber building based on component level testing. Proceedings of the 12th World Conference on Timber Engineering, Auckland, New Zealand.* 2012, pages 15–19.

[Pete96]   Petersen, C.: *Dynamik der Baukonstruktionen.* 1. Auflage, korrigierter Nachdruck 2000. Vieweg Verlagsgesellschaft, 1996.

[Piaz13a]   Piazza, M.; Tomasi, R.; Grossi, P.; Costa, A. C.; Candeias, P. X.: *Seismic Performance Of Multi-storey Timber Buildings – RubnerHaus building. Timber Building Project.* Technical report. SERIES – Seismic Engineering Research Infrastructures For European Synergies, 2013.

[Piaz13b]   Piazza, M.; Tomasi, R.; Grossi, P.; Costa, A. C.; Candeias, P. X.; Bartolucci, C.: *Seismic Performance Of Multi-storey Timber Buildings – LegnoCase building. Timber Building Project.* Technical report. SERIES – Seismic Engineering Research Infrastructures For European Synergies, 2013.

[Popo11]   Popovski, M.; Karacabeyli, E.; Ceccotti, A.: *CLT Handbook - Cross laminated timber.* chapter: *Seismic performance of cross-laminated timber buildings.* FPInnovations, 2011.

[Popo12a]   Popovski, M.; Karacabeyli, E.: *Seismic behaviour of cross-laminated timber structures. Proceedings of the 12th World Conference on Timber Engineering, Auckland, New Zealand.* 2012.

[Popo12b]   Popovski, M.; Karacabeyli, E.: *Seismic behaviour of cross-laminated timber structures. Proceedings of the 15th World Conference on Earthquake Engineering, Lisboa, Portugal.* 2012.

[Prak93]   Prakash, V.; Powell, G. H.; Campbell, S.: *Drain-3DX: Base Program Description and User Guide: Version 1.10.* 1993.

[Prie00]   Priestley, M.: *Performance based seismic design. Bulletin of the New Zealand Society for Earthquake Engineering* 33.3 (2000), pages 325–346.

[Prie07a]   Priestley, M.; Calvi, G.; Kowalsky, M.: *Direct displacement-based seismic design of structures. 2007 NZSEE Conference.* 2007.

[Prie07b]   Priestley, M.; Calvi, G.; Kowalsky, M.: *Displacement Based Seismic Design of Structures.* IUSS Press, 2007.

[Prie93]   Priestley, M. N.: *Myths and fallacies in earthquake engineering – conflicts between design and reality. Bulletin of the New Zealand National Society for Earthquake Engineering, New Zealand National Society for Earthquake Engineering* 26.3 (1993), pages 329–341.

[Rahn93]   Rahnama, M.; Krawinkler, H.: *Effects of soft soil and hysteresis model on seismic demands.* 108. John A. Blume Earthquake Engineering Center, 1993.

[Rayl77]   Rayleigh, J. W. S. B.: *The theory of sound.* Volume 1. Macmillan, 1877.

[Rina13]   Rinaldin, G.; Amadio, C.; Fragiacomo, M.: *A component approach for the hysteretic behaviour of connections in cross-laminated wooden structures. Earthquake Engineering & Structural Dynamics* 42.13 (2013), pages 2023–2042. URL: http://dx.doi.org/10.1002/eqe.2310.

[Rina16]   Rinaldin, G.; Fragiacomo, M.: *Non-linear simulation of shaking-table tests on 3-and 7-storey X-Lam timber buildings. Engineering Structures* 113 (2016), pages 133–148.

[Roso08]   Rosowsky, D. V.; Pang, W.: *Direct displacement design for multistory woodframe structures in seismic regions. Proceedings of the 10th World Conference on Timber Engineering, Miyazaki, Japan.* 2008.

[Salv96]   Salvitti, L. M.; Elnashai, A. S.: *Evaluation of behaviour factors for RC buildings by nonlinear dynamic analysis. Proceedings of the 11th World Conference on Earthquake Engineering, Acapulco, Mexico.* 1996.

[Sand06]   Sandhaas, C.: *Projekt SOFIE – Erdbebenverhalten von Häusern aus XLAM. 5.Grazer Holzbau-Fachtagung, TU Graz, Austria* (2006).

[Sand12]   Sandhaas, C.: *Erdbebenverhalten von mehrgeschossigen Gebäuden aus Brettsperrholz. Karlsruher Tage 2012-Holzbau: Forschung für die Praxis* (2012).

[Sche14]   Schellenberg, A.: *OpenSeesWiki.* last access 13.04.2016. 2014. URL: http://opensees.berkeley.edu/wiki/index.php/Single_Friction_Pendulum_Bearing_Element.

[Schi13]   Schickhofer, G.; Flatscher, G.; Costa, A. C.; Candeias, P. X.: *Seismic Performance Of Multi-storey Timber Buildings – TUGraz Building. Timber Building Project.* Technical report. SERIES – Seismic Engineering Research Infrastructures For European Synergies, 2013.

References

[Schm06]   Schmidt-Thomé, P.: *The Spatial Effects and Management of Natural and Technological Hazards in Europe*. Technical report. The ESPON Monitoring Committee and the partners of the projects mentioned, Luxemburg, 2006. URL: http://www.espon.lu.

[Scot10]   Scott, M. H.; Fenves, G. L.: *Krylov Subspace Accelerated Newton Algorithm: Application to Dynamic Progressive Collapse Simulation of Frames. Journal of Structural Engineering* 136.5 (2010), pages 473–480. URL: http://dx.doi.org/10.1061/(ASCE)ST.1943-541X.0000143.

[Seim11]   Seim, W.; Hummel, J.: *Optimberquake: Deliverable 1: Preliminary design and testing program*. Technical report. University of Kassel, 2011.

[Seim13a]   Seim, W.; Hummel, J.: *Optimberquake: Deliverable 2D: CLT wall elements – monotonic and cyclic testing*. Technical report. University of Kassel, 2013.

[Seim13b]   Seim, W.; Hummel, J.; Vogt, T.: *Optimberquake: Deliverable 2C: Anchoring units – monotonic and cyclic testing*. Technical report. University of Kassel, 2013.

[Seim14]   Seim, W.; Hummel, J.; Vogt, T.: *Earthquake design of timber structures – Remarks on force-based design procedures for different wall systems. Engineering Structures* 76 (2014), pages 124–137.

[Seim15]   Seim, W.; Kramar, M.; Pazlar, T.; Vogt, T.: *OSB and GFB as sheathing materials for timber-framed shear walls: Comparative study of seismic resistance. Journal of Structural Engineering* E4015004 (2015), pages 1–14.

[Sene97]   Seneviratna, G.; Krawinkler, H.: *Evaluation of inelastic MDOF effects for seismic design*. John A. Blume Earthquake Engineering Center, Stanford, 1997.

[Shib76]   Shibata, A.; Sozen, M. A.: *Substitute-structure method for seismic design in R/C. Journal of the Structural Division* 102.1 (1976), pages 1–18.

[Simp15]   Simpson Strong-Tie: *Profilkatalog – Qualitätsverbinder für Holzkonstruktionen*. 2014/15. URL: www.strongtie.de.

[Smit88]   Smith, J.: *Vibration of Structures: Applications in civil engineering design*. Chapman and Hall, 1988.

[Soze83]   Sozen, M. A.: *Lateral drift of reinforced concrete structures subjected to strong ground motions. Bulletin of the New Zealand National Society for Earthquake Engineering* 16.2 (1983).

[Stew87]   Stewart, W.: *The seismic design of plywood sheathed shear walls*. PhD thesis. University of Canterbury. Department of Civil Engineering, 1987.

[Stoj08]   Stojmanovska, M.; Hristovski, V.: *Experimental and analytical investigations of solid wooden wall panel elements subjected to lateral loads. Proceedings of 14th World Conference on Earthquake Engineering, Beijing, China* (2008).

[Sull04]   Sullivan, T.; Calvi, G.; Priestley, M.: *Initial stiffness versus secant stiffness in displacement based design. Proceedings of 13th World Conference on Earthquake Engineering, Vancouver, Canada*. 2004.

[Sull06]   Sullivan, T.; Priestley, M.; Calvi, G.: *Direct displacement-based design of frame-wall structures. Journal of earthquake engineering* 10.01 (2006), pages 91–124.

[Sust11] Sustersic, I.; Fragiacomo, M.; Dujic, B.: *Influence of connection properties on the ductility and seismic resistance of multi-storey cross-lam buildings. Meeting 44 of the Working Commission W18-Timber Structures (CIB W18), Alghero, Italy.* CIB-W18/44-15-1. 2011.

[Sust12] Sustersic, I.; Fragiacomo, M.; Dujic, B.: *Influence of the connection behaviour on the seismic resistance of multi-storey crosslam buildings. Proceedings of the 12th World Conference on Timber Engineering, Auckland, New Zealand.* 2012.

[Sust15] Sustersic, I.; Fragiacomo, M.; Dujic, B.: *Seismic Analysis of Cross-Laminated Multistory Timber Buildings Using Code-Prescribed Methods: Influence of Panel Size, Connection Ductility, and Schematization. Journal of Structural Engineering* 142.4 (2015), pages 1–14.

[Teib09] Teibinger, M.; Dolezal, F.; Metzinger, I.: *Deckenkonstruktionen für den mehrgeschossigen Holzbau – Schall- und Brandschutz Detailkatalog.* Technischer Bericht. Holzforschung Austria, 2009.

[Thie13] Thiel, A.: *ULS and SLS design of CLT and its implementation in the CLTdesigner. The State-of-the-Art in CLT Research. COST Action FP1004: Focus Solid Timber Solutions – European Conference on Cross Laminated Timber (CLT), Graz, Austria.* Edited by R. Harris; A. Ringhofer; G. Schickhofer. 2013.

[Uriz10] Uriz, P.: *OpenSeesWiki.* last access 13.04.2016. 2010. URL: http://opensees.berkeley.edu/wiki/index.php/SAWS_Material.

[Vidi94] Vidic, T.; Fajfar, P.; Fischinger, M.: *Consistent inelastic design spectra: strength and displacement. Earthquake Engineering and Structural Dynamics* 23 (1994), pages 507–521.

[Vogt12] Vogt, T.; Hummel, J.; Seim, W.: *Timber framed wall elements under cyclic loading. Proceedings of the 12th World Conference on Timber Engineering, Auckland, New Zealand.* 2012.

[Wall13] Wallner-Novak, M.; Koppelhuber, J.; Pock, K.: *Brettsperrholz Bemessung-Grundlagen für Statik und Konstruktion nach Eurocode. Cross Laminated Timber Design – Construction and Design according to Eurocode. Vienna, Austria, proHolz Austria* (2013).

[Werk08] Werkle, H.: *Finite Elemente in der Baustatik - Statik und Dynamik der Stab- und Flächentragwerke.* 3., aktualisierte und erweiterte Auflage. Vieweg & Sohn Verlag Wiesbaden, 2008.

[Wrig08] Wriggers, P.: *Nonlinear finite element methods.* Springer Science & Business Media, 2008.

Standards and Guidelines

[ASCE 7]   *Minimum design loads for buildings and other structures.* American Society of Civil Engineers. 2010.

[ASTM E 2126-11]   *Standard Test Methods for Cyclic (Reversed) Load Test for Shear Resistance of Vertical Elements of the Lateral Force Resisting Systems for Buildings.* American Society for Testing and Materials. ASTM International, West Conshohocken, PA, USA. 2011.

[ATC-40]   *Seismic evaluation and retrofit of concrete buildings.* Applied Technology Council, Redwood City. 1996.

[DIN EN 1998-1]   *Eurocode 8: Design of structures for earthquake resistance – Part 1: General rules, seismic actions and rules for buildings (German version EN 1998-1:2004 + AC:2009).* European Committee for Standardization, Brussels. December 2010.

[DIN EN 1998-1/NA]   *National Annex – Nationally determined parameters – Eurocode 8: Design of structures for earthquake resistance – Part 1: General rules, Seismic actions and rules for buildings.* European Committee for Standardization, Brussels. January 2011.

[EN 12512]   *Timber structures – test methods – cyclic testing of joints made with mechanical fasteners.* 2001.

[EN 1990]   *Eurocode – Basis of structural design.* European Committee for Standardization, Brussels. October 2002.

[EN 1991-1-1]   *Eurocode 1: Actions on structures – Part 1-1: General actions – Densities, self-weight, imposed loads for buildings.* European Committee for Standardization, Brussels. October 2002.

[EN 1995-1-1]   *Eurocode 5: Design of timber structures – Part 1-1: General – Common rules and rules for buildings.* European Committee for Standardization, Brussels. September 2008.

[EN 1998-1]   *Eurocode 8: Design of structures for earthquake resistance – Part 1: General rules, seismic actions and rules for buildings.* European Committee for Standardization, Brussels. December 2010.

[EN 1998-3]   *Eurocode 8: Design of structures for earthquake resistance – Part 3: Assessment and retrofitting of buildings.* European Committee for Standardization, Brussels. April 2006.

[EN 26891]   *Timber structures – Joints made with mechanical fasteners - General principles for the deformation of strength and deformation characteristics (ISO 6891:1983).* July 1991.

[FEMA 273]   *NEHRP guidelines for the seismic rehabilitation of buildings.* Federal Emergency Management Agency, Washington DC. 1996.

[FEMA 274]   *NEHRP commentary on the guidelines for the seismic rehabilitation of buildings.* Federal Emergency Management Agency, Washington DC. 1997.

[FEMA 440]   *Improvement of nonlinear static seismic analysis procedures.* Federal Emergency Management Agency, Redwood City. 2009.

[FEMA P695]   *Quantification of Building Seismic Performance Factors.* Federal Emergency Management Agency, Washington DC. 2009.

[ISO 16670]   *Timber structures – Joints made with mechanical fasteners - Quasi-static reversed-cyclic test method.* December 2003. 2003.

[ISO 21581]   *Timber structures – Static and cyclic lateral load test method for shear walls.* June 2010. 2010.

A Seismic design of reference structures

In this chapter the preliminary seismic design of the the reference structures is demonstrated exemplarily. For the preliminary design it is assumed that perpendicular walls are not connected which refers to the shear wall type (SWT) configuration. Furthermore, the lateral load resisting system is composed of single wall elements (SWE configuration). The configurations are explained in section 5.3.1.

A.1 Resistance of connectors

For the design of the reference structures the load-bearing capacity of the connectors from testing (see sections 4.2) were applied. The maximum loads of angle brackets and hold downs are given in Table 4.1. The load-bearing capacity of connection with self-tapping screws can be found in sections 3.1.2 and 3.1.4. For preliminary design of the connection between slab and wall on the top the shear resistance of the configuration SC-WS is applied. The average of the maximum loads to each configuration are summarised in Table A.1. To account for force interaction (see section 5.2.1) maximum loads were reduced by 15 %. Finally, the resistance F_R which is used for preliminary design was fixed close to the reduced maximum loads. The same resistance was used for hold downs anchored to a concrete base and for anchoring on a CLT slab.

	F_{max} [kN]	$0.85 \cdot F_{max}$ [kN]	F_R [kN]	loading direction	connection with
AB-St-S	36.1	30.6	30.0	1 (shear)	AB between CLT wall and concrete base
AB-Ti-S	23.8	20.2	20.0	1 (shear)	AB between CLT wall and CLT slab
HD-St-S/ HD-Ti-S	9.0	7.7	7.5	1 (shear)	HD between CLT wall and concrete base/ CLT slab
HD-St-T	66.7	56.7	55.0	2 (tension)	HD between CLT wall and concrete base
HD-Ti-T	64.5	54.8		2 (tension)	HD between CLT wall and CLT slab
SC-WS	8.2	7.0	7.0	1 (shear)	SC between CLT wall (top) and CLT slab

AB – angle bracket, HD – hold down, SC – self-tapping screw

Table A.1: Load-bearing capacity and resistance of connectors

A.2 Structural mass

The masses of the structure were determined by means of the information as given in Table A.2 (cf. section 5.3.1).

	in X-direction	in Y-direction	storey height
Dimensions [m]	12.5	7.5	2.75
Walls [m]	$6 \times 2.5 = 15$	$4 \times 2.5 = 10$	
Gravity loads [kN/m^2]	roof slab	floor slab	walls
dead load	1.0	3.0	1.5
live load	–	1.5	–

Table A.2: Dimensions and gravity loads of reference structures

The mass which should be taken into account for seismic action is defined by Eq. (5.13). Accordance to [EN 1998-1] and [EN 1990] the permanent share of the live load was considered with 24 % ($\varphi = 0.8$, $\psi_2 = 0.3$). With the area of the floor ($12.5 \cdot 7.5 = 93.75$), the total length of the walls (see Tab. A.2) and the gravity constant of 9.81 m/s^2 the masses are determined (see Tab. A.3). The masses are concentrated at the roof and the floor level. That yields the lumped masses as given in Table A.4.

		mass [t]
dead load roof slab:	$93.75 \cdot 1.0/9.81$	$= 9.6$
dead load floor slab:	$93.75 \cdot 3.0/9.81$	$= 28.7$
live load floor slab:	$0.8 \cdot 0.3 \cdot 93.75 \cdot 1.5/9.81$	$= 3.4$
dead load walls:	$(15 + 10) \cdot 2.75 \cdot 1.5/9.81$	$= 10.5$

Table A.3: Masses from dead load and live load
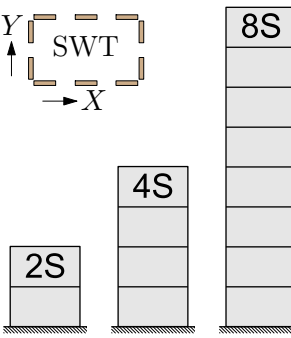
level		m_i [t]
roof:	$9.6 + 10.5/2$	$= 14.9$
floor:	$28.7 + 10.5 + 3.4$	$= 42.6$

Table A.4: Lumped masses in roof and floor level

A.3 Structural period

The procedure which was used to determine consistent structural periods is explained in section 5.3.1. Table A.5 presents the final fundamental periods of the structures as result of this procedure.

T_1	2S	4S	8S
X	0.36 s	0.66 s	1.68 s
Y	0.42 s	0.76 s	1.78 s

Table A.5: Final fundamental periods of the reference structures with two, four and eight storeys for the SWT-SWE configuration

A.4 Seismic loads and reactions

In the following, the determination of the seismic loads and the corresponding reactions is demonstrated exemplarily for the two-storey reference structure. The final fundamental periods are used here. However, loads and reactions were calculated in the same manner when the fundamental periods was estimated initially.

The lateral force method is used to design the structure (see section 2.4.2). The spectral acceleration is read from the design spectrum. The design spectrum was already defined in section 5.3.1.
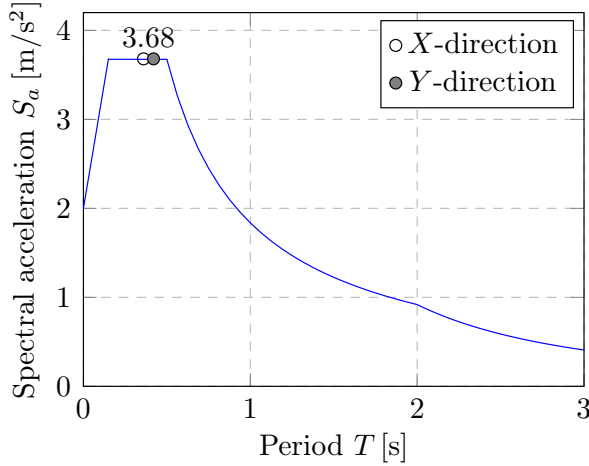
design spectrum – details
type 1, soil class B
$a_g = 0.25\,\mathrm{g}$
$q = 2.0$

Figure A.1: Design spectrum and spectral acceleration for the two-storey SWT-SWE structure

The base shear is calculated with Eq. (2.12). According to [EN 1998-1] the modal correction factor λ is determined by Eq. (A.1)

$$\lambda = \begin{cases} 0.85 & \text{for } T_1 \leq 2 \cdot T_C \text{ and } n < 2 \\ 1.0 & \text{for any other case} \end{cases} \tag{A.1}$$

Here, the number of storeys n is 2. For that reason λ is taken into account with 1.0. Using the masses as given in Table A.4 the base shear results for both directions to

$$F_{b,X} = F_{b,Y} = S_a(T_1) \cdot m \cdot \lambda = 3.68 \cdot (14.9 + 42.6) \cdot 1.0 = 211.6\,[\text{kN}]. \tag{A.2}$$

The equivalent lateral forces are determined with Eq. (2.13) as presented in Table A.6.

storey i	z_i [m]	m_i [t]	$z_i \cdot m_i$	$\dfrac{z_i \cdot m_i}{\sum z_j \cdot m_j}$	F_i [kN]
2	5.5	14.9	82	41.2%	87.2
1	2.75	42.6	117	58.8%	124.4
$\sum$		57.5	199		211.6

Table A.6: Determination of equivalent lateral forces F_i

The lateral loads are distributed to the shear walls proportional to their length. Here, it is assumed that the lateral stiffness is dominates by shear and sliding. Since all walls have

the same length, each wall get the same lateral load. Thus, the lateral load for each wall in each level F_j is obtained by

$$F_j = F_i/n_w. \tag{A.3}$$

The number of walls n_w is 6 in X-direction and 4 in Y-direction as illustrated in Figure A.3. The resulting lateral load for shear walls in X- and Y-direction are documented in Table A.7. Furthermore, Table A.7 includes the reactions to the external loads. The determination of the reactions is explained below.

storey i	z_i [m]	F_j [kN]	V_i [kN]	R_i [kN]	M_i [kNm]	Z_i [kN]	F_j [kN]	V_i [kN]	R_i [kN]	M_i [kNm]	Z_i [kN]
		X-direction, walls 1 to 3 and 6 to 8					Y-direction, walls 4, 5, 9 and 10				
2	5.50	14.5					21.8				
	2.75		14.5	15.1	39.9	8.4		21.8	13.6	59.9	17.2
1	2.75	20.7					31.1				
	0.00		35.2	41.7	136.7	33.8		52.9	34.7	205.3	64.8

Table A.7: Forces and reactions for walls in X- and Y-direction
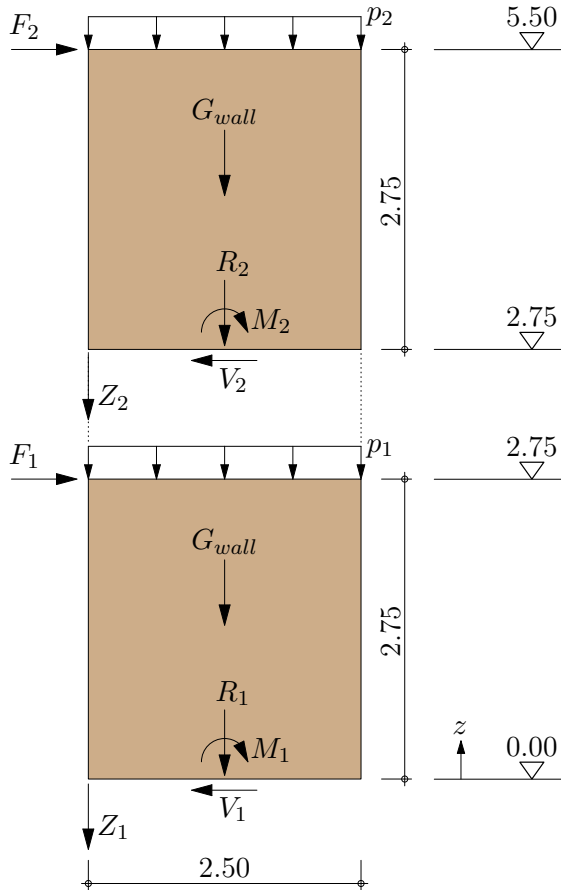
Figure A.2: External loads and reactions at two-storey shear wall

$$G_{wall} = 2.5 \cdot 2.75 \cdot 1.5 = 10.3 \, \text{kN}$$

for wall in X-direction

$b_{ef,X} = 0.5 \cdot 7.5/2 = 1.88 \, \text{m}$
$p_2 \quad = 1.88 \cdot 1.0 = 1.9 \, \text{kN/m}$
$p_1 \quad = 1.88 \cdot (3.0 + 0.3 \cdot 1.5) = 6.5 \, \text{kN/m}$

for wall in Y-direction

$b_{ef,Y} = 0.5 \cdot 2.5 = 1.25 \, \text{m}$
$p_2 \quad = 1.25 \cdot 1.0 = 1.3 \, \text{kN/m}$
$p_1 \quad = 1.25 \cdot (3.0 + 0.3 \cdot 1.5) = 4.3 \, \text{kN/m}$

Table A.8: Data – vertical load for shear walls

For the estimation of the vertical loads which act upon the external walls the influence length b_{ef} is needed. The influence length for walls in X- and Y-direction is illustrated in

Figure A.3. Figure A.2 shows the external loads and the reactions

p_i – vertical load on the top of the wall in level i,
G_{wall} – resultant dead load of the wall,
R_i – resultant vertical load at the bottom of the wall in level i,
F_j – lateral load on the top of the wall in level i,
V_i – shear force in level i,
M_i – overturning moment at the bottom of the wall in level i,
Z_i – tensile force at the bottom of the wall in level i

for the two-storey shear wall. The vertical loads and the dead load of the wall are documented in Table A.8. The determination of the reactions in terms of shear and tensile forces are illustrated in Table A.9. To determine the tensile force Z_i the inner lever is assumed equal to the wall length of 2.5 m.

	wall in X-direction		wall in Y-direction	
V_2 [kN]	F_2	$= 14.5$	F_2	$= 21.8$
R_2 [kN]	$p_2 \cdot 2.5 + G_{wall}$	$= 15.1$	$p_2 \cdot 2.5 + G_{wall}$	$= 13.6$
M_2 [kNm]	$F_2 \cdot 2.75$	$= 39.9$	$F_2 \cdot 2.75$	$= 59.9$
Z_2 [kN]	$\dfrac{M_2}{2.5} - \dfrac{R_2}{2}$	$= 8.4$	$\dfrac{M_2}{2.5} - \dfrac{R_2}{2}$	$= 17.2$
V_1 [kN]	$F_1 + F_2$	$= 35.2$	$F_1 + F_2$	$= 52.9$
R_1 [kN]	$p_1 \cdot 2.5 + G_{wall} + R_2$	$= 41.7$	$p_1 \cdot 2.5 + G_{wall} + R_2$	$= 34.7$
M_1 [kNm]	$F_2 \cdot 5.5 + F_1 \cdot 2.75$	$= 136.7$	$F_2 \cdot 5.5 + F_1 \cdot 2.75$	$= 205.3$
Z_1 [kN]	$\dfrac{M_1}{2.5} - \dfrac{R_1}{2}$	$= 33.8$	$\dfrac{M_1}{2.5} - \dfrac{R_1}{2}$	$= 64.8$

Table A.9: Determination of reactions – shear force V and tensile force Z
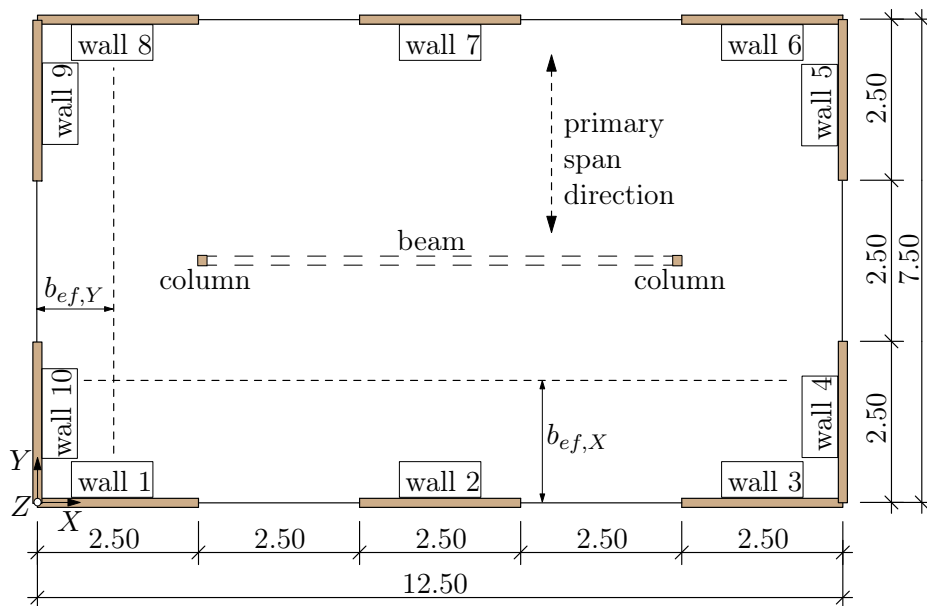
Figure A.3: Floor plan of the reference structure and influence length b_{ef}

A.5 Design of connections

Shear and tensile forces are now be used to design the connections, respectively to determine the required number of connectors. The resistance F_R of the connectors is given in Table A.1. As the shear walls are anchored to the concrete base in the first floor and on the CLT slab in the second floor, different values for the resistance were applied (see Tab. A.10). The tensile resistance of the angle brackets were not considered for preliminary design.

storey i	$F_{R,ab,1}$ [kN]	$F_{R,hd,1}$ [kN]	$F_{R,hd,2}$ [kN]	$F_{R,sc,1}$ [kN]
2	20.0	7.5	55.0	7.0
1	30.0	7.5	55.0	7.0

Table A.10: Resistance of connectors in the first and second storey

The number of connectors n_{con} was determined in this way that the degree of utilisation η becomes less than or equal to 1.0. The index *con* stands for the respective connector (*ab* - angle bracket, *hd* - hold down, *sc* - self-tapping screw).

$$\eta_s = \frac{V}{n_{ab} \cdot F_{R,ab,1} + 2 \cdot n_{hd} \cdot F_{R,hd,1}} \leq 1.0 \tag{A.4}$$

$$\eta_z = \frac{Z}{n_{hd} \cdot F_{R,hd,2}} \leq 1.0 \tag{A.5}$$

$$\eta_{sc} = \frac{F_d}{n_{sc} \cdot F_{R,sc,1}} \leq 1.0 \tag{A.6}$$

$$F_d = \gamma_{Rd} \cdot \Omega \cdot F_{d,AE} \tag{A.7}$$

with

$$\Omega = \frac{1}{\eta_s} \tag{A.8}$$

and

$$F_{d,AE} = V \tag{A.9}$$

— connection with self-tapping screws, with overstrength $\gamma_{Rd} = 1.3$

☐ ductile connection
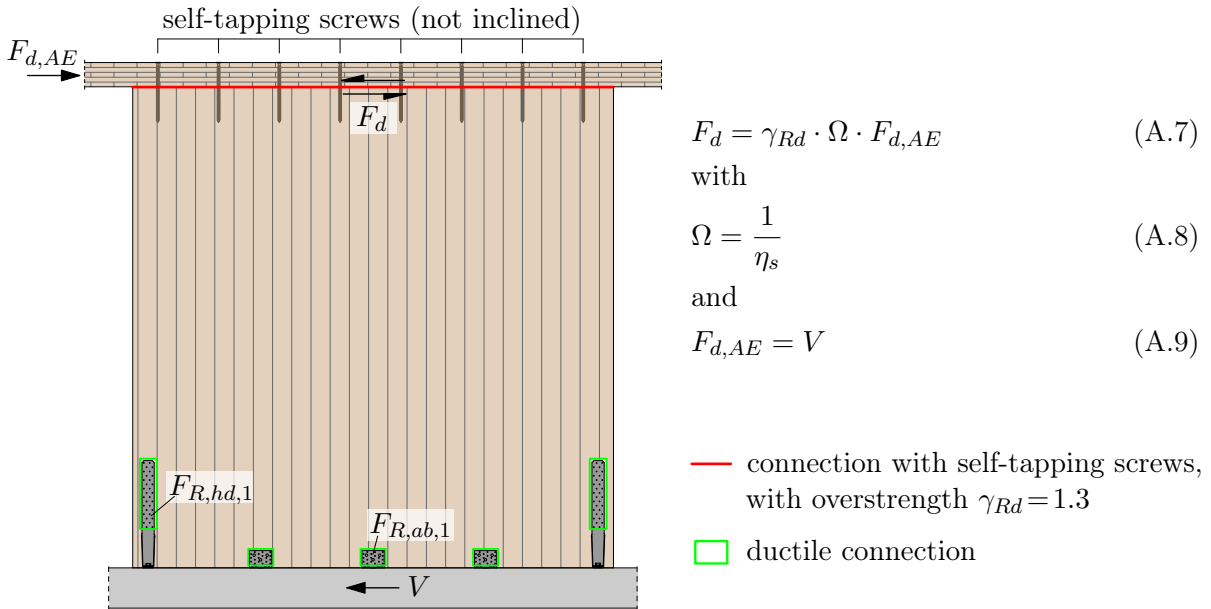
Figure A.4: Lateral load F_d for capacity design of the screw connection between wall and slab

As mentioned in section 5.3.1 the principles of capacity design were considered to design the screw connection between wall and slab. The lateral load F_d the screw connection must be design for is calculated by Eq. (A.7). The overstrength factor γ_{Rd} is taken into account with 1.3 as discussed in section 5.3.1. The overdesign factor Ω is determined by Eq. (A.8).

storey i	X-direction, walls 1 to 3 and 6 to 8						Y-direction, walls 4, 5, 9 and 10					
	V_i [kN]	n_{ab} [–]	η_s [–]	Z_i [kN]	n_{hd} [–]	η_z [–]	V_i [kN]	n_{ab} [–]	η_s [–]	Z_i [kN]	n_{hd} [–]	η_z [–]
2	14.5	0	0.97	8.4	1	0.15	21.8	1	0.62	17.2	1	0.31
1	35.2	1	0.78	33.8	1	0.61	52.9	1	0.88	64.8	2	0.59

Table A.11: Design of anchoring for shear and tensile forces for the two-storey structure
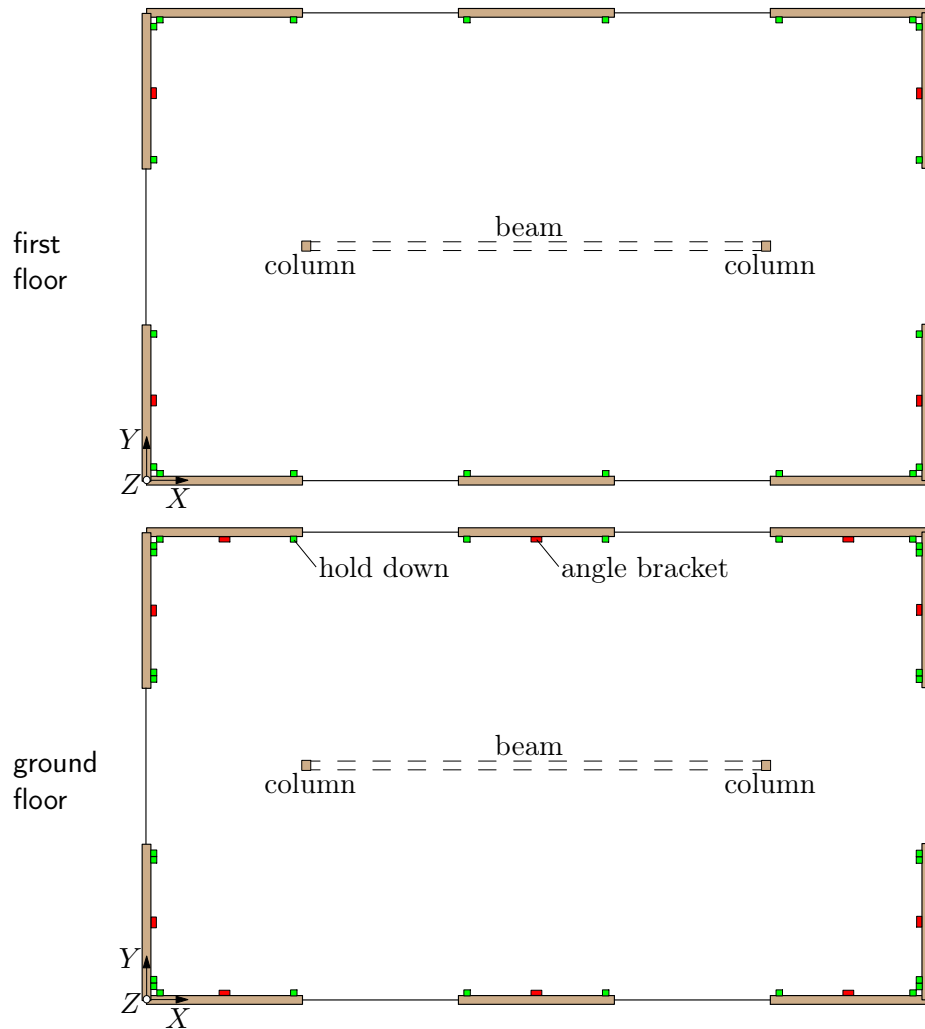
Figure A.5: Floor plan – location and number of connectors for the two-storey structure

	X-direction, walls 1 to 3 and 6 to 8			Y-direction, walls 4, 5, 9 and 10		
storey i	$F_{d,i}$ [kN]	n_{sc} [–]	η_{sc} [–]	$F_{d,i}$ [kN]	n_{sc} [–]	η_{sc} [–]
2	19.5	3	0.93	45.5	7	0.93
1	58.5	9	0.93	78.0	11	1.01

Table A.12: Design of screw connection between wall and slab for the two-storey structure

A.6 Results for the four- and eight-storey structure

The same procedure as for the two-storey building has been used to design the connections of the four- and eight-storey structure. The results are documented in the following subsections.

A.6.1 Four-storey structure

The base shear of the four-storey structure was calculated to

$$F_{b,X} = 328.1 \,[\text{kN}]$$
$$F_{b,Y} = 291.6 \,[\text{kN}]$$

for the X- and the Y-direction, respectively.

	X-direction, walls 1 to 3 and 6 to 8						Y-direction, walls 4, 5, 9 and 10					
storey i	V_i [kN]	n_{ab} [–]	η_s [–]	Z_i [kN]	n_{hd} [–]	η_z [–]	V_i [kN]	n_{ab} [–]	η_s [–]	Z_i [kN]	n_{hd} [–]	η_z [–]
4	10.3	0	0.69	3.8	1	0.07	13.8	0	0.92	8.4	1	0.15
3	32.5	1	0.93	26.2	1	0.48	43.3	2	0.79	45.5	1	0.83
2	47.3	1	0.95	65.0	2	0.59	56.5	2	0.81	97.0	2	0.88
1	54.7	1	0.91	111.8	2	1.02	63.0	1	0.84	155.8	3	0.94

Table A.13: Design of anchoring for shear and tensile forces for the four-storey structure

	X-direction, walls 1 to 3 and 6 to 8			Y-direction, walls 4, 5, 9 and 10		
storey i	$F_{d,i}$ [kN]	n_{sc} [–]	η_{sc} [–]	$F_{d,i}$ [kN]	n_{sc} [–]	η_{sc} [–]
4	19.5	3	0.93	19.5	3	0.93
3	45.5	7	0.93	71.5	10	1.02
2	65.0	10	0.93	91.0	13	1.00
1	78.0	12	0.93	97.5	14	0.99

Table A.14: Design of screw connection between wall and slab for the four-storey structure

A.6.2 Eight-storey structure

The base shear of the eight-storey structure was calculated to

$$F_{b,X} = 342.8 \, [\text{kN}]$$
$$F_{b,Y} = 323.5 \, [\text{kN}]$$

for the X- and the Y-direction, respectively.

	X-direction, walls 1 to 3 and 6 to 8						Y-direction, walls 4, 5, 9 and 10					
storey	V_i	n_{ab}	η_s	Z_i	n_{hd}	η_z	V_i	n_{ab}	η_s	Z_i	n_{hd}	η_z
i	[kN]	[–]	[–]	[kN]	[–]	[–]	[kN]	[–]	[–]	[kN]	[–]	[–]
8	5.2	0	0.35	0.0	1	0.00	7.4	0	0.49	1.4	1	0.03
7	18.2	1	0.52	4.9	1	0.09	25.8	1	0.74	19.2	1	0.35
6	29.3	1	0.84	23.8	1	0.43	41.6	1	0.83	54.4	2	0.49
5	38.6	1	0.77	53.0	2	0.48	54.7	2	0.78	104.0	2	0.95
4	46.0	1	0.92	90.3	2	0.82	65.2	2	0.77	165.2	3	1.00
3	51.6	1	0.79	133.8	3	0.81	73.1	2	0.64	235.1	5	0.85
2	55.3	1	0.69	181.3	4	0.82	78.4	2	0.60	310.7	6	0.94
1	57.2	1	0.64	230.9	4	1.05	81.0	2	0.56	389.3	7	1.01

Table A.15: Design of anchoring for shear and tensile forces for the eight-storey structure

	X-direction, walls 1 to 3 and 6 to 8			Y-direction, walls 4, 5, 9 and 10		
storey	$F_{d,i}$	n_{sc}	η_{sc}	$F_{d,i}$	n_{sc}	η_{sc}
i	[kN]	[–]	[–]	[kN]	[–]	[–]
8	19.5	3	0.93	19.5	3	0.93
7	45.5	7	0.93	45.5	7	0.93
6	45.5	7	0.93	65.0	9	1.03
5	65.0	10	0.93	91.0	13	1.00
4	65.0	10	0.93	110.5	16	0.99
3	84.5	13	0.93	149.5	21	1.02
2	104.0	15	0.99	169.0	24	1.01
1	117.0	17	0.98	188.5	27	1.00

Table A.16: Design of screw connection between wall and slab for the eight-storey structure

B Set of ground motion records

In this chapter the ground motion records which were incorporated for nonlinear time history analyses of SDOF systems and reference structures will be presented. Information to the earthquake event which corresponds the ground motion record is summarised in Table B.1. The accelerograms of each record are depicted in Figures B.1 to B.30.

Beyond the name of the earthquake, the station where the accelerogram was recorded and the date of the earthquake the following data are given in Table B.1:

Comp. – component: east-west (EW) or north-south (NS),
M_w – magnitude,
R – epicentral distance,
PGA – original peak ground acceleration,
SF – scale factor to scale the record to a PGA of 0.3g.
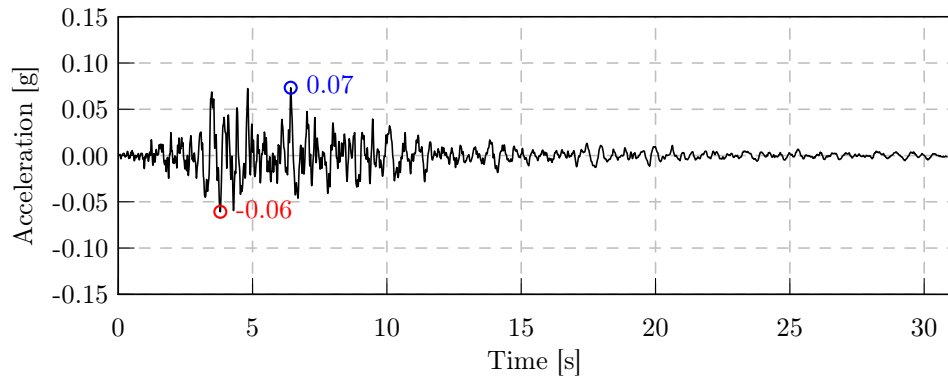
Figure B.1: Record 000170x
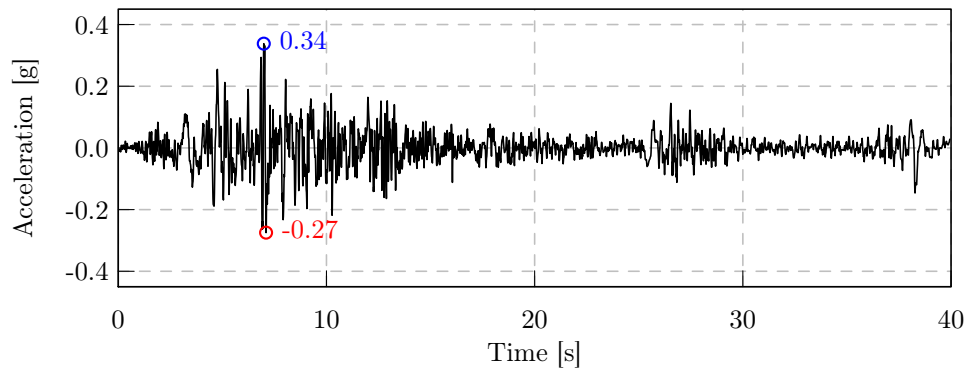
Figure B.2: Record 000182x

| ID	Station ID	Earthquake Name	Date	Comp.	M_w [–]	R [km]	PGA [m/s²]	SF
000170x	ST46	Basso Tirreno	15.04.1978	EW	6.0	18.0	0.72	4.10
000182x	ST54	Tabas	16.09.1978	EW	7.3	12.0	3.32	0.89
000182y	ST54	Tabas	16.09.1978	NS	7.3	12.0	3.78	0.78
000199y	ST67	Montenegro	15.04.1979	NS	6.9	16.0	3.56	0.83
000600y	ST223	Umbria Marche	26.09.1997	NS	6.0	22.0	1.04	2.83
006263y	ST2484	South Iceland	17.06.2000	NS	6.5	7.0	5.02	0.59
006326y	ST2496	South Iceland (aftershock)	21.06.2000	NS	6.4	14.0	1.14	2.58
006341x	ST2497	South Iceland (aftershock)	21.06.2000	EW	6.4	20.0	0.50	5.84
006497y	ST3133	Duzce 1	12.11.1999	NS	7.2	31.0	1.01	2.92
007329x	ST87	Faial	09.07.1998	EW	6.1	11.0	4.12	0.71
IN0022y	SMN015	W Tottori Prefecture	06.10.2000	NS	6.6	19.0	1.52	1.93
IN0075y	KGS004	NW Kagoshima Prefecture	02.04.1997	NS	5.4	12.3	0.98	2.99
IN0080x	KGS004	NW Kagoshima Prefecture	13.05.1997	EW	6.0	12.0	1.22	2.42
IN0114x	ST108	South Iceland	17.06.2000	EW	6.5	13.2	1.24	2.38
IN0145y	SZO016	S Suruga Bay	10.08.2009	NS	6.2	18.5	3.13	0.94
IN0278y	NIG022	MID NIIGATA PREF	11.03.2011	NS	5.6	26.4	0.57	5.18
IN0311x	MRN	EMILIA Pianura Padana	18.05.2012	EW	6.1	13.4	2.57	1.14
IN0312x	MRN	EMILIA Pianura Padana	29.05.2012	EW	6.0	3.6	2.23	1.32
IN0313x	SAN0	EMILIA Pianura Padana	29.05.2012	EW	6.0	4.7	1.71	1.72
IN0313y	SAN0	EMILIA Pianura Padana	29.05.2012	NS	6.0	4.7	2.17	1.35
IN0317y	MOG0	EMILIA Pianura Padana	29.05.2012	NS	6.0	16.4	1.68	1.75
IN0335x	TPLC	Darfield	03.09.2010	EW	7.1	23.6	2.74	1.07
IN0412x	HEC	Hector Mine	16.10.1999	EW	7.1	28.6	3.30	0.89
IN0413y	ALT	Irpinia	23.11.1980	NS	6.9	23.8	0.55	5.36
IN0426x	BUI	Friuli 3rd shock	15.09.1976	EW	5.9	11.6	0.91	3.23
IN0446x	EC05	Imperial Valley	15.10.1979	EW	6.5	27.7	3.71	0.79
IN0449x	WSM	Superstition Hills	24.11.1987	EW	6.6	19.5	1.69	1.75
IN0458x	ST24087	Northridge	17.11.1994	EW	6.7	11.0	3.37	0.87
IN0464y	ST5108	Northridge	17.11.1994	NS	6.7	14.7	2.28	1.29
KG0001x	Kalamata	Kalmata (Greece)	09.13.1986	NS	6.2	6.5	2.31	1.28

	records applied for NTHA on reference structures

Table B.1: Ground motion record applied for time history analyses
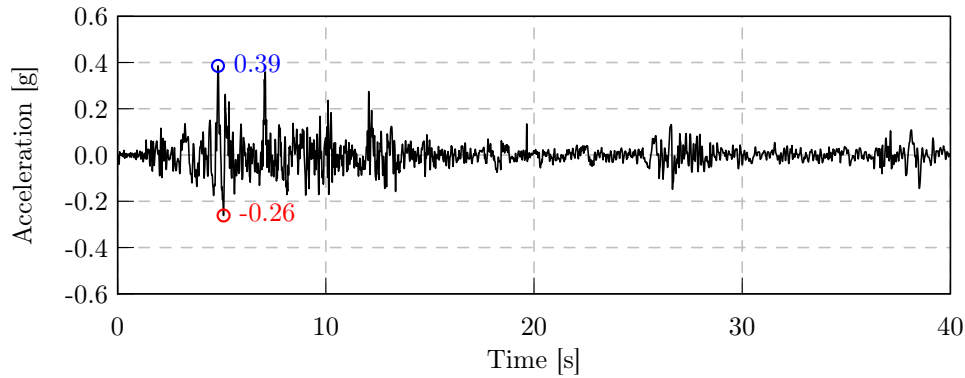
Figure B.3: Record 000182y
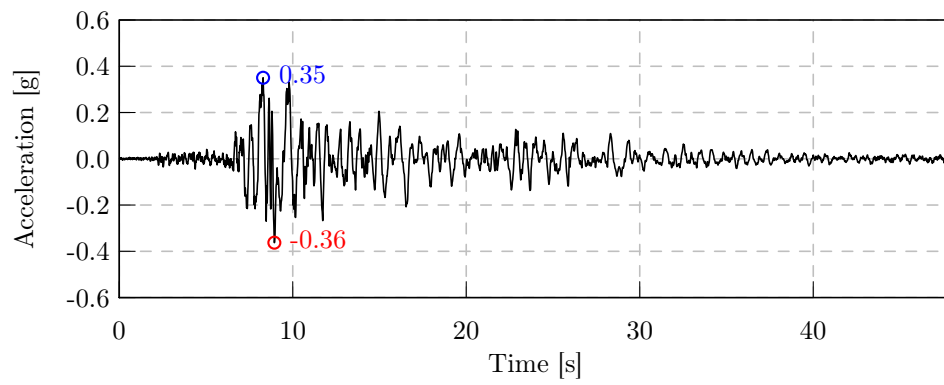
Figure B.4: Record 000199y
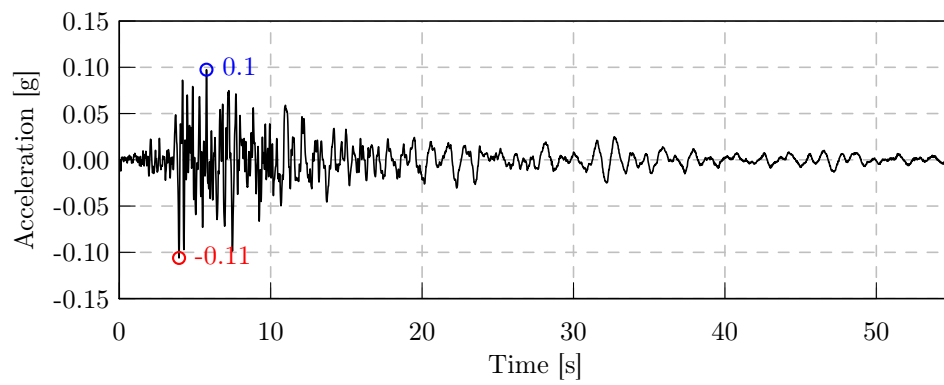
Figure B.5: Record 000600y
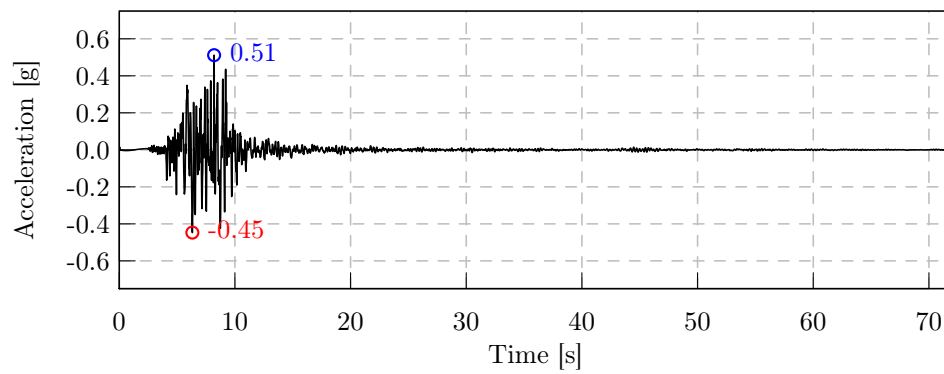
Figure B.6: Record 006263y
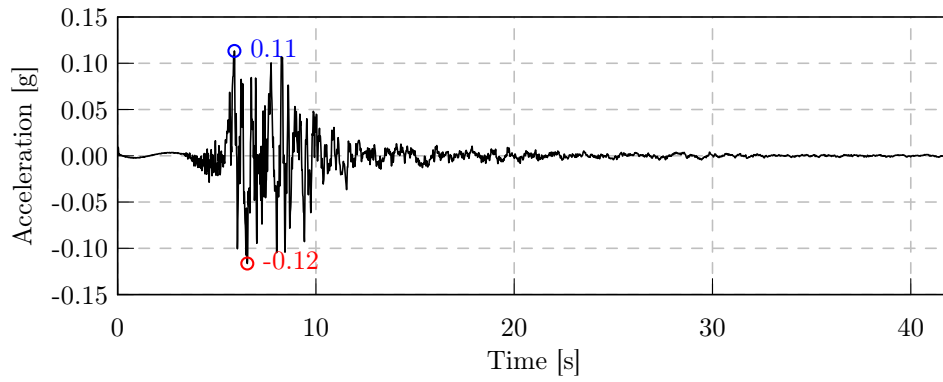
Figure B.7: Record 006326y
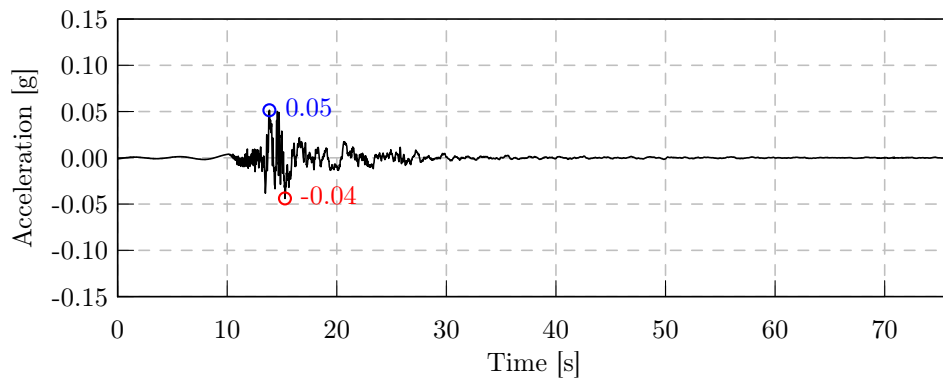
Figure B.8: Record 006341x
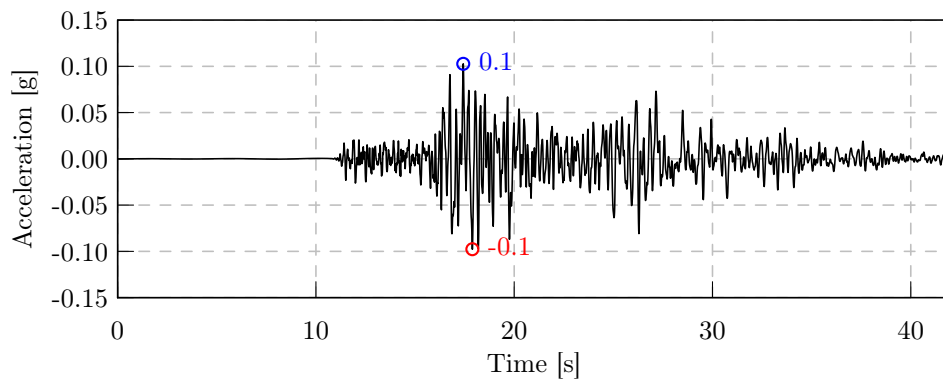
Figure B.9: Record 006497y
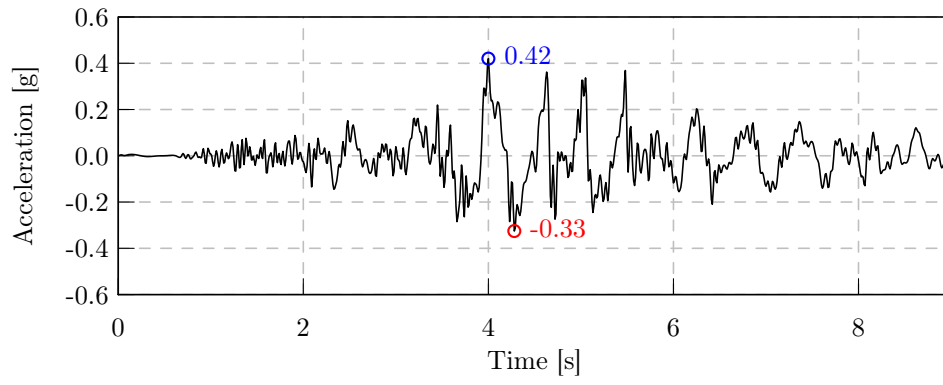
Figure B.10: Record 007329x
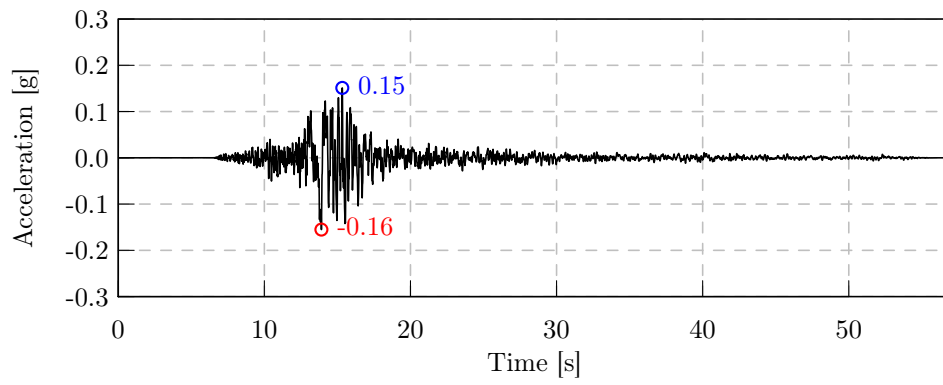
Figure B.11: Record IN0022y
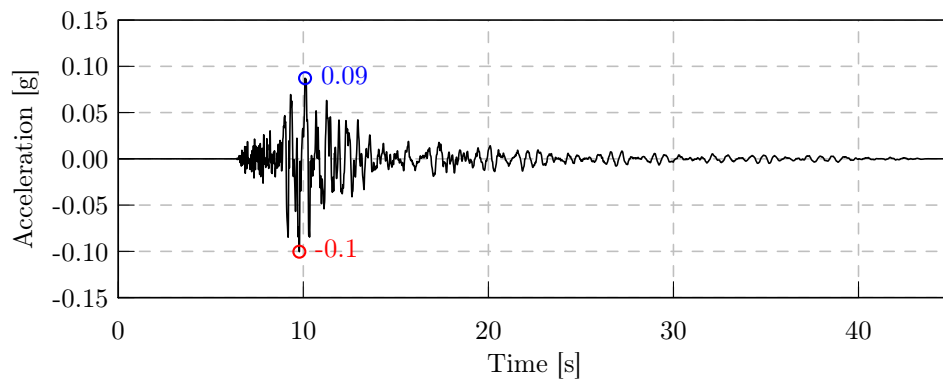
Figure B.12: Record IN0075y
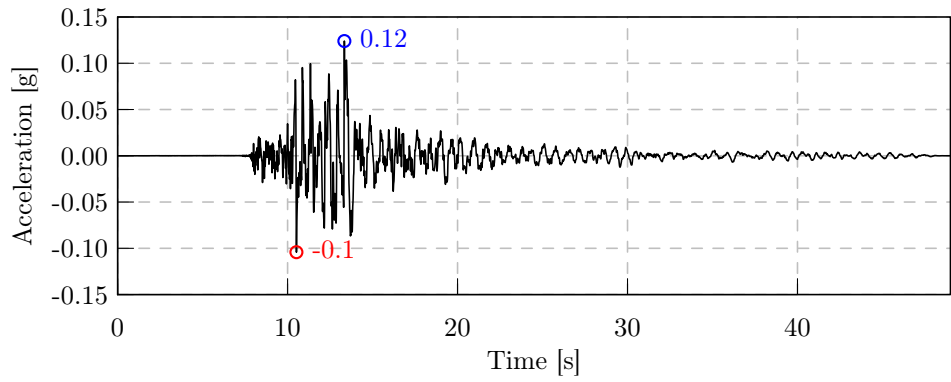
Figure B.13: Record IN0080x
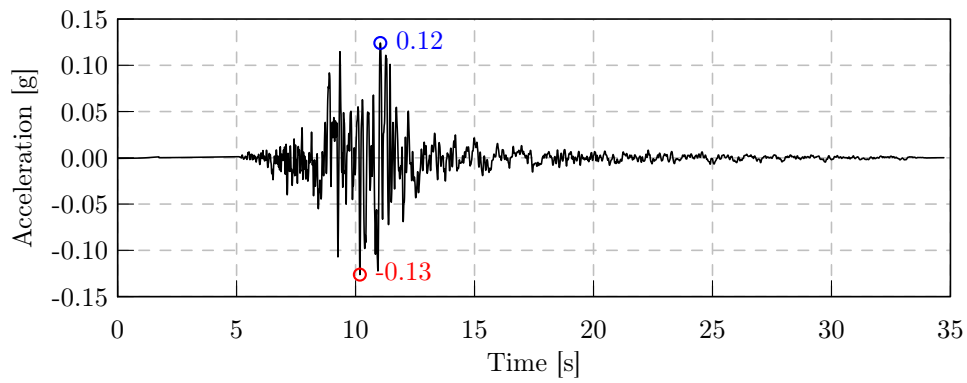
Figure B.14: Record IN0114x
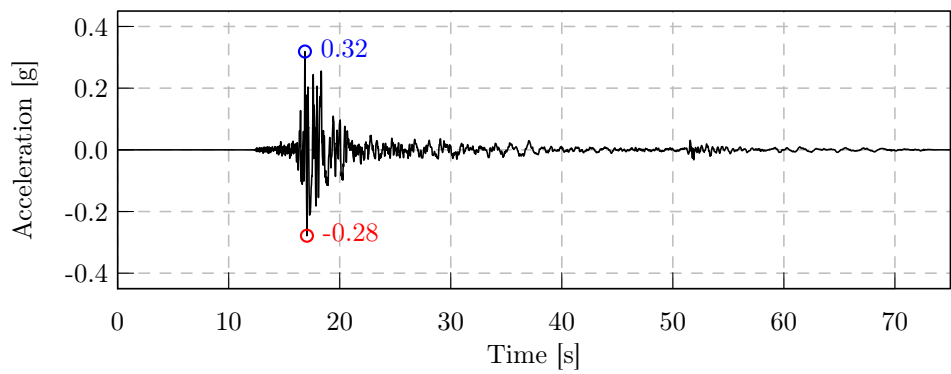
Figure B.15: Record IN0145y
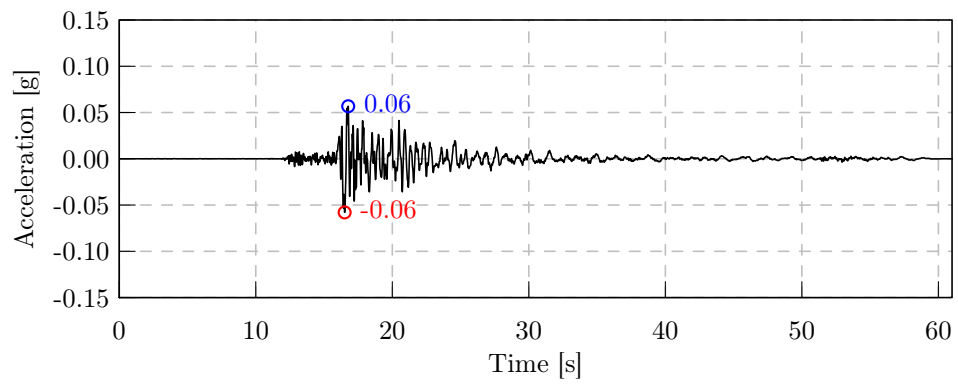
Figure B.16: Record IN0278y
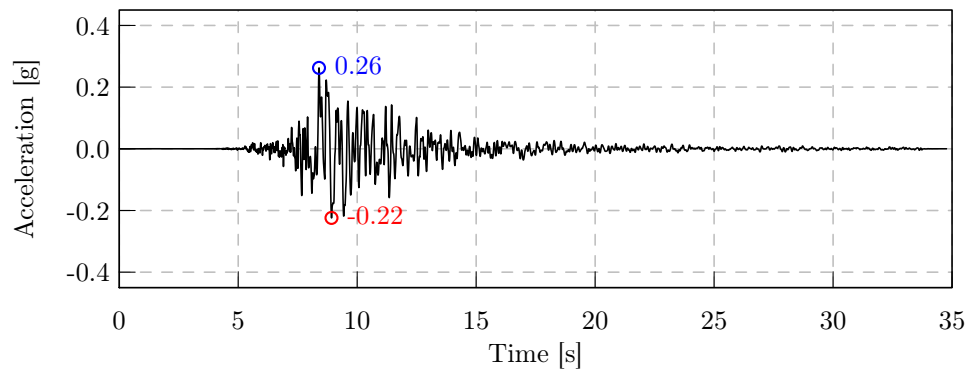
Figure B.17: Record IN0311x
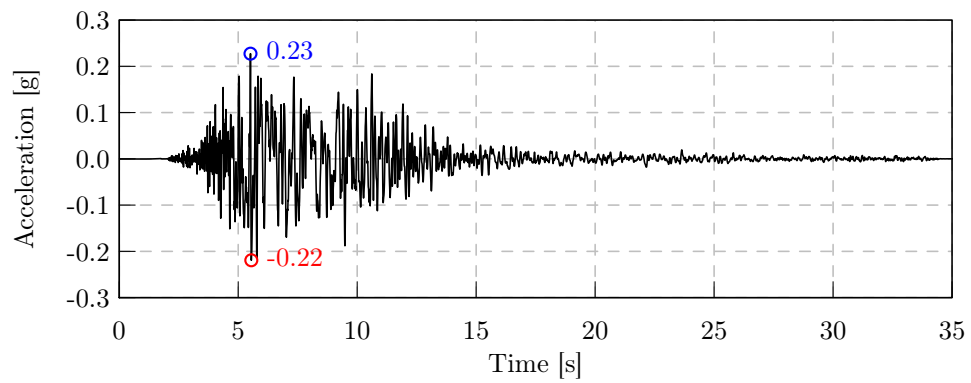
Figure B.18: Record IN0312x
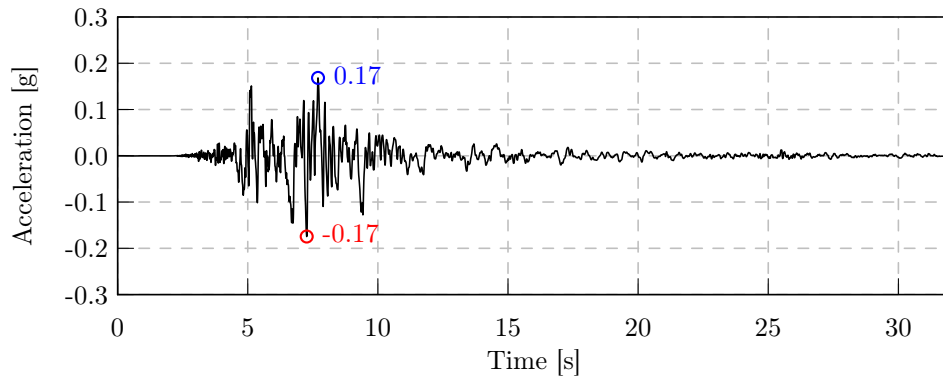
Figure B.19: Record IN0313x
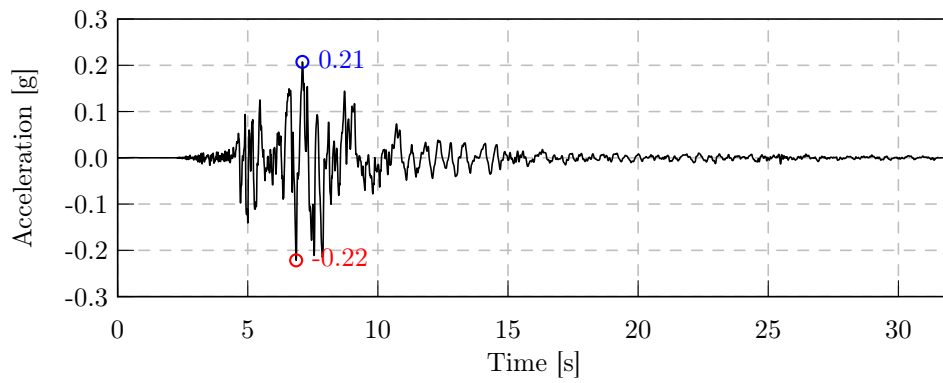
Figure B.20: Record IN0313y
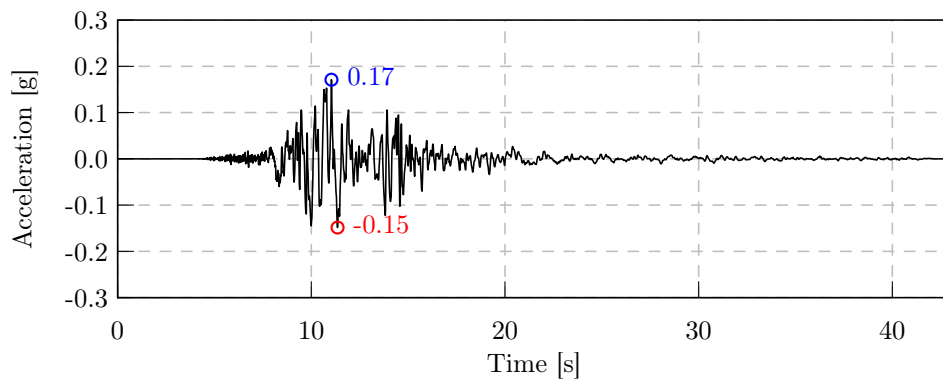
Figure B.21: Record IN0317y
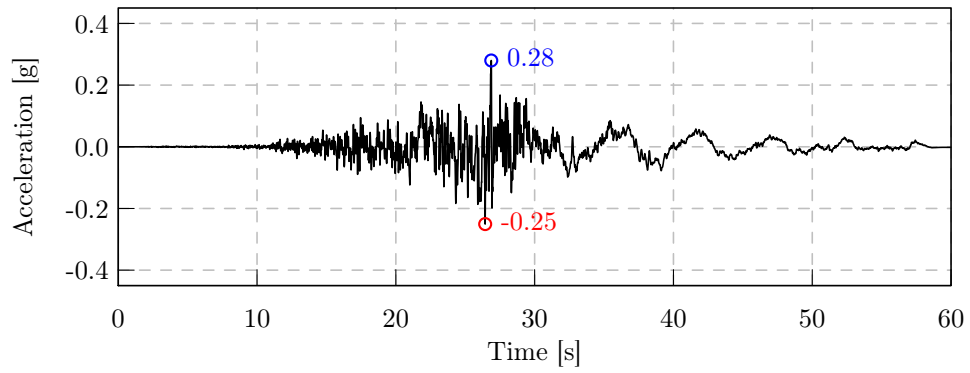
Figure B.22: Record IN0335x
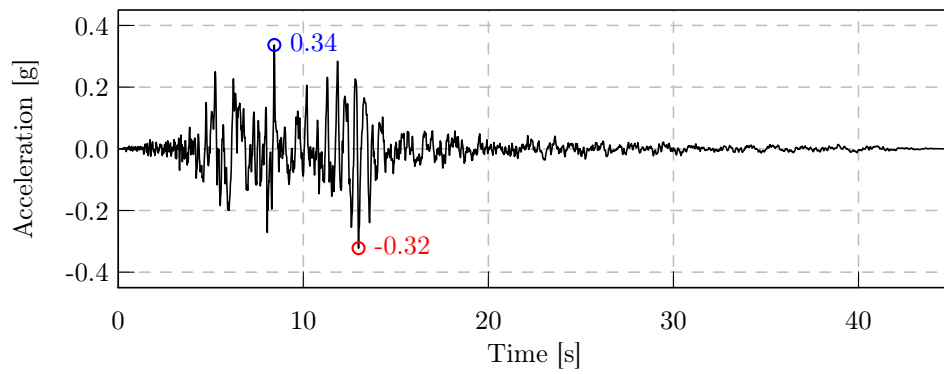
Figure B.23: Record IN0412x
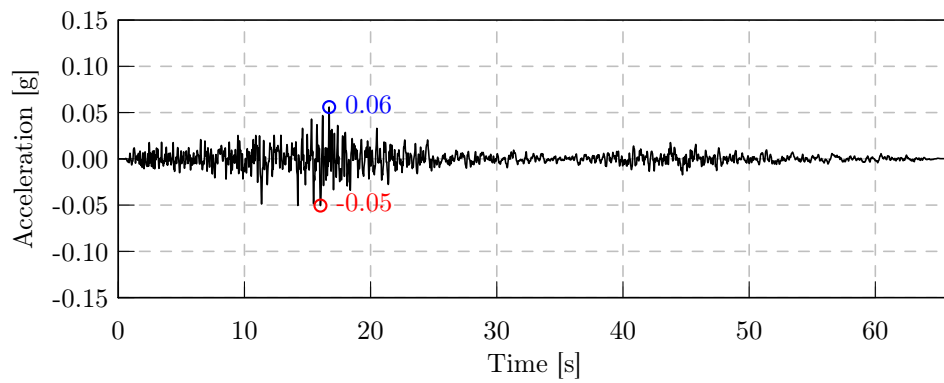
Figure B.24: Record IN0413y
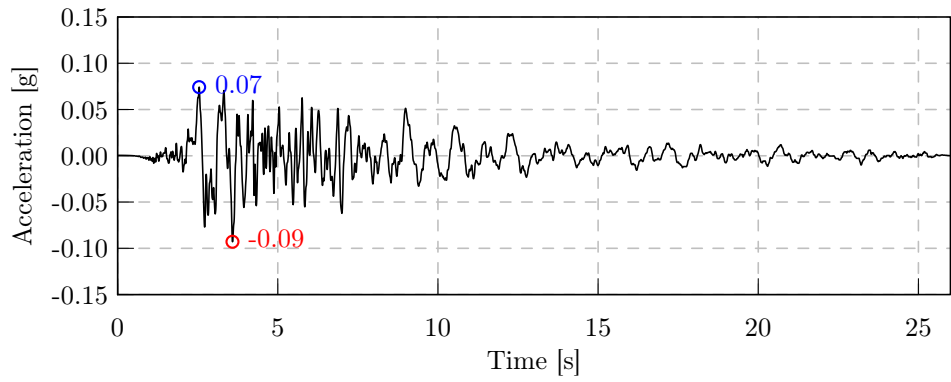
Figure B.25: Record IN0426x
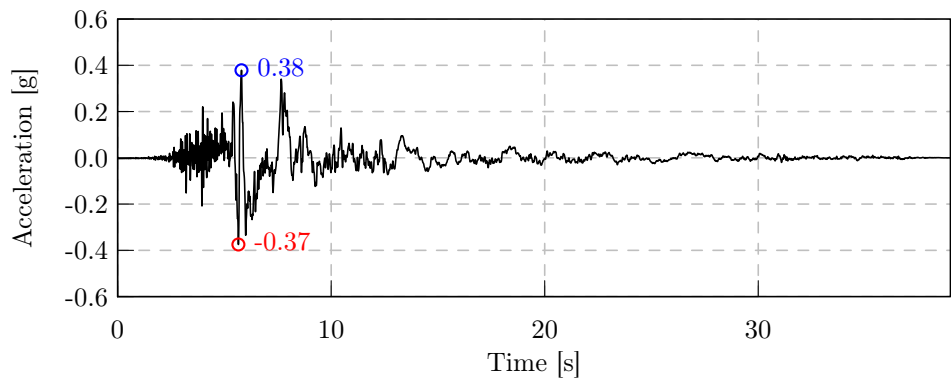
Figure B.26: Record IN0446x
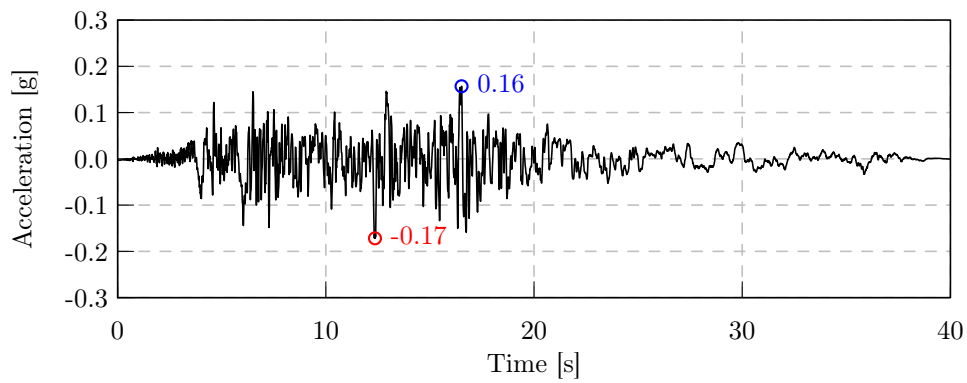
Figure B.27: Record IN0449x
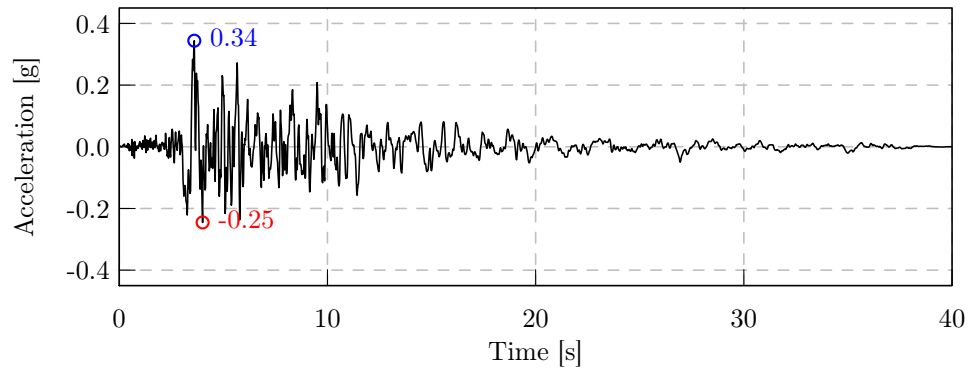
Figure B.28: Record IN0458x
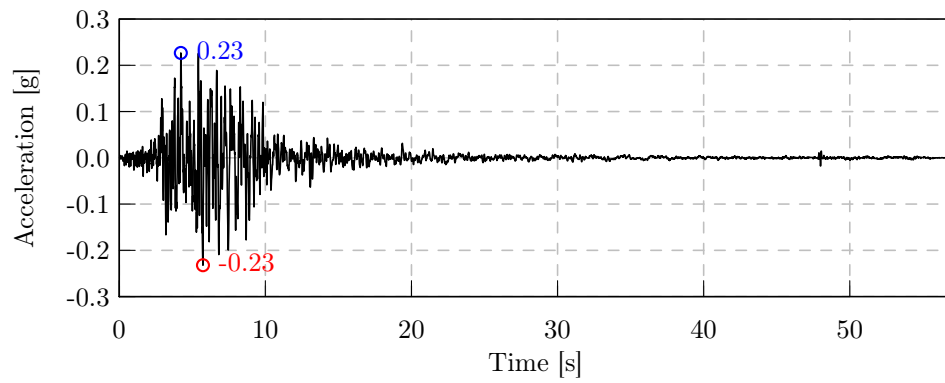
Figure B.29: Record IN0464y
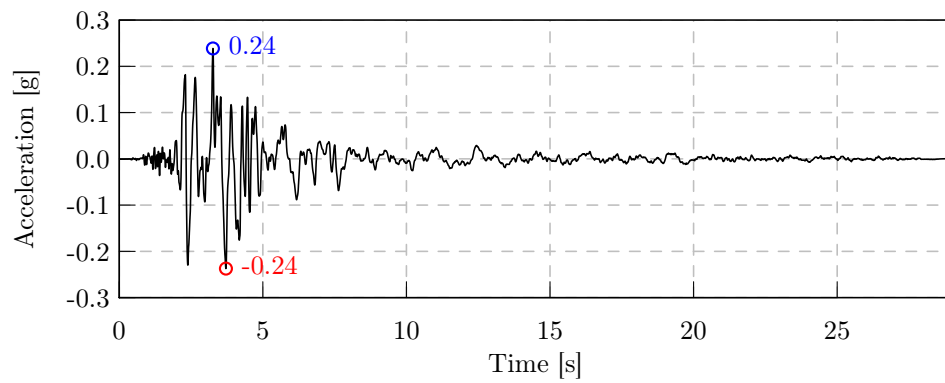
Figure B.30: Record KG0001y

C Results of DBD

In the following sections the results of displacement-based are summarised in order of the storey number: two, four and eight. The sections contains Tables that list the results of DBD for all configurations of the reference structure (see Fig. 5.13)

SWT – shear wall type,
BT – box type,
SWE – single wall elements,
CWO – continuous wall with openings

and all DBD procedures which were discussed in section 6.5

CSM, ATC-40 – capacity spectrum method according to [ATC-40],
CSM, $\xi = 0.15$ – capacity spectrum method with constant effective damping of 15 %,
N2M, EC8 – N2 method according to [EN 1998-1],
N2M, CLT/EC8 – N2 method incorporating the new $R_\mu - \mu - T$ relationship for CLT structures (see section 6.1).

The results are subdivided for the two loading directions (Dir) X and Y as well as for the load patterns
P1 – uniform load pattern,
P2 – linear load pattern.

Results for the following parameters are given in the Tables:

S_d – spectral displacement of the performance point,
S_a – spectral dacceleration of the performance point,
m^* – equivalent mass (see sections 2.4.3 and 6.4),
Γ – participation factor (see sections 2.4.3 and 6.4),
F_b – base shear, $F_b = S_a \cdot m^* \cdot \Gamma$,
u_i – lateral displacement at the reference points in each floor level i.

The determination of the lateral displacements u_i is explained in section 6.6.1.

In some cases no performance point was found. Here cells in the Table are left empty. The graphical determination of the performance points is documented at the end of this chapter.

C.1 Two-storey structure

| configuration | | Dir | P | S_d | S_a | m^* | Γ | F_b | u_2 | u_1 |
plan	elevation			[mm]	[m/s^2]	[t]	[–]	[kN]	[mm]	[mm]
CSM, ATC-40										
SWT	SWE	X	1	43.8	4.3	47.5	1.19	244.3	52.2	40.1
BT	SWE	X	1	43.1	4.7	48.2	1.18	267.1	50.9	39.9
SWT	CWO	X	1	40.0	4.2	53.2	1.08	243.9	43.2	39.0
BT	CWO	X	1	39.5	4.8	53.0	1.08	274.3	42.7	38.3
SWT	SWE	Y	1	50.6	3.8	53.8	1.07	217.2	54.1	49.5
BT	SWE	Y	1	50.1	4.1	53.6	1.07	237.7	53.6	48.8
SWT	CWO	Y	1	49.2	3.8	57.4	1.00	216.7	49.2	49.2
BT	CWO	Y	1	46.9	4.2	57.3	1.00	240.3	46.9	46.8
SWT	SWE	X	2	46.1	4.5	39.2	1.36	238.3	62.6	35.9
BT	SWE	X	2	44.7	4.7	41.1	1.33	256.5	59.4	36.6
SWT	CWO	X	2	42.0	4.4	44.4	1.26	246.5	52.9	36.7
BT	CWO	X	2	41.0	4.8	44.3	1.26	268.6	51.7	35.8
SWT	SWE	Y	2	52.0	3.8	46.7	1.21	217.5	62.9	47.1
BT	SWE	Y	2	51.1	4.2	46.6	1.21	234.2	61.9	46.2
SWT	CWO	Y	2	48.7	3.9	49.8	1.14	219.1	55.5	45.6
BT	CWO	Y	2	48.1	4.3	49.4	1.15	243.8	55.3	44.9
CSM, $\xi = 0.15$										
SWT	SWE	X	1	40.0	4.3	47.5	1.19	242.7	47.6	36.6
BT	SWE	X	1	37.5	4.6	48.2	1.18	260.1	44.3	34.7
SWT	CWO	X	1	39.8	4.3	53.2	1.08	247.6	43.0	38.8
BT	CWO	X	1	36.4	4.7	53.0	1.08	270.0	39.3	35.2
SWT	SWE	Y	1	45.9	3.7	53.8	1.07	215.1	49.1	44.9
BT	SWE	Y	1	43.2	4.0	53.6	1.07	227.7	46.2	42.1
SWT	CWO	Y	1	44.5	3.9	57.4	1.00	221.2	44.5	44.5
BT	CWO	Y	1	41.6	4.1	57.3	1.00	236.4	41.6	41.5
SWT	SWE	X	2	39.8	4.3	39.2	1.36	229.5	54.2	31.1
BT	SWE	X	2	38.6	4.5	41.1	1.33	243.1	51.3	31.6
SWT	CWO	X	2	39.2	4.4	44.4	1.26	244.7	49.4	34.3
BT	CWO	X	2	36.2	4.7	44.3	1.26	264.2	45.6	31.6
SWT	SWE	Y	2	46.0	3.7	46.7	1.21	210.6	55.7	41.7
BT	SWE	Y	2	43.7	3.9	46.6	1.21	221.6	52.8	39.4
SWT	CWO	Y	2	44.5	3.9	49.8	1.14	218.9	50.8	41.7
BT	CWO	Y	2	41.8	4.1	49.4	1.15	233.5	48.0	39.0
N2M, EC8										
SWT	SWE	X	1	45.0	4.3	47.5	1.19	245.7	53.5	41.1
BT	SWE	X	1	44.5	4.7	48.2	1.18	268.8	52.5	41.1
SWT	CWO	X	1	38.4	4.3	53.2	1.08	246.5	41.5	37.4
BT	CWO	X	1	40.4	4.8	53.0	1.08	275.0	43.6	39.1
SWT	SWE	Y	1	53.2	3.9	53.8	1.07	221.7	56.9	52.0
BT	SWE	Y	1	51.8	4.2	53.6	1.07	239.3	55.4	50.4

Table C.1: Results of DBD for the two-storey reference structure (part 1)

| configuration | | Dir | P | S_d | S_a | m^* | Γ | F_b | u_2 | u_1 |
plan	elevation			[mm]	[m/s^2]	[t]	[–]	[kN]	[mm]	[mm]
SWT	CWO	Y	1	49.4	3.9	57.4	1.00	221.5	49.4	49.4
BT	CWO	Y	1	49.7	4.3	57.3	1.00	247.2	49.7	49.6
SWT	SWE	X	2	48.8	4.5	39.2	1.36	242.6	66.3	38.0
BT	SWE	X	2	49.4	4.9	41.1	1.33	265.1	65.7	40.5
SWT	CWO	X	2	42.2	4.4	44.4	1.26	246.6	53.2	36.9
BT	CWO	X	2	43.1	4.9	44.3	1.26	274.4	54.3	37.6
SWT	SWE	Y	2	55.0	3.9	46.7	1.21	221.1	66.5	49.8
BT	SWE	Y	2	54.9	4.3	46.6	1.21	241.0	66.4	49.5
SWT	CWO	Y	2	50.5	3.9	49.8	1.14	220.2	57.5	47.3
BT	CWO	Y	2	50.3	4.3	49.4	1.15	246.7	57.8	47.0
N2M, CLT/EC8										
SWT	SWE	X	1	39.2	4.3	47.5	1.19	242.1	46.7	35.9
BT	SWE	X	1	39.6	4.6	48.2	1.18	262.1	46.7	36.6
SWT	CWO	X	1	34.3	4.2	53.2	1.08	244.2	37.0	33.4
BT	CWO	X	1	34.3	4.7	53.0	1.08	266.7	37.0	33.2
SWT	SWE	Y	1	47.6	3.8	53.8	1.07	215.9	51.0	46.6
BT	SWE	Y	1	46.3	4.0	53.6	1.07	228.0	49.6	45.2
SWT	CWO	Y	1	44.7	3.8	57.4	1.00	219.1	44.7	44.7
BT	CWO	Y	1	44.3	4.2	57.3	1.00	239.7	44.3	44.2
SWT	SWE	X	2	43.5	4.4	39.2	1.36	235.0	59.2	33.9
BT	SWE	X	2	43.9	4.7	41.1	1.33	256.3	58.4	36.0
SWT	CWO	X	2	36.9	4.4	44.4	1.26	243.3	46.5	32.3
BT	CWO	X	2	37.8	4.8	44.3	1.26	265.3	47.6	32.9
SWT	SWE	Y	2	49.2	3.8	46.7	1.21	213.4	59.5	44.6
BT	SWE	Y	2	48.8	4.1	46.6	1.21	229.1	59.0	44.0
SWT	CWO	Y	2	45.4	3.9	49.8	1.14	220.6	51.7	42.5
BT	CWO	Y	2	45.5	4.2	49.4	1.15	241.4	52.4	42.6

Table C.1: Results of DBD for the two-storey reference structure (part 2)

C.2 Four-storey structure

| configuration | | Dir | P | S_d | S_a | m^* | Γ | F_b | u_4 | u_3 | u_2 | u_1 |
plan	elevation			[mm]	[m/s^2]	[t]	[–]	[kN]	[mm]	[mm]	[mm]	[mm]
CSM, ATC-40												
SWT	SWE	X	1	74.0	2.9	90.1	1.40	363.3	103.6	86.5	60.7	36.0
BT	SWE	X	1	71.9	3.0	89.9	1.40	377.8	100.7	84.2	59.0	34.3
SWT	CWO	X	1	66.1	2.7	118.8	1.18	375.1	78.0	74.3	63.5	52.7
BT	CWO	X	1	60.6	3.2	103.1	1.27	418.5	77.0	72.0	53.5	34.1
SWT	SWE	Y	1									
BT	SWE	Y	1	87.3	2.3	97.5	1.35	297.0	117.8	100.5	78.4	49.8
SWT	CWO	Y	1									
BT	CWO	Y	1	80.1	2.1	126.1	1.12	292.7	89.8	85.9	79.9	68.9
SWT	SWE	X	2	77.5	2.7	74.7	1.52	305.7	117.9	88.9	52.0	24.9
BT	SWE	X	2	78.0	2.8	76.4	1.50	323.2	117.0	89.7	54.0	25.5
SWT	CWO	X	2	64.7	2.7	78.0	1.48	306.3	95.7	75.2	44.2	22.6
BT	CWO	X	2	65.4	3.1	83.5	1.42	362.1	92.9	77.7	47.6	24.4
SWT	SWE	Y	2	96.9	2.2	78.7	1.54	264.5	149.2	108.3	75.8	39.9
BT	SWE	Y	2	93.1	2.3	81.0	1.50	278.3	139.7	105.7	73.5	37.9
SWT	CWO	Y	2	81.2	2.0	84.9	1.49	247.8	121.0	89.9	68.7	40.6
BT	CWO	Y	2	88.8	2.2	109.6	1.26	304.0	111.9	97.7	85.3	66.0
CSM, $\xi = 0.15$												
SWT	SWE	X	1	63.5	2.7	90.1	1.40	340.9	88.9	74.3	52.1	30.9
BT	SWE	X	1	61.4	2.8	89.9	1.40	351.5	86.0	71.9	50.3	29.3
SWT	CWO	X	1	62.0	2.8	118.8	1.18	388.2	73.1	69.6	59.5	49.4
BT	CWO	X	1	54.4	3.2	103.1	1.27	412.6	69.2	64.7	48.1	30.6
SWT	SWE	Y	1									
BT	SWE	Y	1	76.7	2.2	97.5	1.35	294.3	103.5	88.3	68.9	43.8
SWT	CWO	Y	1									
BT	CWO	Y	1	84.3	2.0	126.1	1.12	287.3	94.4	90.3	84.0	72.4
SWT	SWE	X	2	67.6	2.5	74.7	1.52	288.2	102.7	77.4	45.3	21.7
BT	SWE	X	2	65.9	2.6	76.4	1.50	298.2	98.8	75.7	45.6	21.5
SWT	CWO	X	2	61.5	2.8	78.0	1.48	322.3	91.0	71.6	42.0	21.5
BT	CWO	X	2	57.2	3.0	83.5	1.42	355.6	81.2	67.9	41.6	21.3
SWT	SWE	Y	2	83.7	2.0	78.7	1.54	248.6	128.8	93.5	65.4	34.4
BT	SWE	Y	2	80.2	2.1	81.0	1.50	260.0	120.3	91.1	63.3	32.7
SWT	CWO	Y	2									
BT	CWO	Y	2	78.5	2.2	109.6	1.26	301.6	98.9	86.4	75.3	58.3
N2M, EC8												
SWT	SWE	X	1	79.0	3.0	90.1	1.40	375.8	110.6	92.4	64.8	38.4
BT	SWE	X	1	78.0	3.1	89.9	1.40	392.2	109.2	91.3	63.9	37.2
SWT	CWO	X	1	66.7	2.7	118.8	1.18	371.8	78.7	75.0	64.1	53.2
BT	CWO	X	1	63.1	3.2	103.1	1.27	418.4	80.1	74.9	55.7	35.4
SWT	SWE	Y	1	85.8	1.9	97.1	1.36	249.5	116.7	98.9	77.2	49.4
BT	SWE	Y	1	91.5	2.3	97.5	1.35	300.1	123.5	105.3	82.2	52.2

Table C.2: Results of DBD for the four-storey reference structure (part 1)

| configuration | | Dir | P | S_d | S_a | m^* | Γ | F_b | u_4 | u_3 | u_2 | u_1 |
plan	elevation			[mm]	[m/s^2]	[t]	[–]	[kN]	[mm]	[mm]	[mm]	[mm]
SWT	CWO	Y	1	70.8	1.8	112.4	1.22	248.8	86.3	79.9	68.7	49.1
BT	CWO	Y	1	79.9	2.1	126.1	1.12	293.0	89.5	85.7	79.6	68.7
SWT	SWE	X	2	83.9	2.8	74.7	1.52	315.1	127.5	96.1	56.2	26.9
BT	SWE	X	2	84.0	2.9	76.4	1.50	334.5	126.0	96.6	58.2	27.4
SWT	CWO	X	2	64.2	2.7	78.0	1.48	316.1	95.1	74.8	43.9	22.5
BT	CWO	X	2	68.6	3.1	83.5	1.42	373.2	97.4	81.5	50.0	25.5
SWT	SWE	Y	2	103.3	2.2	78.7	1.54	270.7	159.1	115.4	80.8	42.5
BT	SWE	Y	2	100.7	2.4	81.0	1.50	287.2	151.0	114.3	79.5	41.0
SWT	CWO	Y	2	79.9	2.0	84.9	1.49	254.6	119.1	88.4	67.6	40.0
BT	CWO	Y	2	93.1	2.2	109.6	1.26	302.1	117.3	102.5	89.4	69.2
N2M, CLT/EC8												
SWT	SWE	X	1	69.6	2.8	90.1	1.40	350.8	97.5	81.4	57.1	33.9
BT	SWE	X	1	69.3	2.9	89.9	1.40	363.7	97.0	81.1	56.8	33.0
SWT	CWO	X	1	60.8	2.7	118.8	1.18	383.9	71.7	68.3	58.4	48.4
BT	CWO	X	1	57.4	3.2	103.1	1.27	421.2	72.8	68.1	50.6	32.2
SWT	SWE	Y	1	78.9	2.0	97.1	1.36	264.4	107.2	90.8	70.9	45.4
BT	SWE	Y	1	83.4	2.3	97.5	1.35	304.5	112.6	96.0	75.0	47.6
SWT	CWO	Y	1	66.4	1.8	112.4	1.22	251.1	81.0	75.0	64.5	46.1
BT	CWO	Y	1	73.5	2.0	126.1	1.12	289.1	82.3	78.8	73.2	63.1
SWT	SWE	X	2	75.2	2.7	74.7	1.52	302.9	114.3	86.2	50.4	24.1
BT	SWE	X	2	74.7	2.8	76.4	1.50	317.5	112.1	85.9	51.7	24.4
SWT	CWO	X	2	58.4	2.8	78.0	1.48	322.2	86.5	68.0	39.9	20.4
BT	CWO	X	2	61.7	3.1	83.5	1.42	364.1	87.6	73.3	44.9	23.0
SWT	SWE	Y	2	92.9	2.1	78.7	1.54	256.1	143.1	103.8	72.7	38.3
BT	SWE	Y	2	90.0	2.2	81.0	1.50	271.7	134.9	102.1	71.0	36.6
SWT	CWO	Y	2	73.2	2.1	84.9	1.49	259.4	109.1	81.0	61.9	36.6
BT	CWO	Y	2	85.0	2.2	109.6	1.26	309.2	107.1	93.5	81.6	63.2

Table C.2: Results of DBD for the four-storey reference structure (part 2)

C.3 Eight-storey structure

configuration		Dir	P	S_d	S_a	m^*	Γ	F_b
plan	elevation			[mm]	[m/s^2]	[t]	[–]	[kN]
CSM, ATC-40								
SWT	SWE	X	1	136.0	1.3	169.1	1.47	332.6
BT	SWE	X	1	136.6	1.4	168.7	1.47	342.0
SWT	CWO	X	1	115.1	1.5	255.6	1.18	451.9
BT	CWO	X	1	116.0	1.7	252.8	1.18	497.7
SWT	SWE	Y	1	136.0	1.2	164.6	1.47	296.8
BT	SWE	Y	1	136.8	1.3	164.7	1.47	306.5
SWT	CWO	Y	1	122.5	1.6	219.1	1.23	436.2
BT	CWO	Y	1	126.5	1.8	220.3	1.23	479.9
SWT	SWE	X	2	135.1	1.1	159.7	1.49	254.8
BT	SWE	X	2	139.4	1.1	157.2	1.49	265.7
SWT	CWO	X	2	116.9	1.6	197.4	1.32	410.6
BT	CWO	X	2	123.3	1.7	199.7	1.31	445.3
SWT	SWE	Y	2	142.7	1.0	152.4	1.49	229.9
BT	SWE	Y	2	135.7	1.0	152.9	1.49	230.4
SWT	CWO	Y	2	123.1	1.5	169.1	1.41	353.8
BT	CWO	Y	2	126.8	1.6	172.9	1.39	383.0
CSM, $\xi = 0.15$								
SWT	SWE	X	1	128.7	1.3	169.1	1.47	322.7
BT	SWE	X	1	128.0	1.3	168.7	1.47	329.7
SWT	CWO	X	1	113.3	1.5	255.6	1.18	456.3
BT	CWO	X	1	105.7	1.6	252.8	1.18	483.4
SWT	SWE	Y	1	129.4	1.2	164.6	1.47	288.9
BT	SWE	Y	1	129.2	1.2	164.7	1.47	297.0
SWT	CWO	Y	1	109.7	1.6	219.1	1.23	421.3
BT	CWO	Y	1	105.6	1.6	220.3	1.23	439.8
SWT	SWE	X	2	130.1	1.0	159.7	1.49	249.4
BT	SWE	X	2	129.7	1.1	157.2	1.49	255.0
SWT	CWO	X	2	110.5	1.6	197.4	1.32	404.3
BT	CWO	X	2	106.0	1.6	199.7	1.31	422.9
SWT	SWE	Y	2	130.5	1.0	152.4	1.49	218.8
BT	SWE	Y	2	130.4	1.0	152.9	1.49	225.4
SWT	CWO	Y	2	117.4	1.5	169.1	1.41	348.0
BT	CWO	Y	2	112.7	1.5	172.9	1.39	365.6
N2M, EC8								
SWT	SWE	X	1	172.4	1.5	169.1	1.47	381.7
BT	SWE	X	1	170.1	1.6	168.7	1.47	386.4
SWT	CWO	X	1	123.6	1.4	255.6	1.18	433.2
BT	CWO	X	1	126.1	1.7	252.8	1.18	492.5
SWT	SWE	Y	1	181.5	1.4	164.6	1.47	347.2
BT	SWE	Y	1	178.4	1.5	164.7	1.47	356.4

Table C.3: Results of DBD for the four-storey reference structure – spectral values, modal parameters, base shear (part 1)

| configuration | | Dir | P | S_d | S_a | m^* | Γ | F_b |
plan	elevation			[mm]	[m/s^2]	[t]	[–]	[kN]
SWT	CWO	Y	1	130.1	1.5	219.1	1.23	414.5
BT	CWO	Y	1	133.6	1.8	220.3	1.23	480.3
SWT	SWE	X	2	186.4	1.3	159.7	1.49	304.5
BT	SWE	X	2	186.4	1.3	157.2	1.49	312.4
SWT	CWO	X	2	133.3	1.6	197.4	1.32	415.1
BT	CWO	X	2	134.2	1.7	199.7	1.31	452.6
SWT	SWE	Y	2	186.4	1.2	152.4	1.49	264.8
BT	SWE	Y	2	186.4	1.2	152.9	1.49	273.7
SWT	CWO	Y	2	143.7	1.6	169.1	1.41	370.2
BT	CWO	Y	2	142.0	1.7	172.9	1.39	397.0
N2M, CLT/EC8								
SWT	SWE	X	1	156.5	1.4	169.1	1.47	359.2
BT	SWE	X	1	146.8	1.5	168.7	1.47	360.4
SWT	CWO	X	1	116.5	1.5	255.6	1.18	447.4
BT	CWO	X	1	115.9	1.7	252.8	1.18	498.4
SWT	SWE	Y	1	160.6	1.3	164.6	1.47	317.1
BT	SWE	Y	1	160.1	1.3	164.7	1.47	326.1
SWT	CWO	Y	1	124.4	1.6	219.1	1.23	437.7
BT	CWO	Y	1	119.5	1.7	220.3	1.23	463.1
SWT	SWE	X	2	168.2	1.2	159.7	1.49	282.4
BT	SWE	X	2	168.6	1.2	157.2	1.49	290.3
SWT	CWO	X	2	121.8	1.6	197.4	1.32	412.9
BT	CWO	X	2	120.4	1.7	199.7	1.31	439.3
SWT	SWE	Y	2	169.8	1.1	152.4	1.49	248.8
BT	SWE	Y	2	170.8	1.2	152.9	1.49	267.1
SWT	CWO	Y	2	128.7	1.5	169.1	1.41	358.4
BT	CWO	Y	2	126.5	1.6	172.9	1.39	381.6

Table C.3: Results of DBD for the four-storey reference structure – spectral values, modal parameters, base shear (part 2)

configuration plan	elevation	Dir	P	u_8 [mm]	u_7 [mm]	u_6 [mm]	u_5 [mm]	u_4 [mm]	u_3 [mm]	u_2 [mm]	u_1 [mm]
CSM, ATC-40											
SWT	SWE	X	1	199.9	179.6	156.6	132.2	104.5	77.6	50.6	23.0
BT	SWE	X	1	200.9	180.3	157.0	132.5	104.7	77.6	50.5	23.0
SWT	CWO	X	1	135.8	134.7	130.8	123.7	115.6	104.5	91.4	66.9
BT	CWO	X	1	136.9	135.7	131.5	124.0	115.3	103.5	89.6	65.1
SWT	SWE	Y	1	200.0	180.3	155.8	128.5	101.4	73.5	46.0	17.6
BT	SWE	Y	1	201.2	181.4	156.8	129.5	102.1	74.1	46.3	17.9
SWT	CWO	Y	1	150.7	148.0	139.9	126.6	113.9	98.6	81.0	14.6
BT	CWO	Y	1	155.6	153.2	144.8	131.5	118.4	102.8	83.5	16.3
SWT	SWE	X	2	201.4	179.3	154.4	125.7	97.8	69.5	42.2	16.1
BT	SWE	X	2	207.7	184.3	157.2	131.3	97.1	67.9	40.6	16.0
SWT	CWO	X	2	154.3	149.9	138.3	120.6	99.8	77.1	54.4	21.3
BT	CWO	X	2	161.5	157.1	145.3	128.1	107.6	82.6	56.8	23.4
SWT	SWE	Y	2	212.7	189.4	159.5	129.1	95.0	64.8	37.3	12.1
BT	SWE	Y	2	202.2	180.3	152.2	121.1	91.3	62.6	35.9	11.8
SWT	CWO	Y	2	173.5	163.8	144.5	112.9	88.9	64.5	41.4	12.1
BT	CWO	Y	2	176.2	168.1	149.0	119.2	93.6	67.9	43.1	13.2
CSM, $\xi = 0.15$											
SWT	SWE	X	1	189.2	170.0	148.2	125.1	98.9	73.5	47.9	21.7
BT	SWE	X	1	188.2	168.9	147.1	124.1	98.0	72.7	47.3	21.5
SWT	CWO	X	1	133.7	132.6	128.8	121.8	113.8	102.9	90.0	65.8
BT	CWO	X	1	124.8	123.7	119.9	113.0	105.1	94.4	81.7	59.3
SWT	SWE	Y	1	190.2	171.5	148.2	122.2	96.4	69.9	43.8	16.8
BT	SWE	Y	1	189.9	171.2	148.0	122.2	96.4	69.9	43.7	16.9
SWT	CWO	Y	1	134.9	132.5	125.2	113.3	101.9	88.3	72.5	13.1
BT	CWO	Y	1	129.9	127.9	120.9	109.8	98.8	85.8	69.7	13.6
SWT	SWE	X	2	193.9	172.6	148.7	121.0	94.1	66.9	40.7	15.5
BT	SWE	X	2	193.2	171.4	146.2	122.1	90.3	63.1	37.7	14.9
SWT	CWO	X	2	145.9	141.8	130.7	114.0	94.4	72.9	51.4	20.1
BT	CWO	X	2	138.9	135.1	124.9	110.2	92.5	71.0	48.8	20.1
SWT	SWE	Y	2	194.5	173.2	145.8	118.0	86.9	59.3	34.1	11.1
BT	SWE	Y	2	194.4	173.3	146.4	116.5	87.8	60.2	34.6	11.3
SWT	CWO	Y	2	165.6	156.4	138.0	107.8	84.8	61.6	39.6	11.6
BT	CWO	Y	2	156.7	149.5	132.5	106.0	83.2	60.4	38.3	11.8
N2M, EC8											
SWT	SWE	X	1	253.4	227.6	198.5	167.6	132.4	98.4	64.2	29.1
BT	SWE	X	1	250.0	224.3	195.4	164.8	130.2	96.6	62.8	28.6
SWT	CWO	X	1	145.8	144.6	140.4	132.8	124.1	112.2	98.1	71.8
BT	CWO	X	1	148.8	147.5	142.9	134.8	125.3	112.5	97.4	70.7
SWT	SWE	Y	1	266.7	240.4	207.8	171.4	135.2	98.1	61.4	23.5
BT	SWE	Y	1	262.3	236.5	204.4	168.8	133.1	96.6	60.3	23.4
SWT	CWO	Y	1	160.0	157.2	148.5	134.4	120.9	104.7	86.0	15.5
BT	CWO	Y	1	164.3	161.7	152.9	138.8	125.0	108.6	88.2	17.2

Table C.4: Results of DBD for the four-storey reference structure – lateral displacements (part 1)

| configuration | | Dir | P | u_8 | u_7 | u_6 | u_5 | u_4 | u_3 | u_2 | u_1 |
plan	elevation			[mm]	[mm]	[mm]	[mm]	[mm]	[mm]	[mm]	[mm]
SWT	SWE	X	2	277.7	247.2	212.9	173.3	134.8	95.8	58.2	22.2
BT	SWE	X	2	277.7	246.4	210.2	175.5	129.8	90.7	54.2	21.4
SWT	CWO	X	2	175.9	170.9	157.6	137.4	113.8	87.9	62.0	24.3
BT	CWO	X	2	175.9	171.1	158.2	139.5	117.2	89.9	61.9	25.5
SWT	SWE	Y	2	277.7	247.3	208.2	168.5	124.0	84.6	48.7	15.8
BT	SWE	Y	2	277.7	247.6	209.1	166.4	125.5	86.0	49.4	16.2
SWT	CWO	Y	2	202.6	191.3	168.8	131.9	103.8	75.3	48.4	14.2
BT	CWO	Y	2	197.4	188.3	166.9	133.5	104.8	76.1	48.3	14.8
N2M, CLT/EC8											
SWT	SWE	X	1	230.1	206.7	180.2	152.2	120.2	89.4	58.3	26.4
BT	SWE	X	1	215.8	193.7	168.6	142.3	112.4	83.4	54.2	24.7
SWT	CWO	X	1	137.4	136.2	132.3	125.2	117.0	105.8	92.5	67.7
BT	CWO	X	1	136.7	135.5	131.3	123.8	115.1	103.4	89.5	65.0
SWT	SWE	Y	1	236.1	212.8	183.9	151.7	119.7	86.8	54.3	20.8
BT	SWE	Y	1	235.3	212.2	183.4	151.4	119.4	86.6	54.1	21.0
SWT	CWO	Y	1	153.1	150.4	142.1	128.6	115.7	100.2	82.3	14.9
BT	CWO	Y	1	146.9	144.6	136.7	124.1	111.8	97.1	78.9	15.4
SWT	SWE	X	2	250.6	223.1	192.2	156.4	121.6	86.5	52.6	20.0
BT	SWE	X	2	251.2	222.9	190.1	158.8	117.4	82.1	49.1	19.3
SWT	CWO	X	2	160.7	156.2	144.0	125.6	104.0	80.3	56.7	22.2
BT	CWO	X	2	157.7	153.4	141.9	125.1	105.1	80.6	55.5	22.8
SWT	SWE	Y	2	253.0	225.3	189.7	153.5	113.0	77.1	44.4	14.4
BT	SWE	Y	2	254.5	226.9	191.6	152.5	115.0	78.8	45.2	14.8
SWT	CWO	Y	2	181.5	171.4	151.2	118.1	93.0	67.5	43.4	12.7
BT	CWO	Y	2	175.9	167.8	148.7	119.0	93.4	67.8	43.0	13.2

Table C.4: Results of DBD for the four-storey reference structure – lateral displacements (part 2)
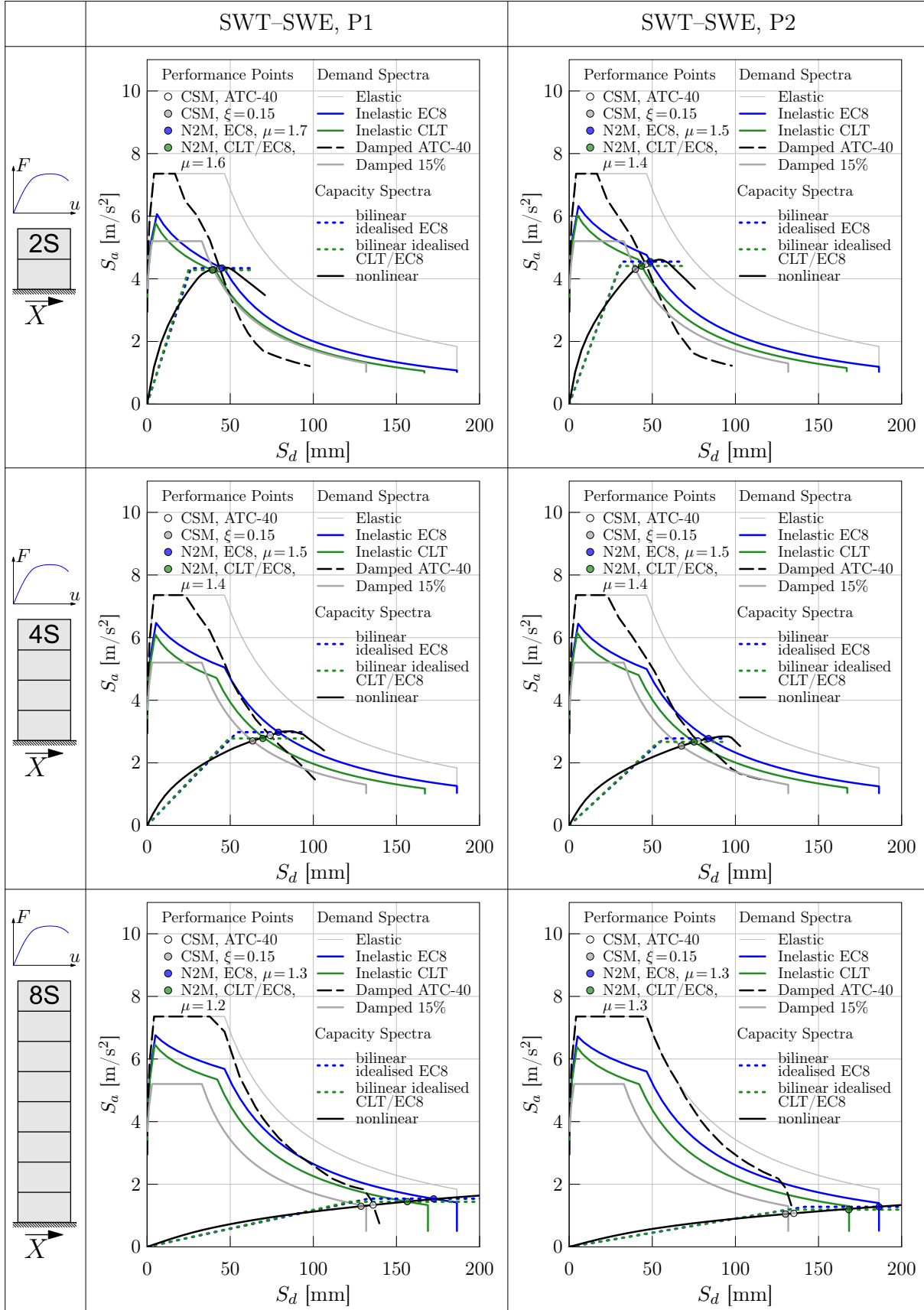
Figure C.1: Determination of performance points for the SWT–SWE configuration in X-direction
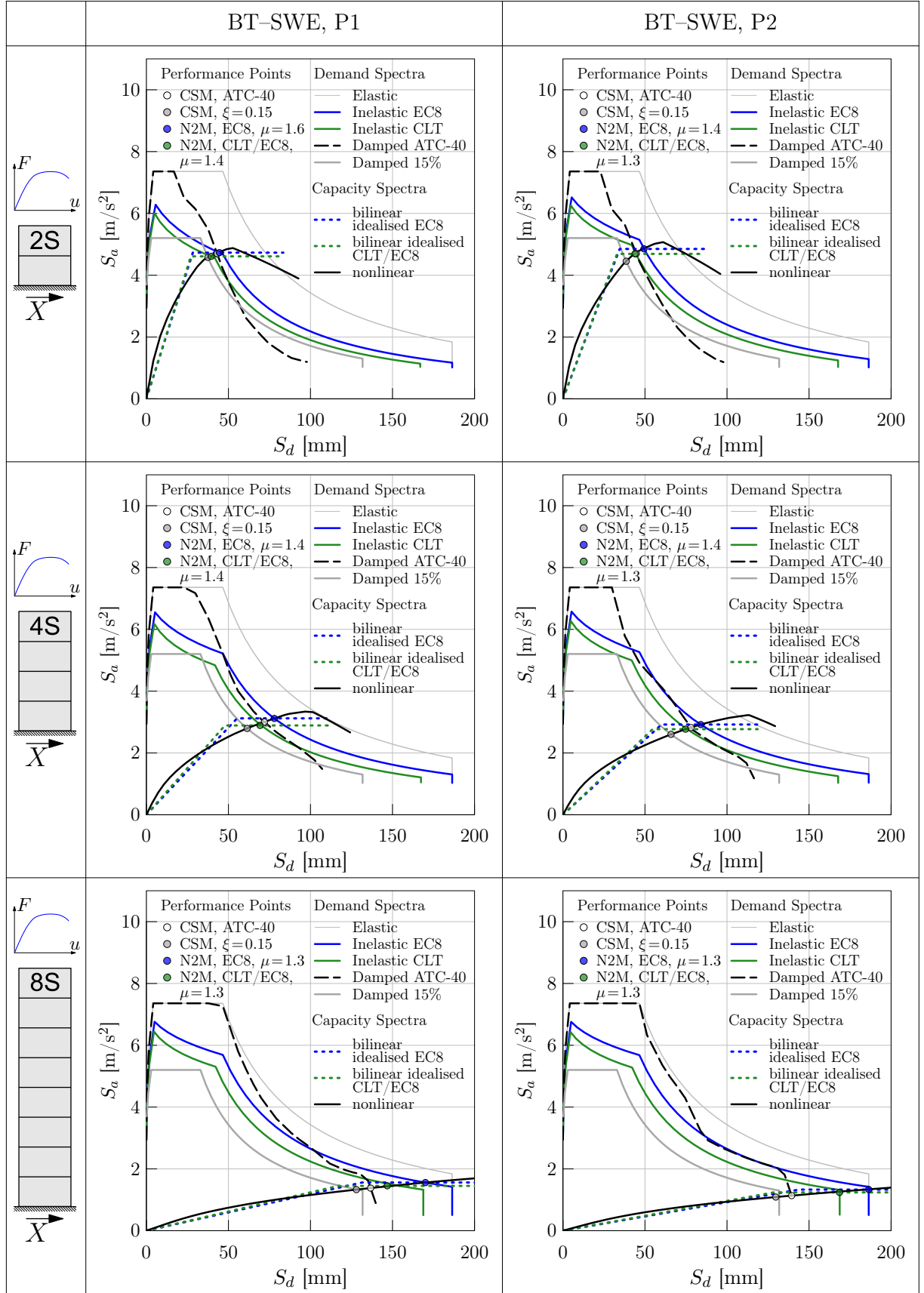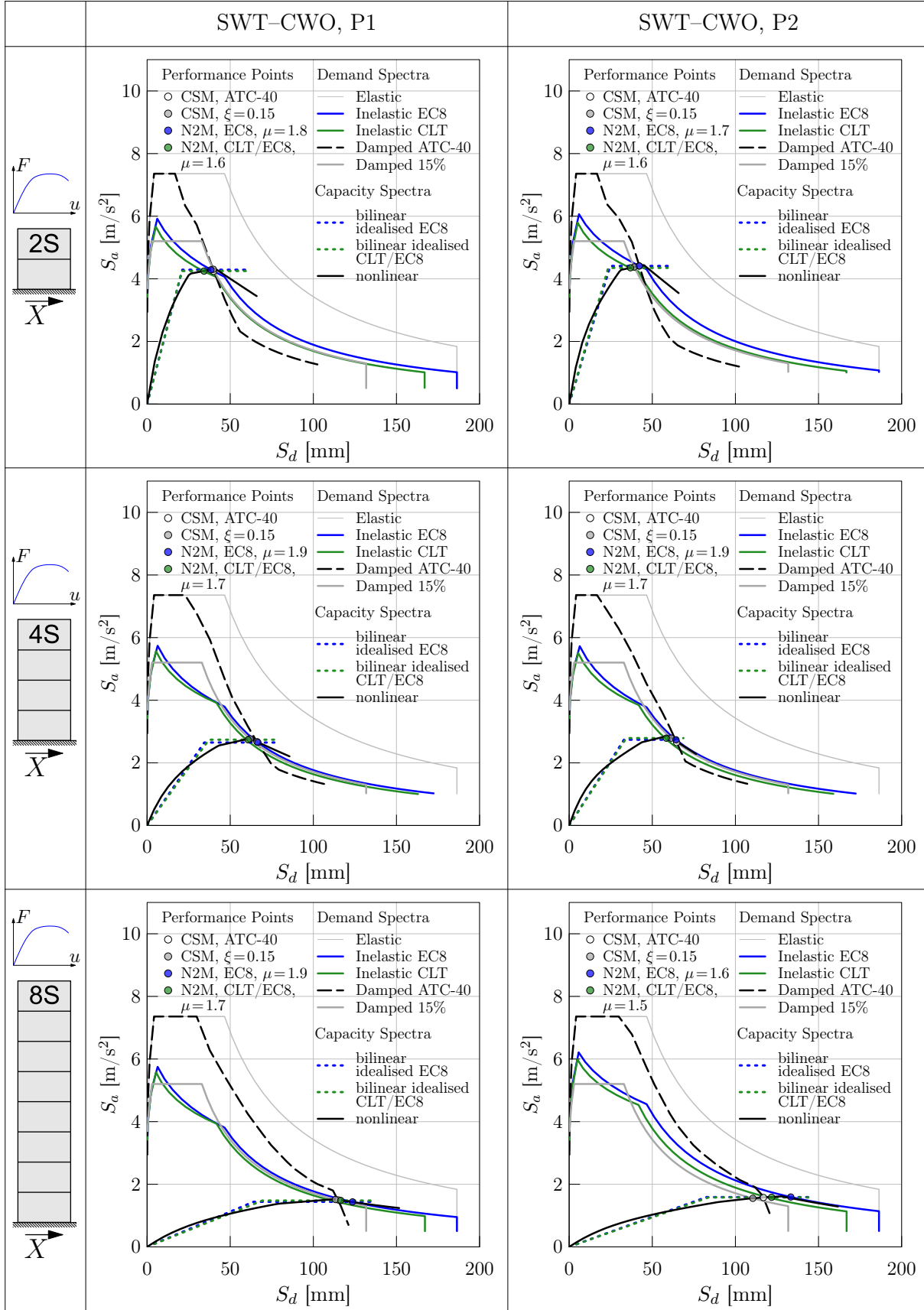
Figure C.2: Determination of performance points for the BT–SWE configuration in X-direction

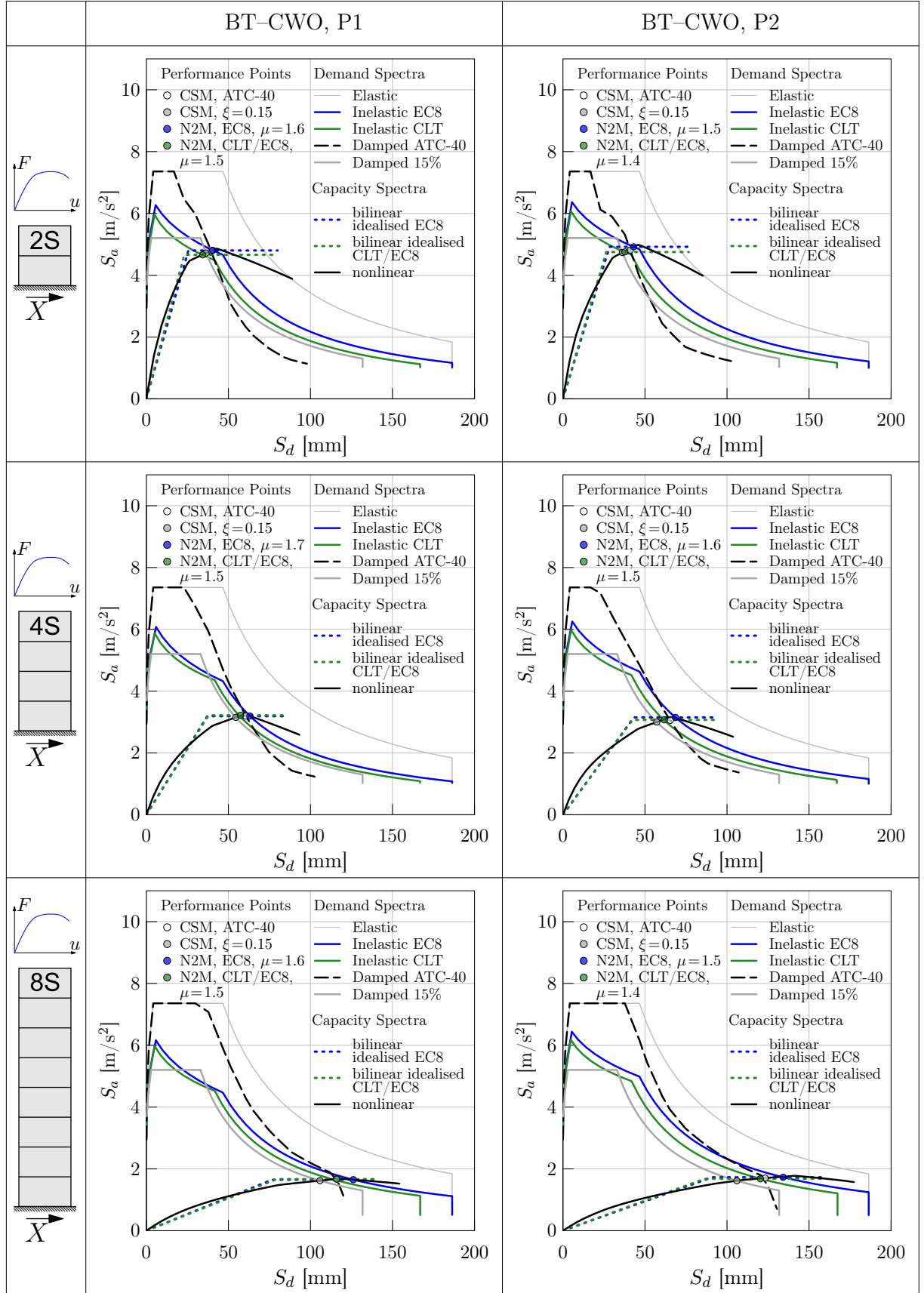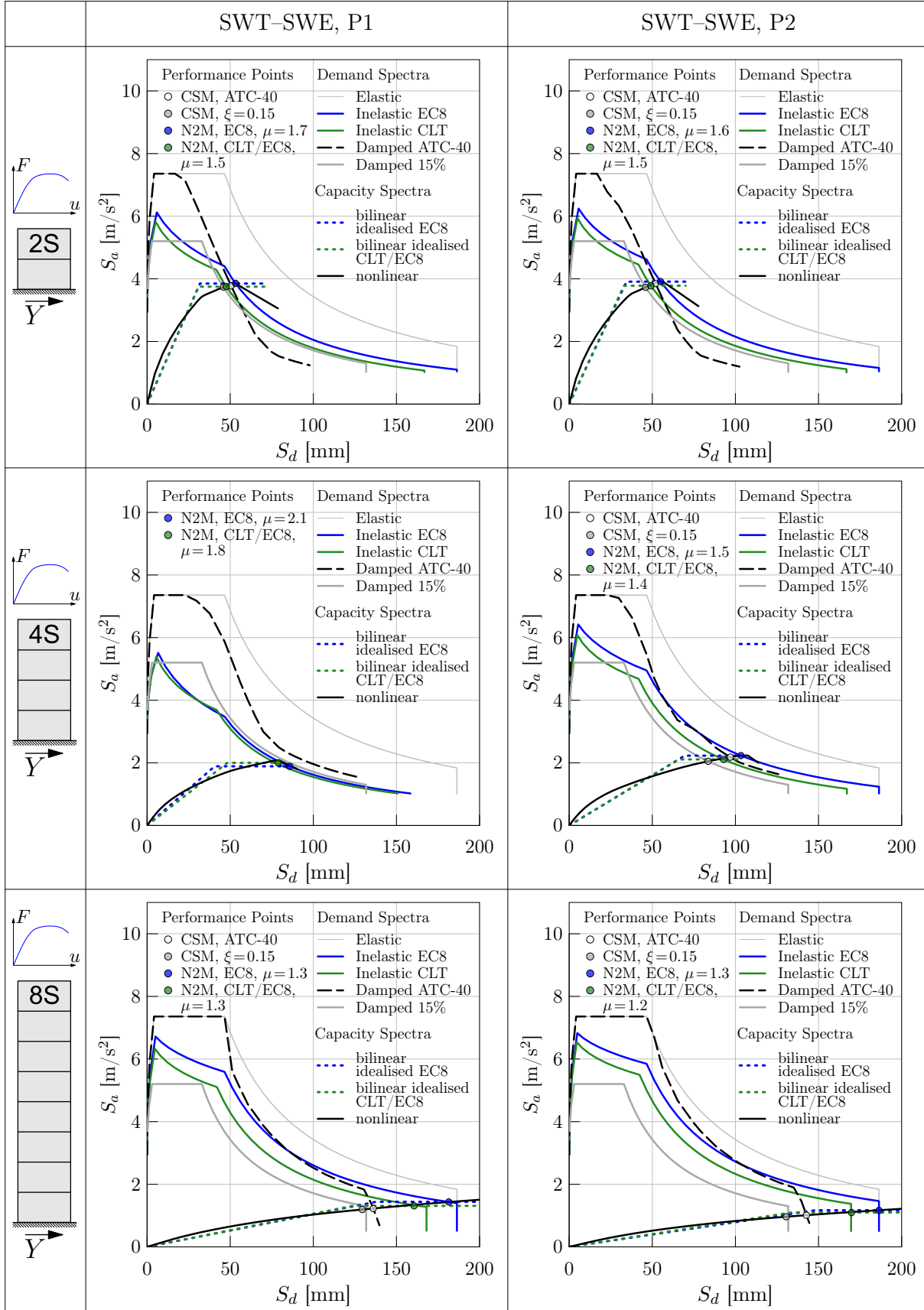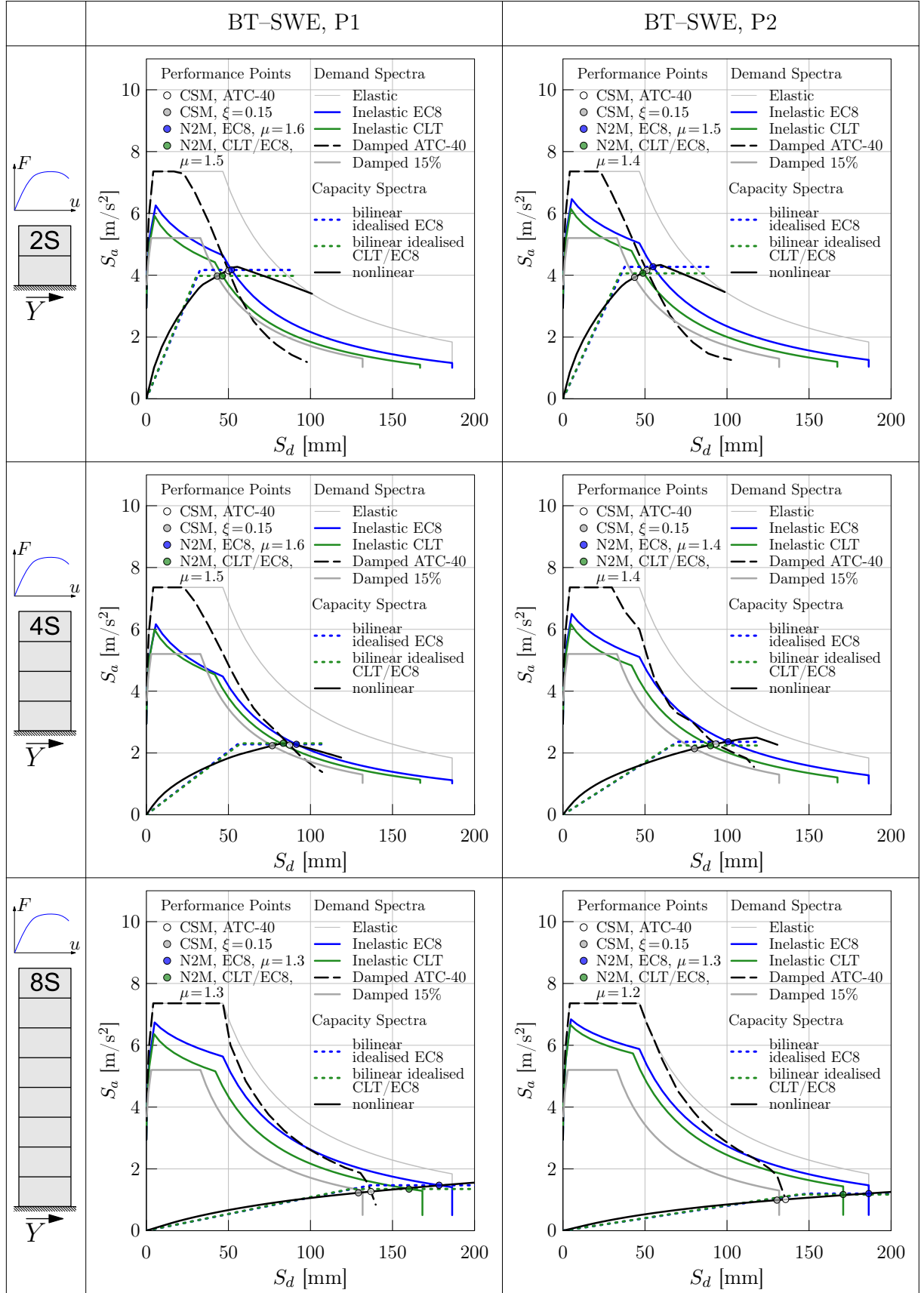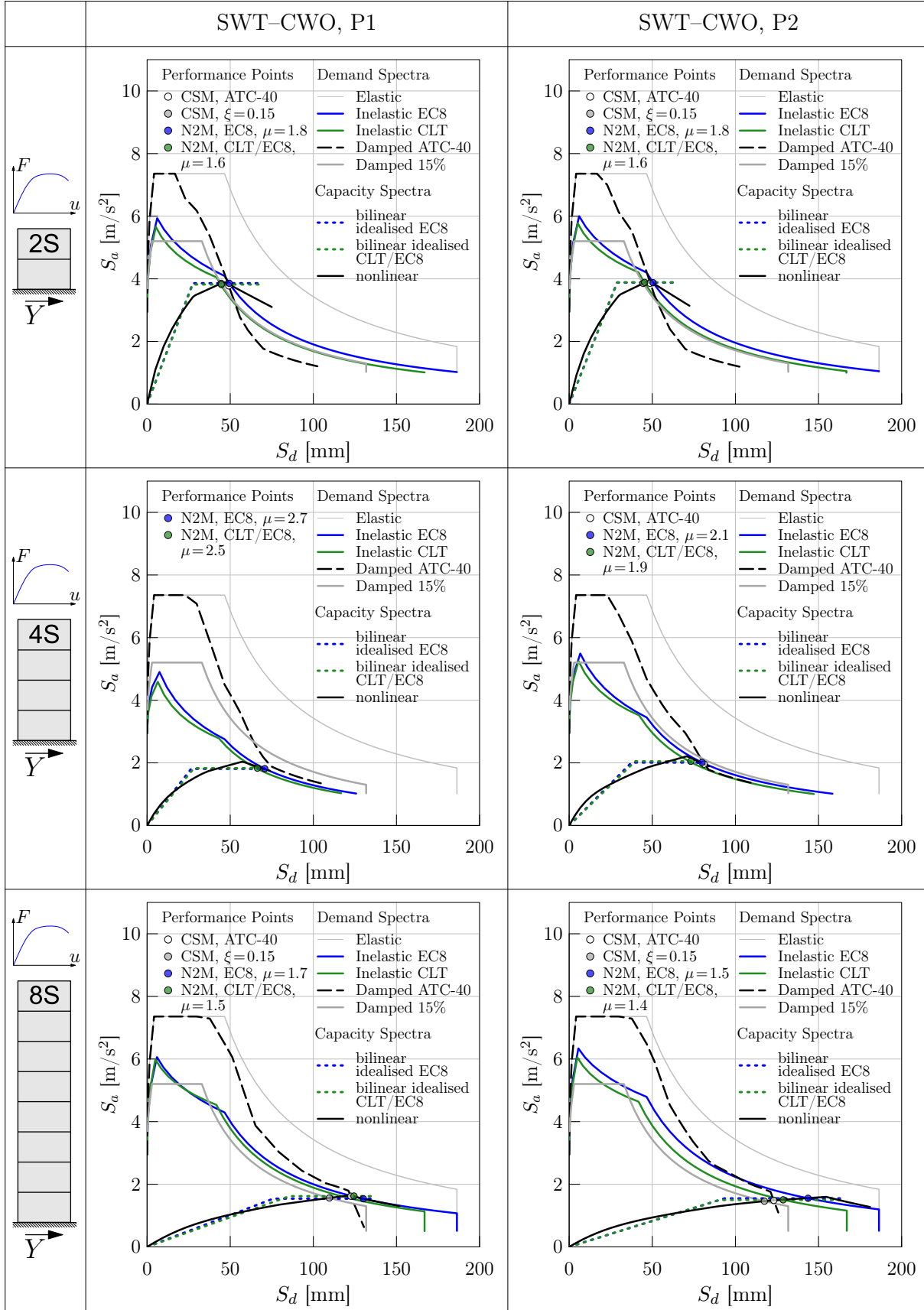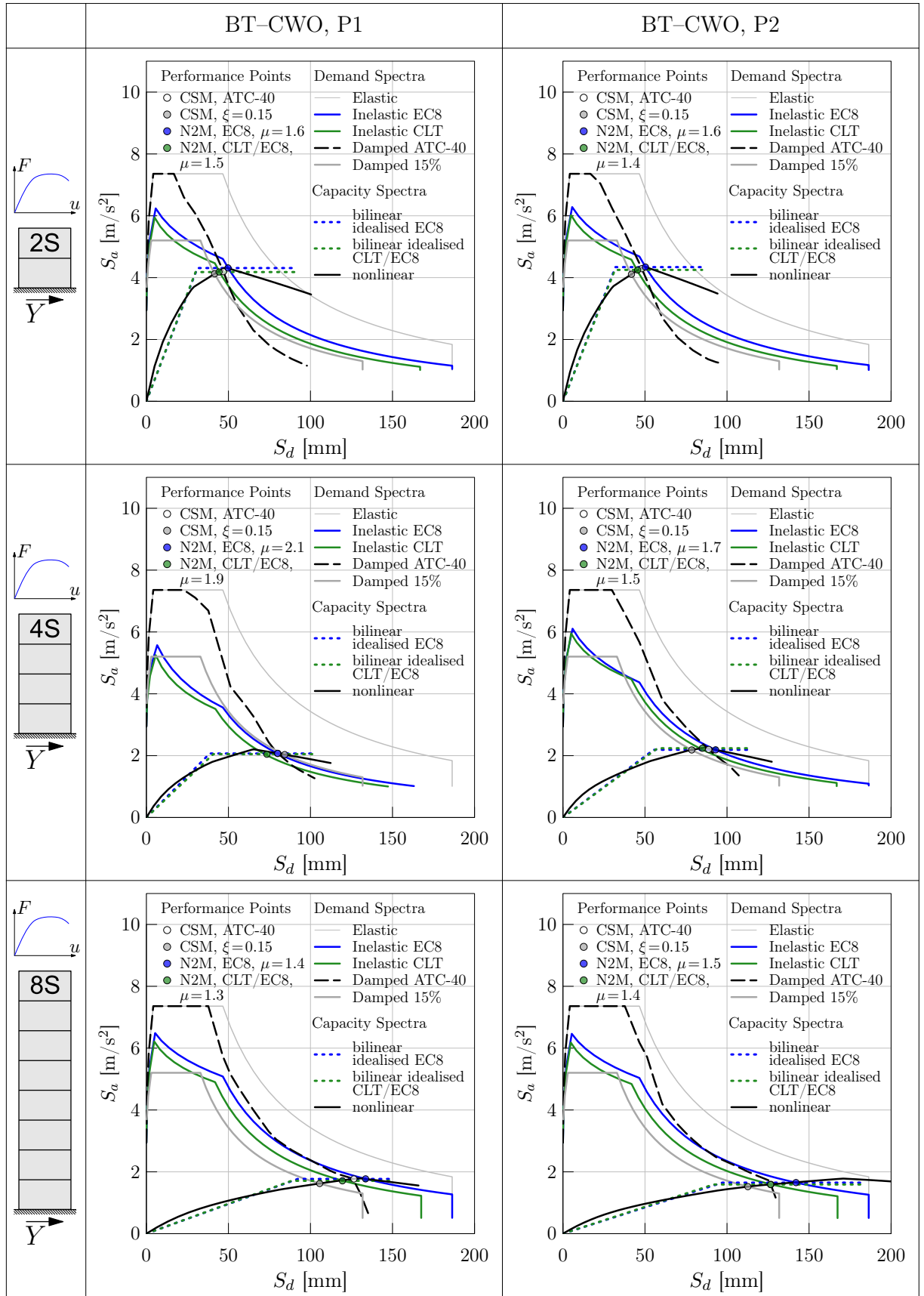**Figure C.3:** Determination of performance points for the SWT–CWO configuration in X-direction

Figure C.4: Determination of performance points for the BT–CWO configuration in X-direction

Figure C.5: Determination of performance points for the SWT–SWE configuration in Y-direction

Figure C.6: Determination of performance points for the BT–SWE configuration in Y-direction

Figure C.7: Determination of performance points for the SWT–CWO configuration in Y-direction

Figure C.8: Determination of performance points for the BT–CWO configuration in Y-direction

Schriftenreihe
Bauwerkserhaltung und Holzbau
Universität Kassel

Heft 1   Karsten Schilde: *Untersuchungen zum Verbund zwischen Beton und nachträglich aufgeklebten Kohlefaserlamellen am Zwischenrisselement.* Universität Kassel, 2005. ISBN 3-89958-149-0.

Heft 2   Carsten Pörtner: *Untersuchungen zum Verbund zwischen eingeklebten stiftförmigen faserverstärkten Kunststoffen und Holz.* Universität Kassel, 2005. ISBN 3-89958-191-1.

Heft 3   Uwe Pfeiffer: *Experimentelle und theoretische Untersuchungen zum Klebeverbund zwischen Mauerwerk und Faserverbundwerkstoffen.* Universität Kassel, 2009. ISBN 978-3-89958-780-7.

Heft 4   Martin Schäfers: *Entwicklung von hybriden Bauteilen aus Holz und hochfesten bzw. ultrahochfesten Betonen – Experimentelle und theoretische Untersuchungen.* Universität Kassel, 2010. ISBN 978-3-89958-986-3.

Heft 5   Heiko Koch: *Untersuchungen zum Last-Verformungsverhalten historischer Holztragwerke – Der abgestirnte Zapfen.* Universität Kassel, 2011. ISBN 978-3-86219-140-6.

Heft 6   Tobias Vogt: *Entwicklung eines Berechnungsmodells zur Beschreibung des Tragund Verformungsverhaltens von Holzrahmenwänden unter Berücksichtigung lokaler Effekte.* Universität Kassel, 2015. ISBN 978-3-86219-920-4.

Heft 7   Lars Eisenhut: *Geklebter Verbund aus Holz und hochfestem Beton. Untersuchungen zum Langzeitverhalten.* Universität Kassel, 2015. ISBN 978-3-86219-994-5.

Heft 8   Johannes Hummel: *Displacement-based seismic design for multi-storey cross laminated timber buildings.* Universität Kassel, 2017. ISBN 978-3-7376-0288-4.